

**ATTRIBUTE-DRIVEN FLUID REPLACEMENT MODELING AND
RESERVOIR CHARACTERISATION OF TETEMU FIELD,
ONSHORE NIGER DELTA, NIGERIA**

Rotimi SALAMI
B.Sc. (Obafemi Awolowo University, Ile-Ife)
M.Sc. (Ibadan)
172963

**A Thesis submitted to the Department of Geology
in partial fulfillment of the
requirements for the award of the degree of**

Doctor of Philosophy

of the

University of Ibadan

August 2023.

CERTIFICATION

This is to certify that this research was carried out by Rotimi SALAMI (172963) under my supervision and approved by the examination committee of the Department of Geology, Faculty of Science, University of Ibadan in Partial fulfillment for the award of Ph.D. degree in Geology.

.....

Supervisor
M.E. Nton
B.Sc. (Hons) (Calabar), M.Sc., Ph.D. (Ibadan)
Professor of Petroleum geology and sedimentology
Department of Geology
University of Ibadan

DEDICATION

This research is dedicated to the all sufficient God, the source of life, who has made it possible to complete this task with His help.

ACKNOWLEDGEMENTS

My profound gratitude goes to my supervisor, Prof. M. E. Nton, for his continuous support and contribution since the days of Master's degree program to this Ph.D. research work. Sir, I appreciate this privilege to work under your supervision. I appreciate Addax Petroleum Development Company, Nigeria for the provision of the data utilized for this research. My appreciation goes to Asset Management Team for their valuable assistance in securing the data and Mrs. Olare Jemine, for her assistance. I appreciate the help of Mr. Komolafe Olayinka, NAPIMS, Lagos for his effort on the release of data.

I appreciate all my lecturers in the University of Ibadan; these include: The Head of Department, Prof. O. A. Okunlola, Prof. A. I Olayinka, Prof. O. A. Ehinola, Prof. G. O. Adeyemi, Prof. A. S. Olatunji, Dr. O. C. Adeigbe, Prof. M. A Oladunjoye, Prof. O. A. Boboye, Prof. A. T. Bolarinwa, Dr.O. O. Oshinowo, Dr. M. A. Adeleye, Prof. I. A. Oyediran, Dr.(Mrs) Ajayi and Dr. Aladejana among others. I am very grateful to Dr. M. O. Adeniyi, The Sub-Dean, Faculty of Science, University of Ibadan, for her guidance and corrections on the abstract for this Thesis. My special thanks goes to Dr. Kikelomo Ilori in the Post-graduate college, University of Ibadan for her corrections. Thank you for the words of encouragement and soul-lifting.

I appreciate my wife, Mrs. Oluwakemi SALAMI, for her support and encouragement. David, ROTIMI-SALAMI, Eunice, ROTIMI-SALAMI, and Elizabeth, ROTIMI-SALAMI, are well appreciated for their encouragement and love. Thank you for being a wonderful family. I must not forget to acknowledge my uncle, Prof. Dipo, Salami. Thank you for being a father indeed to me.

I am grateful to all my friends. I also thank the entire training team of Petroplay Nigeria for their love and support during the training sessions. Many thanks to Dr. Oladele Sunday and Mr. John Onanyemi for their assistance during the course of this work. Thank you to everyone that assisted me in this research. I am very grateful.

ABSTRACT

Change in saturation levels occurs in reservoirs during hydrocarbon production resulting in fluid replacement. This impacts on the mechanical and elastic properties of reservoirs and consequently, alters production model and forecast. Increasing occurrence of altered production model has necessitated the need to understand how these properties can trigger fluid replacement in hydrocarbon reservoirs. Mechanical and elastic properties can be harnessed to constrain Fluid Replacement Modeling (FRM) in two scenarios: increasing water and gas saturations (S_g) at various reservoir conditions. This research was designed to produce geological model to predict the responses of rock properties to fluid replacement and reservoir behaviour.

The FRM and reservoir characterisation were carried out using petrophysical and rock-physics analyses of wells A1, A2 and A3 of Tetemu Field, onshore Niger Delta. Petrophysics was employed to determine lithology, Net-Gross Ratio (NGR), shale volume (V_{shale}), porosity (ϕ_e) and saturations which were estimated by Gamma Ray (GR), neutron-density and resistivity logs. Depositional environments were deduced by GR signatures. Rock-physics was used to determine reservoir's stress state, elastic and mechanical properties' responses to increasing saturation. Young (E), Bulk (K) and Shear (G) moduli, Unconfined Compressive Strength (UCS), Compressibility (Cb) and Poisson ratio (ν) were derived from elastic properties such as Compressional wave velocity (Vp). Sand production potentials were estimated using G/Cb.

Four hydrocarbon reservoirs (A, B, C and D) were delineated. The NGR reduces from proximal to distal due to reduction in depositional energy. The reservoirs were relatively clean with V_{shale} less than 15.0% threshold. The V_{shale} increased in the direction of lower hydrodynamic flow. Reservoirs were deposited in fluvial channel, progradational and deltaic sands. Dynamic Rock Physics Template (RPT) showed pore pressure depletion in reservoirs A and D of A1 as well as A, B and D of A2. The density increase was attributed to increasing G and K when brine replaced hydrocarbon. Unconventional attenuation of Vp from 3.09-3.04, 3.13-3.08, 3.92-3.86, 3.53-3.49 and 3.87-3.80 km/s in A of A1 and A3, and D of A1, A2 and A3, respectively, were due to dissolved gases. The values of E and K increased exponentially from 21.45-21.67 GPa and 16.93-18.28 GPa in A of A2. The value of ν was higher in oil and brine but negligible in gas-sand. The G/Cb for all reservoirs were greater than 0.8×10^{12} psi² threshold. Increasing S_g resulted in reduction in E and UCS. The observed pore pressure depletion from RPT could cause well instability due to induced matrix stress. Anomalous behaviours of elastic parameters were attributed to dissolved gases, while a decrease in UCS and E in A and D of A1 and A3 will cause wellbore collapse. None of the reservoirs produced sand during hydrocarbon production. Enhanced recovery modeling generated decreased K and E which reduced the stiffness and brittleness of the reservoirs.

Unconventional attenuation of compressional wave velocity and the responses of bulk modulus in gas provided a pathway for prediction of reservoirs' responses to changing fluid saturations during hydrocarbon production. These models could be employed as templates for monitoring hydrocarbon reservoir performance.

Keywords: Reservoir fluid replacement, Rock compressibility, Bulk modulus, Pore pressure, Rock physics

Word count: 499

TABLE OF CONTENTS

	Page
Title page	i
Certification	ii
Dedication	iii
Acknowledgements	iv
Abstract	v
Table of Contents	vi
List of Figures	x
List of Tables	xvii
CHAPTER ONE: INTRODUCTION	
1.1 Background to The Study	1
1.2 Research Statement	3
1.3 Aim and Objectives	3
1.4 Scope of The Research	4
1.5 Location of The Study Area	5
CHAPTER TWO: LITERATURE REVIEW	
2.1 Previous Works Review on Rock Physics and Reservoir Characterisation	8
2.2 Basic Theory of The Study	12
2.2.1 Well Log Analysis	12
2.2.2 Petrophysical Analysis	12
2.2.2.1 Lithological Identification	12
2.2.2.2 Well Correlation	12
2.2.2.3. Volume of Shale (Vsh)	12
2.2.2.4 Net-Gross Ratio (NGR)	13
2.2.2.5 Porosity	14
2.2.2.5.1 Effective Porosity	14
2.2.2.5.2 Sonic Porosity Determination	14
2.2.2.5.3 Density Derived Porosity Determination	15

2.2.2.5.4 Neutron-Density Porosity	15
2.2.2.6 Saturation	16
2.2.2.7 Irreducible Water Saturation	19
2.2.2.8 Bulk Volume of Water	19
2.2.2.9 Fluid Distribution and Fluid Contacts	20
2.2.3 Identification of Depositional Environments	20
2.2.3.1 Irregular Shapes	20
2.2.3.2 Funnel Shapes	20
2.2.3.3 Cylindrical Shapes	20
2.2.3.4 Bell Shapes	21
2.2.4 Rock Physics - Fluid Substitutions	21
2.2.4.1 Reservoir Fluid And Seismic Properties	24
2.2.4.1.1 Deriving Share Wave Velocity	25
2.2.4.2 Wyllie Time-Average Equation	26
2.2.4.3 Gassmann's Equations	29
2.2.4.4 Static, Dynamic And Mechanical Properties	31
2.2.4.4.1 Poisson Ratio (ν)	34
2.2.4.4.2 Unconfined Compressive Strength	35
2.2.5 Sand Production	36
2.2.5.1 Shear Modulus to Bulk Compressibility Ratio	39
2.2.5.2 Schlumberger Sand Production Index (S/I)	39
2.2.5.3 Sand Production Mechanisms	39
2.2.5.3.1 Formation Strength	40
2.2.5.3.2 Changing in-situ Stresses	40
2.2.5.3.3 Production Rate	40
2.3 Regional Geological Settings	41
2.3.1 Basin Evolution and Tectonic Elements	45
2.3.2 Niger Delta Basin Stratigraphy	48
2.3.2.1 Akata Formation	48

2.3.2.2 Agbada Formation	50
2.3.2.3 Benin Formation	50
2.3.3 Niger Delta Depobelts	51
2.3.4 Niger Delta Basin Structures	53
2.3.4.1 Growth Fault	53
2.3.4.2 Shale Diaper	55
2.3.5 Niger Delta Basin and Petroleum Occurrence	59
2.3.6 Niger Delta Source Rocks	63
2.3.7 Niger Delta Basin Reservoir Rocks	66
2.3.8 Traps and Seals in The Niger Delta	66

CHAPTER THREE: MATERIALS AND METHODS OF STUDY

3.1 Data Gathering	70
3.2. Well Log Analysis	70
3.2.1 Petrophysical Parameters Evaluation	71
3.2.1.1 Lithological Identification	71
3.2.1.2 Well Correlation	71
3.2.1.3 Volume of Shale	71
3.2.1.4 Net-to-Gross Ratio (NGR)	72
3.2.1.5 Porosity	72
3.2.1.5.1 Neutron-Density Porosity	72
3.2.1.6 Saturation	73
3.2.1.7 Bulk Volume of Water	74
3.2.1.8 Fluid Distribution and Fluid Contacts	74
3.2.2 Identification of Depositional Environments	74
3.2.3 Rock Physics - Fluid Substitutions	75
3.2.3.1 Reservoir Fluid and Seismic Properties	75
3.2.3.2 Deriving Shear Wave (V_s) Information	76
3.2.3.3 Gassmann's Equations	77
3.2.3.4 Static, Dynamic and Mechanical Reservoir Properties	78
3.2.3.4.1 Bulk Modulus	78

3.2.3.4.2 Shear Modulus	79
3.2.3.4.3 Young's Modulus	79
3.2.3.4.4 Poisson's Ratio	80
3.2.3.4.5 Unconfined Compressive Strength (UCS)	80
3.2.4 Sand Production	81
3.2.4.1 Shear Modulus to Bulk Compressibility Ratio	81
 CHAPTER FOUR: RESULTS AND DISCUSSION	
4.1 Petrophysical Data Estimation	83
4.1.1 Net-to- Gross (N/G) Ratio	90
4.1.2 Volume of Shale (Vshale)	90
4.1.3 Porosity (ϕ)	91
4.1.4 Hydrocarbon and Water Saturation	92
4.2 Reservoir Fluid Distribution and Fluid Contacts	92
4.3 Reservoir Depositional Environments and Facies	104
4.4 Derivation of Reservoirs Shear Wave Information in The Study Area	109
4.5 Fluid Substitution Modeling	116
4.5.1 Static, Dynamic, Elastic and Mechanical Responses of The Reservoirs to Stress State	116
4.6 Dynamic, Elastic and Geomechanical Responses During Fluid Replacement	132
4.6.1 Increasing Water Saturation	132
4.6.1.1 Fluid Saturation's Effects on Elastic Properties of The Field Reservoirs	132
4.6.1.2 Responses of The Reservoir's Mechanical Properties to Fluid Replacement	146
4.6.1.2.1 Young Modulus	146
4.6.1.2.2 Bulk Modulus	147
4.6.1.2.3 Shear Modulus	148
4.6.1.2.4 Unconfined Compressive Strength (UCS)	149

4.6.1.2.5 Poisson Ratio	151
4.6.2 Increasing Gas Saturation (Enhanced Recovery)	153
4.6.2.1 The Impact of Higher Gas Saturation on The Seismic Characteristics of Reservoirs	153
4.6.2.2 Geomechanical Responses of The Reservoirs to Increasing Gas Saturation	174
4.6.2.2.1 Bulk Modulus, K	174
4.6.2.2.2 Young Modulus, E	175
4.6.2.2.3 Shear Modulus, G	175
4.6.2.2.4 Unconfined Compressive Strength (UCS)	175
4.6.2.2.5 Poisson Ratio, ν	176
4.7 Sand Production Potential	176
CHAPTER FIVE: SUMMARY, CONCLUSIONS AND RECOMMENDATIONS	
5.1 Summary	188
5.2 Conclusion	191
5.3 Recommendations	192
5.4 Contributions to Knowledge	192
REFERENCES	193

LIST OF FIGURES

Number		
Page		
1.1	Niger Delta Concession Map Highlighting The Location of The Tetemu Field. Inset is The Map of Nigeria (After Doust and Omatsola,1990)	6
1.2	Tetemu Field's A1, A2, And A3 Wells Are Shown on The Field's Base Map	7
2.1	Depositional Environments from SP Log Shape, Fiddier Creek Field, Weston County, United State of America. (From Tomasso & Wo, 2009)	22
2.2	Strain Types and The Relationship Between Stress and Strain (Zoback, 2007)	32
2.3	Map Showing Petroleum Systems and Province Outline in The Niger Delta (Adapted from Petroconsult, 1996)	42
2.4	Stratigraphic Section of The Niger Delta, Showing The Three Formations and The Continental Basement (After Stacher, 1995)	44
2.5	Separation of Gondwanaland into South America and Africa in A Triple Junction Within The Gulf of Guinea; The Failed Arm Formed The Benue Trough (After Tuttle <i>et al.</i> , 1999)	47
2.6	Niger Delta Stratigraphy Showing The Three Formations (Adapted from Shannon and Naylor,1989)	49
2.7	Main Depobelts in The Niger Delta (After Stacher, 1995)	52
2.8	Niger Delta Structural Profile Showing Listric Extension Faults, Diapirs and Gentle Fold Thrusts (After Ojo, 1996)	54
2.9	Structural Features and Related Traps in Niger Delta (Amended from Stacher, 1995)	56
2.10	Structural Styles in Niger Delta Showing The Formation of Shale Diapir (After Corredor <i>et al.</i> , 2005)	57
2.11	Formation of Diapiric Structures from Mud Volcano (After Van Rensbergen <i>et al.</i> , 1999)	58
2.12	Map Showing Niger Delta Prolific Oil Centres, Shale Prone Areas And Early Delta Lobes (Amended from Reijers <i>et al.</i> , 1997)	60
2.13	Cross-Section of The Niger Delta's Center Region Featuring The	

Sequence Stratigraphic Model, Mechanisms for Trapping Hydrocarbons, And Pathways for Their Migration. (After Stacher, 1995)	62
2.14 Seismic Line Extracted from The Western Niger Delta's Deepwater Region.. (Adapted from Olabode <i>et al.</i> , 2010)	65
2.15 Hydrocarbon Traps and Seals in The Niger Delta (After Stacher, 1995)	67
3.1 Summarized Workflow Chart of The Research Study	82
4.1 Well Correlation Panel Showing Lithofacies of Interest of Tetemu Field	84
4.2 A Well Correlation Diagram Showing The Continuity of Reservoirs along The Correlated Wells A2-A1-A3	86
4.3 The Distribution of Fluids (Water and Gas) in Reservoir A of Well A1 in The Tetemu Field, Indicating The Location of The Gas-Water Contact (GWC) at A Depth of 6679.5ft.	95
4.4 Fluid Distribution (Only Oil) in Reservoir B of Well A1 of The Study Area	96
4.5 Gas, Oil and Water Distribution in Reservoir C and D, With OWC at 2520.39 m (8269ft) in Reservoir C and GOC at 2608.78 m (8559ft) in Reservoirs D, Well A1 of The Study Field	97
4.6 Oil Distribution in The Reservoir A of Well A2 of The Study Area	98
4.7 Oil Distribution in The Reservoir B of Well A2 of The Study Field	99
4.8 Hydrocarbon Distributions Within The Reservoirs C and D of Well A2 of The Study Field	100
4.9 Gas and Water Distributions in The Reservoir A of Well A3 of Tetemu Field, With Gas-Water Contact at 6689ft	101
4.10 Oil Distribution in The Reservoir B of Well A3 of The Study Area	102
4.11 Fluid (Oil) Distribution in The Reservoirs C and Gas-Water Interphase in Reservoir D of Well A3 of The Study Area, With Gas-Water Contact (GWC) at 8540.5 Ft	103
4.12 Identification of Depositional Environment of Reservoir A Using GR Log Signatures	105
4.13 Identification of Depositional Environment of Reservoir B across The Three Wells Using GR Log Shapes	106

4.14 Identification of Depositional Environments of Reservoirs C and D across The Three Wells Using GR Log Shapes	108
4.15 Cross Plot Between Field P-Wave Log and Computed P-Wave Log for Reservoir D at Well A-1. There Is A Perfect Correlation between Both Logs With An Error of $1.8184e^{-007}$	110
4.16 Cross Plot between Field P-Wave Log and Computed P-Wave Log for Reservoir A at Well A-2. There Is A Very Good Correlation between Both Logs With An Error of $1.41522e^{-007}$	111
4.17 Cross Plot between Field P-Wave Log and Computed P-Wave Log for Reservoir D at Well A-3. There Is A Very Good Correlation between Both Logs With A Minimal Error of $2.10003e^{-007}$	112
4.18 Cross Plot of P-Wave vs. Computed S-Wave Log for Reservoir D at Well A-1, With An Empirical Trend Superimposed. X and Y in The Empirical Equation Are Vp and Vs Respectively	113
4.19 Cross Plot of P-Wave vs. Computed S-Wave Logs for Reservoir A at Well A-2, With An Empirical Trend Superimposed. X and Y in The Empirical Equation Are Vp and Vs Respectively	114
4.20 Cross plot of P-wave vs. computed S-wave log for reservoir D at well A-3, with an empirical trend superimposed. Note that x and y in the empirical equation are Vp and Vs respectively	115
4.21 The Vp/Vs Against P-Impedance Cross-Plots on Dynamic Rock-Physics Template (RPT) for Reservoir A in Well A-1 for Different Values of Water Saturation: A) Field Data at 43% Water Saturation; B, C, D Are Synthetic Data at 60%, 80% And 100% Water Saturation Respectively. The Arrows Indicate Different Geologic Trends (Conceptually): 1-Increasing Water Saturation; 2-Increasing Pore Pressure; 3-Decreasing Pore Pressure (Adapted from Avseth and Ødegaard, 2004)	117
4.22 The Vp/Vs Against P-Impedance Cross-Plots on Dynamic RPT for Reservoir D in Well A-1 for Different Values of Water Saturation: A) Field Data at 49.51% Water Saturation; B, C, D Are Synthetic Data at 70%, 90% And 100% Water Saturation Respectively. The Arrows Indicate	

- Different Geologic Trends (Conceptually): 1-Increasing Water Saturation;
2 Increasing Pore Pressure; 3-Decreasing Pore Pressure
(Adapted from Avseth and Ødegaard, 2004) 118
- 4.23 The Vp/Vs Against P-Impedance Cross-Plots on Dynamic RPT for
Reservoir A in Well A-2 for Different Values of Water Saturation:
A) Field Data at 50.9% Water Saturation; B, C, D Are Synthetic Data
at 70.9%, 88.4% And 100% Water Saturation Respectively. The Arrows
Indicate Different Geologic Trends (Conceptually): 1-Increasing Water
Saturation; 2-Increasing Pore Pressure; 3-Decreasing Pore Pressure
(Adapted from Avseth and Ødegaard, 2004) 119
- 4.24 The Vp/Vs Against P-Impedance Cross-Plots on Dynamic RPT for
Reservoir B in Well A-2 for Different Values of Water Saturation:
A) Field Data at 46.68% Water Saturation; B, C, D Are Synthetic Data
at 66.68%, 86.68% And 100% Water Saturation Respectively.
The Arrows Indicate Different Geologic Trends (Conceptually):
1-Increasing Water Saturation; 2-Increasing Pore Pressure;
3-Decreasing Pore Pressure (Adapted from Avseth and Ødegaard, 2004) 120
- 4.25 The Vp/Vs Against P-Impedance Cross-Plots on Dynamic RPT for
Reservoir D in Well A-2 for Different Values of Water Saturation:
A) Field Data at 42.12% Water Saturation; B, C, D Are Synthetic Data
at 62.12%, 82.12% And 100% Water Saturation Respectively.
The Arrows Indicate Different Geologic Trends (Conceptually):
1-Increasing Water Saturation; 2-Increasing Pore Pressure;
3-Decreasing Pore Pressure (Adapted from Avseth and Ødegaard, 2004) 121
- 4.26 The Vp/Vs Against P-Impedance Cross-Plots on Dynamic RPT for
Reservoir A in Well A-3 for Different Values of Water Saturation:
A) Field Data at 47.88% Water Saturation; B, C, D Are Synthetic Data
at 67.88%, 87.88% and 97.88% Water Saturation Respectively.
The Arrows Indicate Different Geologic Trends (Conceptually):
1-Increasing Water Saturation; 2-Increasing Pore Pressure;
3-Decreasing Pore Pressure (Adapted from Avseth and Ødegaard, 2004) 122

- 4.27 The V_p/V_s Against P-Impedance Cross-Plots on Dynamic RPT for Reservoir D in Well A-3 for Different Values of Water Saturation:
 A) Field Data at 33.68% Water Saturation; B, C, D Are Synthetic Data at 53.68%, 73.68% And 93.68% Water Saturation Respectively.
 The Arrows Indicate Different Geologic Trends (Conceptually):
 1-Increasing Water Saturation; 2-Increasing Pore Pressure;
 3-Decreasing Pore Pressure
 (Adapted from Avseth and Ødegaard, 2004) 123
- 4.28 Responses of Reservoir Elastic Parameter to Reservoir Fluid Replacement During Hydrocarbon Production As Water Saturation Increases Gradually from 0 to 100%: Plot A-F Revealed The Variation of Density, ρ (g/cm^3) With Increasing Water Saturation, S_w (%) in The Field Reservoirs. 133
- 4.29 Responses of Reservoir Elastic Parameters (Density, ρ and Compressional Wave Velocity, V_p) to Reservoir Fluid Replacement During Hydrocarbon Production As Water Saturation, S_w Increases Gradually from 0 to 100%: Plot H-L Showed The Behaviours of The Reservoir Compressional Wave Velocity, V_p and Density With Respect to Fluid Replacement by Adopting A Forward Modeling Approach 134
- 4.30 Responses of Reservoir Elastic Parameters (Compressional Wave Velocity, V_p and Shear Wave Velocity, V_s) to Reservoir Fluid Replacement During Hydrocarbon Production As Water Saturation, S_w Increases Gradually from 0 to 100%: Plot M-R Showed The Behaviours of The Reservoir Compressional Wave Velocity, V_p and Shear Wave Velocity, V_s With Respect to Fluid Replacement by Adopting A Forward Modeling Approach. 135
- 4.31 Responses of Reservoir Shear Wave Velocity, V_s to Fluid Replacement During Hydrocarbon Production As Water Saturation Increases Gradually from 0 to 100%: Plot S-U Showed The Behaviours of The Reservoir Shear Wave Velocity With Respect to Fluid Replacement Using Forward Modeling Approach. 136

4.32 Responses of Reservoir Mechanical Parameters (Young Modulus, E) to Reservoir Fluid Replacement During Hydrocarbon Production As Sw Increases from 0 to 100%: Plot 1-6 Showed The Reactions of The Reservoirs With Respect to Fluid Replacement Using A Forward Modeling Technique.	137
4.33 : Responses of Reservoir Mechanical Parameters (Young Modulus and Bulk Modulus) to Reservoir Fluid Subtitution During Hydrocarbon Production As Water Saturation Increases from 0 to 100%: Plot 1-6 Showed The Behaviours of The Reservoir During Fluid Replacement by Adopting A Forward Modeling Method.	138
4.34 Responses of Bulk Modulus and Shear Modulus to Fluid Subtitution During Hydrocarbon Production As Sw Increases from 0 to 100%: Plot 1-6 Showed The Behaviours of The Reservoir During Fluid Replacement Using A Forward Modeling Method.	139
4.35 Responses of Reservoir Mechanical Parameters (Shear Modulus and Unconfined Compressive Strength) to Fluid Replacement As Sw Increases from 0 to 100%: Plot 1-6 Revealed The Trend of Behaviours of The Reservoir During Fluid Replacement Using A Forward Modeling Method.	140
4.36 Responses of UCS to Fluid Replacement (plot 1-4) As Sw Increases from 0 to 100%: Plot 5-6 Revealed The Variation of UCS With Density.	141
4.37 Plot 1-5 Showed The Variation of The Reservoir Strength, UCS With Reservoir Rock Density While Plot 6 Revealed The Response of The Poisson Ratio to Fluid Replacement As Sw Increases from 0 to 100%.	142
4.38 Plot 1-6 Revealed The Response of The Poisson Ratio to Fluid Replacement As Sw Increases from 0 to 100% During Oil and Gas Production.	143
4.39 The Plots of Reservoirs' Elastic Parameters Behaviours During Enhanced Recovery Operations by Adopting A Forward Modeling Approach As Gas Saturation Increases from 0-80% in The Reservoirs: 1) Showed Gradual Reduction in Density, ρ As Gas Saturation, S_g	

Increases in Reservoir C of Well A1, Plot 2, 3, 4,5 and 6 Displayed Similar Trend During Hydrocarbon Production.	160
4.40 Reservoirs Elastic Parameters, Shear Wave Response to Increasing Gas Saturation, from 0 to 80% During Enhanced Operations by Forward Modeling: Plot 1-6 Showed Gradual Increase in The Value of Vs During Fluid Replacement.	161
4.41 Plots 1- 6 Revealed The Reservoir’s Behaviours With Respect to Compressional Waves Velocity, Vp During Oil and Gas Production As Sg Increases from 0 to 80% Using A Forward Modeling Approach.	162
4.42 Reservoirs Mechanical Parameters (E) Response to Increasing Sg, from 0 to 80%: Plot 1-6 Showed Responses of Specific Reservoirs During Hydrocarbon Production.	163
4.43 Reservoirs’ Bulk Modulus Responses to Increasing Gas Saturation, from 0 to 80% During Enhanced Recovery by Forward Modeling: Plot 1-6 Showed Responses of The Reservoirs During Production.	164
4.44 Shear Modulus Behaviours to Increasing Sg from 0 to 80% During Production: Plot 1-6 Showed Responses of Specific Reservoirs.	165
4.45 Unconfined Compressive Strength, UCS Response to Increasing Gas Saturation, from 0 to 80% During Enhanced Recovery Operations by Forward Modeling: Plot 1-6 Showed Responses of Specific Reservoirs During Hydrocarbon Production.	166
4.46 Poisson Ratio Response to Increasing Sg, from 0 to 80% During Production: Plot 1-6 Showed Responses of Specific Reservoirs.	167

LIST OF TABLES

TABLE

2.1: Velocity and Acoustic Slowness (Transit Time) Values for Common Reservoir Fluids and Lithologies (after Carmichael, 1982)	28
2.2: The Empirical Formulas Showing The Connections Between Unconfined Compressive Strength (UCS) And Various Parameters in Sandstone. (After Chang <i>et al.</i> , 2006)	37
2.3: Values of Unconfined Compressive Strength of Some Rocks (Adapted from Attewell and Farmer, 1976)	38
4.1: Interpretation of The Log Signatures in Fig.4.1 for Reservoirs' Depositional Environments	85
4.2: Petrophysical Parameters of Well A1 Reservoirs of The Study Field	87
4.3: Petrophysical Parameters of Well A2 Reservoirs	88
4.4: Petrophysical Parameters of Well A3 Reservoirs of Tetemu Field	89
4.5: Reservoir Fluid Distribution And Fluid Contacts in The Study Field	94
4.6: Elastic Parameters of Reservoir A of Well A1 of Tetemu Field	124
4.7: Elastic Parameters of Reservoir D of Well A1 of Tetemu Field	126
4.8: Elastic Parameters of Reservoir A of Well A2 of Tetemu Field	127
4.9: Elastic Parameters of Reservoir B of Well A2 of Tetemu Field	128
4.10: Elastic Parameters of Reservoir D of Well A2 of Tetemu Field	129
4.11: Elastic Parameters of Reservoir A of Well A3 of Tetemu Field	130
4.12: Elastic Parameters of Reservoir D of Well A3 of Tetemu Field	131
4.13 Elastic Constants Calculation for The Prediction of Sand Production in Reservoir A of Well A1 of The Study Field	154
4.14: Summary of The Data and Calculated Elastic Constants for Sand Production Prediction in Reservoir D of Well A1 of The Study Field	155
4.15: The Calculated Elastic Constants for Sand Production Prediction in Reservoir D of Well A1 of The Study Field.	156
4.16: Summary of The Data and Calculated Elastic Constants for Sand Production Prediction in Reservoir B of Well A2 of The Study Field	157
4.17: Summary of The Data and Calculated Elastic Constants for Sand Production Prediction in Reservoir D of Well A2 of The Study Field	158

4.18: Summary of The Data and Calculated Elastic Constants for Sand Production Prediction in Reservoir A of Well A3 of The Study Field	159
4.19: Summary of The Data and Calculated Elastic Constants for Sand Production Prediction in Reservoir D of Well A3 of The Study Field	168
4.20: Summary of The Petrophysical /Mechanical Parameters of Well A1 of The Study Field	169
4.21: Summary of The Petrophysical /Mechanical Parameters of Well A2 of The Study Field	170
4.22: Summary of The Petrophysical /Mechanical Parameters of Well A3 of The Study Field	171
4.23: The Enhanced Operation Responses, Calculated Elastic and Geomechanical Parameters of Reservoir C of Well A1 of The Study Field	172
4.24: The Modeling Responses (EOR), Calculated Elastic and Geomechanical Parameters of Reservoir A of Well A2 of The Study Wells	173
4.25: The Modeling Responses (EOR), Calculated Elastic and Geomechanical Parameters of Reservoir B of Well A2 of The Study Field	178
4.26: The Enhanced Operation and Calculated Elastic / Geomechanical Parameters of Reservoir C of Well A2 of The Study Field	179
4.27: The Enhanced Oil Recovery and Calculated Elastic / Geomechanical Parameters of Reservoir B of Well A3 of The Study Field	180
4.28: The Enhanced Operation Responses, Calculated Elastic and Geomechanical Parameters of Reservoir C of Well A3 of The Study Field	181
4.29: Computed P and S- Waves Impedenaces, Poisson Ratio and Velocity Ratio in Reservoir C of Well A1 of The Study Field	182
4.30: Computed P and S- Waves Impedenaces, Poisson Ratio and Velocity Ratio in Reservoir A of Well A2 of The Field	183
4.31: Computed P and S- Waves Impedenaces, Poisson Ratio and Velocity Ratio in Reservoir B of Well A2 of The Study Field	184
4.32: Computed P and S- Waves Impedenaces, Poisson Ratio and Velocity Ratio in Reservoir C of Well A2 of The Field	185

4.33: Computed P and S- Waves Impedenaces, Poisson Ratio and Velocity Ratio in Reservoir B of Well A3 of The Study Field	186
4.34: Computed P and S- Waves Impedenaces, Poisson Ratio and Velocity Ratio in Reservoir C of Well A3 of The Field	187

CHAPTER ONE

INTRODUCTION

1.1 Background to The Study

Fluid substitution plays a significant role in the analysis of seismic attributes and offers interpreters a valuable tool to simulate and quantify different fluid scenarios that could potentially cause observed changes in amplitude with offset (AVO) or time-lapse responses (Smith *et al.*, 2003). This knowledge has helped over time to better understand rock-fluid relationship and interaction at different pore - fills and saturation levels (Han and Batzle, 2004). The effects of porosity, mineral composition, and fluid on seismic velocities can be modeled by combining empirical relationships and theoretical formulations (Han and Batzle, 2004).

For proper application of fluid substitution theories and ascertaining the weaknesses and strengths of various methods commonly used by researchers today, it is essential to fully understand basic concepts of rock's elastic moduli and the saturating fluid bulk modulus. On the contrary, reservoir characterization encompasses the integration of all accessible data to establish the shape, distribution of physical parameters, and fluid flow properties within a petroleum reservoir (Adiela, 2016). The objective is to precisely and quantitatively simulate the architecture, connectivity, and fluid flow properties of a reservoir, including porosity, permeability, and fluid saturations.

Reservoir characterization involves reservoir modeling activities, to simulate the flow of fluids (Stephen, 2007). It also involves the absolute comprehension of a reservoir, including its response to the production strategy, with the aim of developing a detailed understanding of its characteristics (Kramers, 1994). The Niger Delta region, located along the coast of the Gulf of Guinea in West Africa's equatorial zone, is a prolific delta spanning between Longitudes 5⁰ and 8⁰ E and Latitudes 3⁰ and 6⁰ N. The basin is recognized as one of the

world's most prolific Tertiary deltas in terms of hydrocarbon production (Selley, 1997). Numerous researchers have thoroughly investigated the sedimentology, stratigraphy, paleoenvironments and structural arrangement of the reservoirs within the delta. They include; Selley,1998, Rider, 1999; Ekweozor, 2004 and several others. The Agbada Formation of the basin, which is an unconsolidated sand is the hydrocarbon producing bed. It is made up of alternation of shales and sandstones and it ranges from 30m /100ft to 4600m /15,000ft in thickness (Ekweozor, 2004).

In the Niger Delta basin, the Agbada Formation stands out as the primary reservoirs for hydrocarbon deposits, while the shale formations serve as effective barriers both vertically and horizontally, ensuring the containment of the hydrocarbons. Geologic models play a crucial role in identifying reservoir heterogeneities and addressing uncertainties arising from limited well data, insufficient resolution in geophysical data sets, and challenges associated with indirectly measuring reservoir parameters through seismic, logging, and production data (Adeoti *et al.*, 2014).

The process of reservoir modeling can facilitate precise estimation of the probability distribution of hydrocarbons, assist in geosteering wells to optimal locations, and provide valuable input for reservoir simulation. Within the oil and gas industry, reservoir modeling encompasses the creation of a computer-based model of a petroleum reservoir. This process aims to enhance the accuracy of reserve estimation and facilitate decision-making concerning field development strategies (Singh *et al.*, 2013).

A reservoir model is a representation of the physical space within a reservoir, where the reservoir volume is discretized into a grid consisting of distinct cells. This grid can be either regular or irregular in its arrangement. Typically, reservoir models employ a three-dimensional array of cells; however, there are instances where one-dimensional (1D) or two-dimensional (2D) models are utilized as well (Stephen, 2007). Each cell within the reservoir model is assigned values for attributes such as porosity, permeability, and water saturation. The value of each attribute is uniformly applied throughout the volume of the reservoir that is represented by the respective cell (Stephen, 2007). Commercially available software is utilized for the construction, simulation, and analysis of reservoir models.

Reservoir models are created for a range of purposes in the exploration and production industry (Singh *et al.*, 2013). These purposes encompass development planning, reserve

estimation, evaluating acquisitions or farm-in opportunities, redeveloping mature fields, managing assets over the production lifecycle, making decisions regarding production cessation or abandonment, as well as execution and monitoring of operations. Fluid substitution affects reservoir properties and wellbore stability during oil and gas production. The fluid substitution effects may result in unexpected changes in the production model and forecast and this could completely nullify the working model during production (Smith *et al.*, 2003). In this study, certain reservoir properties which were sensitive to the changing level of fluid saturation were harnessed to constrain fluid substitution models.

1.2 Research Statement

During production, there is a change in saturation levels and therefore fluid substitution occurs (Smith *et al.*, 2003). Fluid substitution usually imparts on the geo-mechanical properties and stability of the wellbore. Unfortunately, however, little or no attention is given to it during field evaluation or development. According to Smith *et al.*, (2003), the fluid substitution effect can result in drastic changes in the initially established production model and forecast, which could completely nullify the working model as production continues.

Certain seismic and mechanical properties are sensitive to the changing level of fluid saturation, meaning, one can harness the sensitivity of the attributes to constrain fluid substitution models. It is therefore important to model such properties such as, seismic velocities, geomechanical properties and density of reservoirs at various reservoir conditions.

1.3 Aim and Objectives

This study is aimed at producing a detailed geological model; driven by seismic attributes, which can serve as a predictive tool for reservoir monitoring and testing the responses of rock properties with changing fluids and fluid saturation during production.

The study objectives are to;

- i. analyse the petrophysical data of the three wells and determining the flow units,

- ii. evaluate the reservoir fluid types and contacts and reconstructing the environment of depositions,
- iii. derive a localized and modified Castagna and Gassmann's fluid substitution equation,
- iv. establish the pore pressure regime and stress state of the reservoirs of the Field,
- v. determine the seismic and mechanical responses of the reservoirs,
- vi. estimate the sand production potentials of the Field.

1.4 Scope of The Research

The scope of this research will involve a comprehensive reservoir characterization process that utilizes well log suites and seismic data. This approach aims to determine the properties of reservoir rocks and understand their responses as fluid saturation changes during production. To achieve this, the acquired data are quality checked to filter errors and remove unwanted signals. Then, the analysis of well logs was done to determine the well correlation, lithological identification and estimate the reservoir petrophysical properties. Resistivity, Neutron, and Density logs were utilized to ascertain fluid distributions within the reservoirs and identify the various contacts. The GR log data was utilized to establish the deposition environments for all delineated reservoirs within the field.

To investigate the responses of each reservoir to fluid substitution during production, these involved the building of fluid replacement modeling that will consider two production scenarios (increasing water and gas saturation). The parameters such as velocities of compressional and shear waves, density of the rock and elastic moduli are important ingredients required in Rock Physics Template (RPT) to establish production models. Since, the shear wave, V_s could not be extracted from the log, a combination of Gassmann fluid replacement relation and Castagna's equation was used to compute shear wave for each reservoir at each well location. This is necessary in order to reduce errors that are commonly associated with Castagna's derived shear wave information, particularly in unconsolidated reservoirs such as Niger Delta.

The combination of these two empirical relations helped to create a localized Castagna's relation for the study field which could form the basis for subsequent works. Then, the crossplots of velocity ratios against acoustic impedance along each pay interval are used to determine the reservoir stress conditions and pore pressure. Finally, the elastic parameters of each reservoir at different levels of water and gas saturations were calculated to determine their responses to various production scenario (increasing water and gas saturations). In addition, the sand generation potentials for each reservoir during hydrocarbon production were estimated using the empirical ratios of shear modulus to compressibility.

1.5 Location of The Study Area

Tetemu field is situated within the onshore portion of the Niger Delta and belongs to one of the producing companies (Fig. 1.1). The study wells A1, A2, and A3 are situated within the field's core area, as indicated in the base map (Figure 1.2).

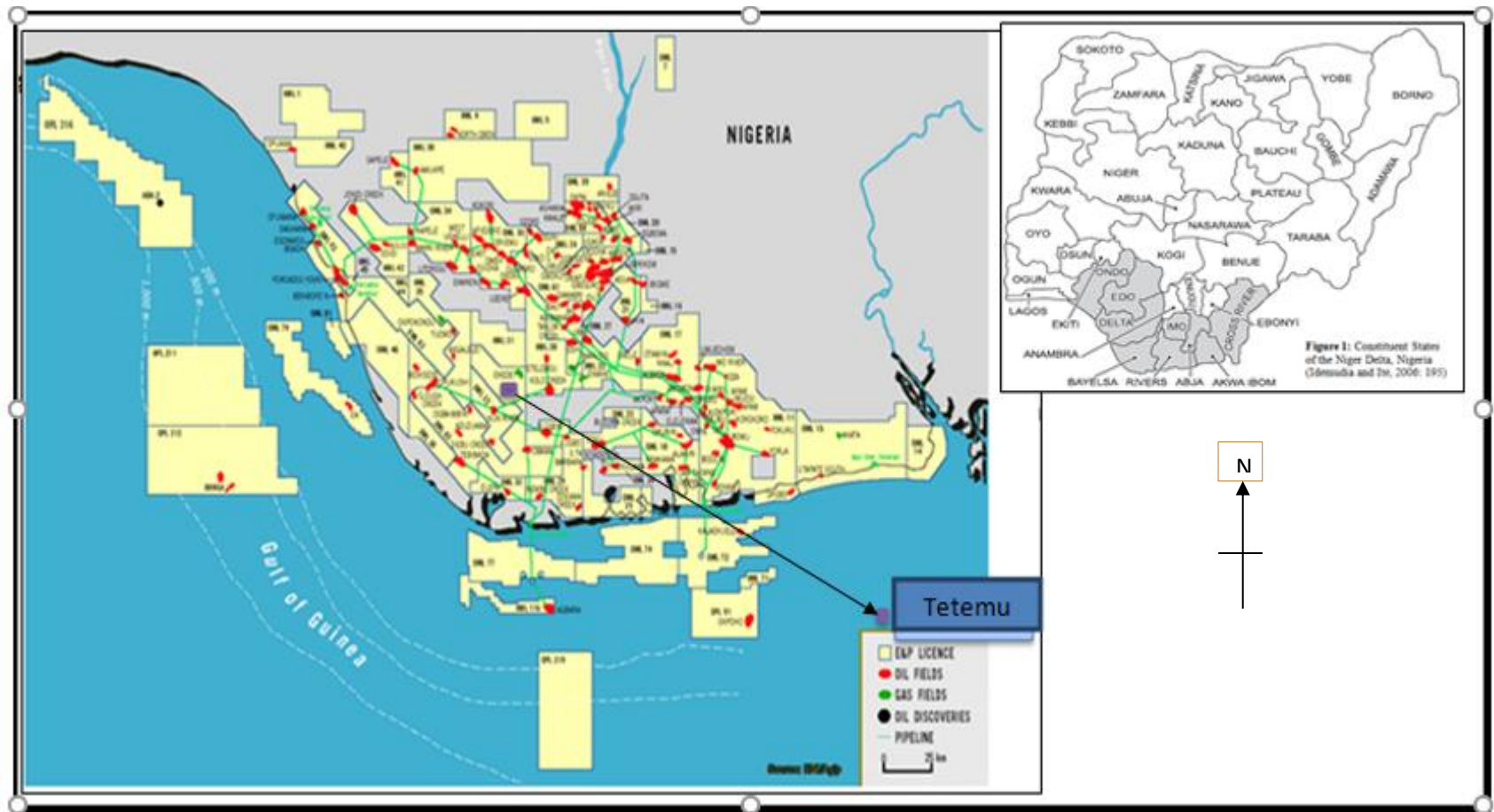


Figure 1.1: Niger Delta Concession Map Hghlighting The Location of The Tetemu Field. Inset Is The Map of Nigeria (After Doust and Omatsola,1990)

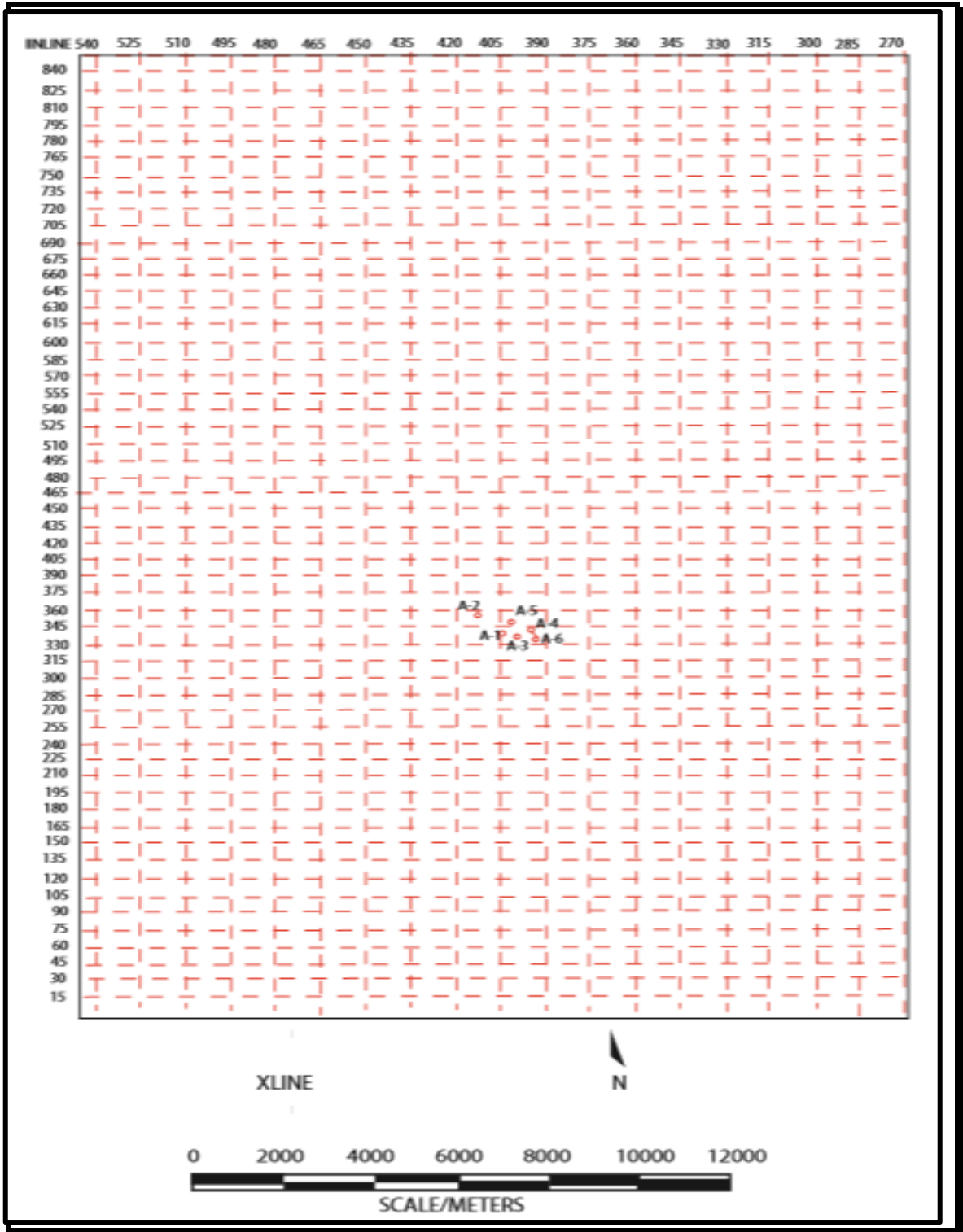


Figure 1.2: The Base Map of The Tetemu Field Displays The Locations of Wells A1, A2, And A3.

CHAPTER TWO

LITERATURE REVIEW

2.1 Review of Previous Works on Rock Physics and Reservoir Characterisation

Han and Batzle, (2004), conducted research on the Gassmann's equation and its impact on seismic velocities due to fluid saturation. Their work highlighted the weaknesses in some of the underlying assumptions in the Gassmann's equation. They established that some factors could be introduced into the equation to make it more physically useful and reliable such as the use of a simplified Gassmann's relation which provides a clear understanding of how fluid saturation influences the bulk modulus of the rock, thereby elucidating the physical mechanisms that control these effects.

Smith *et al.*, (2003) established a workflow to execute the Gassmann's relation and provided a guideline for the execution of fluid substitutions. They also highlighted the invasion effect, computed from a deep resistivity device (such as LLD or ILD).

Lawson-Jack *et al.*, (2019) studied the deformability and strength of the reservoirs of part of the Niger Delta field by employing well logs to evaluate the mechanical parameters such as shear, bulk and young moduli, unconfined compressive strength, poisson ratio and compressibility of reservoir rock during production. The results revealed that the reservoir units demonstrate decreased values for Poisson's ratio, shear modulus, bulk modulus, Young's modulus, as well as reduced unconfined compressive strength, while demonstrating higher values of compressibility and porosity compared to the shale units.

Based on their research, it was suggested that there is a significant potential for sanding during production, unless the critical flow rate is kept below 17.1MPa. This is important to prevent pressure differentials and frictional drag forces from exceeding the compressive strength of the rock, that could potentially result in the production of sand. Purnamasari, *et*

al., (2014) proposed three models, namely the friable-sand model, the contact cement model, and the constant cement model, to describe the transition of water-saturated rock to gas-saturated rock. They also utilized Gassmann theory as a predictive tool to estimate pore fluid characteristics based on the elastic properties of water-saturated sandstone reservoirs. Their conclusion highlighted that rock physics models play a crucial role in establishing the relationship between velocity trends and porosity, as well as velocity trends and clay content in reservoir rocks.

Singh, *et al.*, (2013) in their study on factors affecting 3D reservoir interpretation and modeling on Greenfield and Brownfield in Madrid, Spain, established the factors responsible for uncertainty in production forecast. According to them, these include inadequate geological (static) models, inadequate simulation (dynamic) models, very high value of original or remaining hydrocarbon in-place (OHIP), and a lack of comprehensive tools for effectively integrating all available data. They developed models that involved a closed-loop workflow which facilitated close interaction between static and dynamic models, enabling them to capture the complete range of uncertainties and assess their impacts on production forecasts.

Fidelis and Akaha, (2016) presented a geomechanical assessment of an oil field located onshore in the Niger Delta. They established that, evaluation of geomechanical properties, in-situ stress, and pore pressure of the reservoir are important requirements in achieving an optimal production and enhanced recovery for stable and productive wells design. They used wireline logs to estimate geomechanical properties of the wells and established the instability indicators of the wellbore. Adeoti *et al.*, (2014) utilized well logs and 3-D seismic data in an offshore Niger Delta field to demonstrate the efficacy of 3-D static modeling as a valuable tool for gaining a deeper understanding of the spatial distribution of discrete and continuous reservoir properties.

They established a framework that can be used in future endeavors to predict reservoir performance and understand production behavior. According to Adeoti *et al.*, (2014), the precision and dependability of the utilized data play a crucial role in the effective implementation of reservoir modeling and in comprehending the properties of the reservoir within the surrounding rock. The utilization of modeling techniques facilitated the three-

dimensional visualization of the subsurface, leading to an improved comprehension of reservoir heterogeneities. This, in turn, contributed to enhancing recovery rates, as low recovery rates often result from inefficient sweep caused by limited knowledge of inter-well-scale heterogeneities (Patrick *et al.*, 2002).

It is important to acknowledge that a reservoir can only be developed and produced once, and any mistakes or errors can have significant and detrimental consequences in terms of both loss and inefficiency (Lucia and Fogg, 1990; Lake *et al.*, 1991; Worthington, 1991; Haldersen and Dasleth, 1993; Dubrule, 2003). Accurate reservoir modeling is crucial to accurately estimate reserves and identify the most efficient methods for economically recovering the maximum amount of petroleum from the reservoir. Dubois *et al.*, (2003) integrated core data, wireline logs, fluid properties, and production/test data to construct a comprehensive static model for the entire Hugoton Field, which encompasses the Hugoton and Panoma areas in Kansas and the Guymon-Hugoton region in Oklahoma.

This modeling effort was undertaken for asset management projects related to the field. Through their efforts, they successfully created a detailed model that effectively captured both vertical and lateral heterogeneity at various scales, including the well, multi-well, and field levels. This model serves as a valuable tool for reservoir management purposes. Oladipo, (2011) carried out a reservoir characterization survey in an onshore, Niger Delta field. In the study, a three-dimensional static model of the reservoir was constructed by integrating various data sources, including 3-D seismic data, well logs, deviation data, core samples, checkshot data, Pressure-Volume-Temperature (PVT) data, and production data. He identified seven hydrocarbon-bearing reservoir sands which were characterized by building a high resolution geological model from stratigraphic, structural and petrophysical models. He reached the conclusion that the reservoir primarily consists of deltaic deposits, specifically shoreface and barrier bar sand deposits, indicating a predominantly paralic facies environment.

Emeka *et al.*, (2015), combined biostratigraphy, well logs, checkshot data, and seismic data to construct a comprehensive earth model of the Alpha Field in the Niger Delta. The main objective of this modeling effort was to facilitate reservoir simulation and aid in well planning activities. They established that the construction of the earth model assisted in

stochastic simulation of the connectivity and spatial distribution of the sedimentary facies. They identified three oil bearing reservoir sands which included sands 1, 2 and 3. They also established that sand 1 was deposited in distributary mouth-bar/bar sand/regressive barrier island; sand 2 was deposited in channel fills and while reservoir sand 3 was deposited in distributary mouth-bar/channel fills. From their findings, the field is economically viable, with STOIP and GIIP estimated to be 75-90 MMSTB and 50 MMSCF respectively.

Toluwalope *et al.*, (2015) combined seismic and well logs data to carry out field development plans for Obisesan oil field, Niger Delta by building a geological model using qualitative and quantitative approaches. They delineated five reservoir sands, from which four were oil-bearing, while structures such as anticlinal, unconformities, sand lenses and channel sands served as major traps in the field. Obi-Chidi and Adiola, (2016) conducted a study focused on facies modeling and petrophysical properties of an X-Field within the onshore region in the Niger Delta. Their study focused on integrating seismic and well log data to develop a static model of the reservoir within the field. They delineated three sands, E1, E2 and F1, and inferred that they were associated with high energy environment.

Mode and Anyiam, (2007) published a report detailing the reservoir characterization of the "Paradise Field" in the Niger Delta. In their study, they identified and delineated four reservoirs based on data obtained from five wells. They determined that the hydrocarbon saturation in the wells exhibited an increasing trend towards the distal portion of the dip section, ranging from 40% to 90%. Correspondingly, there was a corresponding decrease in water saturation within the intervals of interest. The study concluded that the reservoirs have good permeability and porosity to accommodate large hydrocarbon yield, which may improve significantly as sedimentation proceeds basinwards.

Khamehchi and Reisi, (2015) determined the shear and bulk modulus ratio in some oilfields in Iran, with the aim of evaluating sand production during oil/gas production. In their study, empirical relationship involving shear modulus and bulk compressibility was connected to the influx of sand. The above reviews could be expanded and improved upon by critically analysing the responses of the reservoir rock parameters to fluid substitution during production by employing the integration of well-based rock physics with petrophysics analyses.

2.2 Basic Theory of The Study

2.2.1 Well Log Analysis

Ellis and Singer, (2007) stated that the interpretation of well logs entailed integrating the responses of logging tools, geological understanding, and supplementary measurements or information to extract the most comprehensive petrophysical information regarding subsurface formations. The petrophysical analysis encompassed the examination of the physical and chemical attributes of rocks and the fluids they contain. It particularly emphasized properties associated with pore systems, including the distribution of fluids within them and their flow characteristics, as highlighted by Archie, (1950).

2.2.2 Petrophysical Analysis

2.2.2.1 Lithological Identification

The GR measures the amount of shale in a reservoir (Schlumberger, 1989). Schlumberger (1989) states that a leftward deflection on the gamma-ray (GR) log indicates the presence of sand bodies, whereas a rightward deflection indicates the presence of shale units. The scale of GR log is set between 0-150 API, with 65 API units as the central cut off point. This means values greater than 65 API are shale while sandstones are less than 65 API.

2.2.2.2 Well Correlation

The gamma-ray (GR) and resistivity logs are valuable tools for correlation purposes, applicable in both open and cased boreholes Schlumberger, (1989). Daniel and Richard, (2003) emphasize the significant role of well logs in correlating equivalent strata between different wells. Wells are correlated by applying the lithological signatures that indicate similar depositional processes and environment (Daniel and Richard, 2003).

2.2.2.3. Volume of Shale (Vsh)

This involves identifying the zones characterized by a low volume fraction of shale (Vshale), commonly referred to as clean zones, as described by Ellis and Singer, (2008). According to Schlumberger, (1989), the magnitude of the GR signal typically rises in correlation with an increase in shale content. In recent times, alternative approaches have

been utilized to estimate the volume of shale. These include methods such as analyzing the separation between neutron and density measurements, examining the distribution obtained from nuclear magnetic resonance (NMR), and performing elemental spectroscopy analysis, as outlined by Ellis and Singer, (2008). As stated by Asquith (2004), the magnitude of the gamma-ray (GR) count within the Formation of interest is indicative of its shale content. The GR log can be employed to determine the shale volume by calculating the GR index in equation (2.1) from Asquith and Gibson, (1982) formula:

$$I_{gr} = \frac{GR_{log} - GR_{min}}{GR_{max} - GR_{min}} \quad (2.1)$$

Where;

I_{gr} = GR index demonstrating a linear response to the amount of clay or shale present

GR_{log} = Gamma ray log measurement taken at the specific depth being investigated

GR_{min} = GR log value obtained from a nearby zone consisting of clean sand.

GR_{max} = GR log value recorded from a neighboring shale formation.

By applying Larionov, (1969) equation involving Tertiary rocks, shale volume (V_{sh}) can be expressed as:

$$V_{sh} = (2^{2I_{gr}} - 1) \times 0.083 \quad (2.2)$$

Where;

V_{sh} = shale volume

I_{gr} = GR index

2.2.2.4 Net-Gross Ratio (NGR)

This parameter quantifies the percentage of clean sand within a reservoir unit. The gross sand represents the entire thickness, while the non-net sand refers to the shale-rich intervals within the gross sands, which divide it into distinct flow units. Consequently, the net sand is calculated as the difference between the gross sand and the non-net sand. Asquith, (2004) explains that the NGR measurement serves as an indicator of the reservoir sand quality,

with higher NGR values corresponding to better sand quality. The net sand was determined using equation (2.3) as described by Asquith, (2004).

$$\text{NGR} = \text{Net sand} / \text{Gross sand} \quad (2.3)$$

$$\text{Note that, Net sand} = \text{gross sand} - \text{Non-net sand} \quad (2.4)$$

2.2.2.5 Porosity

In order to investigate the hydrocarbon potential of reservoirs (sand units), the porosity values is extracted from the porosity logs. The amount of porosity gives the volume of the reservoir containing fluids. As it is a fraction, it can be described as a number e.g. 0.25 or commonly as a percentage, 25%. According to Guo, (2019) porosity values can range from zero to over 50%. In normal reservoirs, it ranges between 20% - 39%.

2.2.2.5.1 Effective Porosity

Porosity refers to the interconnected pore volume or empty spaces present within a rock, which enable the flow of fluids or permeability within a reservoir, as defined by Schlumberger, (1989). It excludes isolated pores and the volume of pores occupied by water adsorbed on clay minerals or other grains. According to Schlumberger, (1989), total porosity encompasses all void spaces in the rock, regardless of their contribution to fluid flow. Effective porosity, on the other hand, is typically lower than total porosity. It is calculated by subtracting the volume of clay-bound water (CBW) from the total porosity.

Four logging devices, namely Sonic, Density, Neutron, and NMR, were employed to estimate porosity (Asquith, 2004).

2.2.2.5.2 Sonic Porosity Determination

Wyllie *et al.*, (1956) introduced a linear relationship, referred to as a time-average or weighted-average relationship, between porosity and transit time for clean and consolidated formations that possess uniformly distributed small pores. This relationship is expressed by

$$\text{Equation 2.5:} \quad \Phi_{\text{sonic}} = \frac{\Delta t_{\text{log}} - \Delta t_{\text{ma}}}{\Delta t_{\text{f}} - \Delta t_{\text{ma}}} \quad (2.5)$$

Where;

Φ_{sonic} = porosity derived from sonic measurement

Δt_{ma} = interval transit time of the rock matrix

Δt_{log} = interval transit time of the formation; and

Δt_{f} = interval transit time of the fluid in the wellbore

2.2.2.5.3 Density Derived Porosity Determination

The bulk density (ρ_b) of a formation is influenced by factors such as porosity, matrix density, and the density of the pore fluid, which can be mud, salt, fresh mud, or hydrocarbons. To determine the density-derived porosity, it is necessary to have knowledge of the fluid type and the density of the matrix, as explained by Schlumberger, (1989).

Therefore, the density-derived porosity can be expressed as;

$$\Phi_{\text{den}} = \frac{\rho_{\text{ma}} - \rho_b}{\rho_{\text{ma}} - \rho_f} \quad (2.6)$$

Where:

Φ_{den} = density-derived porosity

ρ_{ma} = density of the matrix

ρ_b = formation bulk density (measure from log)

ρ_f = fluid density (It is 0.7 for gas, 1.1 for salt mud and 1.0 for fresh mud)

2.2.2.5.4 Neutron-Density Porosity

This combination logs can be estimated using this formula:

$$\Phi_{N-D} = \sqrt{\frac{\emptyset N^2 + \emptyset D^2}{2}} \quad (2.7)$$

Where,

\emptyset_{N-D} = neutron-density derived porosity

\emptyset_D = porosity measured from density log

\emptyset_N = porosity measured from neutron log

2.2.2.6 Saturation

Saturation can be determined by employing the resistivity logs. In essence, when a porous formation is saturated with conductive brine, its resistivity will be relatively low. On the other hand, if a significant portion of non-conductive hydrocarbon is present in the formation, then the resistivity of the formation will be relatively high (Ellis and Singer, 2008). However, changes in formation porosity also affect resistivity. When porosity increases, the value of R_t decreases, assuming water saturation remains constant. The presence of hydrocarbons in the formation can be either in the form of oil or gas, and distinguishing between the two can be determined by comparing measurements of formation density and neutron porosity, as indicated by Ellis and Singer, (2008).

According to Asquith and Krygowski, (2004), the saturation of a formation refers to the quantity of a specific fluid present in the pore spaces. Saturation can be determined by combining resistivity and porosity logs, as emphasized by Asquith, (2004). Porosity logs reflect the characteristics of the pore space, while resistivity logs indicate the properties of the fluids within the pore space. By combining these two measurements, the saturation can be determined (Asquith, 2004).

The resistivity formation factor, F , is defined by the following equation:

$$F = \frac{R_o}{R_w} \quad (2.8)$$

Where:

F = Formation Factor.

When porosity remains constant, the resistivity formation factor, F , remains constant.

With an increase in porosity, the resistivity, R_o , decreases, resulting in a decrease in the resistivity formation factor, F.

R_w = It represents the resistivity of the formation water at the temperature of the formation.

R_o = It refers to the resistivity of the rock when it is completely saturated with water.

Experimental results have indicated an inverse relationship between F and ϕ^m in the virgin zone.

$$F = \frac{a}{\phi^m} \quad (2.9)$$

Where:

m = cementation exponent.

a = lithology constant.

ϕ = porosity

Saturation can be represented as a ratio of resistivities, where R_t corresponds to the resistivity of the virgin formation. When the formation is solely filled with water, R_t is equal to R_o , and the saturation, S_w , becomes 1. The saturation exponent, n, is an empirical parameter determined by Archie through experimental analysis.

$$S_w^n = \frac{R_o}{R_t} \quad (2.10)$$

Where:

n = saturation exponent, an empirical constant.

R_t = virgin formation resistivity

R_o = resistivity of the rock saturated in water only

Substituting for R_o :

$$S_w^n = \frac{FR_w}{R_t}$$

Substituting for F:

$$S_w^n = \frac{a}{\phi^m} \frac{R_w}{R_t} \quad (2.11)$$

The Archie's equation establishes a connection between porosity, resistivity, and the water content represented by S_w . If porosity (ϕ) increases, the saturation (S_w) will decrease while keeping R_t constant. Similarly, if R_t increases while maintaining the same porosity, it will have a similar effect on saturation. The water content is commonly represented by the water saturation, S_w . It is calculated based on the amount of water present in the formation and is uniquely characterized by its salinity. In a mixture of hydrocarbon and water, the saturation of hydrocarbon, S_h , can be calculated as 1 minus the water saturation, S_w .

It is worth noting that the proportion of the formation occupied by water can be determined by multiplying the porosity (ϕ) by the water saturation (S_w), while the total fraction of the formation occupied by hydrocarbon can be obtained by multiplying the porosity (ϕ) by the hydrocarbon saturation (S_h). These relationships have been discussed in literature, including works by Schlumberger, (1989); Tomasso, (2010). Therefore, Hydrocarbon saturation, S_h was estimated using the relationship in equation (2.12).

$$S_h = 1.0 - S_w \quad (2.12)$$

Where:

S_h = hydrocarbon saturation, which represents the fraction of the pore volume that is filled with hydrocarbon.

S_w = water saturation in the uninvaded zone, which indicates the fraction of the pore volume that is filled with water.

2.2.2.7 Irreducible Water Saturation

The irreducible water saturation, also known as critical water saturation, represents the maximum water saturation that a formation can hold without allowing water to flow. This saturation is determined by the permeability and porosity of the formation and is determined through specialized core analysis techniques. The critical water saturation is crucial information as it can be compared with the in-place water saturation calculated from downhole electric logs. In low permeability reservoirs, it is possible for the critical water saturation to be relatively high, even exceeding 60%, while still allowing the well to produce only hydrocarbons.

The calculation of irreducible water saturation involves the use of the following relationship:

$$S_{w_{irr}} = \sqrt[2]{F/2000} \quad (2.13)$$

Where, $S_{w_{irr}}$ represents the irreducible water saturation and F is the formation factor.

The well log data were additionally utilized to assess the strength of the reservoir rock and extract mechanical and elastic parameters, including Young, bulk and shear moduli, Poisson ratio, unconfined compressive strength (UCS) and compressibility. Well log data were used to carry out fluid substitution using Gassmann's equation and establish a Castagna equation derived for the suitability of the Niger Delta Scenario. The log-derived elastic and mechanical properties were used to estimate sand production potential in order to evaluate the possibility of producing sand and the stability of the reservoir during production.

2.2.2.8 Bulk Volume of Water

The bulk volume of water (BVW) refers to the proportion of the total rock volume that is filled with water. It differs from the water saturation, which represents the percentage of the pore space occupied by water. The BVW is an important factor in determining fluid mobility within the reservoir. The calculation of BVW involves the use of the following formula:

$$BVW = S_w \times \phi \quad (2.14)$$

BVW is the bulk volume of water, S_w represents water saturation and ϕ is the rock porosity

2.2.2.9 Fluid Distribution and Fluid Contacts

Resistivity readings can be used as a general indication for fluid type in hydrocarbon reservoirs. According to Schlumberger, (1989) sand units that show high deep resistivity readings are interpreted as fresh-water or oil-bearing zones but sands whose values show low deep resistivity readings, correspond to zones of water. The determination of fluid types within the pores of the rock can be achieved by analyzing the correlation between the Density and Neutron logs. Higher values on the density log indicate the presence of hydrocarbons, which can be helpful in interpreting the data and identifying the crossover points. As supported by Asquith and Krygowski, (2004), large magnitude of the cross-over indicated gaseous hydrocarbon and oil was inferred when there was a small degree in the cross-over.

2.2.3 Identification of Depositional Environments

The shaliness of the formation is measured by the GR log and it is used for the identification of depositional environment and lithofacies (Emery and Myers, 1996). According to Serra and Sulpice, (1975) SP and resistivity logs shapes are used as a classification scheme for sand bodies. The identified principal shapes are; the funnel, bell and cylindrical shapes.

2.2.3.1 Irregular Shapes

The GR log shapes are interpreted as fluvial flood plain, distal deep marine slope and storm dominated shelf. According to Emery and Myers, (1996), this particular GR pattern lacks distinctive characteristics and is indicative of the deposition of shales or silts through aggradation. The irregular trends could be interpreted as a basin plain environment (Coleman and Prior, 1980).

2.2.3.2 Funnel Shapes

These log motifs represent increasing sand unit (coarsening-upward succession) which could be crevasse splays or prograding delta, prograding marine shelf fans and regressive barrier bars (Selley, 1998). As stated by Selley, (1998), crevasse splays refer to deltaic sediments that were deposited after the flooding of a riverbank, resulting in fan-shaped formations on the delta plain. The classification of crevasse splays as a type of deltaic deposit was established by Gluyas and Swarbrick, (2004). These log trend could be

interpreted as a shallow marine progradation and deltaic progradation. GR log shapes show trend in grain size and they represent facies successions as shown by sedimentological association (Schlumberger, 1989). Lower GR readings indicated an increase in grain size while higher GR values indicate small grain sizes. The sedimentological significance of this relationship allows for a direct correlation between log shapes and sedimentary facies, as highlighted by Nton and Salami, (2016).

2.2.3.3 Cylindrical Shapes

These log patterns show even block with sharp top and base with the GR log readings that are relatively consistent and have no definite changes in the interbeds thickness or grain sizes and sharp contacts at both lower and upper boundaries. This log motif represents aggradation that could be a eolian, braided stream, submarine canyon-fill, distributary channel-fill, evaporite filled basin and carbonate shelf margin (Nton and Salami, 2016).

2.2.3.4 Bell Shapes

These log motifs show increasing clay contents with GR value increasing upwards from a minimum value. They can be smooth or serrated. It is referred to as smooth if the sand unit is homogeneous while it is serrated when it is interbedded with shale. These shapes could be interpreted as transgressive shelf sand, tidal channel or deep tidal channel, alluvial/fluvial channel and fluvial or deltaic channel (Shell, 1982; Selly, 1998; Nelson and James, 2000). The shape types are shown in the figure 2.1.

2.2.4 Rock Physics - Fluid Substitutions

The field of rock physics elucidates the connection between surface, well, and laboratory measurements of elastic parameters and the intrinsic properties of rocks, including porosity, mineralogy, pore shapes, pore fluids, pore pressures, permeability, viscosity, stresses, and the overall architecture of the reservoir (Sayers and Chopra, 2009). Rock physics plays a

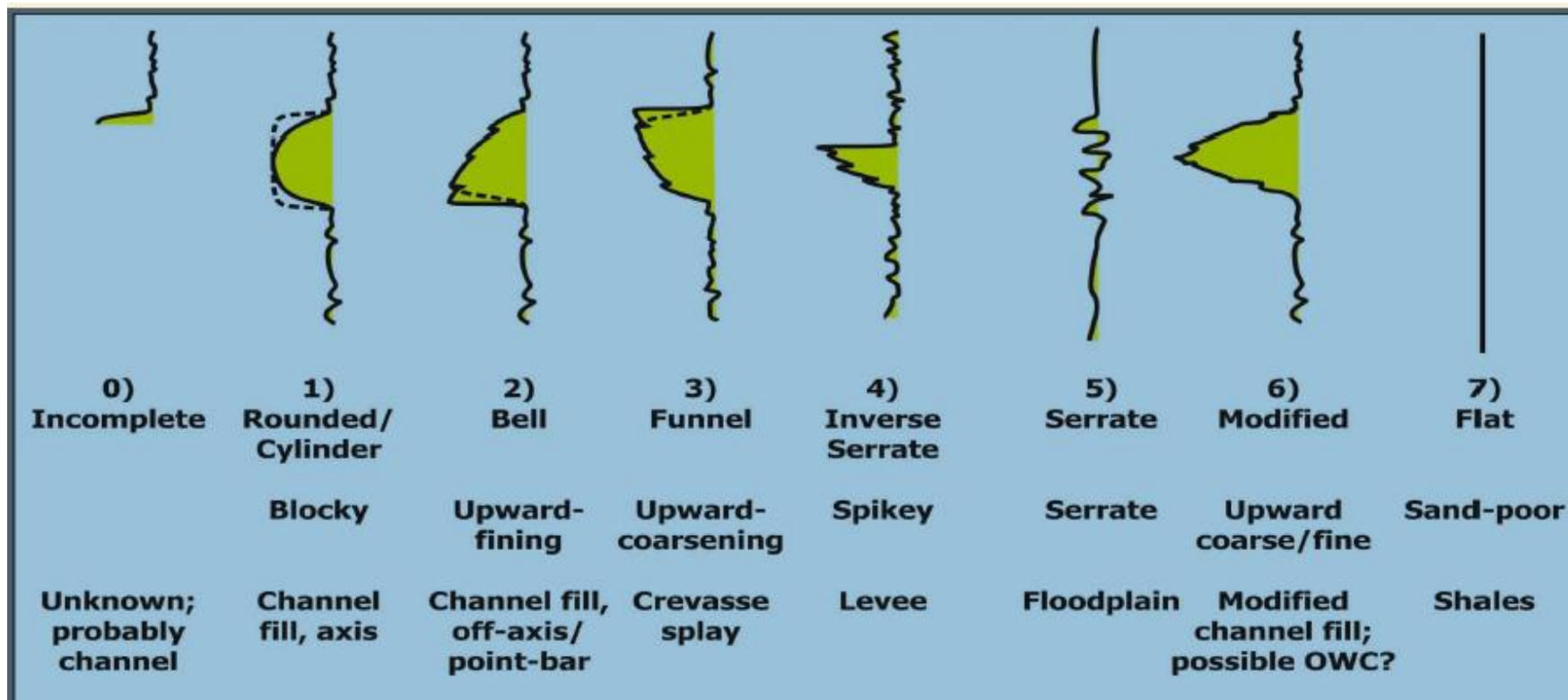


Figure 2.1: Depositional Environments from SP Log Shape, Fiddier Creek Field, Weston County, United State of America. (From Tomasso & Wo, 2009).

crucial role in enhancing our comprehension of the physical characteristics of reservoirs. Typically, when a well is drilled, measurements are conducted to gather valuable data on the elastic and physical properties of subsurface rocks, including velocity, density, lithology, porosity, confining stress, pore pressure, saturation, and fracturing, among other factors. Nevertheless, to gain a deeper understanding of these properties beyond the immediate vicinity of the well, seismic data is employed.

Rock physics serves as the bridge between these properties and seismic data, allowing for the inference of lateral and vertical variations in reservoir properties. This type of study has now become an essential component of reservoir characterization in many cases (Sayers and Chopra, 2009). According to Sayers and Chopra, (2009), the advancements in rock physics over the past five decades can be categorized into five primary areas. These areas encompass laboratory measurements, interpretation of borehole measurements, modeling, deformational analysis, and seismic reservoir characterization. Laboratory measurements involve conducting tests on rock samples under various conditions. Interpretation of borehole measurements includes techniques such as well logging and borehole seismic analysis.

Modeling focuses on developing theoretical models to determine the elastic properties of rocks under specific conditions, as well as upscaling methods to estimate seismic properties based on available reservoir properties. Deformational analysis aims to quantify how rocks respond to stress. Lastly, seismic reservoir characterization involves the application of rock physics principles to seismic data for the purpose of characterizing reservoirs. These models often incorporate adjustable parameters, such as pore aspect ratio or critical porosity, which can be empirically determined using local data. Additionally, when core V_p and V_s data or dipole shear wave logs are available, certain shear wave velocity (V_s) prediction methods can be calibrated to local conditions. The calibration of rock physics models can also assist in selecting an appropriate fluid mixture model, such as homogeneous or patchy distribution, as discussed by Dvorkin *et al.*, (1999).

Fluid substitution plays a crucial role in seismic rock physics analysis, serving as a valuable tool for identifying and quantifying fluids within a reservoir, as highlighted by Kumar, (2006). The low-frequency Gassmann theory, proposed by Gassmann, (1951), is the most

commonly used theoretical approach for fluid substitution. The primary objective of fluid substitution is to replicate the seismic characteristics, including seismic velocities and density, of a reservoir under specific reservoir conditions such as temperature, pressure, porosity, water salinity, and mineral type. It allows for modeling different pore fluid saturations, ranging from complete water saturation to exclusive presence of oil or gas saturation. The purpose is to accurately simulate the seismic response of the reservoir given its fluid composition (Kumar, 2006).

2.2.4.1 Reservoir Fluid and Seismic Properties

The pore fluids filling sedimentary rocks vary in composition and physical properties. Pressure and temperature variations influence the physical phases and compositions of fluids, consequently impacting the seismic response of rocks, as noted by Mavko *et al.*, (1998). In a reservoir, the primary fluid types include oil, gas, and brines. These different fluid compositions possess distinct physical properties that contribute to the overall seismic behavior of the rock. The composition of the hydrocarbons depends on the source, migration, burial depth, pressure, temperature, biodegradation and production (Batzle and Wang, 1992).

In hydrocarbon saturated rocks, the gas-oil ratio (GOR) is defined as the ratio of the volume of gas released from solution to the volume of oil at standard conditions, is an important factor that controls seismic response (Batzle and Wang, 1992). The maximum amount of gas that can dissolve in solution is a function of the composition of the gas, the oil, as well as the pressure and temperature (Mavko *et al.*, 1998). The compressional velocity (V_p), shear velocity (V_s), and density play a crucial role in determining the seismic response of a rock. However, it is important to note that V_p and V_s may not provide the most accurate indications of fluid saturation effects since they are primarily influenced by shear modulus and bulk density, as highlighted by Han and Batzle (2004). The estimation of seismic velocity in an isotropic material can be achieved by considering the known rock moduli and density.

2.2.4.1.1 Deriving Shear Wave Velocity (Vs) Information

In the literature, various empirical equations proposed by Picket, 1963; Castagna *et al.*, 1985; Krief *et al.*, 1990; Greenberg and Castagna, 1992 are available to determine the relationships between P and S wave velocities in siliciclastic rocks. Castagna *et al.*, (1985) proposed an empirical relation that allows the estimation of shear wave velocity (Vs) from compressional wave velocity (Vp) in brine-saturated, multimineral rocks. This relation is based on empirical, polynomial Vp-Vs relationships established in pure monomineralic lithologies. Greenberg and Castagna, (1992) derived empirical relationships to estimate shear wave velocity (Vs) from compressional wave velocity (Vp) in brine-saturated, multimineral rocks.

These relationships were established based on empirical, polynomial Vp-Vs relations in pure monomineralic lithologies, as previously determined by Castagna *et al.*, (1993). In brine-saturated composite lithologies, the shear wave velocity can be approximated by taking a simple average of the arithmetic and harmonic means of the shear velocities of the constituent pure lithologies.

$$V_s = \frac{1}{2} \left\{ \left[\sum_{i=1}^L X_i \sum_{j=0}^{N_i} a_{ij} V_p^j \right] + \left[\sum_{i=1}^L X_i \left(\sum_{j=0}^{N_i} a_{ij} V_p^j \right)^{-1} \right]^{-1} \right\} \quad (2.15)$$

$\sum_{i=1}^L X_i = 1$

Castagna *et al.*, (1993) provided polynomial regression coefficients for pure monomineralic lithologies, which describe the relationship between shear wave velocity (Vs) and compressional wave velocity (Vp) as

$$V_s = a_{i2} V_p^2 + a_{i1} V_p + a_{i0} \quad (2.16)$$

Where

L = number of monomineralic lithologic constituents

Xi = volume fractions of lithological constituents

a_{ij} = empirical regression coefficients

N_i = order of polynomial for constituent i

Vp and Vs represent the compressional and shear wave velocities, respectively, in composite brine-saturated, multi-mineralic rocks. Within the domains of petrophysics and rock physics, the concept of the mudrock line, which is sometimes referred to as Castagna's equation or Castagna's relation, embodies an empirical linear correlation linking the

compressional wave and the shear wave velocities in siliciclastic rocks saturated with brine (Castagna *et al.*, 1985).

The equation reads:

$$V_p = 1.36 + 1.16 \cdot V_s \quad (2.17)$$

Where;

V_p = Compressional wave velocity (Km/s),

V_s = Shear wave velocity (Km/s)

2.2.4.2 Wyllie Time-Average Equation

This equation plays a fundamental role in rock physics analysis. It is an important relationship among the rock velocity, porosity, pore fluid and compressibility (Dvorkin and Nur, 1998). As stated by Dvorkin *et al.*, (2001), parameters like velocity, porosity, and pore-fluid compressibility are crucial factors in rock physics analysis. The equation mentioned here serves as an additional tool to estimate porosity from well logs and to identify the type of in-situ pore fluid, as emphasized by Wyllie *et al.*, (1956).

Acoustic tools are highly valuable for measuring porosity as the compressional wave velocity (V_p) of sound in fluids is lower compared to that in rocks. According to Tixier *et al.*, (1959) the acoustic energy takes a longer time to the receiver from the transmitter if the pore spaces in rocks are filled with water (that is, high porosity means low velocity). The measured travel time or velocity is equal to the sum of the framework (rock matrix) velocity, pore filling fluid and rock lining the pores. Tixier *et al.*, (1959) pointed out that the travel time of the rock matrix, represented by Δt_{ma} , can be influenced by changes in both lithology and the confining pore pressure, which is associated with compaction.

Wyllie time-average equation involves the computation of porosity if the travel time, t or transit time, Δt (velocity) of the borehole fluids and the matrix are known (Wyllie *et al.*, 1956) [see equations 2.18-2.20]

Therefore, v :

$$\frac{1}{v} = \frac{\phi}{v_f} + \frac{(1 - \phi)}{v_{ma}}, \quad (2.18)$$

where

ϕ = rock fractional porosity

v (ft/sec) = formation velocity

v_f (ft/sec) = interstitial fluids velocity

v_{ma} (ft/sec) = rock matrix velocity

The transit time (Δt) can be expressed as:

$$\Delta t = \phi \Delta t_f + (1 - \phi) \Delta t_{ma} \quad (2.19)$$

or

$$\phi = \frac{\Delta t - \Delta t_{ma}}{\Delta t_f - \Delta t_{ma}} \quad (2.20)$$

Where,

Δt ($\mu\text{sec}/\text{ft}$) = acoustic transit time

Δt_f ($\mu\text{sec}/\text{ft}$) = interstitial fluids' acoustic transit time

Δt_{ma} ($\mu\text{sec}/\text{ft}$) = rock matrix's acoustic transit time

Carmichael, (1982) reported values for Δt_f and Δt_{ma} with respect to travel time as shown in Table 3.1.

$$t_{\log} = t_f \phi + t_{ma}(1 - \phi)$$

$$t_{\log} = t_f \phi + t_{ma} - t_{ma} \phi$$

$$t_{\log} - t_{ma} = t_f \phi - t_{ma} \phi$$

$$t_{\log} - t_{ma} = (t_f - t_{ma}) \phi$$

∴

$$\phi = \frac{t_{\log} - t_{ma}}{t_f - t_{ma}} \quad (2.21)$$

Reservoir fluids and borehole's velocity except gas do not show obvious variation; velocity (Δt_f) of the fluid of 5,300 ft/sec (189 $\mu\text{sec}/\text{ft}$) may be suggested for drilling fluids (fresh). Salt muds has a lower value of 185 $\mu\text{sec}/\text{ft}$ (Carmichael, 1982). It is important that the lithology be calculated or estimated to pick the correct velocity of the matrix (Carmichael, 1982). The Wyllie's formular is applicable for compacted and consolidated formations. But a correction factor is essential for unconsolidated formations (Eq. 2.22) Carmichael, (1982). The existence of clay or shale within the sand matrix leads to an elevation in Δt , and the extent of this elevation is directly correlated with the total volume of the clay fraction.

Table 2.1: Velocity and Acoustic Slowness (Transit Time) Values for Common Reservoir Fluids and Lithologies (after Carmichael, 1982)

Fluid	V_f (ft/sec)	Δt_f (μsec/ft)	
Water with 20% NaCl	5,300	189	
Water with 15% NaCl	5,000	200	
Water with 10% NaCl	4,800	208	
Water (pure)	4,600	218	
Oil	4,200	238	
Methane	1,600	626	
Air	1,100	910	
Lithology (matrix)	V_{ma} (ft/sec)	Δt_{ma} (μsec/ft) (compressional)	Δt_{ma} (μsec/ft) (Shear)
Sandstone			
Unconsolidated	17,000 or less	58.8 or more	93
semiconsolidated	18,000	55.6	92.9
consolidated	19,000	52.6	92.9
Limestone	21,000	47.6	
Dolomite	23,000	43.5	72
Shale	6,000 to 16,000	167 to 62.5	
Salt (halite)	15,000	67	116
Coal			
Lignite	7,150	140	
Bituminous	8,300	120	
Anthracite	9,500	105	
Granite	20,000	50	
Minerals			
Calcite	22,000	46	89
Quartz	18,000x	51	74
Evaporites			
Anhydrite	20,000	54	98
Gypsum	19,000	53	
Trona		65	
Iron Minerals			
Limonite		57	103
Pyrite		38	59
Siderite		44	85
Hematite		46	72
Micas			
Biotite		51	224
Muscovite		47	79

For compacted shales, the acoustic transit time = 100 μsec/ft

The compaction coefficient (C) of shale typically falls within the range of 1.0 to 1.3, although it can vary based on regional geology (Carmichael, 1982).

Porosity can be estimated for a sandstone in which $\Delta t_{sh} > 100 \mu\text{sec}/\text{ft}$ in the adjacent shale using an empirical formula in Eq. 2.23:

$$\phi = \frac{\Delta t - \Delta t_{ma}}{\Delta t_f - \Delta t_{ma}} \times \frac{1}{C_p}, \quad (2.22)$$

Where

C_p is correction factor

$$C_p = \frac{\Delta t_{sh}(C)}{100}, \quad (2.23)$$

Δt_{sh} ($\mu\text{sec}/\text{ft}$) = specific acoustic transit time for adjacent shales

In an effort to correct the weakness of the Wyllie time-average formula, an empirical relationship involving velocity and porosity was introduced by Raymer *et al.*, (1980) called Raymer-Hunt-Gardner equation (Eq. 2.24). According to Dvorkin and Nur, (1998) this equation is used in unconsolidated and consolidated units thus removing the necessity for compaction correction. The relationship gives a better porosity correlation over a range of porosity. However, Dvorkin and Nur, (1998) reported that neither of the empirical relations is sufficient in a high-porosity, uncemented and unconsolidated rocks.

$$\phi_{\log} = -\alpha - [\alpha^2 + (\Delta t_{ma} / \Delta t_{\log}) - 1]^{0.5}, \quad (2.24)$$

Where

$$\alpha = (\Delta t_{ma} / 2\Delta t_f) - 1.$$

In oil and gas, the acoustic travel time is higher than in water. High values of apparent porosity in the formation may be influenced by the unflushed hydrocarbons within an interval.

2.2.4.3 Gassmann's Equations

This equation provides a simple model for estimating fluid saturation effects on bulk modulus, and is the most common theoretical approach for performing fluid substitutions (Smith *et al.*, 2003). The Gassmann's equation relates the saturated bulk modulus of the rock to its porosity, the bulk modulus of the porous frame, the bulk modulus of the mineral matrix, and the bulk modulus of the pore-filling fluids:

$$K_{sat} = K^* + \frac{\left(1 - \frac{K^*}{K_o}\right)^2}{\frac{\phi}{K_{fl}} + \frac{(1-\phi)}{K_o} - \frac{K^*}{K_o^2}}, \quad (2.25)$$

Where K_{sat} = the saturated bulk modulus (undrained of pore fluids),

K_{ϕ} = the bulk modulus of the mineral matrix,

K_{fl} = the bulk modulus of the pore fluid,

K^* = the bulk modulus of the porous rock frame (drained of any pore-filling fluid) and

ϕ = porosity

In the application of this equation, the bulk modulus of the porous rock frame is first determined (the bulk modulus of the rock drained of its initial pore-filling fluid), then calculating the bulk modulus of the rock saturated with any desired fluid. The knowledge of the density of the in-situ pore-filling fluid density, bulk modulus and the new fluid to model are essential before performing a fluid substitution. The underline assumptions that the fluid is homogenous, distributed uniformly within the pore space, helps to determine the bulk modulus of the fluid mixture through the isostress, or Reuss average as shown in Equ.2.26.

$$K_{fl} = \left[\sum_{i=1}^n S_i / K_i\right]^{-1} \quad (2.26)$$

Where K_{fl} is the bulk modulus of the fluid mixture,

K_i is the bulk modulus of the individual phases

S_i is their saturation. For a simple two-component hydrocarbon-water system, equation (2.26) becomes

$$K_{fl} = \left[\frac{S_w}{K_w} + (1-S_w)/K_{hc}\right]^{-1} \quad (2.27)$$

The variables in Gassmann's equation are well constrained or can be directly measured which make this equation simple and unique. Gassmann's equation assumed that the pore

pressure is at equilibrium between pores at low frequencies such as seismic frequencies; unlike other theories in fluid substitution that are favourable at higher frequency ranges due to the assumptions of isolated inclusions and the geometry of the inclusions in their equations (Batzle and Wang, 1992).

2.2.4.4 Static, Dynamic and Mechanical Reservoir Properties

Rock deformation due to applied stress are governed by four laws (Wong and David, 1997; Zoback, 2007). The four fundamental laws that describe the behavior of isotropic and homogeneous materials are linear elastic, elastic-plastic, poroelastic behavior and viscoelastic. (Zoback, 2007). In a linear elastic material, the applied stress is directly proportional to the strain, and the deformation is reversible. In a poroelastic material, the saturating fluid's stiffness within a rock is influenced by the external force applied to it (Lawson-Jack *et al.*, 2019).

When subjected to stress, elastic-plastic materials initially respond elastically, meaning they deform proportionally to the applied stress. However, once the yield point is reached, they undergo plastic deformation without any limit. Visco-elastic materials on the other hand exhibits permanent deformation after application of stress (Wong and David, 1997; Zoback, 2007). The Figure 2.2 shows the relationship between stress and strain in various idealized deformation. In an isotropic and homogeneous material, principal stresses and strains act in the same direction (Zoback, 2007).

The second-order strain tensor component is expressed in Fig.2.2(a-c) as:

$$\epsilon_{ij} = \frac{1}{2} \left(\frac{\delta u_i}{\delta x_j} + \frac{\delta u_j}{\delta x_i} \right) \quad (2.28)$$

Where; ϵ_{ij} is a second-order strain tensor component, $\delta u_i / \delta x_j$, and $\delta u_j / \delta x_i$, are principal stress and strain acting in the same directions respectively (Fig.2.2). The theory of elasticity, where no significant deformation occurs in a rock due to the application of stress and the assumption that the applied stress is linearly proportional to the resulting strain which is reversible is often valid. The relationship between applied stress and resultant strain in such materials can be expressed as follows:

$$S_{ij} = \lambda \delta_{ij} \epsilon_{oo} + 2G \epsilon_{ij} \quad (2.29)$$

Where;

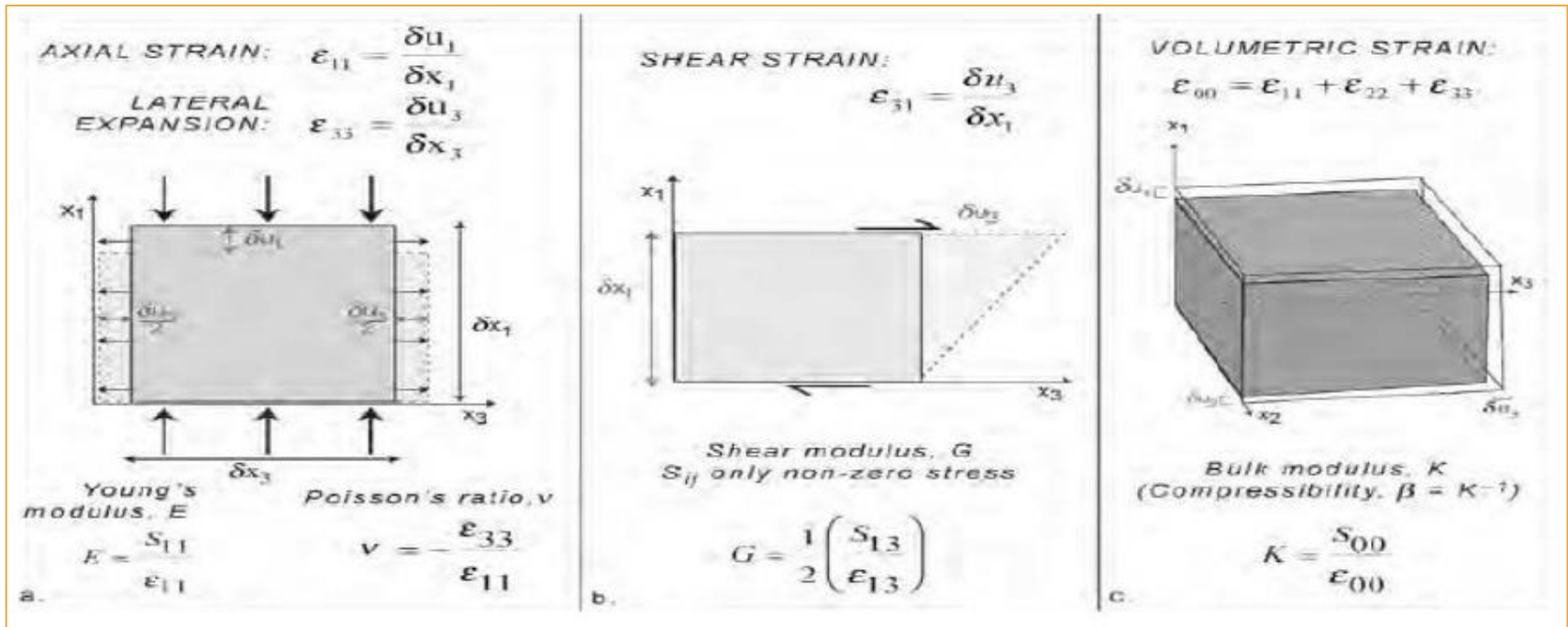


Figure 2.2: Strain Types And The Relationship between Stress and Strain (Zoback, 2007).

\mathcal{E}_{oo} = the volumetric strain (Kronecker delta)

$$\delta_{ij} = 1, I = j, \delta_{ij} = 0,$$

Equation 2.29 can be expanded to have:

$$S_1 = (\lambda + 2G) \mathcal{E}_1 + \lambda \mathcal{E}_2 + \lambda \mathcal{E}_3 = \lambda \mathcal{E}_{oo} + 2G \mathcal{E}_1 \quad (2.30)$$

$$S_2 = \lambda \mathcal{E}_1 + (\lambda + 2G) \mathcal{E}_2 + \lambda \mathcal{E}_3 = \lambda \mathcal{E}_{oo} + 2G \mathcal{E}_2 \quad (2.31)$$

$$S_3 = \lambda \mathcal{E}_1 + \lambda \mathcal{E}_2 + (\lambda + 2G) \mathcal{E}_3 = \lambda \mathcal{E}_{oo} + 2G \mathcal{E}_3 \quad (2.32)$$

From the above, Equation 2.30 represents lateral expansion and axial strain in a uniaxially compressed sample. Also, Equation 2.31 shows the resulting shear strain induced from a shear stress application. Equation 2.32 describes the volumetric strain resulting from the compression of a body due to an isostatic mean stress (Zoback, 2007).

Where λ is the Lamé's constant while K and G are the bulk and shear moduli respectively. It should be noted that all elastic moduli such as; Young modulus, Bulk modulus, Shear modulus, poisson ratio and compressibility, all assumed homogenous isotropic rock.

The bulk modulus (K) refers to the resistance of a substance to undergo compression when subjected to hydrostatic forces. and is given as:

$$K = S_{oo} / \mathcal{E}_{oo} \quad (2.33)$$

The Young's modulus (E) denotes the measure of rigidity exhibited by a rock when subjected to unconfined compression. It is expressed as,

$$E = S_{11} / \mathcal{E}_{oo} \quad (2.34)$$

S_{11} is the only non-zero stress.

Shear modulus, G, is the ratio of shear stress to the corresponding shear strain, that is,

$$G = \frac{1}{2} (S_{13} / \mathcal{E}_{13}) \quad (2.35)$$

Poisson's ratio, U , is the ratio of lateral expansion to axial shortening. It is expressed as,

$$U = \mathcal{E}_{33} / \mathcal{E}_{11} \quad (2.36)$$

The data required to estimate the reservoir geomechanical parameters comprise of shear wave (Vs) and compressional wave (Vp) velocities computed from the acoustic logs and other logs data consist of various measurements such as gamma ray, sonic, resistivity, density, neutron and caliper logs. In order to enhance reservoir productivity, well performance and minimizing risk during drilling, it is essential to determine the mechanical properties of the reservoirs (Fjaer, *et al.*, 1992). According to Fjaer, *et al.*, (1992)

determination of reservoir mechanical properties is critical in well placement, drilling programs and well completion design.

Mechanical properties could be elastic or inelastic. Elastic properties include bulk modulus, young modulus, shear modulus and poisson's ratio while inelastic properties are formation strength and fracture gradient (Fjaer, *et al.*, 1992). Elasticity can be described as any rock property that causes resistance to deformation in shape or volume. The elastic behavior of substances can be properly described by Hooke's law which states that the applied force (stress) is proportional to the resulting deformation (strain) (Montmayeur and Graves, 1986).

2.2.4.4.1 Poisson Ratio (ν)

This is defined as the lateral expansion to axial shortening ratio (Smith *et al.*, 2003). When subjected to a longitudinal stress, it represents the proportion between the longitudinal and lateral strain (Lawson-Jack *et al.*, 2019).

It is expressed as,

$$\nu = \mathcal{E}_{33}/\mathcal{E}_{11} = \mathcal{E}_{lat} / \mathcal{E}_{ax} \quad (2.37)$$

Where;

\mathcal{E}_{lat} = strain in the lateral direction and

\mathcal{E}_{ax} = strain in the axial direction.

Poisson ratio can be derived from sonic log measurement and it is expressed in terms of slowness, which is referred to as interval transit times, (ΔT) (reciprocal of velocity) in microseconds per foot unit. Moos, (2006) reported that the ratio of compressional wave slowness (ΔV_p) and the shear wave slowness (V_s) can be used to calculate the Poisson's ratio.

Hence,

$$\nu = 0.5 \frac{\left[\left(\frac{V_p}{V_s} \right)^2 - 1 \right]}{\left[\left(\frac{V_p}{V_s} \right)^2 - 1 \right]} \quad (2.38)$$

The highest possible value for the Poisson's ratio (ν) is 0.5 in theory.

In which:

V_p refers to the velocity of compressional waves,

V_s refers to the velocity of shear waves.

The young modulus, shear modulus, bulk modulus and poisson's ratio can be derived from velocity ratio (V_p/V_s) and density (ρ) (Montmayeur and Graves, 1985). The bulk modulus (K) and shear modulus (G) are related to poisson's ratio by Equations 2.39 and 2.40 (Darvishpour *et al.*, 2019):

$$K = E / 3(1-2\nu) \quad (2.39)$$

Also,

$$G = E / 2(1+\nu) \quad (2.40)$$

2.2.4.4.2 Rock Strength - Unconfined Compressive Strength (UCS)

Unconfirmed Compressive Strength (UCS) stands for the maximum axial compressive stress that a rock can bear under zero confining stress (Attewell and Farmer, 1976). Due to the fact that stress is applied along the longitudinal axis, the Unconfined Compression Test, is also known as Uniaxial Compression Test (Attewell and Farmer, 1976). In the absence of core samples, a number of relationships, involving rock strength, can be used to quantify geomechanical characteristics of wellbore (Bradley, 1979). Generally, these relationships involve metrics that have a direct influence on rock strength, such as; the elastic modulus and porosity (Bradley, 1979). The UCS depends on elastic modulus, meaning that a higher elastic modulus corresponds to greater strength (Chang *et al.*, 2006),

The relationship between uniaxial compressive strength (UCS) and Young modulus (E) can be expressed as;

$$UCS = 2.28 + 4.1E \quad (2.41)$$

Also, unconfined compressive strength (UCS) can also be expressed as in equation (2.41) below:

$$UCS = 1200 \exp^{(-0.036\Delta T_c)} \quad (2.42)$$

$$UCS = 10 \left(\frac{304.8}{\Delta T_c - 1} \right) \quad (2.43)$$

Where UCS represents the rock unconfined compressive strength while ΔT_c is the change in the transit time of the compressional wave measured in us/ft and E signifies the Young modulus.

According to Chang *et al.*, (2006) a number of empirical relations shown in Table 2.2 can be used to calculate UCS. The unconfined compressive strength (UCS) and angle of internal friction of sedimentary rocks are important parameters that are useful in addressing a range of geomechanical problems such as; limiting wellbore instabilities during drilling (Moos *et al.*, 2003), estimating sanding potential (Santarelli *et al.*, 1989) and quantitatively constraining stress magnitudes using observations of wellbore failure (Zoback *et al.*, 2003). The use of these above empirical relations is the only way to estimate strength in many situations due to the absence of cores for laboratory tests (Chang *et al.*, 2006).

The basis for these relations is the fact that similar factors that affect rock strength, also affect other physical properties such as velocity, elastic moduli and porosity (Chang *et al.*, 2006). In many cases, such empirical relationships have been suggested for sedimentary rocks, mainly because the information on (UCS) is greatly demanded in reservoirs for drilling and maintenance of wellbores (Chang *et al.*, 2006). According to Xu *et al.*, (2016), the compressive strength of the rock increases with rock density and decreases with rock porosity and also the magnitude of the UCS increases with depth.

According to Attewell and Farmer (1976), based on the values of Uniaxial Compressive Strength (UCS), rocks can be characterized from very weak to very strong. The strength value of 10-20 (MPa) is considered as very weak, 20-40 (MPa) is weak, 40-80 (MPa) is medium while strength of range of 80-160 (MPa) is strong. Attewell and Farmer (1976), also presented the range of the Uniaxial Compressive Strength (UCS) for a large amount of typical rock types as shown in Table 2.3.

2.2.5 Sand Production

Sand production occurs due to sand influx and creates a serious problem during oil/gas production (Ahad *et al.*, 2020). Such problems may include; casing or tubing buckling, abrasion of downhole casing or tubing, sand bridging, in flow lines and/or tubing, compaction and erosion and casing or liners failure (Khomehchi and Reisi, 2015).

Table 2.2: The Empirical Formulae Showing The Connections between Unconfined Compressive Strength (UCS) And Various Parameters in Sandstone. (After Chang *et al.*, 2006)

Equation Number	UCS (MPa)	Region where developed	General comments	Reference
1	$0.035V_p - 31.5$	Thuringia, Germany		Freyburg, (1972)
2	$1200\exp(-0.036\Delta t)$	Bowen Basin, Australia	Fine grained, both consolidated and unconsolidated sandstones with all porosity range	McNally, (1987)
3	$1.4138 \times 10^7 \Delta t^{-3}$	Gulf Coast	Weak and unconsolidated sandstones	
4	$3.3 \times 10^{-20} \rho^2 V^4 p [(1 + \nu) / (1 - \nu)]^2 (1 - 2\nu) [1 + 0.78V_{clay}]$	Gulf Coast	Applicable to sandstones with UCS > 30 MPa	Fjaer et al., (1992)
5	$1.745 \times 10^{-9} \rho V^2 p^{-21}$	Cook Inlet, Alaska	Coarse grained sandstones and conglomerates	Moos et al., (1999)
6	$42.1\exp(1.9 \times 10^{-11} \rho V^2 p)$	Australia	Consolidated sandstones with $0.05 < \phi < 0.12$ and UCS > 80 MPa	
7	$3.87\exp(1.14 \times 10^{-10} \rho V^2 p)$	Gulf of Mexico		
8	$46.2\exp(0.027E)$			
9	$2.28 + 4.1089E$	Worldwide		Bradford et al., (1998)
10	$254 (1 - 2.7\phi)^2$	Sedimentary basins worldwide	Very clean, well-consolidated sandstones with $\phi < 0.3$	Vemik et al., (1993)
11	$277\exp(-10\phi)$		Sandstones with $2 < \text{UCS} < 360 \text{ MPa}$ and $0.002 < \phi < 0.33$	

Table 2.3: Values of Unconfined Compressive Strength of Some Rocks (Adapted from Attewell and Farmer, 1976).

Typical Rock Types	Uniaxial compressive Strength (Mpa)
Granite	100-250
Diorite	150-300
Diabase	100-350
Gabbro	150-300
Basalt	100-300
Gneiss	50-200
Marble	100-250
Slate	100-200
Quartzite	150-300
Sandstone	20-170
Shale	5-100
Limestone	30-250
Dolomite	30-250

Sand production can be predicted using several methods such as well logs, production data, laboratory testing, acoustic, analogy and intrusive sand monitoring devices (Khamehchi and Reisi, 2015). Vahidoddin *et al.*, (2012) reported that it is crucial to assess the potential for sand production in sandstone oil and gas reservoirs in order to determine the need for sand control measures during production. This is because the economic implications of sand production are huge and critical to require regular improvement in techniques and methods of prediction. Reservoir sand production can be calculated using a number of relationship such as:

2.2.5.1 Shear Modulus (G) to Bulk compressibility (Cb) Ratio

This can be expressed as,

$$G/Cb \tag{2.44}$$

Where,

G = Shear modulus

Cb = Bulk compressibility

Tiab and Donaldson, (2004) suggested that the empirical relation implied that a threshold for sanding existed when $G/Cb = 0.8 \times 10^{12} \text{ psi}^2$, whereas values less than $0.8 \times 10^{12} \text{ psi}^2$ suggest a high probability of sanding. This empirical relationship considered only whether sanding will be a challenge at present conditions. The method states whether a well will be a sand producer, but a maximum sand-free rate cannot be calculated from the given ratio of G/Cb (Ghalambor *et al.*, 2015)

2.2.5.2 Schlumberger Sand Production Index (S/I)

This can be expressed as the product of bulk and shear moduli.

$$S.I = G * K \tag{2.45}$$

Where K and G are the Bulk and Shear moduli respectively.

2.2.5.3 Sand Production Mechanisms

Sand production mechanisms are responsible for sand influx during production and they include; viscous drag forces, formation strength, wellbore pressure drop and flow stability (Khamehchi and Reisi, 2015). Nevertheless, the primary factors that play a significant role in causing sand production are the strength of the formation, in-situ stress levels, and the rate of production (Khamehchi and Reisi, 2015; Ahad *et al.*, 2020).

2.2.5.3.1 Formation Strength

The process of hydrocarbon production is associated with reservoir depletion which leads to decrease in reservoir pore pressure and corresponding increase in the effective overburden pressure. The total overburden pressure is the sum of effective overburden pressure and pore pressure of the reservoir. Formation collapse may occur if the formation strength is less than the effective stress (Khamehchi and Reisi, 2015; Ahad *et al.*, 2020).

2.2.5.3.2 Changing in-situ Stresses

The minimum horizontal stress (δ_h) can be determined through a formation integrity test (leak-off), while the overburden stress (δ_v) can be estimated based on the density of the overlying layers. The intermediate and minimum stresses in a young deltaic basin are roughly equal. But, generally, the intermediate stress (δ_H) is almost 10% bigger than the minimum stress (Bourgoyne *et al.*, 1986).

According to (Wu *et al.*, 2010), the in-situ stresses within hydrocarbon reservoirs undergo modifications as the reservoir pressure depletes over the lifespan of a field. When the reservoir boundary experiences no lateral strain during depletion, Equation (2.46) can be utilized to calculate the variation in the in-situ stresses as:

$$\Delta\delta_H = \Delta\delta_h = \alpha \times (1-2\nu)/(1-\nu) \times \Delta P_p \quad (2.46)$$

Where;

$\Delta\delta_H$ = change in the horizontal maximum stress,

$\Delta\delta_h$ = change in the horizontal minimum stress,

ΔP_p = change in depletion of reservoir pore pressure,

ν = poisson ratio and

α = Poroelastic constant as defined by Biot (Wu *et al.*, 2010)

2.2.5.3.3 Production Rate

Sand flows into the wellbore as production rate increases and this resulted into a significant gradient in fluid pressure. The combination of fluid flow and pressure are the mechanisms that cause failure of a consolidated sand. Penberthy Jr. and Shaughnessy (1992) reported that the mechanisms are closely related and establishing the actual mechanism may be a moot point. Parameters that influence sand production include; composition of reservoir fluids, orientation of wellbore, depletion and many others (Veeken *et al.*, 1991).

2.3 Regional Geological Settings

According to Reijers, (2011), the Tertiary Niger Delta is located within the geographical coordinates of Longitudes 5° and 8°E and Latitudes 3° and 6°N. As shown in Figure 1.1, Klett *et al.*, (1997) depict the Gulf of Guinea as the surrounding area of the delta province. The southern Nigeria and southwest Cameroon geology defines the Niger Delta province's onshore area (Figure 2.3). The Benin Flank at the northern edge is formed by the southern edge of the basement massif of West Africa, extending in an east-northeast direction. The northeastern boundary is defined by the Cretaceous outcrops found on the Abakaliki High and the Calabar Flank, which acts as a hinge line separating it from the adjacent Precambrian area.

Tuttle *et al.*, (1999) indicate that the offshore boundaries of the Niger Delta province are determined by the western boundary of the Dahomey basin and the eastern extent of the Volcanic Line in Cameroon. The basin has undergone southwestward progradation since the Eocene age, which has led to the creation of depobelts. According to Ekweozor, (2004), these depobelts signify the most vibrant and actively changing areas of the delta throughout its various stages of development. The depobelts within the Niger Delta constitute a vast regressive delta, ranking among the largest in the world, occupying approximately 300,000 km² in area (Kulke, 1995).

The delta is distinguished by an estimated sediment volume of 500,000 km³ (Ekweozor, 2004; Hospers, 1965) and a depocenter in the basin with a thickness exceeding 10 km, as reported by Kaplan *et al.*, (1994). The sedimentary basin along the coast of Nigeria has experienced three distinct depositional cycles, as documented by Short and Stauble, (1967). The initial depositional cycle in the coastal sedimentary basin of Nigeria

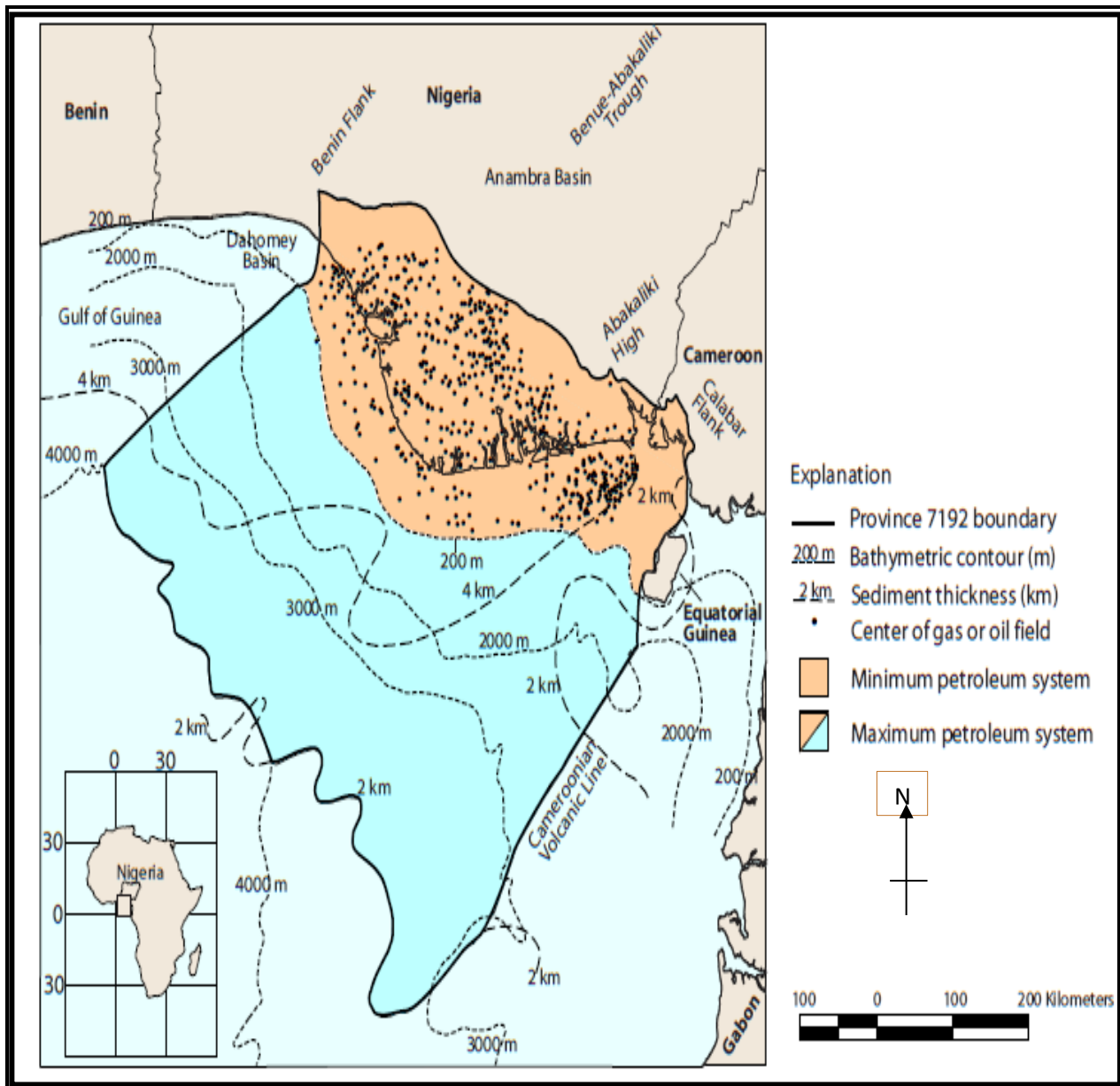


Figure.2.3: Map Showing Petroleum Systems and Province Outline in The Niger Delta (Adapted from Petroconsult, 1996)

initiated in the middle Cretaceous through a marine incursion, which was eventually concluded by a relatively gentle folding phase during the Santonian period. The second cycle of deposition encompassed the development of a proto-delta in the late Cretaceous, culminating in a significant marine transgression during the Paleocene period. The third depositional cycle, spanning from the Eocene to the present, signified the uninterrupted expansion and development of the primary Niger Delta.

The subsurface composition of the Niger Delta is classified into three lithostratigraphic units. These units consist of the lower Akata Formation, which is predominantly shaly, an intermediate sequence known as the Agbada Formation, that is made up of alternating shale and sandstone, and the upper Benin Formation, which is primarily sandy. Figure 2.4 illustrates the widespread presence of the three units - the Akata Formation, the Agbada Formation, and the Benin Formation - throughout the entire delta region. These formations span from the early Tertiary period to the present, as noted by Stacher, (1995). The Afam clay is identified as a constituent of the Benin Formation, which originated during the Miocene period, and it is interpreted as a deposit filling an ancient valley, as suggested by Short and Stauble, (1967).

As reported by Ekweozor, (2004), hydrocarbon extraction in the Niger Delta primarily occurs in unconsolidated sandstone formations, specifically within the Agbada Formation. Agbada Formation consists of intercalation of shales within the sandstones and has thickness variation of 30m to 4600m. As stated by Selley, (1997), the Niger Delta is acknowledged as one of the most productive Tertiary Deltas globally in terms of petroleum production. Several researchers, such as Weber, 1971; Weber and Daukoru ,1975; Selley, 1997, conducted studies on the stratigraphy, sedimentology, structural configuration, and paleoenvironment in which the reservoir rocks of the Niger Delta have accumulated.

The primary hydrocarbon reservoirs within the Niger Delta are the sandstones found in the Agbada Formation, while shale formations serve as both lateral and vertical seals for these reservoirs. The basin is located on the southern edge of Nigeria within the Gulf of Guinea. The basin encompasses a sedimentary sequence exceeding 12 km in thickness, characterized as a deltaic sequence that has prograded over time (Avbovbo, 1978; Kulke, 1995).

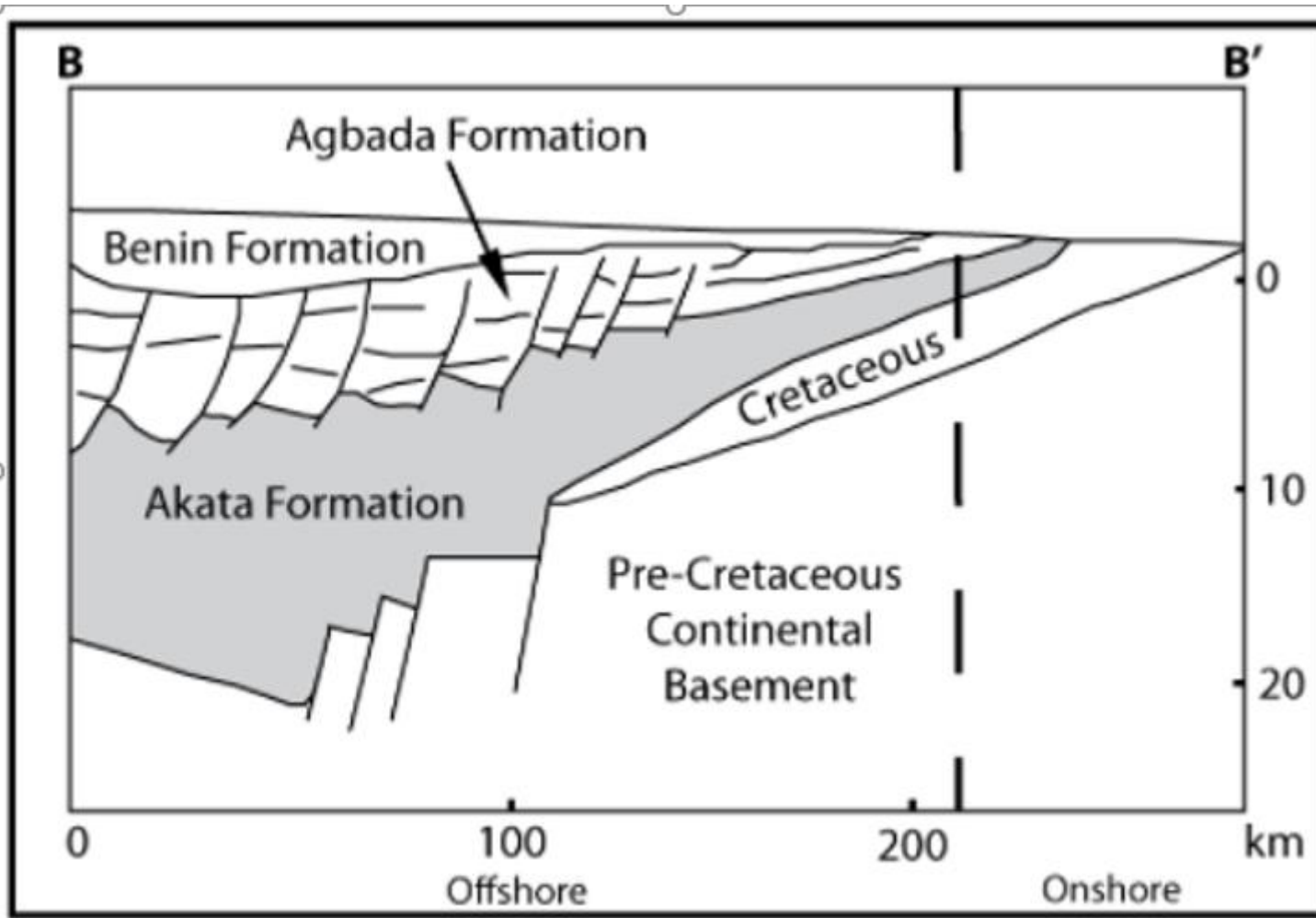


Figure 2.4: Stratigraphic Section of The Niger Delta, Showing The Three Formations And The Continental Basement (After Stacher, 1995)

The Niger Delta basin originated at the convergence point of three arms within a triple junction, which formed during the separation of the African and South American plates during the Albian period (Oyedele *et al.*, 2012; Whiteman, 1982). Two of these arms, running along the southwestern and southeastern coasts of Nigeria, underwent subsidence and became collapsed continental margins in the South Atlantic. However, the third arm experienced a different geological process and evolved into the Benue Trough.

According to Evamy *et al.*, (1978), the progradation of the delta commenced during the Eocene period due to epeiorogenic activities that took place along the Calabar and Benin Flanks. The progradation persisted until the formation of the current delta. The development of the proto-delta stopped by marine transgression during the Paleocene (Weber and Daukoru, 1975). Subsequently, as the sea gradually advanced towards the south, a regressive phase emerged during the Eocene period. The continuous regressive phase, which has persisted until the present time, is occasionally interrupted by minor transgressions. The formation of the present-day Niger Delta has been shaped by these intermittent interruptions, extending from the Eocene period to the present time.

At the base of the basin, there exists a substantial marine shale layer that transitions upward into a combination of shallow marine, fluvial sands, silts, and clays, forming the paralic segment of the delta. The uppermost section of the sequence is characterized by a thick and non-marine sand unit. The Akata, Agbada, and Benin Formations are the respective names given to these units (Oyedele *et al.*, 2012). Although diachronous in nature, these lithostratigraphic units of the Cenozoic Niger Delta complex are significantly influenced by prominent syndimentary features in the subsurface, including roll-over anticlines, growth faults, and diapiric structures, as highlighted by Oyedele *et al.*, (2012).

2.3.1 Basin Evolution and Tectonic Elements

The formation of the Niger Delta basin is closely connected to the creation of the Benue Trough in Nigeria, which took place during the initial separation of the South American and African continental crusts in the Late Jurassic (Burke, 1972; Whiteman, 1982). Following the initial separation of the South American and African continental plates, the opening of the Atlantic Ocean resulted in a marine incursion in Nigeria. This is evident from the deposition of marine sediments in the Benue Trough and the Anambra

Basin during the Lower Cretaceous period, as illustrated in Figure 2.5. In the early Tertiary period, the Niger Delta began to take shape at the confluence of the Benue Trough and the Atlantic Ocean, facilitated by the increased influx of clastic sediments from nearby highlands, primarily transported by the Niger River (Doust and Omatsola, 1990).

As outlined by Burke, (1972), the evolution of the delta and its tectonic settings extend beyond the regressive clastic wedge that emerged after the Eocene period. The configuration of the continental edge in equatorial coast of West Africa is shaped by fracture zones, which are evident as ridges and trenches within the deeper regions of the Atlantic Ocean (Whiteman, 1982). Lehner and De Ruiter, (1977) noted that the occurrence of ridge-like fracture zones divides the continental margin into separate basins. In Nigeria, these ridges also serve as boundary faults delineating the Cretaceous Abakaliki-Benue trough, which extends extensively into the West African shield.

The Abakaliki-Benue trough represents an unsuccessful extension arm of a rift triple junction that was linked to the initiation of the formation of the South Atlantic. Lehner and De Ruiter, (1977) state that the rifting process commenced during the Late Jurassic and continued until the Middle Cretaceous. Eventually, the process of rifting gradually came to a complete halt during the Late Cretaceous. Following the conclusion of the rifting phase, the primary mechanism of deformation shifted towards gravity tectonic. According to Kulke, (1995) the mobile shale generated internal deformation which occurred in response to the following processes; The initial stage involved the creation of shale diapirs originating from the over-pressurized, loosely compacted clays of delta-slope and prodelta within the Akata Formation, which experienced increased loading due to the Agbada Formation denser sand within the delta-front.

The second phase entailed slope instability due to the lack of lateral support towards the basin for the under-compacted clays found in the Akata Formation (Kulke, 1995). Within each depobelt of the basin, complex structural features were formed as a result of gravity tectonic processes preceding the sedimentary deposition of the Benue Formation. These features include roll-over anticlines, shale diapirs, collapsed growth fault crests, steeply dipping and closely spaced flank faults, as well as back-to-back structures (Ekweozor, 2004; Xiao and Suppe, 1992). Evamy *et al.*, (1978) reported that the creation of traps that is responsible for the oil and gas storage in the

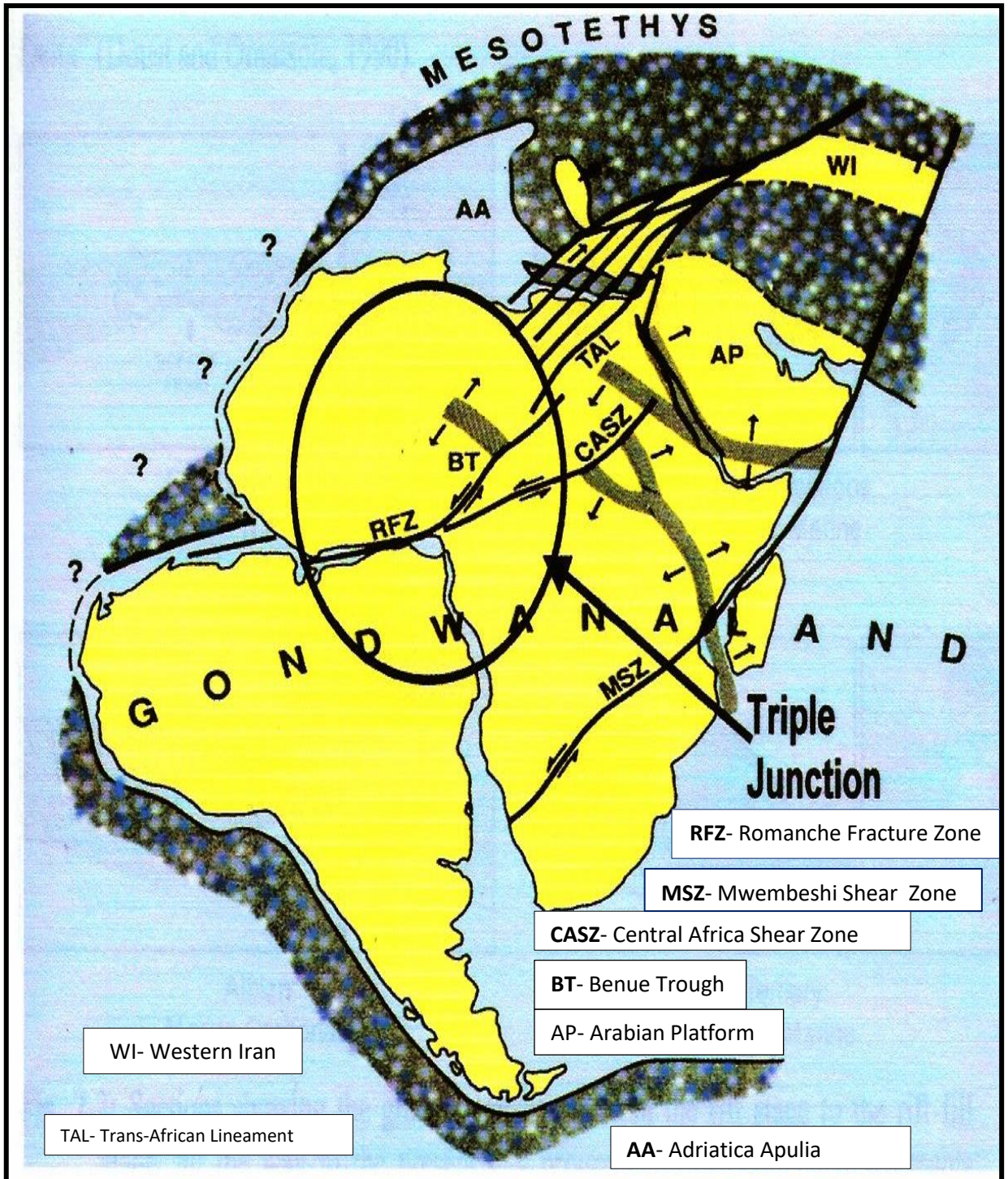


Figure 2.5: Separation of Gondwanaland into South America and Africa in A Triple Junction within The Gulf of Guinea; The Failed Arm Formed The Benue Trough (After Tuttle *et al.*, 1999).

present day delta was due to the wide spread syn-sedimentary faulting that resulted in the deformation of the entire delta. The basin deformation was a large event that was induced by growth faulting and it affected both the Agbada and Akata Formations. The basin progradation has been accompanied by the formation of growth faults, along with the development of rollover anticlines and shale diapirs (Evamy *et al.*, 1978).

2.3.2 Niger Delta Basin Stratigraphy

The basin originated as a multifaceted sequence of clastic sediments characterized by a regressive pattern of deposition, with thicknesses varying between 9000 and 12000 meters (Tuttle *et al.*, 1999). The results obtained from deep wells in the basin consistently reveal a well-defined three-part lithostratigraphic succession, with a noticeable regressive sequence clearly delineated, as reported by Short and Stauble, (1967). Short and Stauble (1967) identified that the Tertiary Niger Delta complex can be categorized into three main facies based on the dominant environmental conditions observed. The environments encompassed within the Tertiary Niger Delta complex consist of the continental, transitional, and marine environments.

In a dynamic delta system like the Niger Delta, sediments are deposited layer by layer in a vertical succession within these environments. While there may be variations in facies at the local scale, three overarching regional and diachronous depositional lithofacies are identifiable. The three Formation range from Eocene to Recent. The Akata Formation is the oldest, while the youngest is the Benin Formation which is underlain by the Agbada Formation (Fig.2.6).

2.3.2.1 Akata Formation

Among the formations within the Niger Delta, this particular formation represents the earliest and the oldest. This formation primarily comprises marine pro-delta megafacies, characterized by the presence of shales interbedded with turbidite sandstone and siltstone. The formation exhibits a thickness ranging from 0 to 600 meters and consists predominantly of dark grey shale, particularly in the upper portion. According to Doust and Omatsola (1990), the shale exhibits over-pressuring and emerges as diapirs along the continental slope, while also appearing as Imo shale in the onshore northeastern region of the delta.

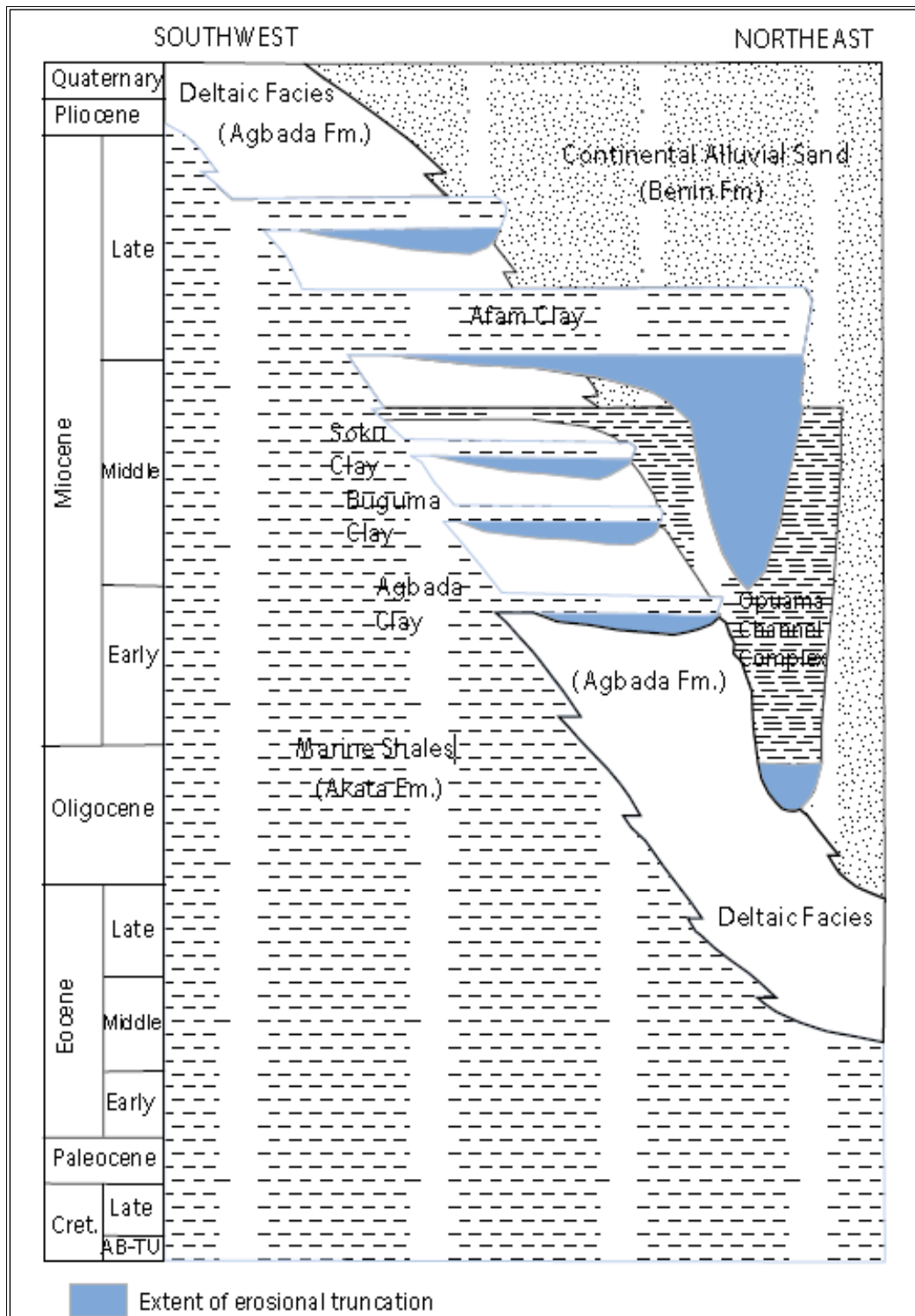


Figure 2.6: Niger Delta Stratigraphy Showing The Three Formations (Adapted from Shannon and Naylor,1989)

The age of this shale formation spans from the Paleocene to the Holocene.

2.3.2.2 Agbada Formation

The sandstone sequence overlies the Akata Formation, which is the oldest formation within the basin. This is the reservoir unit of the basin and comprised alternation of sand, shale and clay in different proportions, thus representing cyclic sequences of off-lap unit (Frank and Cordry 1967; Short and Stauble, 1967). Short and Stauble, (1967) reported that a thicker shale portion and alternation of thinner sandstone units were recognized at the lower portion while the sandstone at the upper section has sandstone-shale unit. According to Reyment, (1965) delta topset, delta front, and fluvio-deltaic environments are the depositional environments.

2.3.2.3 Benin Formation

This Formation is the youngest unit in the basin and comprised fluvial gravels and sands. Reyment, (1965) refers to this formation as the Coastal Plain Sands, which can be observed at various locations within the delta area, including Benin, Owerri, Onitsha provinces, and other areas. The deposit is characterized by a significant volume of highly porous, freshwater-bearing sandstones. It exhibits intercalations of shale, which become more prevalent towards the lower boundary of the unit. The formation is primarily of continental origin. The Formation has a fine grained texture and they are commonly granular. It is partly unconsolidated and consists of poorly sorted, sub-rounded to well rounded grain sizes.

The sand is distinguished by its whitish or yellowish-brown color, which is attributed to the composition of a limonitic coat (Short and Stauble, 1967). It contains remains of plants and streak of lignite with feldspar grain and haematite (Weber, 1971). Benin Formation was Miocene-Recent in age. As indicated by Short and Stauble, (1967), the thickness of this formation ranges from 0 to 2100 meters. According to Short and Stauble, (1967), the maximum thickness of this unit is observed in the central region of the delta, which coincides with areas of significant subsidence. It exhibits a combination of deltaic, marine, lagoonal, and estuarine characteristics within an upper deltaic continental environment (Reyment 1965; Short and Stauble, 1967). Till this present day, no commercial quantity of oil has been found in the Formation.

2.3.3 Niger Delta Depobelts

The three formations in the basin were deposited during each of the five siliciclastic cycles of offlapping sedimentation. According to Stacher, (1995), these depobelts (cycles) have width of 30-60 km and prograde 250 km southwestward over oceanic crust into the Gulf of Guinea. According to Doust and Omatsola, (1990) they are characterised by synsedimentary faulting that was induced by variable rates of subsidence and supply of sediment. According to Doust and Omatsola, (1990), the interaction between the rate of sediment supply and subsidence caused the formation of distinct depobelts when the basin's capacity to accommodate further crustal subsidence was exceeded. Subsequently, sediment deposition shifted towards the sea, resulting in the creation of a fresh depobelt.

According to Evamy *et al.*, (1978) and Doust and Omatsola, (1990), every depobelt is an independent entity that aligns with a change in the regional slope of the basin. These depobelts are bounded on the landward side by growth faults and on the seaward side by significant counter-regional faults or the growth fault of the subsequent depobelt towards the sea. Three depobelt regions were categorized based on their structural characteristics (Doust and Omatsola, 1990). The initial depobelt province is the northern one, situated above a relatively shallow basement. The northern depobelt province exhibits the oldest growth faults, characterized by a rotational pattern, even spacing, and a gradual increase in steepness towards the seaward direction.

The central depobelt, constituting the second province, displays distinct structures, including rollover crests that progressively move towards the sea for each growth fault. The third depobelt province, known as the distal depobelt, is characterized as the most intricate one, primarily because of internal gravity-driven tectonic processes occurring on the contemporary continental slope. According to Cohen and McClay, (1996) these cycles (depobelts) are characterized by distinct, paleontological, transgressive horizons of shale, and they include depocenters and related smaller-scale structures. In addition to the above, Stacher, (1995) recognized five depobelts in the basin which are regional; they include Offshore depobelts, Coastal Swamp, Central Swamp, Greater Ughelli and Northern Delta (Fig.2.7).

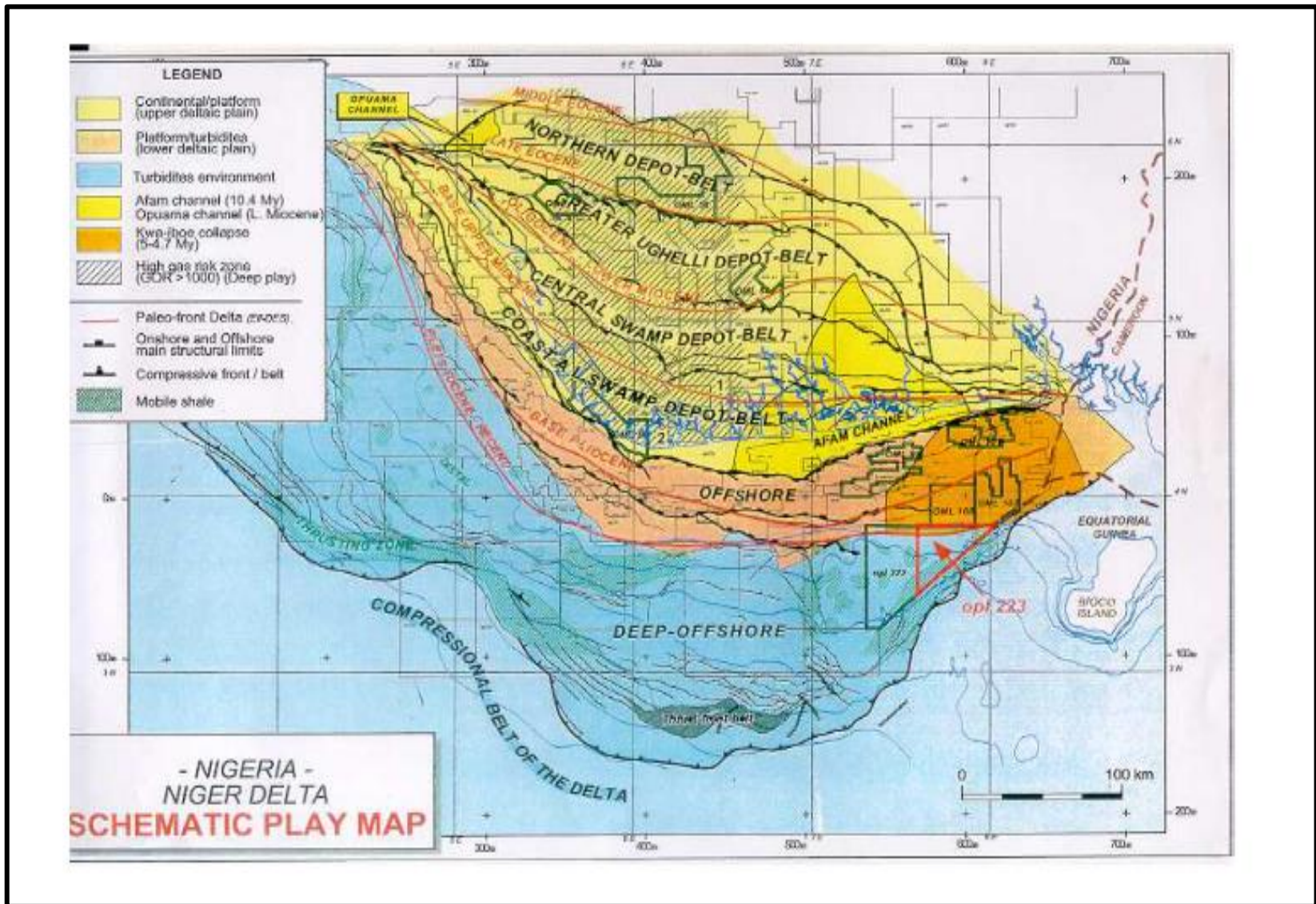


Figure 2.7: Main Depobelts in The Niger Delta (After Stacher, 1995)

2.3.4 Niger Delta Basin Structures

In terms of its structure, the Niger Delta basin can be divided into different zones that exhibit specific variations in structural styles and deformation towards the basin's interior (Figure 2.8). These variations are connected on a regional level through the gradual gravitational sinking of a thick deltaic prism (Damuth, 1994; Hooper *et al.*, 2002; Magbagbeola and Brian, 2007). According to them, the zones include: a zone of outer compressional and imbricate toe-thrust structural pattern below the lower slope, a zone of translational and diapiric structures and ridges of shale below the upper slope; and zone of inner extensional and listric growth faults below the outer shelf.

Corredor *et al.*, (2005) and Ejedawe, (2007) used a high resolution bathymetry and seismic imaging to further characterised the basin structural styles into five distinct structural zones. The structural zones identified by Corredor *et al.* (2005) and Ejedawe (2007) include the following: The outer fold and thrust belt: It is characterized by thrust faults with related folds that verge both towards the basin and the hinterland. The transitional detachment fold zone: Located below the lower continental slope, this zone exhibits minimal deformation interspersed with detachment folds. These folds occur above a thick shale unit known as the Akata Formation.

The inner fold and thrust faults: This zone consists of typically imbricated thrust faults and related folds. The mud-diapir zone: Situated below the upper continental slope, this zone is marked by active, passive, and reactive mud diapirs. These include massifs and shale ridges, shale overhands, and vertical mud diapirs that give rise to mud volcanoes on the seafloor. Located beneath the continental shelf, the extensional zone is recognised by basinward-dipping and counter-regional normal growth faults. It is also marked by the presence of related rollovers together with the depocenters. Corredor *et al.*, (2005) reported that deformations across the structural zones are still very active today.

2.3.4.1 Growth Fault

Merki, (1972); Evamy *et al.*, (1987) reported that the common structures in the basin are connected to the deformation, occurring at the same time as the deposition of the delta. This deformation process is responsible for the formation of growth faults. These structures were caused by the

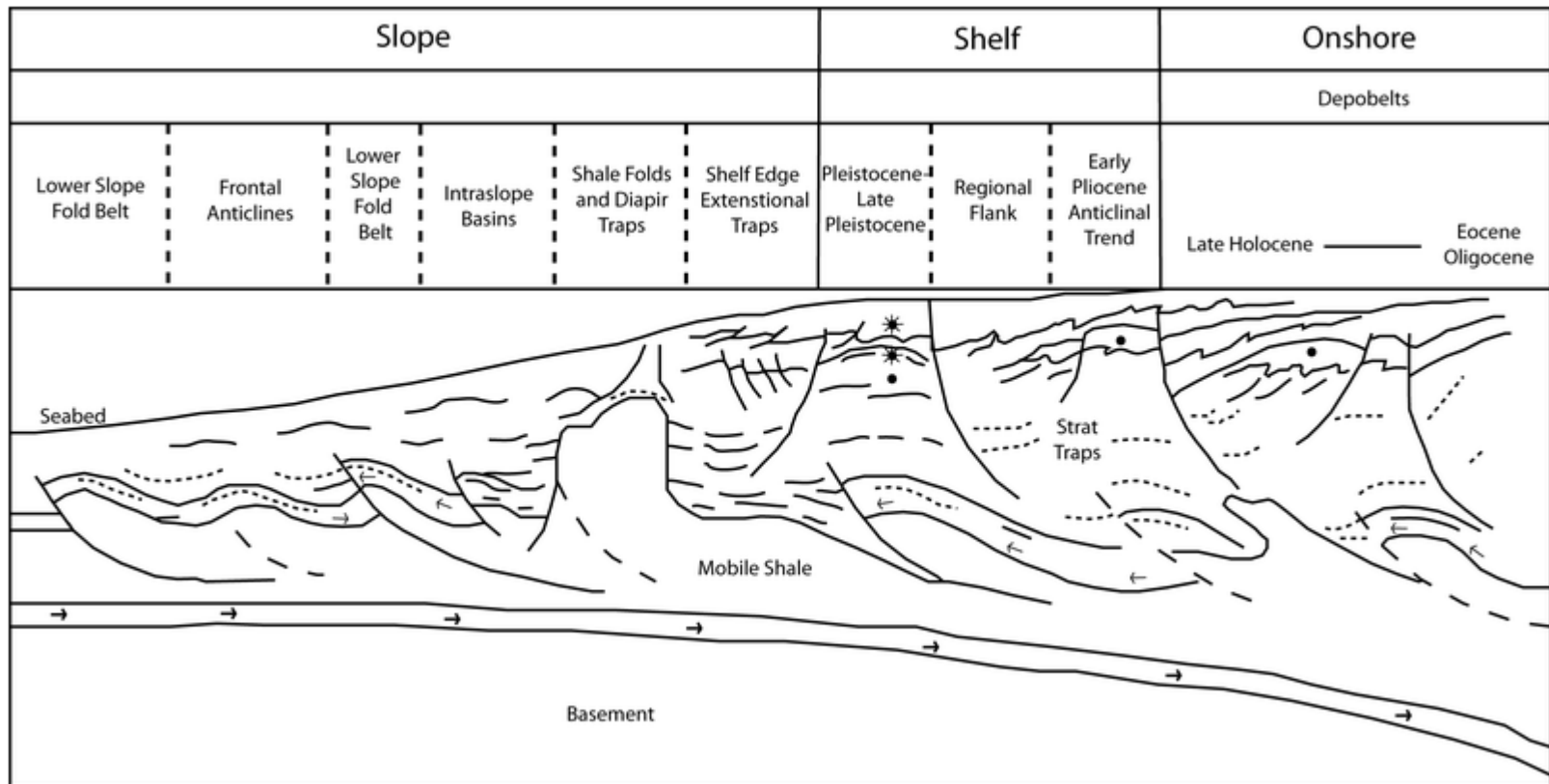


Figure 2.8: Niger Delta Structural Profile Showing Listric Extension Faults, Diapirs and Gentle Fold Thrusts (After Ojo, 1996).

combination of gravitational instability and rapid sedimentation that took place while the sandstone units (Agbada and Benin sands) were being deposited over the undercompacted, mobile prodelta shale (Akata). This relationship is illustrated in Figure 2.9. In addition to the growth faults, the Niger Delta basin also contains rollover anticlines, shale ridges, and shale diapirs, which are visible in the schematic structural profile of the delta as described by Tuttle *et al.*, (1999). According to Tearpock and Bischke, (2003), rollover structures are extremely common features of thin-skinned extensional systems resulting from gravity force.

According to Tearpock and Bischke, (2003) a growth fault moves as the sediments are being deposited. The deposition of sediments along the shoreline exerts a gravitational force that causes the basin side of the fault to be pulled downward. The sediments exhibit greater thickness and accumulation on the side of the fault that has undergone downward displacement. Within the growth fault, the fault plane gradually changes its direction and becomes less inclined as it extends deeper into the subsurface (Tuttle *et al.*, 1999). The growth fault occurs in loose sediments and the deeper the sediments the larger the fault displacement (Tearpock and Bischke, 2003). Obiadi and Obiadi, (2016) state that the key features of the Niger Delta basin are syndepositional growth faults and associated roll-over anticlinal structures. These structures are essential in creating and modifying the space required for sediment deposition and accumulation.

2.3.4.2 Shale Diapir

Shale diapiric structures are generated when a volume of shale, with lower density compared to its surrounding strata, deforms the underlying layers and rises buoyantly (Figure 2.10-2.11) (Stoneley, 1966; Reymont, 1969). Shale diapirs originate from the presence of abnormal pressure or overpressure exerted on deep-seated shale by the overlying sediments, as explained by Weber and Daukoru, (1975). According to Tuttle *et al.*, (1999), the shale diapirs are specifically derived from the Akata Formation. They are formed due to inadequate dehydration processes and the overpressuring caused by the denser Agbada Formation that overlies the Akata. In the Niger Delta, there are three formations arranged in chronological order from oldest to youngest: Akata, Agbada, and Benin Formation.

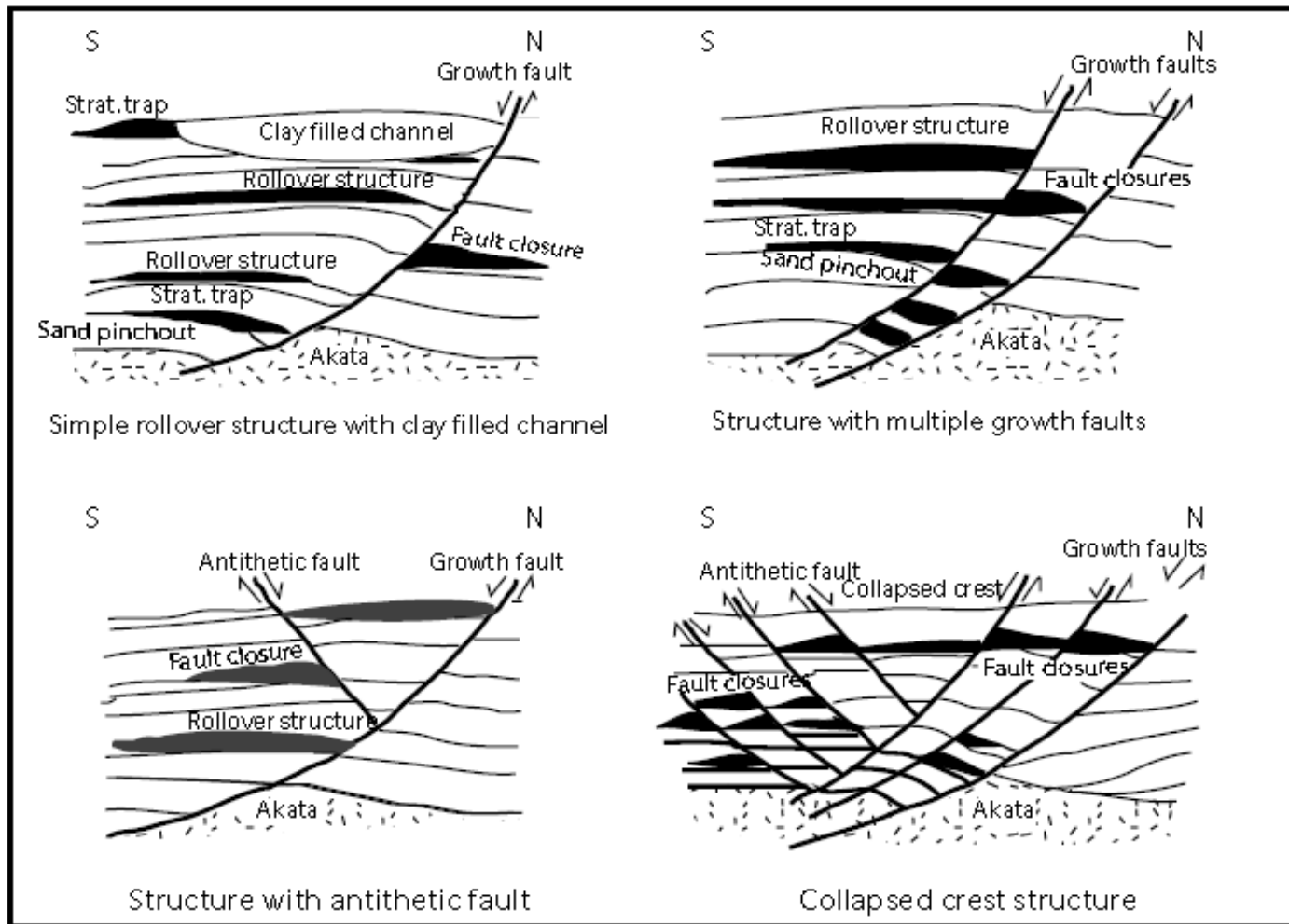


Figure 2.9: Structural Features and Related Traps in Niger Delta (Amended from Stacher, 1995)

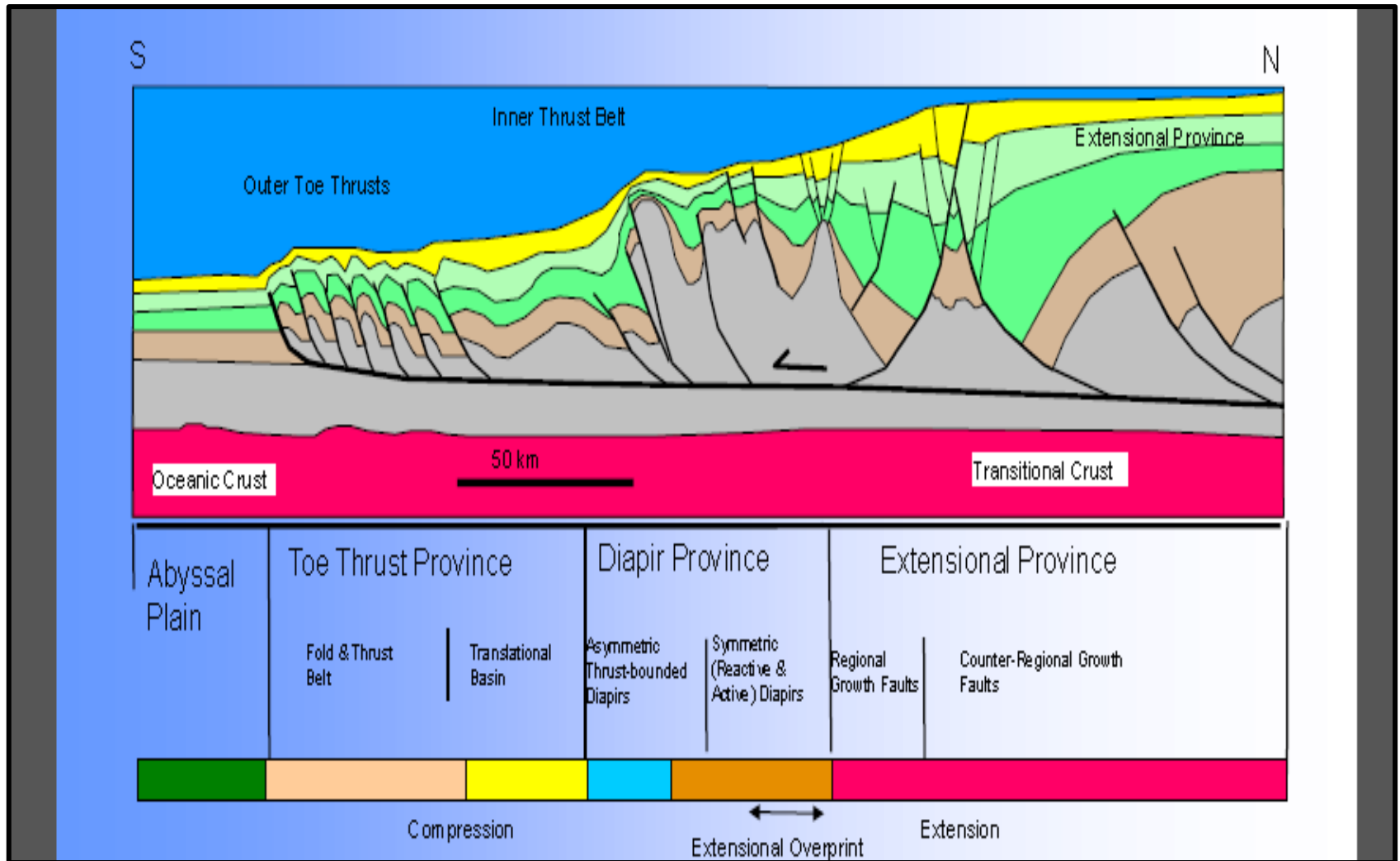


Figure 2.10: Structural Styles in Niger Delta Showing The Formation of Shale Diapir (After Corredor *et al.*, 2005).

Shale Diapir Formation

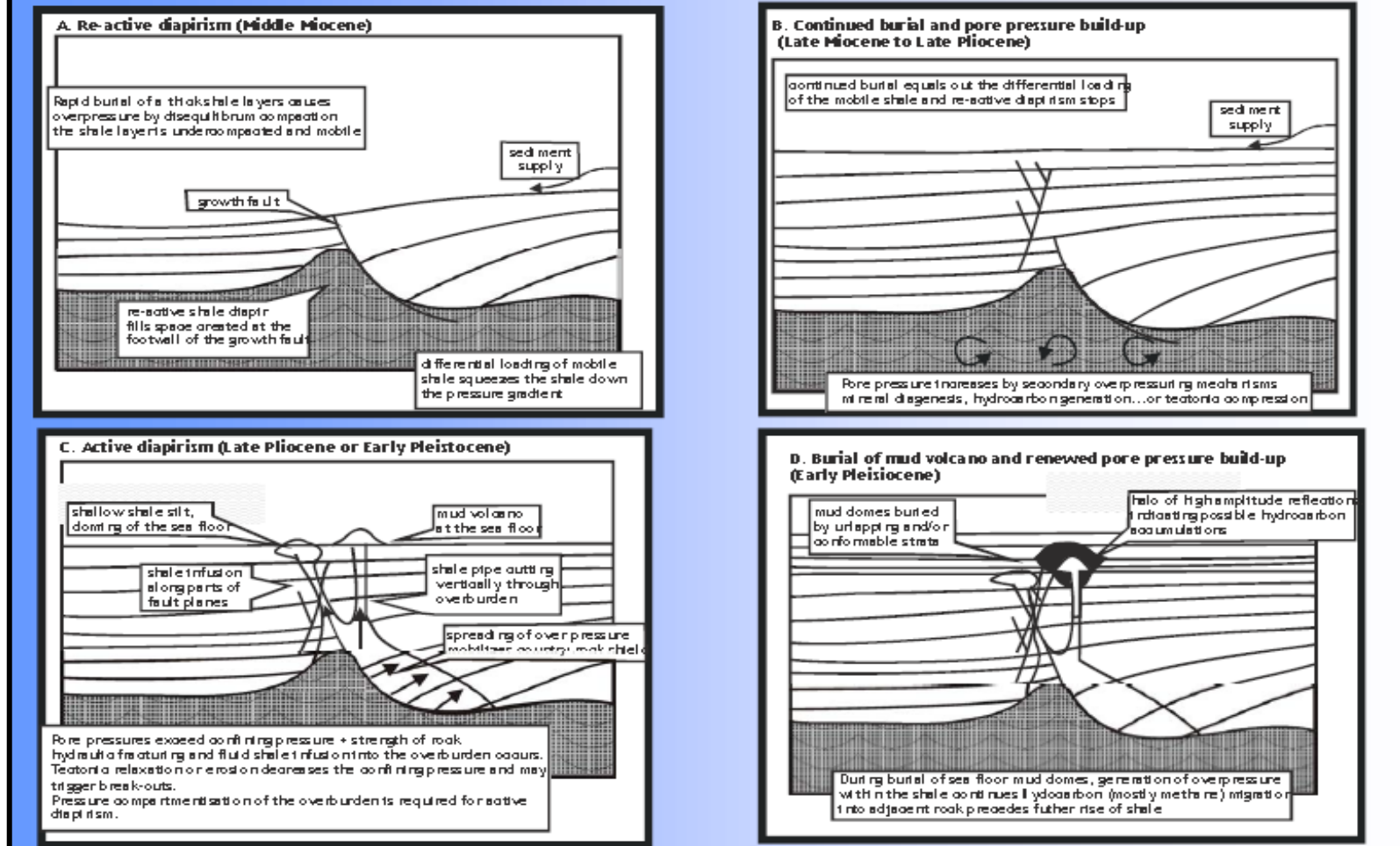


Figure 2.11: Formation of Diapiric Structures from Mud Volcano (After Van Rensbergen *et al.*, 1999)

Akata Formation is the oldest, while Benin Formation is the youngest. According to Weber and Daukoru, (1975), the shale upheaval ridge found in Nigeria can be classified into three distinct types. First, there are zones located behind major growth faults. Second, there are shale bulges situated in front of growth faults, which contribute to the formation of unconformities and collapsed crest structures; and the third took place at the continental slope, where shale formations were pushed outward towards the sea due to varying pressure on the mobile shale.

As sedimentation persisted, the clay upheaval ridges in the offshore became buried in a similar manner to salt domes. Subsequently, these clay ridges have the potential to transform into authentic diapiric structures. Marine surveys have revealed the presence of diapiric structures beneath the continental slope and rise, approximately 100km southeast of the basin, as noted by Stoneley, (1966). These diapirs seem to have substantial connections within the sedimentary section, with the source layer potentially dating back to the Aptian-Albian age, as indicated by Reyment, (1969).

2.3.5 Niger Delta Basin and Petroleum Occurrence

Hydrocarbon deposits are distributed in different regions within the Agbada Formation. Nevertheless, distinct directional patterns within the area give rise to an "oil-rich belt" where the largest oil field is located, accompanied by a relatively low gas-to-oil ratio (Evamy *et al.*, 1978; Ejedawe, 1981). The oil-rich belt extends from the northwestern offshore region to the southeastern offshore area, covering a range of patterns oriented in a north-south direction near Port Harcourt, as depicted in Figure 2.12. This belt corresponds to the boundary between continental and oceanic crust and is located within the region characterized by the highest sedimentary thickness.

Originally, the distribution of hydrocarbons was attributed to the timing of trap formation in relation to the migration of petroleum (Evamy *et al.*, 1978). Ejedawe, (1981) states that the localization of oil-rich areas within the oil-rich belt is connected to the presence of five delta lobes, which are fed by four distinct rivers. In addition, Ejedawe, (1981) deduced that the main factors responsible for the abundance of oil within the belt are the elevated geothermal gradient at the central part of the delta and the relatively older age of sediments

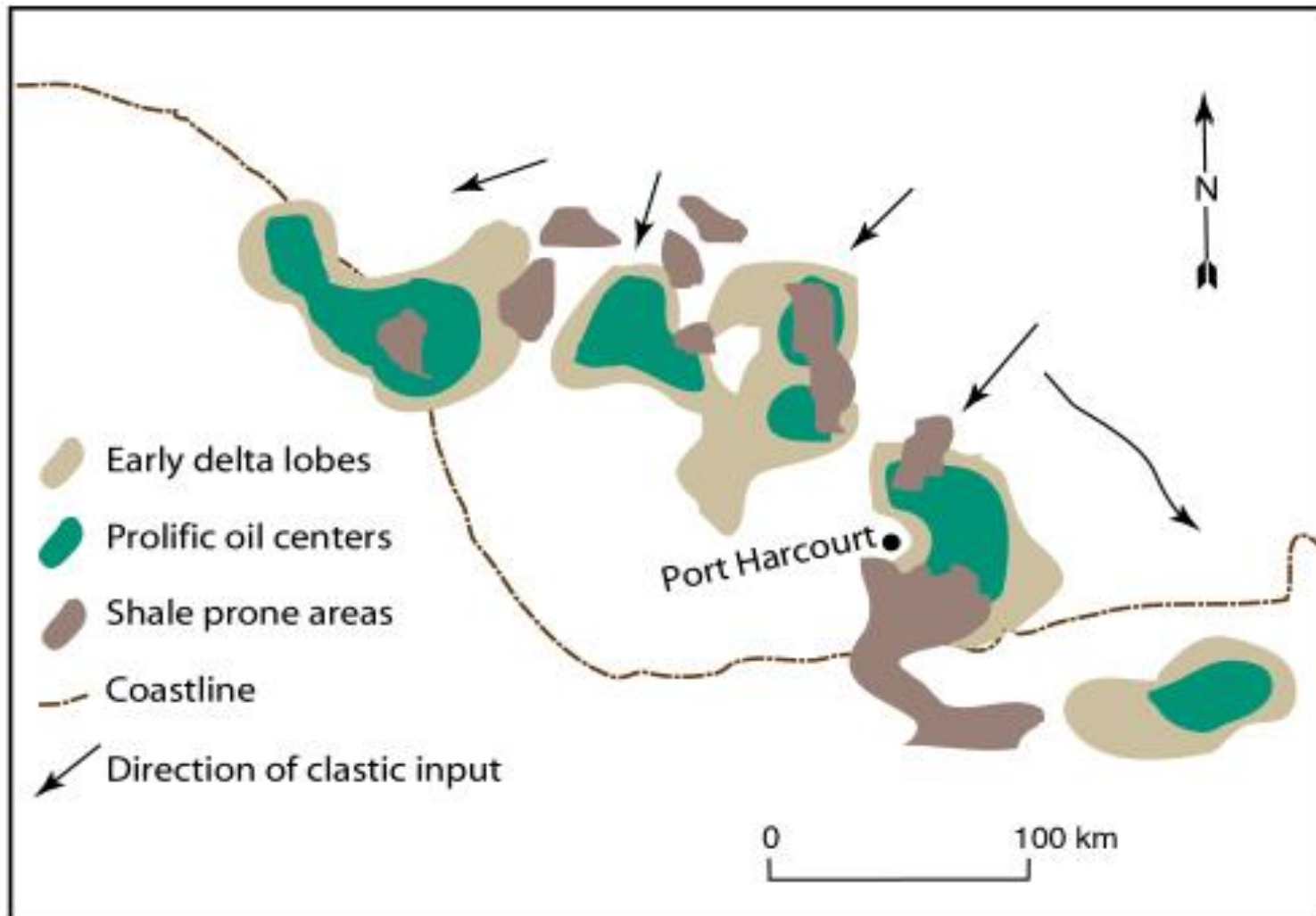


Figure 2.12: Map Showing Niger Delta Prolific Oil Centres, Shale Prone Areas And Early Delta Lobes (Amended from Reijers *et al.*, 1997)

within the belt, in comparison to those found in the offshore region. The interplay of these factors contributed to a higher level of maturation per unit depth of the sediments within the belt.

The presence of rollover structures is particularly concentrated in the depobelts, with fewer paralic sequences to the south, which aligns with the location of the oil-rich belt, as noted by Weber, (1987). The distribution of hydrocarbons within the basin was influenced by the heterogeneity of the source rocks, with a greater contribution originating from paralic sequences in the western region, and/or segregation resulting from re-migration, as proposed by Doust and Omatsola, (1990). Haack *et al.*, (1997) suggested that the shale formations, which act as source rocks, were influenced by pre-Tertiary structures that are connected to basement structures.

This relationship is supported by the correlation of source rock deposition near the delta lobes with the positioning of the oil-rich belt. The gas: oil ratios (GOR) has high values at the northernmost, easternmost and the center of the delta (excluding area of abundant oil). The ratio increases seaward in all the depobelts and farther from the depositional centres, along strike direction. The location of Gas-Oil Ratios (GORs) can be explained by several factors, including re-migration resulting from post-depositional tilting in the lower part of the depobelt, the upward displacement of accumulations due to the flushing of gas from higher maturity zones, and the variation in source rock properties (Doust and Omatsola, 1990).

Stacher, (1995) devised a model for the hydrocarbon habitat in the Niger Delta using the approach of sequence stratigraphy, as illustrated in Figure 2.13. The model was developed to connect the deposition of the source rock (Akata Formation) and the reservoirs and seals (Agbada Formation) to sea level in the central part of the basin, which include the oil-rich belt. Stacher, (1995) proposed that the Pre-Miocene Akata shale was accumulated in deep-water environments during periods of low sea levels, and it is subsequently overlain by the Miocene Agbada sequence system tracts. Within the central portion of the basin, the reservoir unit (Agbada Formation) conforms to a shallow ramp model, characterized by highstand system tracts containing hydrocarbon-bearing sands, as well as transgressive

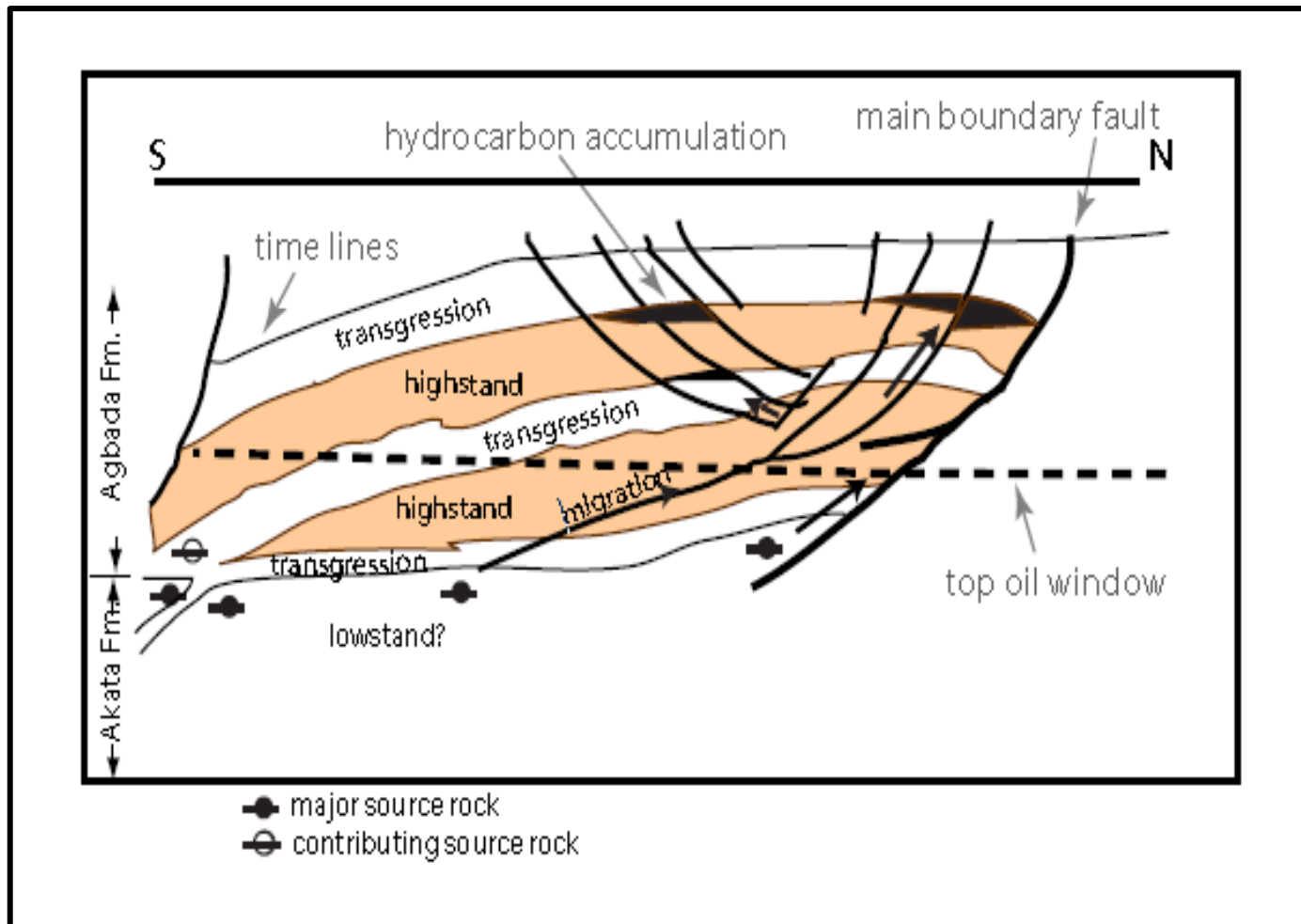


Figure.2.13: Cross-Section of The Niger Delta's Center Region Featuring The Sequence Stratigraphic Model, Mechanisms for Trapping Hydrocarbons, And Pathways for Their Migration.

system tracts composed of sealing shale layers. Petroleum migration is induced by faulting in Agbada Formation which produced the structural traps to formed accumulated petroleum when combined with stratigraphic traps. The shale unit served as an effective seal layer above the sand unit, while also facilitating clay smearing within the faults.

2.3.6 Niger Delta Source Rocks

Extensive research has been undertaken on the source rock of petroleum in the Niger Delta, as demonstrated by numerous studies including those carried out by Evamy *et al.*, (1978), Ekweozor and Okoye (1980), Lambert-Aikhionbare and Ibe, (1984), and several others. Several studies have proposed that the contributions of hydrocarbons originate from the interbedded marine shale found within the Agbada Formation, as well as the marine Akata and Cretaceous shales (Frost, 1977; Evamy *et al.*, 1978; Ekweozor and Okoye, 1980; Lambert-Aikhionbare and Ibe, 1984; Ekweozor and Daukoru, 1984; Stacher, 1995; Haack *et al.*, 1997). The presence of organic content in the Agbada-Akata Formations, as reported by Ekweozor and Okoye, (1980), Nwachukwu and Chukwura, (1986), has been deemed significant enough to classify these formations as good source rocks.

As reported by Stacher (1995), although there are intervals present, they are inadequate to generate a globally significant oil region and remain underdeveloped in certain sections of the basin. Through an analysis of the type and quantity of organic matter, Evamy *et al.*, (1978) determined that the oil in the Niger Delta originated primarily from the marine shale of the Akata Formation and the interbedded shale found within the lower portion of the Agbada Formation. The Niger Delta oil was attributed to the shale within the Agbada Formation in the eastern part of the delta and the marine shale from the Akata Formation in the western delta, as determined by Ekweozor *et al.*, (1979). This conclusion was based on the analysis of $\alpha\beta$ -hopanes and oleananes fingerprints, which helped identify the source of the crude oil.

According to the findings of Ekweozor and Okoye, (1980), the rocks that are younger than the deeply buried lower sections of the paralic sequence exhibit immaturity as indicated by geochemical markers like vitrinite reflectance. Lambert-Aikhionbare and Ibe, (1984) deduced that the shale of lower Agbada Formation has enough maturity for hydrocarbon generation based on different thermal maturity profile. They concluded that the migration

effectiveness could be less than 12% from the marine Akata shale, suggesting that only a small amount of fluid would have migrated from the shale. Ejedawe *et al.*, (1984) concluded, based on maturation data, that the gas in the Niger Delta originated from the Akata shale, while the oil was sourced from the Agbada shale located in the central part of the delta. In different parts of the basin, it was determined that both shales serve as sources for the oil.

According to Doust and Omatsola, (1990), the organic matter responsible for hydrocarbon generation originates from the deltaic offlap sequences and the sediments of the lower Coastal Plain. This suggests that both the Akata and Agbada Formations potentially contain dispersed layers of source rock, although the majority of it is concentrated within the Agbada Formation. Doust and Omatsola, (1990) proposed that the deep turbidite fans and delta slope of the Akata Formation serve as the source rocks in deep water. The organic matter in these environments is derived from land sources, but it could become biodegraded and got enriched in amorphous substance and hydrogen-rich material. The Akata Formation is the sole source rock that has consistent depth of burial with that of the oil window and it is also volumetrically significant (Stacher, 1995).

Other workers such as Frost, (1997) suggested that the Pre-Albian super source rock, Cretaceous marine shale, below the delta could be a potential source rock. Although, the Cretaceous portion do not have data for source-rock evaluation because it has never been drilled below the delta due to the great depth (Frost, 1997). To enable oil migration from the Cretaceous layer into the reservoirs of the Agbada Formation, a complex network of faults and fractures would have been required due to the substantial thickness of the Akata shale, exceeding 6,000 meters (Figure 2.14). According to Olabode *et al.*, (2010) there is no available data to validate the existence of such network.

The chemical composition of the majority of oils yielded contradictory findings regarding the hypothesis of the Early Cretaceous source rock. Nwachukwu *et al.*, (1995) recorded low V: V+Ni ratios of (0.12) in the basin crude, lower than what was recorded from the onshore seeps of Cretaceous oils in the northern part of the basin (Kulke, 1995). Geomark Research Inc. (1998), reported a similar V+Ni ratios for both Miocene oils and the Cretaceous oils. The oils found in the Niger Delta region contain a notable concentration of Oleanane, a

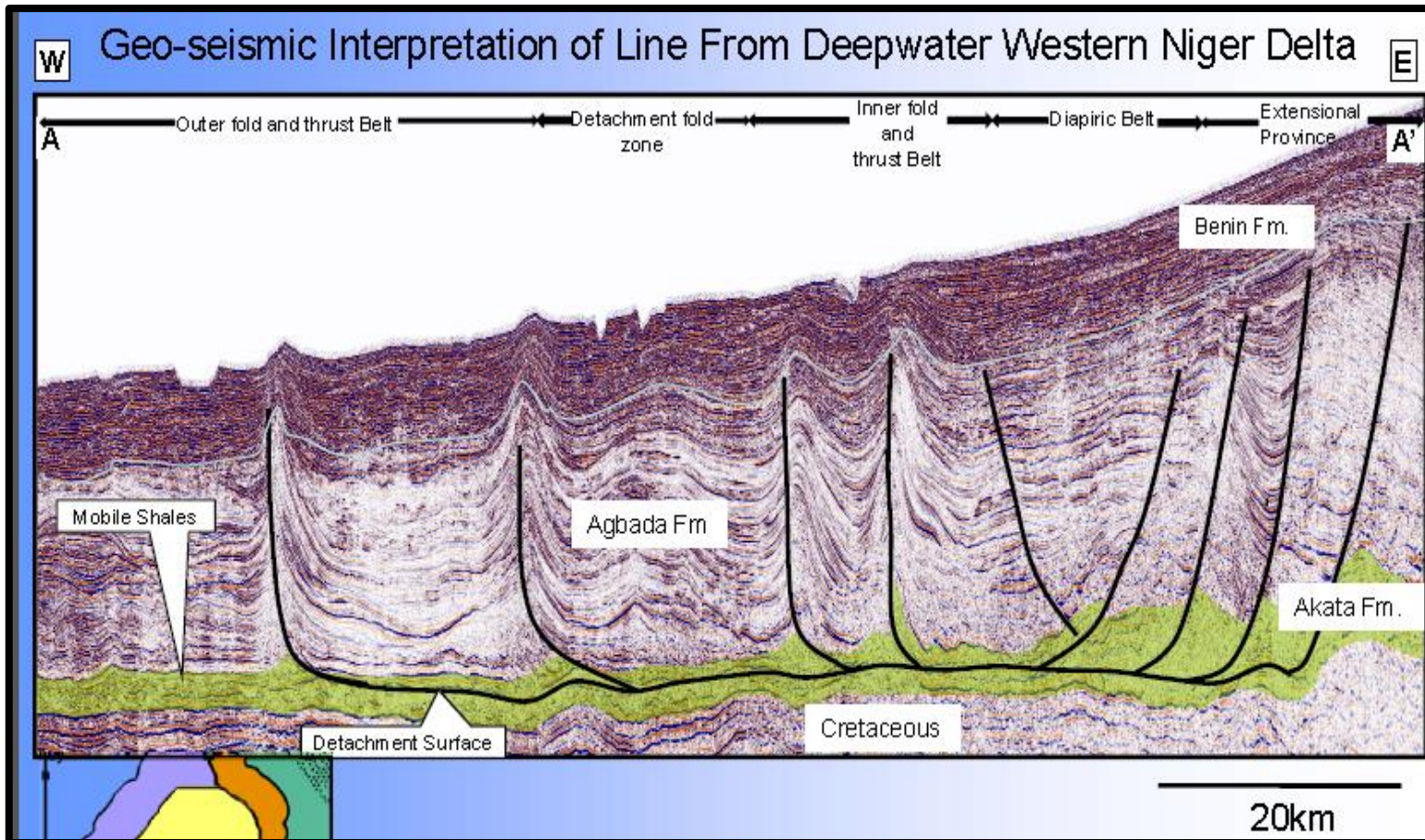


Figure 2.14: Seismic Line Extracted from The Western Niger Delta's Deepwater Region (Adapted from Olabode *et al.*, 2010).

compound that became widely spread during the Late Cretaceous-Tertiary period (Nwachukwu *et al.*, 1995). Using older rocks basin model as a reference, Haack *et al.*, (1997) proposed that oil in theoretical deep-water reservoirs of the Niger Delta could potentially be derived, at least partially, from Upper Cretaceous.

2.3.7 Niger Delta Basin Reservoir Rocks

Petroleum is extracted from the unconsolidated sandstone reservoirs present in the Agbada Formation within the basin. Evamy *et al.*, (1978) reported that the reservoirs characteristics in this Formation are determined by the environment of deposition and the depth of burial. These deposits, ranging from Eocene to Pliocene in age, are typically stacked with varying thicknesses, ranging from less than 15 meters to 45 meters (Evamy *et al.*, 1978). The presence of thicker reservoirs is likely indicative of composite bodies composed of stacked channels, as suggested by Doust and Omatsola (1990). Kulke, (1995) states that the most favourable reservoirs in the basin, in terms of both quality and geometry, are point bars formed within barrier bars and distributary channels intersected by channels filled with sand.

According to Edwards and Santogrossi, (1990) reservoirs in the delta are paralic sand units having porosity of 40%, 2 darcys permeability, 100 m thickness and Miocene in age. The lateral variation of the reservoir is influenced by growth faults, which cause an increase in thickness towards the downthrown block of the fault (Weber and Daukoru, 1975). According to Kulk, (1995) the reservoirs have variable grain sizes in which the fluvial sandstones are coarser than the delta front portion; but the best sorted are the barrier bars and the point bars. Kulke, (1995) reported that it is unconsolidated and contains some minor component of argillo-silicic cement. The potential reservoirs in the outer part of the delta complex are low-stand sand bodies, proximal turbidites and deep-sea channel sands (Burke, 1972; Beka and Oti, 1995).

2.3.8 Traps and Seals in The Niger Delta

Majority of traps in the basin are of a structural nature, although stratigraphic traps are also prevalent, as depicted in Figure 2.15. The structural traps observed in the Niger Delta, as

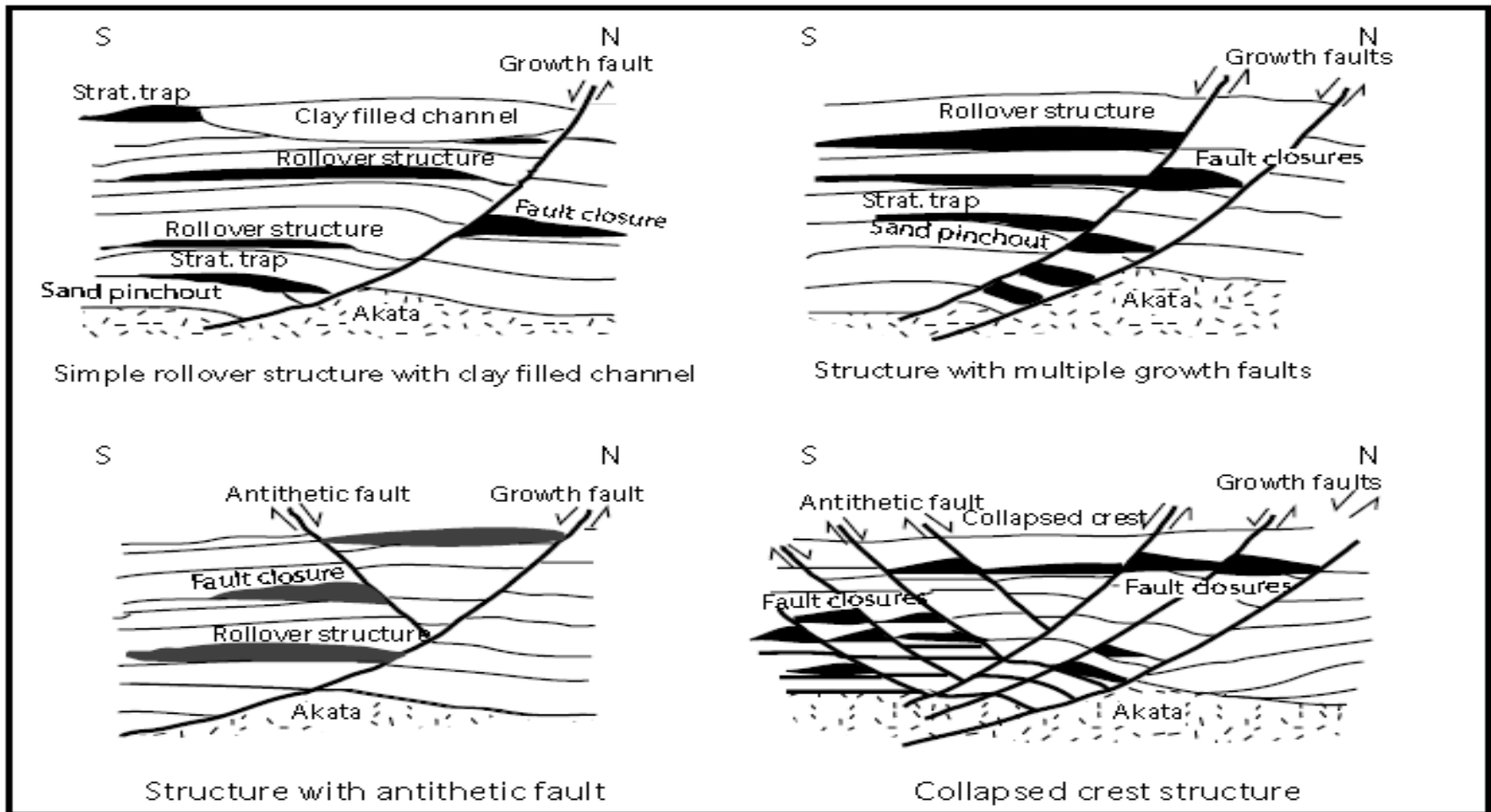


Figure 2.15: Hydrocarbon Traps And Seals in The Niger Delta (After Stacher, 1995).

explained by Evamy *et al.*, (1978); Stacher, (1995), originated from the synsedimentary deformation of the sand unit within the Agbada paralic sequence. The level of structural complexity rises from the northern to the southern regions (Fig.2.15) due to the escalating mobility of the over-pressured and under-compacted shale (Stacher, 1995). Doust and Omatsola, (1990) identified various structural trapping elements in the Niger Delta, encompassing simple rollover anticlines, multiple growth faults, clay-filled channels, collapsed crest structures, and antithetic faults.

Stratigraphic traps hold equal significance to structural traps on the flanks of the Delta. Within this area, pockets of sandstone are interspersed among diapiric structures. As we move towards the delta toe, the sequence of shale and sandstone alternates gradually, eventually shifting towards a predominance of sandstone. Within the Niger Delta, the seal rock comprises shale layers that are present within the reservoir unit, Agbada Formation. These layers of shale function in three categories of seals. Firstly, there are smears of clay formed within a fault that act as seals. Secondly, there are sealing units between the shale layers that are juxtaposed against reservoir sands as a result of faulting, providing a seal.

Lastly, there are vertical seals present (Doust and Omatsola, 1990). Canyons that were created by significant erosion during the early to middle Miocene period can now be found filled with clay on the sides of the delta. These clay deposits serve as the upper seal in certain significant offshore field areas (Doust and Omatsola, 1990). The most striking and prolific structures in the Niger Delta are growth fault with associated rollover anticlines (Figure 2.15). Most of the more than 450 oilfields in the Niger Delta Complex (Petroconsult, 1996a) are associated with rollover anticlines (Whiteman, 1982). Growth faults result from lateral spreading of regressive deltaic sequences caused by sediment density contrast and gravitational instability.

They are synsedimentary in nature and offset active surfaces of deposition (Doust and Omatsola, 1990). These structures often developed near local areas of sediment deposition and expanded as sedimentation occurred. As a result, a larger quantity of sediment could accumulate in the downthrown block in comparison to the upthrown block. In a planar view, growth faults commonly exhibit a crescent shape, with the concave side oriented towards the downthrown block, typically towards the sea (Tearpock and Bischke, 2003). Growth

faults in the Niger Delta commonly flatten with depth (listric) and die out upwards either in or below the base of the sandy Benin Formation (Tearpock and Bischke, 2003).

They mainly affect the Agbada and Akata Formations, reflecting the important element of mud compaction in the evolution of these facies. According to Whiteman, (1982) growth fault planes dip steeply (up to 60°) in the shallower parts of the Agbada succession, decreasing steadily with depth to as low as 30° near the base of the Agbada Formation. These faults often have great displacements, but the fault zones are only as small as a few feet wide (Weber and Daukoru, 1975). Growth faults act as hydrocarbon migratory path from the Akata shale source rocks to the reservoir sands of the Agbada Formation. They also act as seals to migration. Stratigraphic traps are more often synsedimentary, formed at the time of sediment deposition (Fig.2.15).

Such traps are more difficult to recognize in both 2-D and 3-D seismic data when compared to structural traps however, bright spots on seismic data have however helped in locating some stratigraphic traps (Krusi, 1994). In the Niger Delta, they have been found to be associated with regional shale outs, incised valley fills and lowstand valley fans (Krusi, 1994). Local changes in environment of deposition, resulting from changes in fluvial patterns during deposition, may result in significant lateral variations in sediment deposition. As described by Krusi (1994) incised stratigraphic traps can be distinguished into truncation traps against the incised valleys and submarine canyon-fill traps.

They are usually associated with lowstand and early transgressive systems tract. Truncation traps occur where reservoirs are cut and sealed in an updip direction by clay-filled incised valleys or submarine canyon (Krusi, 1994). The lowstand stratigraphic traps are associated with slope fans and basin floor fans. The slope fan stratigraphic trap may develop where channel or overbank (natural levee) sands, are completely enveloped by finer-grained turbidites of the fan apron (Krusi, 1994). Stratigraphic traps associated with basin floor fans may develop where the lowstand basin floor fans are embedded in significantly thicker marine shales.

CHAPTER THREE

METHODOLOGY

3.1 Data Gathering

The data utilized in this study were obtained from the Department of Petroleum Resources (DPR) through the collaboration with Addax Petroleum Development Company of Nigeria. They include; the base map that displays the well locations, wire-line logs, 3-D seismic, well deviation, check shot and production data. The well logs data were utilized for the estimation of petrophysical parameters, estimation of the rock elastic and mechanical properties. Interactive Petrophysics (IP) software for log analysis, version 3.6, 2010 by Senergy software limited and Hampson-Russell Software, CE8 version (September,2008) by CGGVeritas were used for rock physics analysis.

The methodology for this research work include the use of relevant wireline log signatures for petrophysical and rock physics analyses. The following methodologies were adopted in this study:

3.2 Well Log Analysis

The well logs, comprising gamma ray, resistivity, density, sonic, neutron, and compressional wave logs, were provided in American Standard Code for Information Interchange (ASCII) formats and underwent thorough quality checks. They were converted to true vertical depth and loaded into the Interactive Petrophysics (IP) 2010 software for petrophysical study. Logging measurements were analyzed to identify and draw conclusions regarding zones that may be of interest (Ellis and Singer, 2008).

3.2.1 Petrophysical Parameters Evaluation

3.2.1.1 Lithological Identification

The next task after data quality checks and loading is the identification of the lithologies. Lithologic identification was done using Gamma ray (GR) signatures. The GR measures the amount of shale in a reservoir (Schlumberger, 1989). The scale of GR log is set between 0-150 API, with 65 API units as the central cut off point. This means values greater than 65 API was interpreted as shale while sandstones were less than 65 API.

3.2.1.2 Well Correlation

The correlation of wells A1, A2, and A3 within the field was performed by analyzing the gamma-ray (GR) and resistivity log responses. The gamma-ray (GR) and resistivity logs are valuable tools for correlation purposes, applicable in both open and cased boreholes (Schlumberger, 1989). In this study, the log intervals from wells A1, A2, and A3 were compared to identify similarities or characteristic log responses that corresponded to lithological markers. The study wells were correlated by applying the lithological signatures that indicated similar depositional processes and environment. The significant sand units were selected and also correlated between the wells to identify reservoir continuity at different depths across the whole study area.

3.2.1.3. Volume of Shale (Vsh)

The subsequent step involves identifying the zones characterized by a low volume fraction of shale (Vshale), commonly referred to as clean zones, as described by Ellis and Singer, (2008). This was accomplished through gamma ray (GR) measurements. According to Schlumberger, (1989), the magnitude of the GR signal typically rises in correlation with an increase in shale content. As stated by Asquith (2004), the magnitude of the gamma-ray (GR) count within the Formation of interest is indicative of its shale content. The GR log was employed to determine the shale volume by calculating the GR index in equation (3.1) from Asquith and Gibson, (1982) formular:

$$I_{gr} = \frac{GR_{log} - GR_{min}}{GR_{max} - GR_{min}} \quad (3.1)$$

Where;

I_{gr} = GR index demonstrating a linear response to the amount of clay or shale present

GR_{log} = Gamma ray log measurement taken at the specific depth being investigated

GR_{min} = GR log value obtained from a nearby zone consisting of clean sand.

GR_{max} = GR log value recorded from a neighboring shale formation.

By applying Larionov, (1969) equation involving Tertiary rocks, shale volume (V_{sh}) can be expressed as:

$$V_{sh} = (2^{2I_{gr}} - 1) \times 0.083 \quad (3.2)$$

Where;

V_{sh} = shale volume

I_{gr} = GR index

3.2.1.4 Net-Gross Ratio (NGR)

Asquith, (2004) explains that the NGR measurement serves as an indicator of the reservoir sand quality, with higher NGR values corresponding to better sand quality. The NGR was determined using equation (3.3) as described by Asquith, (2004).

$$NGR = \text{Net sand} / \text{Gross sand} \quad (3.3)$$

3.2.1.5 Porosity

In order to investigate the hydrocarbon potential of the reservoirs (sand units), the porosity values were extracted from the porosity logs. The amount of porosity gives the volume of the reservoir containing fluids. According to Guo, (2019) porosity values can range from zero to over 50%. In normal reservoirs, it ranges between 20% - 39%.

3.2.1.5.1 Neutron-Density Porosity

This combination logs were estimated using this formula:

$$\phi_{N-D} = \sqrt{\frac{\phi_N^2 + \phi_D^2}{2}} \quad (3.4)$$

Where,

ϕ_{N-D} = neutron-density derived porosity

ϕ_D = porosity measured from density log

ϕ_N = porosity measured from neutron log

3.2.1.6 Saturation

After the identification of porous, clean formation, the next step was to determine if it contains hydrocarbon or not. This was achieved by employing the resistivity logs. In essence, when a porous formation is saturated with conductive brine, its resistivity will be relatively low. On the other hand, if a significant portion of non-conductive hydrocarbon is present in the formation, then the resistivity will be relatively high (Ellis and Singer, 2008). The presence of hydrocarbons in the formation can be either in the form of oil or gas, and distinguishing between the two was done by comparing measurements of formation density and neutron porosity, as indicated by Ellis and Singer, (2008).

Saturation is expressed as;

$$S_w^m = \frac{a}{\phi^m} \frac{R_w}{R_t} \quad (3.5)$$

The Archie's equation above establishes a connection between porosity, resistivity, and the water content represented by S_w . If porosity (ϕ) increases, the saturation (S_w) will decrease while keeping R_t constant. Similarly, if R_t increases while maintaining the same porosity, it will have a similar effect on saturation. The water content is commonly represented by the water saturation, S_w . In a mixture of hydrocarbon and water, the saturation of hydrocarbon, S_h , can be calculated as 1 minus the water saturation, S_w . Therefore, Hydrocarbon saturation, S_h was estimated using the relationship in equation (3.6).

$$S_h = 1.0 - S_w \quad (3.6)$$

Where:

S_h = hydrocarbon saturation, which represents the fraction of the pore volume that is filled with hydrocarbon.

S_w = water saturation in the uninvaded zone, which indicates the fraction of the pore volume that is filled with water.

3.2.1.7 Bulk Volume of Water

The bulk volume of water (BVW) refers to the proportion of the total rock volume that is filled with water (Schlumberger, 1989). It differs from the water saturation, which represents the percentage of the pore space occupied by water. The BVW is an important factor in determining fluid mobility within the reservoir. The calculation of BVW involves the use of the following formula:

$$BVW = S_w \times \phi \quad (3.7)$$

BVW is the bulk volume of water, S_w represents water saturation and ϕ is the rock porosity

3.2.1.8 Fluid Distribution and Fluid Contacts

The identification of fluid contacts in the reservoir across the three wells was accomplished by analyzing a combination of Resistivity logs and Neutron-Density logs. Resistivity readings can be used as a general indication for fluid type in hydrocarbon reservoirs. According to Schlumberger, (1989) sand units that show high deep resistivity readings are interpreted as fresh-water or oil-bearing zones but sands whose values show low deep resistivity readings, correspond to zones of water. Higher values on the density log indicate the presence of hydrocarbons, which can be helpful in interpreting the data and identifying the crossover points. As supported by Asquith and Krygowski, (2004), large magnitude of the cross-over indicated gaseous hydrocarbon and oil was inferred when there was a small degree in the cross-over.

3.2.2 Identification of Depositional Environments

The depositional settings of the reservoirs in the study field were inferred by analyzing the shapes of the GR logs. The shaliness of the formation was measured by the GR log and it

was used for the identification of depositional environment and lithofacies (Emery and Myers, 1996). According to Serra and Sulpice, (1975) SP and resistivity logs shapes are used as a classification scheme for sand bodies. The identified principal shapes were; the funnel, bell and cylindrical shapes.

3.2.3 Rock Physics - Fluid Substitutions

The next phase of this work after the estimations of the petrophysical parameters is rock physics analysis, which revealed the responses of the reservoir elastic parameters to stress and changing fluid saturations. Rock physics elucidates the connection between surface, well, and laboratory measurements of elastic parameters and the intrinsic properties of rocks, including porosity, mineralogy, pore shapes, pore fluids, pore pressures, permeability, viscosity, stresses, and the overall architecture of the reservoir (Sayers and Chopra, 2009). Rock physics plays a crucial role in enhancing our comprehension of the physical characteristics of reservoirs.

In this study, rock physics modeling played a crucial role in understanding the behavior of both reservoir and non-reservoir zones, and it proved to be highly effective in addressing challenges encountered in log data analysis, as emphasized by Avseth *et al.*, (2001). Fluid substitution plays a crucial role in seismic rock physics analysis, serving as a valuable tool for identifying and quantifying fluids within a reservoir, as highlighted by Kumar, (2006). The low-frequency Gassmann theory, proposed by Gassmann, (1951), is the most commonly used theoretical approach for fluid substitution. It allows for modeling different pore fluid saturations, ranging from complete water saturation to exclusive presence of oil or gas saturation. The purpose is to accurately simulate the seismic response of the reservoir given its fluid composition (Kumar, 2006).

3.2.3.1 Reservoir Fluid and Seismic Properties

The pore fluids filling sedimentary rocks vary in composition and physical properties. In a reservoir, the primary fluid types include oil, gas, and brines. These different fluid compositions possess distinct physical properties that contribute to the overall seismic behavior of the rock. In hydrocarbon saturated rocks, the gas-oil ratio (GOR) is defined as

the ratio of the volume of gas released from solution to the volume of oil at standard conditions, is an important factor that controls seismic response (Batzle and Wang, 1992). The maximum amount of gas that can dissolve in solution is a function of the composition of the gas, the oil, as well as the pressure and temperature (Mavko *et al.*, 1998).

The compressional velocity (V_p), shear velocity (V_s), and density play a crucial role in determining the seismic response of a rock. However, it is important to note that V_p and V_s may not provide the most accurate indications of fluid saturation effects since they are primarily influenced by shear modulus and bulk density, as highlighted by Han and Batzle (2004). The estimation of seismic velocity in an isotropic material can be achieved by considering the known rock moduli and density. In isotropic media, the estimated P-wave and S-wave velocities can be expressed as follows:

$$V_p = \sqrt{\frac{K + 4/3 \mu}{\rho}} \quad (3.8)$$

and

$$V_s = \sqrt{\frac{\mu}{\rho}} \quad (3.9)$$

The equations provided above involve the P-wave velocity (V_p) and S-wave velocity (V_s), where the bulk modulus (K), shear modulus (μ), and mass density (ρ) are essential parameters. To estimate seismic velocity using Gassmann's equations, additional parameters such as elasticity moduli are required, as outlined by Kumar, (2006).

3.2.3.2 Deriving Shear Wave Velocity (V_s) Information

In this study, shear wave (S-wave) log, one of the most essential input parameters was not available. In the literature, various empirical equations proposed by Pickett, 1963; Castagna *et al.*, 1985; Krief *et al.*, 1990; Greenberg and Castagna, 1992 are available to determine the relationships between P and S wave velocities in siliciclastic rocks. In order to determine the shear wave (V_s) from each reservoir of the study field, Castagna *et al.*, (1993) empirical model and Gasmann's relations (Gasmann, 1951) were combined to create localized

models, which were used to compute the shear wave information for each reservoir at each well location. This was necessary in order to reduce the errors that are commonly associated with Castagna derived shear wave information, particularly in unconsolidated reservoirs (Castagna *et al.*, 1993).

Therefore, using a localized model derived from generalized model provided a more accurate means of computing shear wave information for each reservoir (Castagna *et al.*, 1993). Due to non availability of S-wave velocity in this study, the localized model was created using available compressional sonic log. First, Gassmann fluid replacement modeling was used to compute a synthetic P-wave log for a reservoir interval with its initial properties. Then, the resulting synthetic P-wave log was cross-plotted against the field P-wave log to determine the correlation between the two logs. Castagna *et al.*, (1985) proposed an empirical relation that allows the estimation of shear wave velocity (V_s) from compressional wave velocity (V_p) in brine-saturated, multimineral rocks.

The equation reads:

$$V_p = 1.36 + 1.16 * V_s \quad (3.10)$$

Where;

V_p = Compressional wave velocity

V_s = Shear wave velocity.

3.2.3.3 Gassmann's Equations

In this study, Gassmann's equation was employed for Fluid Replacement Modeling (FRM) of the reservoirs during production. The equation provides a simple model for estimating fluid saturation effects on bulk modulus, and is the most common theoretical approach for performing fluid substitutions (Smith *et al.*, 2003). The Gassmann's equation relates the saturated bulk modulus of the rock to its porosity, the bulk modulus of the porous frame, the bulk modulus of the mineral matrix, and the bulk modulus of the pore-filling fluids:

$$K_{sat} = K^* + \frac{\left(1 - \frac{K^*}{K_o}\right)^2}{\frac{\phi}{K_{ft}} + \frac{(1 - \phi)}{K_o} - \frac{K^*}{K_o^2}}, \quad (3.11)$$

Where K_{sat} = the saturated bulk modulus (undrained of pore fluids),

$K\phi$ = the bulk modulus of the mineral matrix,

K_{fl} = the bulk modulus of the pore fluid,

K^* = the bulk modulus of the porous rock frame (drained of any pore-filling fluid) and

\emptyset = porosity

3.2.3.4 Static, Dynamic and Mechanical Reservoir Properties

The following rock elastic properties such as; Bulk modulus, K ; Shear modulus, G ; Young modulus, E ; Compressibility (C_b and C_r); Poisson's ratio, ν ; and unconfined compressive strength (UCS), were determined using various empirical relations. The elastic properties of rock are related and can also be derived from density and acoustic wave velocity (Yale, 1994; Holt *et al.*, 1989). According to Montmayeur and Graves, (1986), compressional and shear velocities (slowness) and density are the data required to estimate the mechanical rock properties. Velocities of compressional and shear waves depend on the elastic properties (young, bulk and shear moduli and rock density).

3.2.3.4.1 Bulk Modulus (K)

The bulk modulus (K), or incompressibility, of an isotropic rock, is the ratio of hydrostatic stress to volumetric strain (Smith *et al.*, 2003). The values of bulk modulus can be calculated either by velocity measurements from the laboratory or log data analysis (Batzle and Wang, 1992). In this study, values for bulk modulus were obtained from analysis of wireline log data as highlighted by Batzle and Wang, (1992). Equation 3.12 establishes a relationship between the bulk modulus (K_{sat}) of a rock and its compressional velocity, bulk density and shear velocity.

$$K = \rho_B \left(V_p^2 - \frac{4}{3} V_s^2 \right), \quad (3.12)$$

Where; ρ_B is the bulk density of the rock,

V_p is the compressional velocity, and

V_s is the shear velocity.

If K_{sat} is calculated from the measurements of velocity and density from the log data, the result will be bulk modulus of the rock with the saturating in-situ pore fluid. But the calculated bulk modulus will be that of the porous rock framework, K if measurement of velocity is carried out under a controlled humidity-dried core samples (Smith *et al.*, 2003).

3.2.3.4.2 Shear Modulus (G)

The shear modulus (G), or shear stiffness, of a rock is the ratio of shear stress to shear strain (Lawson-Jack *et al.*, 2019). It can be derived either from log data analysis or from the laboratory tests. In this study, G is estimated from the Equation (3.13),

$$G = \rho_b v_s^2 \quad (3.13)$$

Where;

ρ_b is the bulk density in grams per cubic centimeter

v_s is share wave velocity in kilometers per second, and

G is the Shear modulus, in gigapascals

According to Smith *et al.*, (2003), if velocities are in km/s and densities in g/cm^3 , the resultant moduli (K and G) will be in (GPa). the saturated bulk modulus (K_{sat}) of a rock is influenced by the composition of the fluid filling its pores, whereas the shear modulus remains unaffected by the presence of pore fluid ($G_{\text{dry}} = G_{\text{wet}}$) (Biot, 1956; Berryman and Milton, 1991; Berryman, 1999).

3.2.3.4.3 Young Modulus (E)

Young modulus is defined as the ability of rock property to resist deformation (Lawson-Jack *et al.*, 2019). It is expressed as the quotient of compressive or tensile strength divided by compressive or tensile strains. (Lawson-Jack *et al.*, 2019). It is expressed as:

$$E = 9GK / (3K + G) \quad (3.14)$$

Where;

E = Young modulus

G = Shear modulus and

K = Bulk modulus

It can also be expressed as,

$$E = 2G (1 + \nu) \quad (3.15)$$

Where; ν is the Poisson's ratio

3.2.3.4.4 Poisson Ratio (ν)

Poisson ratio was derived from sonic log measurement and it is expressed in terms of slowness, which is referred to as interval transit times, (ΔT) (reciprocal of velocity) in microseconds per foot unit. Moos, (2006) reported that the ratio of compressional wave slowness (ΔV_p) and the shear wave slowness (V_s) can be used to calculate the Poisson's ratio.

Hence,

$$\nu = 0.5 \frac{\left[\left(\frac{V_p}{V_s} \right)^2 - 1 \right]}{\left[\left(\frac{V_p}{V_s} \right)^2 - 1 \right]} \quad (3.16)$$

The highest possible value for the Poisson's ratio (ν) is 0.5 in theory.

In which:

V_p refers to the velocity of compressional waves,

V_s refers to the velocity of shear waves.

The young modulus, shear modulus, bulk modulus and poisson's ratio can be derived from velocity ratio (V_p/V_s) and density (ρ) (Montmayeur and Graves, 1985). The bulk modulus (K) and shear modulus (G) are related to poisson's ratio by Equations 3.17 and 3.18

(Darvishpour *et al.*, 2019):

$$K = E / 3(1-2\nu) \quad (3.17)$$

Also,

$$G = E / 2(1+\nu) \quad (3.18)$$

3.2.3.4.5 Rock Strength - Unconfined Compressive Strength (UCS)

The UCS depends on elastic modulus, meaning that a higher elastic modulus corresponds to greater strength (Chang *et al.*, 2006). The relationship between uniaxial compressive strength (UCS) and elastic modulus (E) can be expressed as;

$$UCS = 2.28 + 4.1E \quad (3.19)$$

Where UCS represents the rock unconfined compressive strength while E signifies the Young modulus.

3.2.4 Sand Production

In this study, the potentials for sand production during production in all the reservoirs of the field was estimated using the calculated elastic parameters. Vahidoddin *et al.*, (2012) reported that it is crucial to assess the potential for sand production in sandstone oil and gas reservoirs in order to determine the need for sand control measures during production. This is because the economic implications of sand production are huge and critical to require regular improvement in techniques and methods of prediction.

3.2.4.1 Shear Modulus (G) to Bulk Compressibility (Cb) Ratio

This can be expressed as,

$$G/ Cb \quad (3.20)$$

Where,

G = Shear modulus

Cb = Bulk compressibility

Tiab and Donaldson, (2004) suggested that the empirical relation implied that a threshold for sanding existed when $G/Cb = 0.8 \times 10^{12} \text{ psi}^2$, whereas values less than $0.8 \times 10^{12} \text{ psi}^2$ suggest a high probability of sanding. This empirical relationship considered only whether sanding will be a challenge at present conditions. The method states whether a well will be a sand producer, but a maximum sand-free rate cannot be calculated from the given ratio of G/Cb (Ghalambor *et al.*, 2015).

The summarised workflow is shown in the figure 3.1 below.

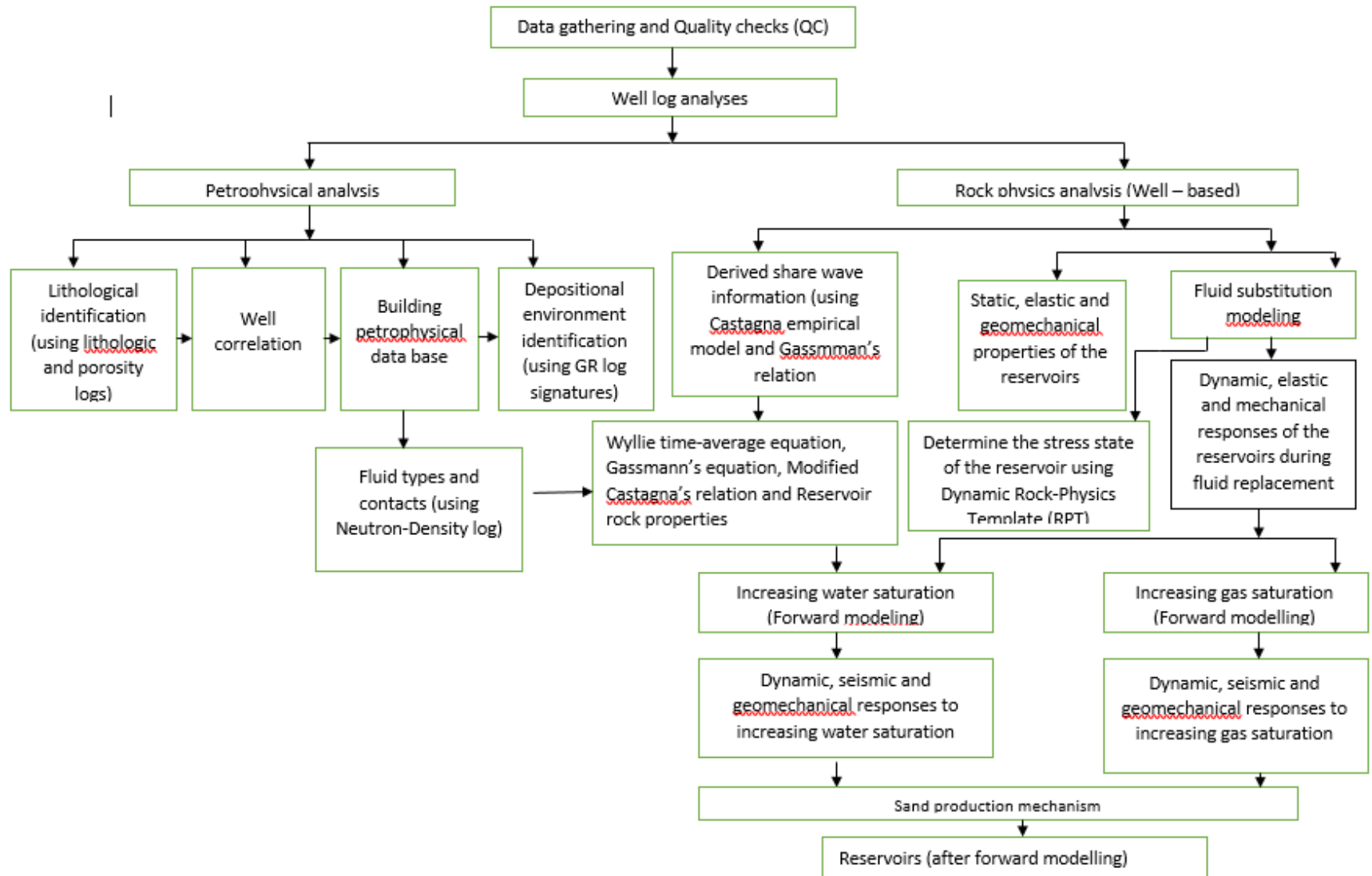


Figure.3.1: The Summarized Workflow Chart of The Research Study

CHAPTER FOUR

RESULTS AND DISCUSSION

4.1 Petrophysical Data Estimation

The lithological composition of the three wells consist of paralic sequence of sandstone which was interbedded with shale as observed in a typical Agbada Formation (Fig.4.1). As supported by Ekweozor, (2004), the upper unit is the coastal plain sand, which is a component of the Benin Formation and consists primarily of gravel and sand deposited by river systems. The unit is of continental origin and comprises extensively porous sandstones that hold freshwater. These sandstones are characterized by their high porosity and are interspersed with shale, which becomes more prevalent towards the lower portion of the unit (refer to Figure 4.1 and Table 4.1). This supports the works of Ejedawe, (2007); Adeoye and Enikanselu, (2009); and Corredor *et al.*, (2005) on the lithological composition of the Benin Formation.

The selected sands were correlated following the correlation line A2-A1-A3 to establish reservoirs' continuity in the study field (Fig.4.2). The log (GR and resistivity) responses in Fig.4.2 showed little variations in the horizons along the correlation line in wells A2, A1 and A3. Tables 4.2– 4.4 present the results of a comprehensive petrophysical analysis carried out on the three wells of Tetemu field. Four reservoir units (A, B, C and D) of interest were delineated and correlated as shown in Fig.4.2. The reservoirs were characterized by various petrophysical parameters such as net-gross ratio, hydrocarbon saturation, porosity, water saturation, shale volume, among others as reported in Tables 4.2-4.4. The petrophysical data were obtained from relevant equations utilized for each specific reservoir unit, drawing on petrophysics.

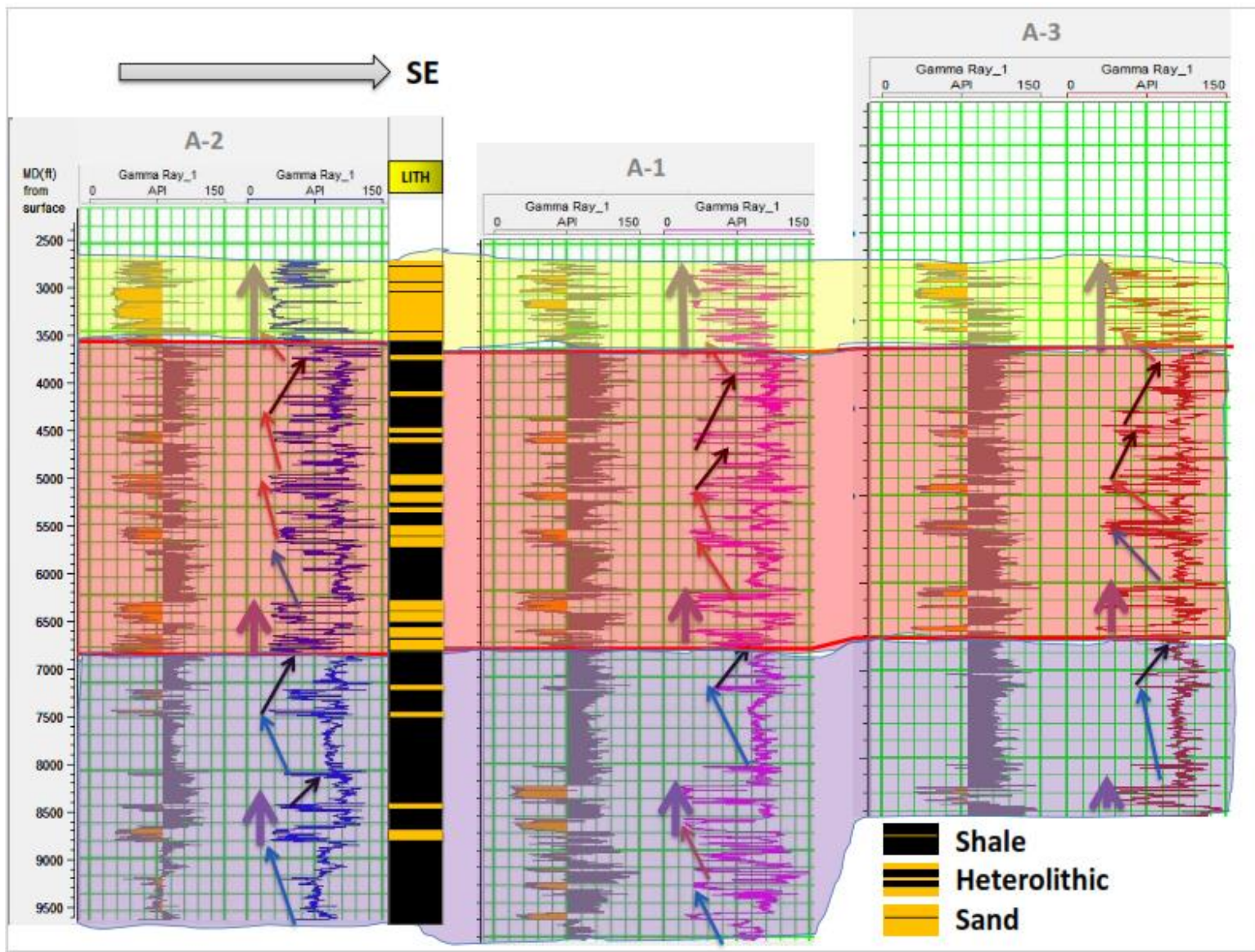


Figure.4.1: The Well Correlation Panel Showing Lithofacies of Interest of Tetemu Field Wells.

Table 4.1: Interpretation of The Log Signatures in Fig.4.1 for Reservoirs' Depositional Environments

Log Signature	Interpretation	Depositional Environment
Coarsening up sequence with an abrupt transition 	Prograding Shelf	Shelf/Shoreface
Coarsening up sequence with a gradual transition 	Prograding Delta	Deltaic
Fining up sequence with high serration 	Retrograding	Tidal Channel
Blocky 	Aggrading	Distributary Channel

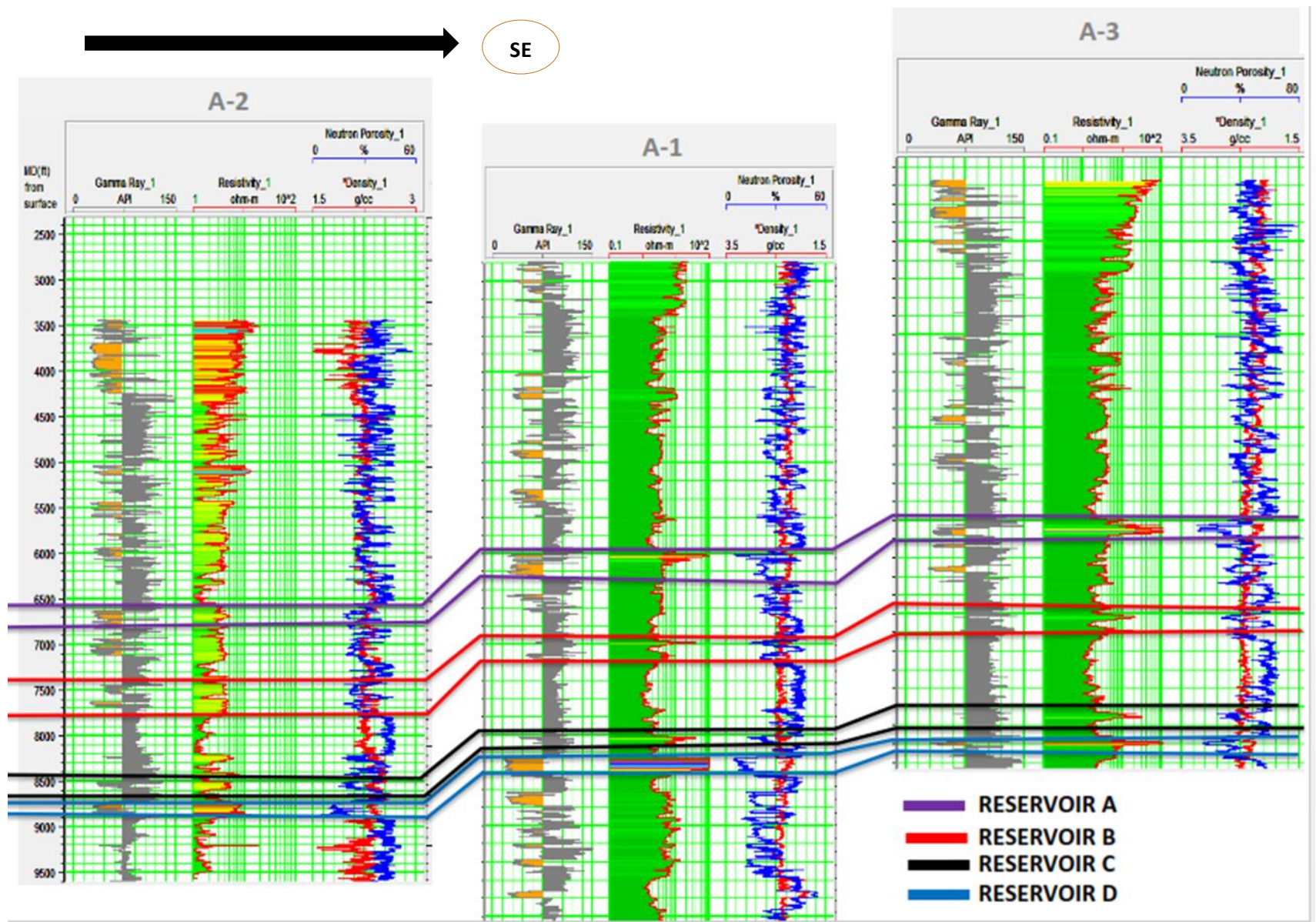


Figure 4.2: A well Correlation Diagram Showing The Continuity of Reservoirs along The Correlated Wells A2-A1-A3

Table 4.2: Petrophysical Parameters of Well A1 Reservoirs of The Study Field.

PETROPHYSICAL SUMMARY AVERAGE FOR A-1 WELL RESERVOIRS																
RESERVOIR SUMMARY																
RESERVOIRS	Sand Top	Sand Bottom	Thinnest Interval Thickness	Thickest Interval Thickness	Gross Sand/Thickness	Net Thickness	N/G	Fluid Type	Fluid Contact	V _{shale}	Total Porosity	Effective Porosity	S _w	S _{xo}	S _h	BVW
	(m)	(m)	(m)	(m)	(m)	(m)				(dec)	(dec)	(dec)	(dec)	(dec)	(dec)	(dec)
RESERVOIR A	2013.71	2089.97	0.15	37.95	76.26	62.66	0.822	GAS/WATER	GWC @ 2035.91	0.145	0.2262	0.2044	0.425	0.449	0.575	0.08
RESERVOIR B	2251.17	2299.56	0.15	6.10	48.39	16.99	0.351	OIL	ODT	0.178	0.2043	0.1775	0.641	0.645	0.359	0.11
RESERVOIR C	2516.58	2535.92	0.30	2.74	19.34	6.86	0.355	OIL / WATER	OWC @ 2520.40	0.111	0.1983	0.1816	0.311	0.36	0.689	0.05
RESERVOIR D	2573.68	2626.50	0.30	20.73	52.82	43.43	0.822	GAS / OIL	GOC @ 2608.78	0.07	0.2088	0.1983	0.309	0.34	0.691	0.06

V_{shale}: Shale volume

S_w: Water saturation

S_h: Hydrocarbon (oil and gas) saturation

S_{xo}: Flushed zone water saturation

BVW: Bulk volume of water

N/G: Net-Gross ratio

GWC: gas- water contact

ODT: oil-down to

OWC: oil-water contact

GOC: gas-oil contact

Table 4.3: Petrophysical Parameters of Well A2 Reservoirs.

PETROPHYSICAL SUMMARY AVERAGE FOR A-2 WELL RESERVOIRS																
RESERVOIRS	Sand Top	Sand Bottom	Thinnest Interval Thickness	Thickest Interval Thickness	Gross Sand/Thickness	Net Thickness	N/G	Fluid Type	Fluid Contact	Vshale	Total Porosity	Effective Porosity	Sw	Sxo	Sh	BVW
	(m)	(m)	(m)	(m)	(m)	(m)				(dec)	(dec)	(dec)	(dec)	(dec)	(dec)	(dec)
RESERVOIR A	2044.54	2104.26	0.61	27.43	59.72	55.01	0.921	OIL	ODT	0.0939	0.2469	0.2283	0.4951	0.8317	0.5049	0.1102
RESERVOIR B	2292.40	2368.30	0.15	29.26	75.90	47.93	0.632	OIL	ODT	0.136	0.2373	0.2105	0.4668	0.8223	0.5332	0.0936
RESERVOIR C	2618.99	2639.86	0.30	4.72	20.87	12.95	0.621	OIL	ODT	0.0945	0.2009	0.1823	0.4847	0.8282	0.5153	0.0869
RESERVOIR D	2681.12	2726.10	0.15	6.86	44.97	24.99	0.556	GAS	GDT	0.0452	0.1805	0.1716	0.4212	0.8071	0.5788	0.0713

V_{shale}: Shale volume

S_w: Water saturation

S_h: Hydrocarbon (oil and gas) saturation

S_{xo}: Flushed zone water saturation

BVW: Bulk volume of water

N/G: Net-Gross ratio

ODT: Oil Down To

GDT: Gas Down To

Table 4.4: Petrophysical Parameters of Well A3 Reservoirs of Tetemu Field

PETROPHYSICAL SUMMARY AVERAGE FOR A-3 WELL RESERVOIRS																
RESERVOIRS	Sand Top	Sand Bottom	Thinnest Interval Thickness	Thickest Interval Thickness	Gross Sand/Thickness	Net Thickness	N/G	Fluid Type	Fluid Contact	V _{shale}	Total Porosity	Effective Porosity	S _w	S _{xo}	S _h	BVW
	(m)	(m)	(m)	(m)	(m)	(m)				(dec)	(dec)	(dec)	(dec)	(dec)	(dec)	(dec)
RESERVOIR A	2010.61	2072.03	0.15	23.93	61.42	42.21	0.687	GAS / WATER	GWC @ 2038.81	0.1678	0.2302	0.2158	0.4788	0.8263	0.5212	0.0931
RESERVOIR B	2258.26	2266.04	4.57	4.57	7.77	4.57	0.588	OIL	ODT	0.0975	0.2624	0.254	0.2153	0.7384	0.7847	0.0535
RESERVOIR C	2518.41	2529.99	0.61	2.59	11.58	5.49	0.474	OIL	ODT	0.1358	0.2073	0.1956	0.2922	0.7641	0.7078	0.0565
RESERVOIR D	2583.79	2632.25	0.61	11.13	48.46	30.10	0.621	GAS / WATER	GWC @ 2603.14	0.1087	0.2006	0.1912	0.3368	0.7789	0.6632	0.0614

V_{shale}: Shale volume

N/G: Net-Gross ratio

S_w: Water saturation

GWC: Gas-water contact

S_h: Hydrocarbon (oil and gas) saturation

ODT: Oil down to

S_{xo}: Flushed zone water saturation

BVW: Bulk volume of water

4.1.1 The Net-Gross (N/G) Ratio

The NGR obtained for reservoir A were, 82% (0.822), 92% (0.921), and 69% (0.687) in wells A1, A2 and A3 respectively (Table 4.2, 4.3 and 4.4). Also, the NGR values for reservoir B across the wells were, 35%, 63% and 59% respectively (Tables 4.2, 4.3 and 4.4). In reservoir C, the computed values of NGR were; 36%, 62%, and 47% in wells A1, A2 and A3 respectively (Tables 4.2-4.4). The NGR values obtained for reservoir D in wells A1, A2 and A3 were; 82%, 56% and 62% respectively (Tables 4.2, 4.3 and 4.4). Reservoirs A and D are the best sand units across the three wells with average values of 82% and 67% (Table 4.2 – 4.4). According to Adepelumi *et al.*, (2011), the value of NGR determines the quality of reservoir. In reservoirs B and C, the calculated values of NGR were comparatively lower (Table 4.2- 4.4).

The energy and direction of the reservoir sands' deposition are determined by the NGR values (Adepelumi *et al.*, 2011). The NGR value reduces as the hydrodynamics flow dropped due to gradual drop in depositional energy from proximal to distal source across the correlated wells A2 – A1- A3 in reservoir A. Although, this observed trend is not consistent with reservoirs B, C and D. In well A2, the NGR value decreased from reservoir A to reservoir D (Table 4.3). Also, this trend is not obvious in other reservoirs, and could be suggested that the deposition of sand reduced from the north towards south along the correlated wells. Also, it was deduced that reservoirs A and D have the best sand quality due to their NGR value; The observed lower sand development in reservoirs B and C may have effect on the reservoir producibility.

4.1.2 Volume of Shale (Vshale)

In well A1, the calculated volume of shale (Vshale) in reservoir A, is 14% (Table 4.2) while the estimated values in reservoirs B, C and D were 17%, 11% and 7%, respectively (Table 4.2). These values were very low and implied that all the reservoirs in well A1 were relatively clean. As highlighted by Nton and Salami, (2016), reservoir with shale volume less than 15% are considered clean. Also, in well A2, the estimated values of (Vshale) were 9%, 13%, 9% and 5% in the reservoirs (A-D) respectively (Table 4.3). The calculated values of (Vshale) for all the reservoirs of well A2 implied that the reservoirs were relatively clean. In well A3, 16%, 10%, 14% and 11% of (Vshale) values were recorded for the four reservoirs (A-D) respectively in the Table 4.4.

Most of the reservoirs in the study field were considered to be relatively clean except reservoir B, (17%) of well A1 and reservoir A (16%) of well A3 with values greater than 15%. These two reservoirs were not considered clean due to over 15% volume of shale. Across the correlated wells, A2-A1-A3, the shale volume increases towards the southern part of the basin (basinward). For instance, the value of V_{shale} in reservoir A increased from 9% in well A2 (Table 4.3) to 14% in well A1 (Table 4.2) and to 16% in well A3 (Table 4.4). Also, in reservoir C, the V_{shale} increased from 9% in well A2 (Table 4.3) to 11% in well A1 (Table 4.2) and to 13% in well A3 (Table 4.4).

The same gradual basinward increment was observed in reservoir D, where the V_{shale} increased from 4% in well A2 (Table 4.3) to 7% in well A1 (Table 4.2) and to 10% in well A3 (Table 4.4). In reservoir B, the trend was slightly different in well A3 (Table 4.4). The value was 13% in well A2 (Table 4.3), 17% in well A1 (Table 4.2) and 9% in well A3 (Table 4.4). Generally, the shale volume increased from proximal to distal portion of Tetemu field (southward), along the lower hydrodynamic flow direction.

4.1.3 Porosity (ϕ)

The effective porosity values decreased with depth in well A2, from 22% in reservoir A to 21% in reservoir B and 18% and 17% in both reservoirs C and D respectively (Table 4.3). Although, this trend is not consistent with wells A1 and A3 porosity values (Tables 4.2 and 4.4) because of variation in porosity values with depth. The effective porosity values are relatively constant, without significant variation across each reservoir. In reservoir A, 20%, 22% and 22% were recorded in well A1, A2 and A3 (Tables 4.2, 4.3 and 4.4). Also, 18%, 21% and 25% were recorded for reservoir B across the three wells (Tables 4.2, 4.3 and 4.4). In reservoir C, 18%, 18% and 19% were recorded in wells A1, A2 and A3 respectively (Tables 4.2, 4.3 and 4.4). Reservoir D has values of 20%, 17% and 19% in wells A1, A2 and A3 (Tables 4.2, 4.3 and 4.4).

This means, compaction and diagenetic changes have very little effect on the porosity across the reservoirs. The observed decreased in porosity value with depth in well A2 (Table 4.3), could be attributed to the continuous deepening of sediments deposition by progradation of the coastline and the movement of depobelt seaward (southward direction). The variations with depth could be due to changes in depositional processes and sedimentary

environments. This is because porosity of sandstones depends on the grain sizes, sorting, compaction and cementation, which control the depositional processes and sedimentary environment (Nton and Salami, 2016).

4.1.4 Hydrocarbon and Water Saturation

The four (4) reservoir units, A, B, C, and D were saturated with oil, gas and water (Table 4.2, 4.3 and 4.4). Reservoir A is a well developed sand across the three wells, with gross thickness and net thickness values of 76.2 m (250 ft) and 62.5 m (205 ft) in well A1 (Table 4.2), 59.4 m (195 ft) and 54.9 m (180 ft) in well A2 (Table 4.3) and 61.3 m (201 ft) and 42.06 m (138 ft) in well A3 (Table 4.4). Reservoir A has 58 %, 50% and 52% hydrocarbon saturation in wells A1, A2 and A3 respectively (Table 4.2, 4.3 and 4.4). In reservoir B, gross thickness and net thickness values were 48.2 m (158 ft) and 16.8 m (55 ft) in well A1 (Table 4.2), 75.9 m (249 ft) and 47 m (157 ft) in well A2 (Table 4.3) and 25 ft (7.6 m) and 15 ft (4.6 m) in well A3 (Table 4.4) respectively with hydrocarbon saturation of 36%, 53% and 78% in wells A1, A2 and A3 respectively (Table.4.2- 4.4).

Also, reservoir C has hydrocarbon saturation of 69%, 52% and 70% in wells A1, A2 and A3 with gross thickness and net thickness of 19.2 m (63 ft) and 6.7 m (22 ft) in well A1, 20.7 m (68 ft) and 12.8 m (42 ft) in well A2 and 11.6 m (38 ft) and 5.5 m (18 ft) in well A3 (Table 4.2- 4.4). In reservoir D, the estimated values of hydrocarbon saturation across three wells A1, A2 and A3 were 69%, 58% and 66% (Table 4.2, 4.3 and 4.4). The estimated gross thickness and net thickness of reservoir D were, 52.7 m (173 ft) and 43.3 m (142 ft) in well A1; 44.8 m (147 ft) and 25.0 m (82 ft) in well A2 and 48.5 m (159 ft) and 29.9 m (98 ft) in well A3 respectively (Table 4.2, 4.3 and 4.4). Well A3 is the most prolific among the three wells, with average value of 67% hydrocarbon saturation. Although, there was no definite trend in hydrocarbon saturation but it was observed that the hydrocarbon saturations were significantly higher seaward in the south as shown in well A3 along the correlated wells.

4.2 Reservoir Fluid Distribution and Fluid Contacts

Adeoye and Enikanoselu, (2009) reported that neutron-density logs, water saturation, shaliness, and resistivity logs are essential ingredients for evaluating reservoir fluids and their respective contacts in the Niger Delta reservoirs. Petrophysics play an important role

in the determination of the horizontal changes in the reservoir fluid content and this can be very helpful as it presumes the reservoir lateral extent in the absence of seismic data and hence prevents failure during hydrocarbon exploration (Adeoye and Enikanoselu, 2009). In this study, there are variations in fluid and their respective columns in each reservoir (Table 4.5).

Reservoir A of well A1, is 62.66 m (205.58 ft) wide (net thickness average) and it contains gaseous hydrocarbon and water having their contact, Gas–Water Contact (GWC) at 2035.91 m (6679.5 ft) (Fig.4.3 and Tablesb 4.2). Reservoir B of well A1, is saturated with oil down to 2299.56 m (7544.5 ft) (Fig. 4.4 and Table 4.2). In reservoirs C and D of well A1, the Oil-Water Contact (OWC) together with the Gas-Oil Contact (GOC) are found at 2520.39 m (8269 ft) and 2608.78 m (8559 ft) respectively as observed in Fig.4.5, Table 4.2 and 4.5. In well A2, reservoir A is saturated with oil and is 55.01 m (180.48 ft) wide (net thickness average) as shown in Fig.4.6 and Table 4.3. Reservoir B of well A2 is 47.93 m (157.25 ft) of net thickness average with 53% hydrocarbon saturation and oil down to 2368.30 m (7770 ft) (Fig.4.7 and Table 4.3).

Reservoirs C and D of well A2 are saturated with oil and gas respectively (Fig.4.8 and Table 4.3) and Gas Down To (GDT) at 2726.10 m (8943.89 ft) in reservoir D (Fig.4.8 and Table 4.3 and 4.5). In well A3, net thickness with average of 42.21 m (138.5 ft) was recorded for reservoir A with GWC at 2038.81 m (6689 ft) (Fig.4.9 and Table 4.4 and 4.5). Reservoir B, in well A3 has just 4.57 m (15 ft) average net thickness with 78% hydrocarbon (oil) saturation (Fig.4.10 and Table 4.4 and 4.5). Reservoir C has 5.49 m (18 ft) net thickness (average) and 71% hydrocarbon saturation, with Oil-Down To (ODT) at 2529.99 m (8300.5 ft) (Fig.4.11 Table 4.4 and 4.5). Reservoir D of well A3 is saturated with water and Gas with GWC at 2603.14 m (8540.5 ft) (Fig.4.11 and Table 4.4 and 4.5). Gas reservoirs' occurrence were inferred from the significant cross-over of the Neutron-Density combination logs as supported by Asquith and Krygowski, (2004) (Fig.4.3, 4.5, 4.8, 4.9 and 4.11).

Table 4.5: The Reservoir Fluid Distribution and Contacts in The Study Field.

WELL	RESERVOIR	FLUID TYPE	FLUID CONTACT
A1	Reservoir A	GAS/WATER	GWC @ 2035.91 m
A1	Reservoir B	OIL	ODT
A1	Reservoir C	OIL / WATER	OWC @ 2520.39 m
A1	Reservoir D	GAS / OIL	GOC @ 2608.78 m
A2	Reservoir A	OIL	ODT
A2	Reservoir B	OIL	ODT
A2	Reservoir C	OIL	ODT
A2	Reservoir D	GAS	GDT
A3	Reservoir A	GAS / WATER	GWC @ 2038.81 m
A3	Reservoir B	OIL	ODT
A3	Reservoir C	OIL	ODT
A3	Reservoir D	GAS / WATER	GWC @ 2603.14 m

Where;

GWC = Gas-water contact

OWC = Oil-water contact

GOC = Gas-oil contact

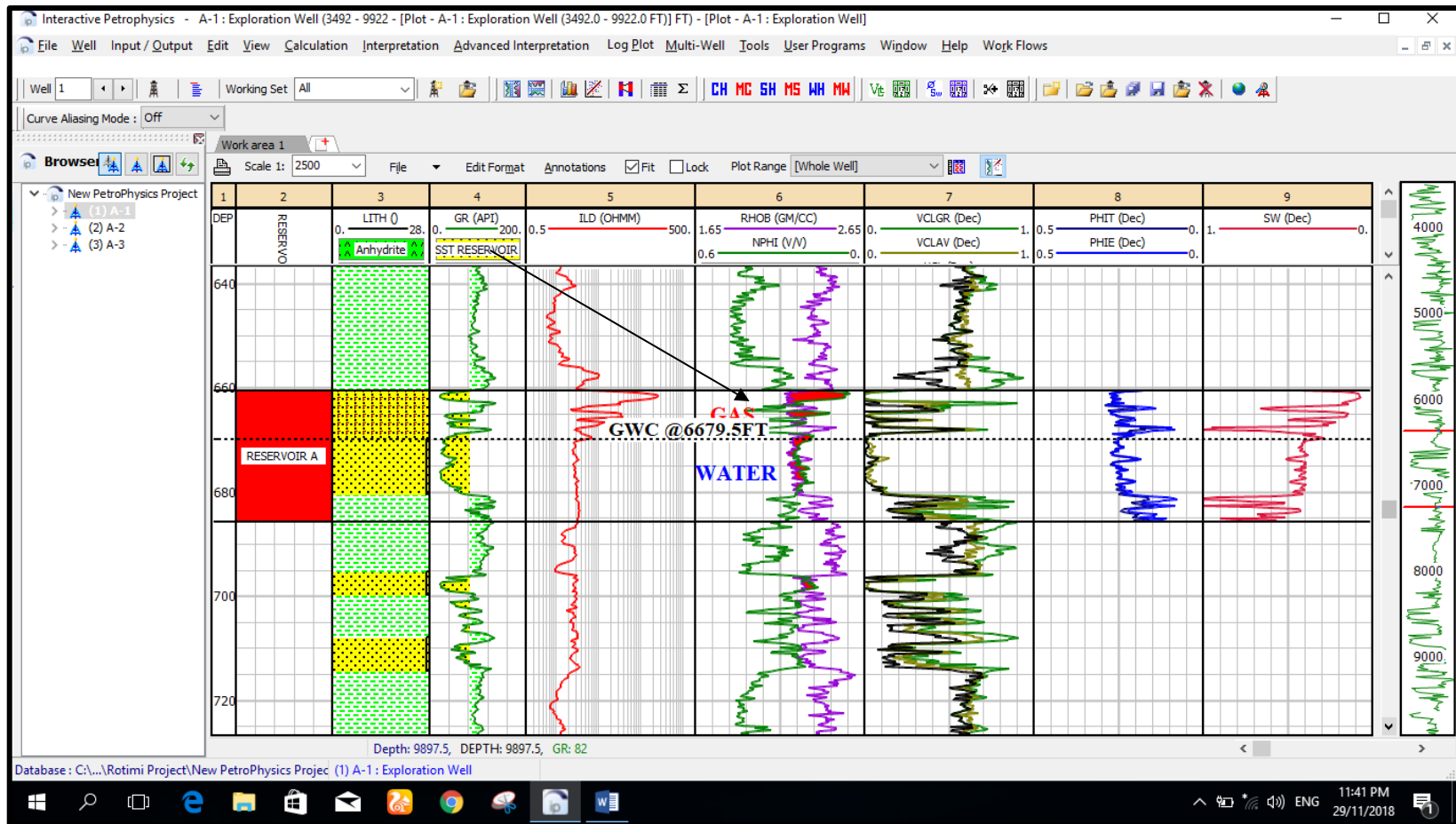


Figure 4.3: The Distribution of Fluids (Water and Gas) in Reservoir A of Well A1 in The Tetemu Field, Indicating The Location of The Gas-Water Contact (GWC) at A Depth of 6679.5ft.

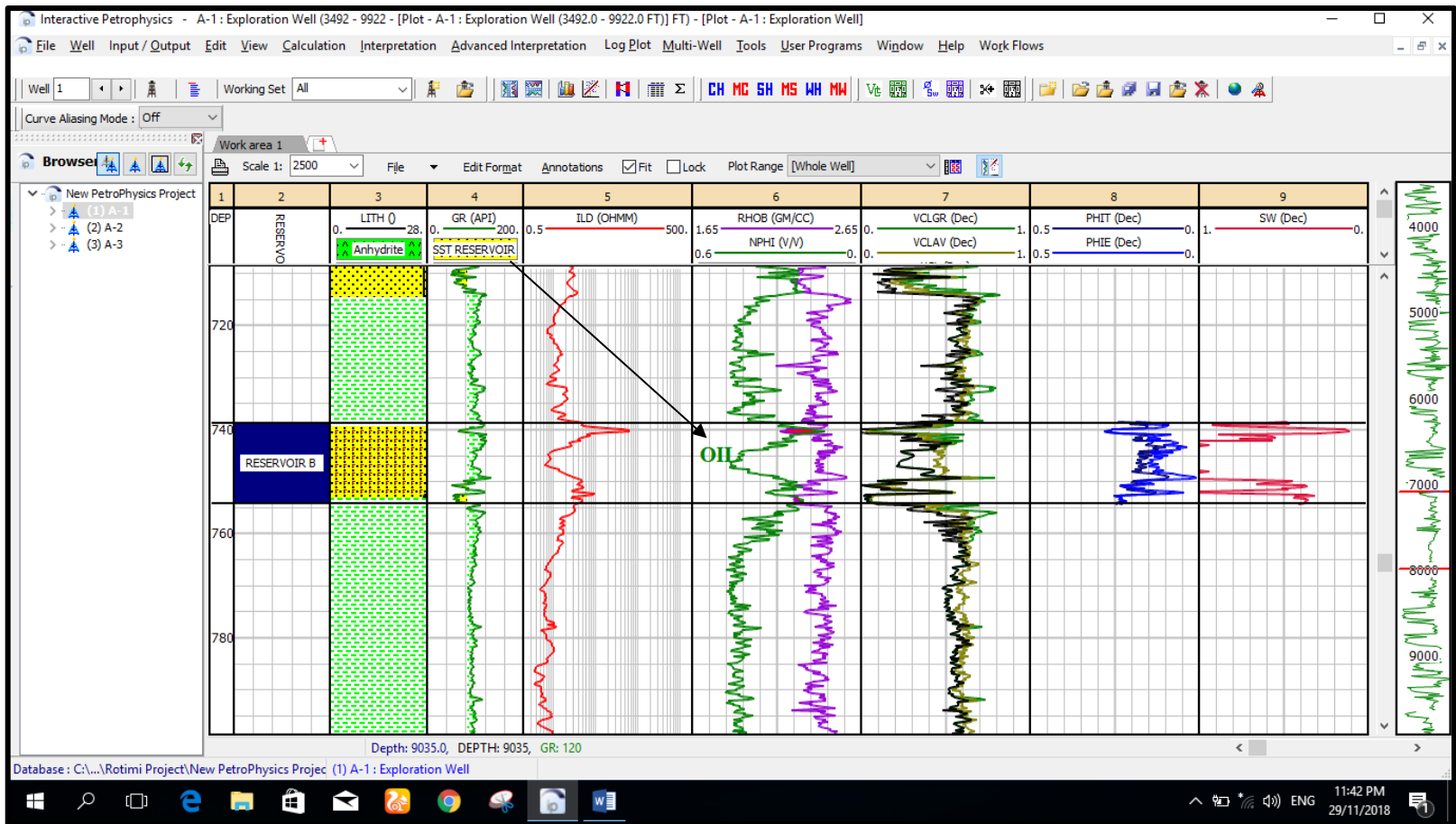


Figure 4.4: The Fluid Distribution (Only Oil) in The Reservoir B of Well A1 of The Study Area.

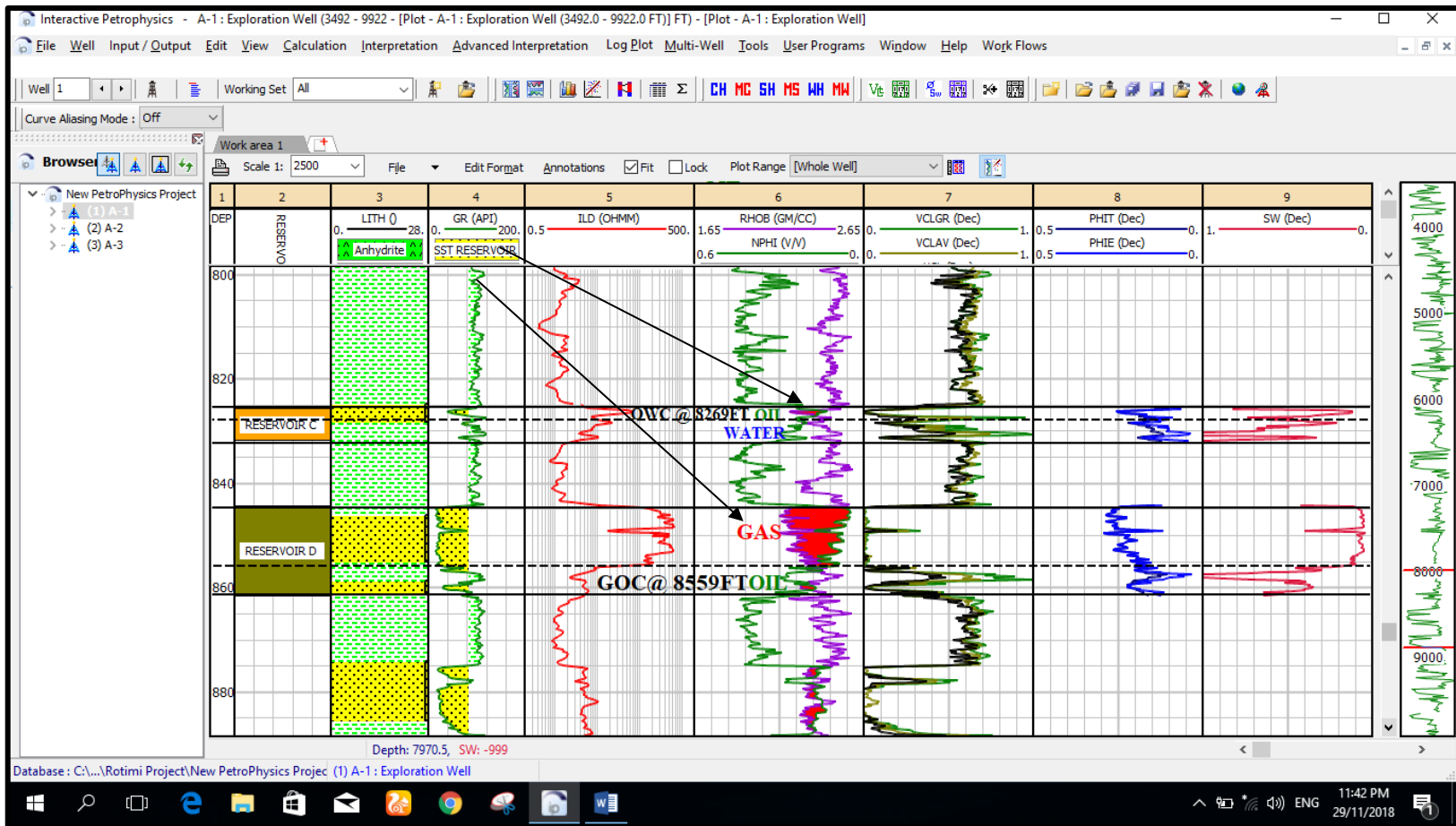


Figure 4.5: Gas, Oil and Water Distribution in Reservoir C and D, With OWC at 2520.39 m (8269ft) in Reservoir C and GOC at 2608.78 m (8559ft) in Reservoirs D, Well A1 of The Study Field.

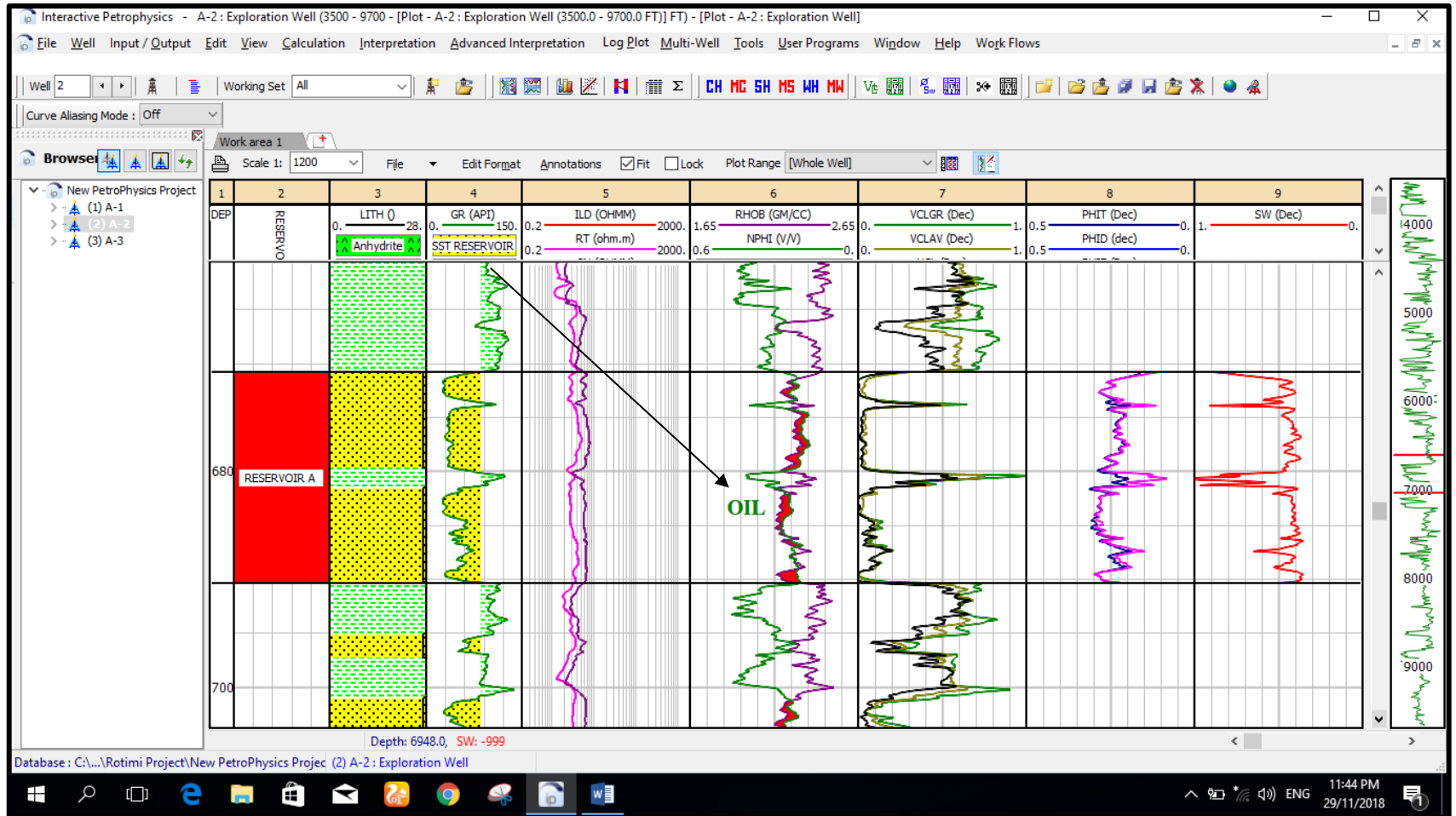


Figure 4.6: Oil Distribution in Reservoir A of Well A2 of Tetemu Field.

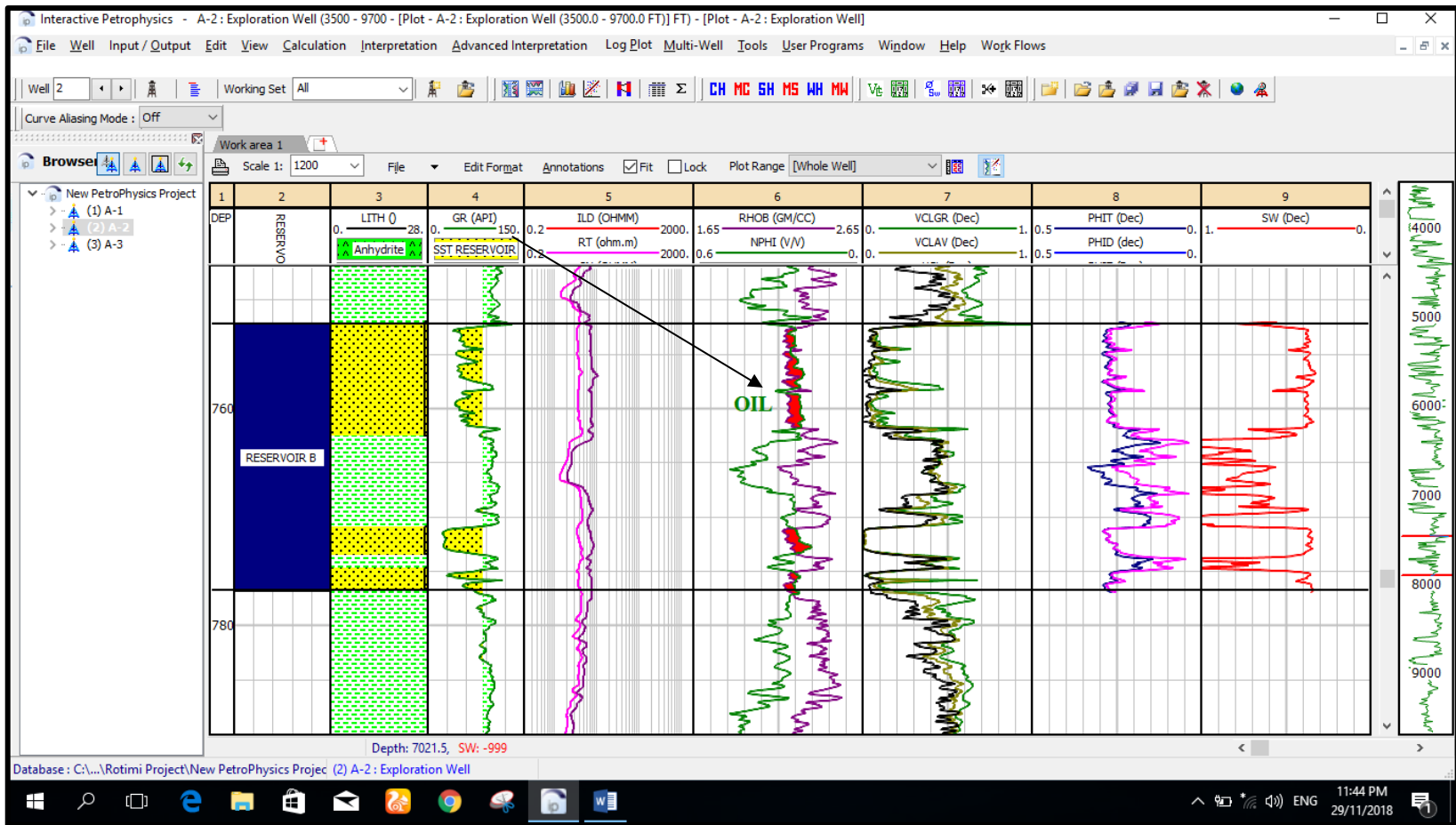


Figure 4.7: Oil Distribution in Reservoir B of Well A2 of The Study Field

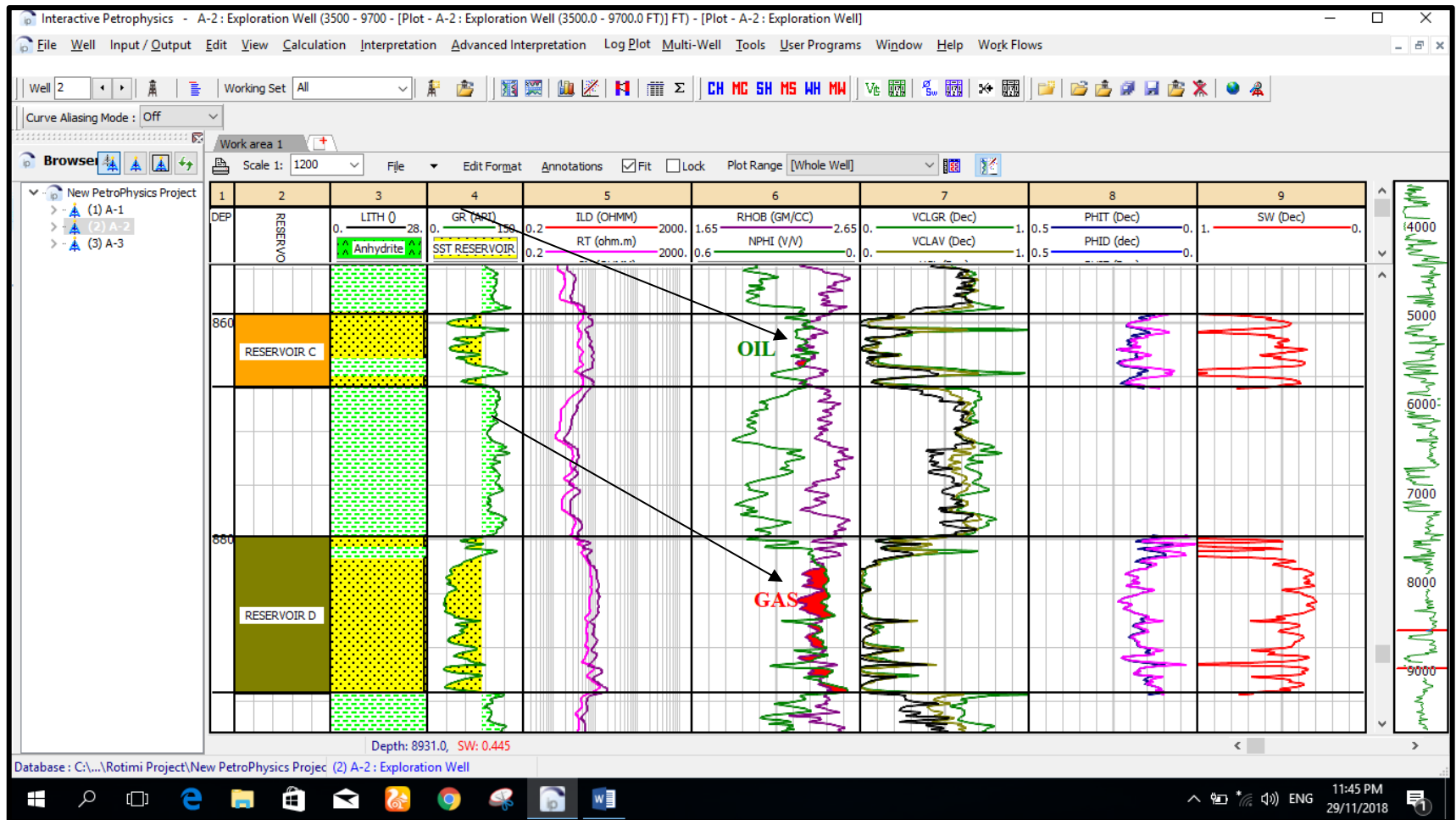


Figure 4.8: The Hydrocarbon Distributions in Reservoirs C and D of Well A2 of Tetemu Field.

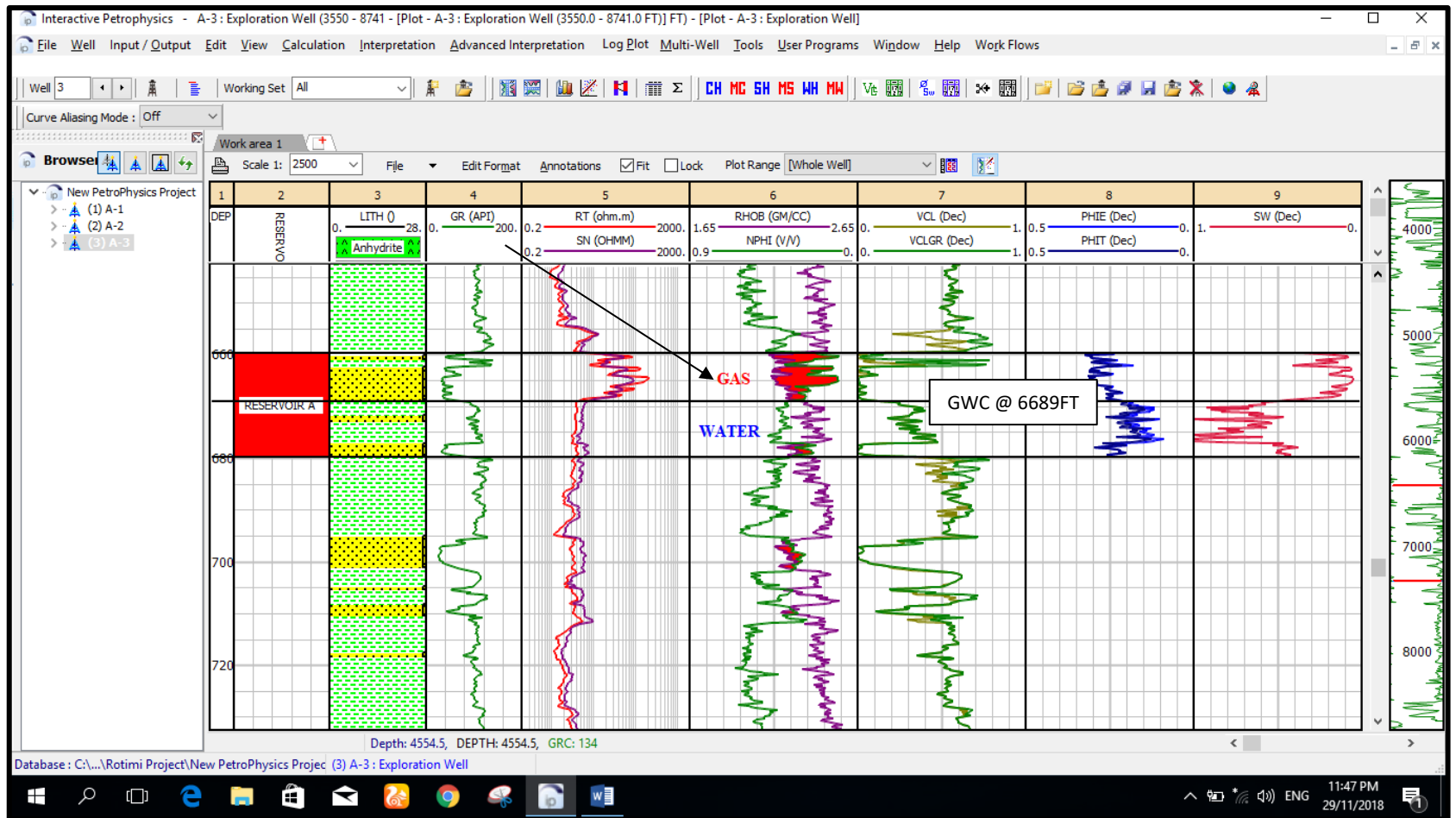


Figure 4.9: The Fluid (Gas and Water) Distributions in The Reservoir A of Well A3, With Gas-Water Contact (GWC) at 2038.81 m (6689ft).

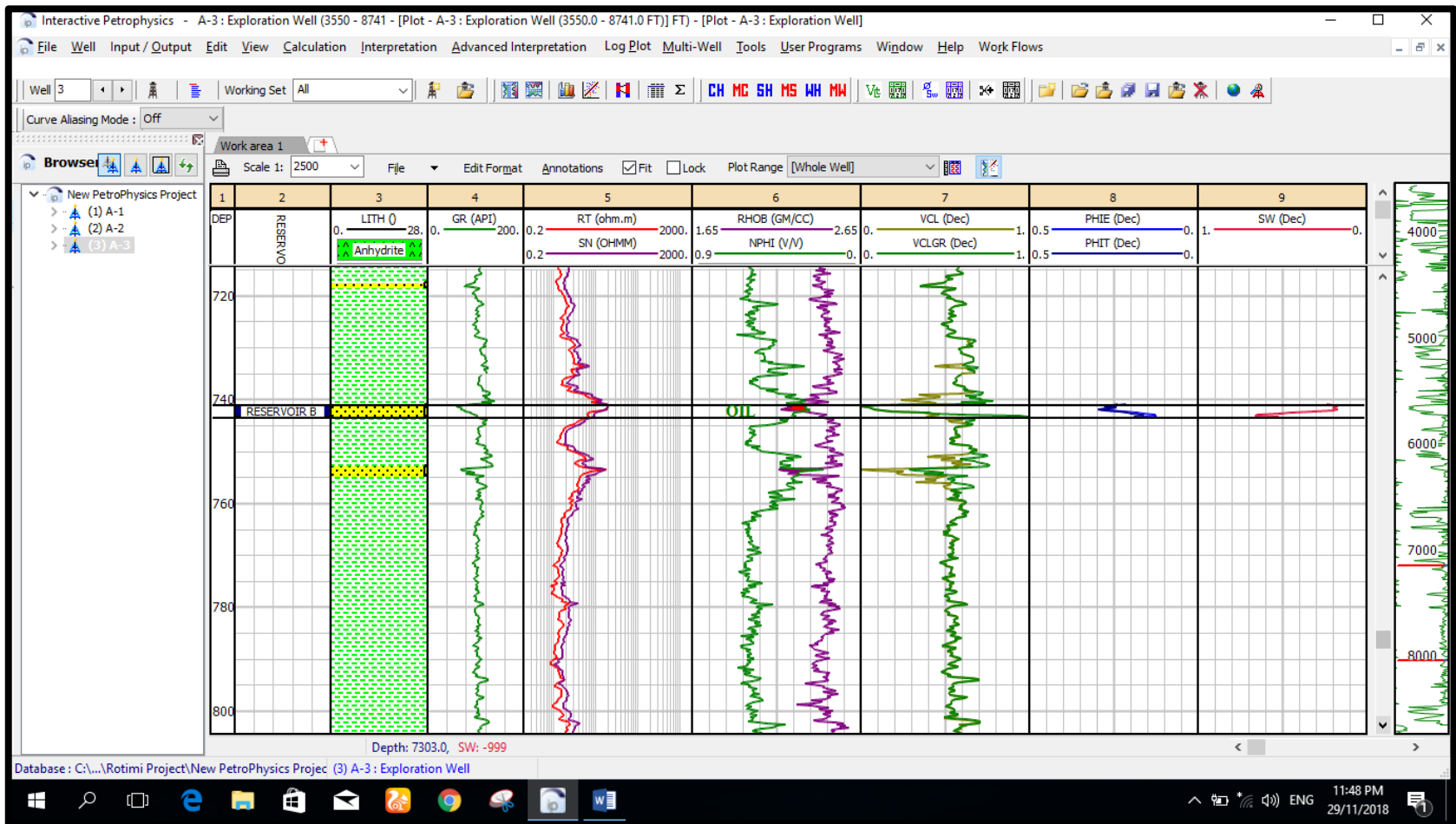


Figure 4.10: The Oil Distribution in The Reservoir B, Well A3 of The Study Area.

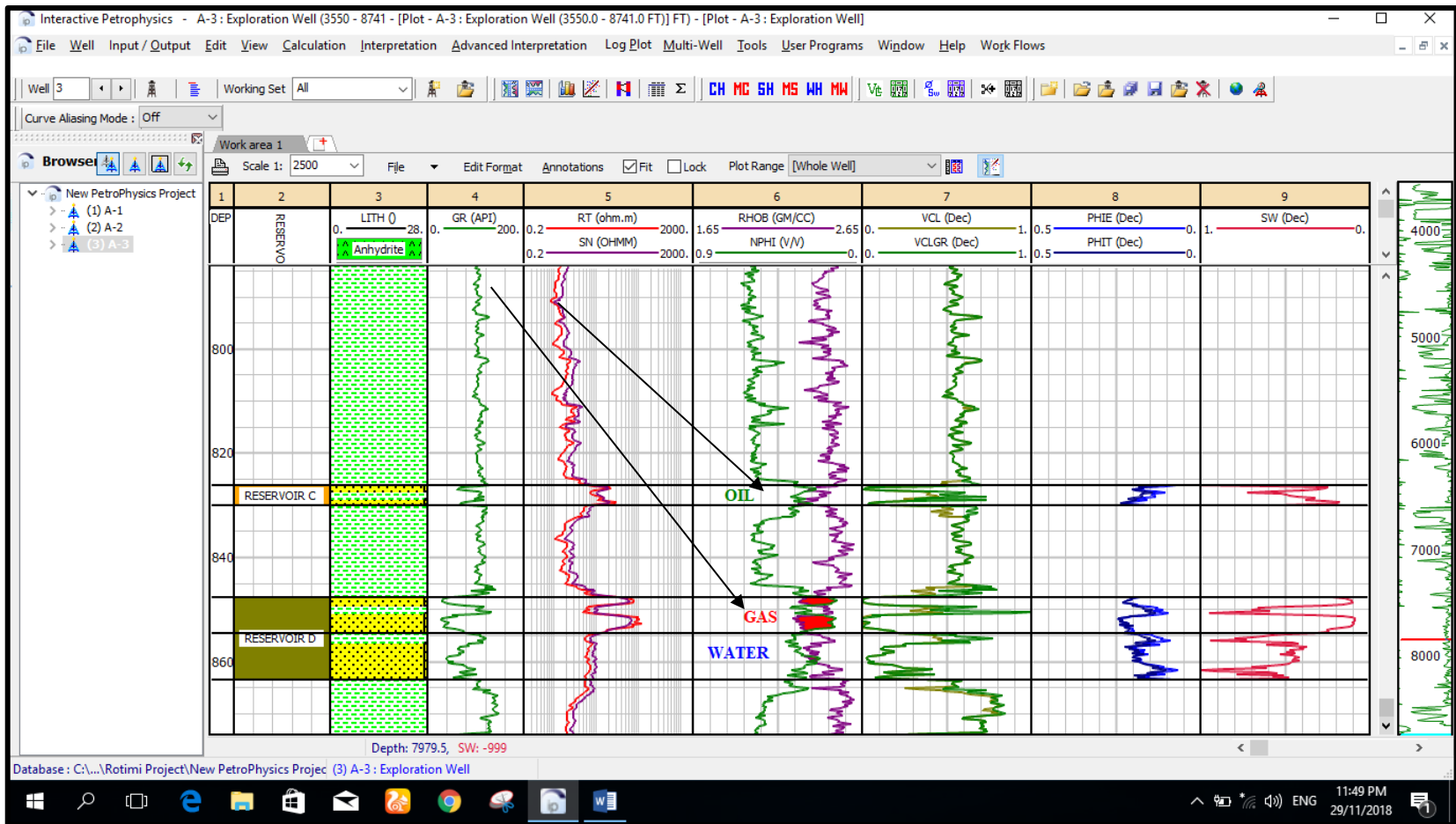


Figure 4.11: The Fluid (Oil) Distribution in The Reservoirs C and Gas-Water Interphase in Reservoir D, Well A3 of The Study Area, With Gas-Water Contact (GWC) at 2603.14 m (8540.5 Ft).

4.3 Reservoir Depositional Environments and Facies

According to Nton and Olumuyiwa, (2012) changes in grain size and sorting is due to gradual changes in shaliness which depends on the environment of deposition and facies. The characteristics of facies and depositional environments determine the overall properties of the sandstone reservoirs (Reijers, 2011; Nton and Olumuyiwa, 2012; Nton and Salami, 2016). The GR log patterns are classified into four types namely; funnel-shaped, Irregular trends, bell-shaped and cylindrical-shaped successions. Interpreted depositional environments include: progradational, fluvial channel sands, deltaic sand deposits and marine shale.

Reservoir A

The cylindrical or blocky log shapes patterns were observed in reservoir A of the three wells (Fig.4.12). Reservoir A was bounded at the lower and upper boundaries across the wells by marine shale (Fig.4.12). The cylindrical GR log shapes thickness ranges from 17.68 m (58 ft) to 30.33 m (99.5 ft) (Fig. 4.12) in this reservoir in the wells. The thickness is about 30.33 m (99.5 ft) in well A2, 17.68 m (58 ft) in well A3 and 22.25 m (73 ft) in well A1 (Fig.4.12). The upper portion of the reservoir A is serrated in wells A1 and A3 (Fig.4.12) due to Gas-Water- Contact (GWC) (Fig.4.12). This log motif with cylindrical-shaped GR logs could be interpreted as inner fan channel and a slope channel environment (Nton and Salami, 2016). Reservoir A was deposited in a slope channel environment as a result of the irregular trends immediately above them and its thicknesses. The shape trends with wider range of thickness could be interpreted as turbidite sands (Emery and Myers, 1996).

Reservoir B

In well A1, the gamma ray log trend showed a funnel shape (Fig.4.13) at the upper part of reservoir B while the lower portion were characterised by blocky and irregular log trend which were serrated (Fig.4.13). The reservoir B showed funnel shape gamma ray log trends at the upper portion in well A2 and well A3 (Fig.4.13). These log trends appeared as serrated (Fig.4.13). This trend indicates sequence with cleaning upward pattern and its characteristic increase within the sand. The coarsening successions can be categorized into three types; crevasse splays or prograding delta, barrier bars (regressive) and prograding marine shelf fans (Selley, 1998). Both crevasse splay and

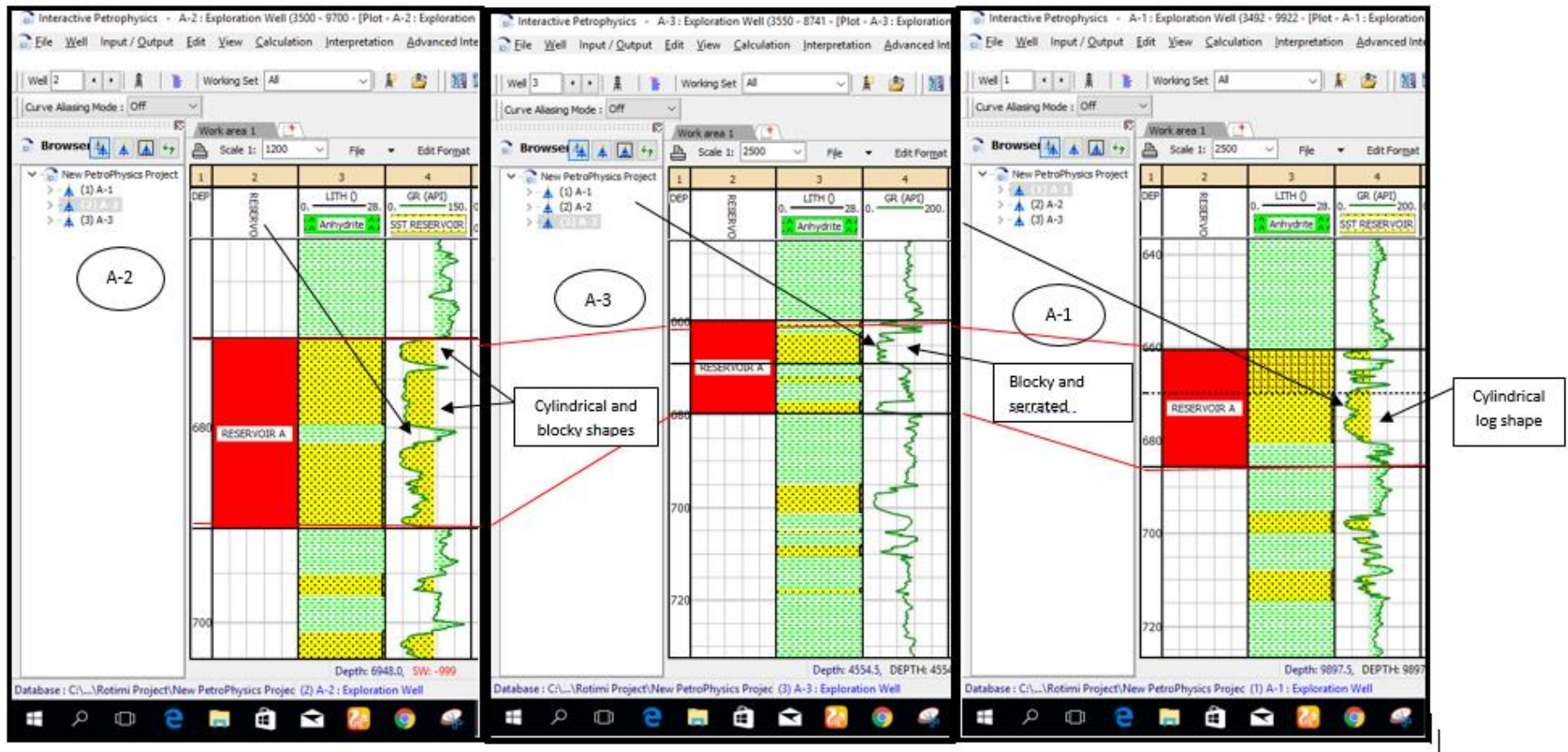


Figure. 4.12: The Identification of Depositional Environment of Reservoir A Using GR Log Signatures.

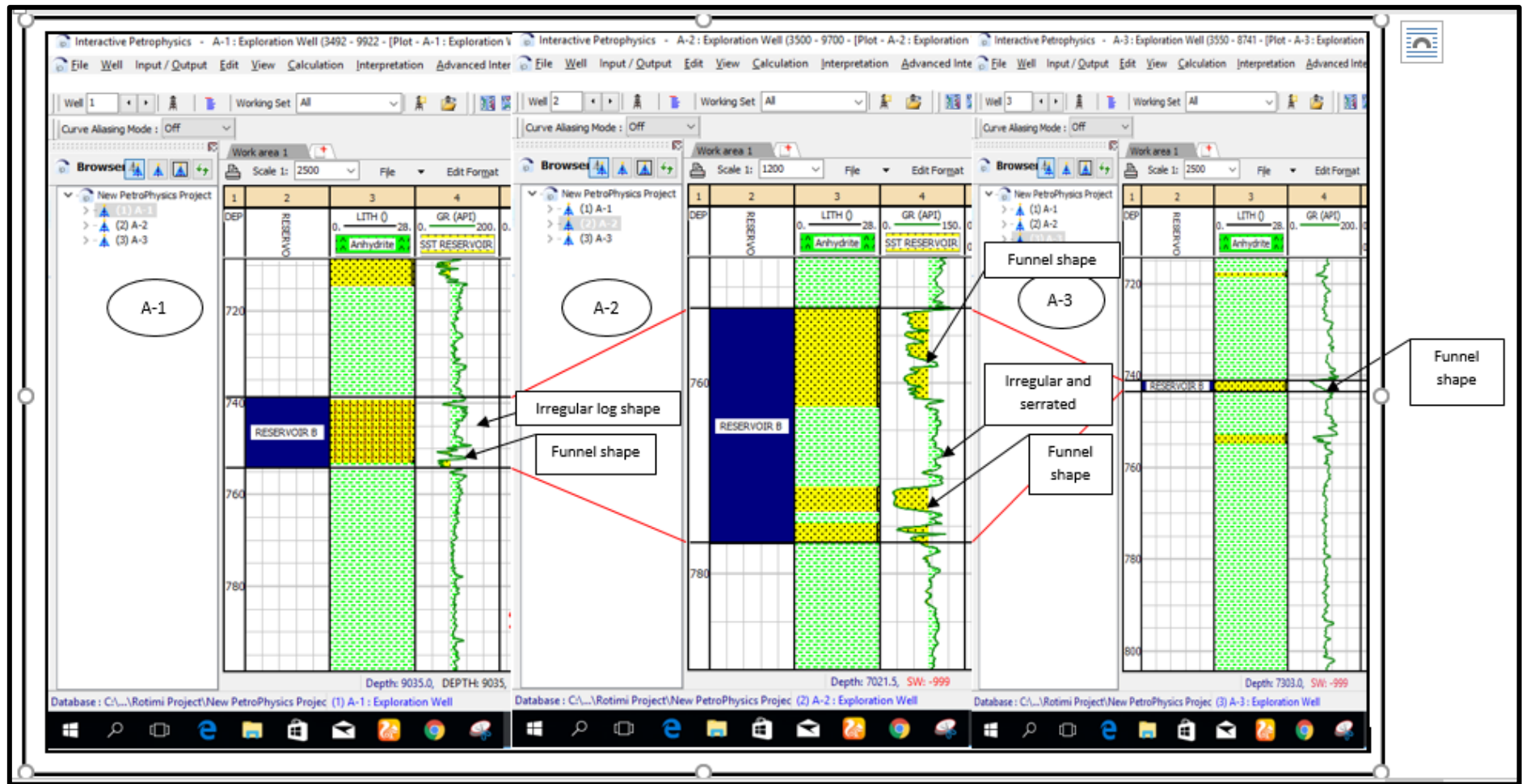


Figure 4.13: Identification of Depositional Environment of Reservoir B across The Three Wells Using GR Log Shapes.

and prograding delta can be differentiated on the basis of depositional scale. The size of the prograding delta is significantly larger in comparison. The funnel-shaped patterns observed in well A2 could be a prograding marine shelf or prograding delta but crevasse splays is inferred in well A1 and A3 on the account of their thicknesses (Rider, 1999).

Reservoir C

The funnel shape gamma ray log trends occurred in the reservoir C of the three wells (Fig.4.14). The lower part of the reservoir C in well A1 is serrated at 2520.39 m (8269 ft) which coincided with Oil-Water-Contact (OWC) (Fig.4.5 or Table 4.5). In well A2, the funnel shape signatures are the dominant trends within the reservoir. This is also similar to the observed log signature within the well A3 (Fig.4.14). This pattern indicates cleaning-up trend deposition, which shows sand content increase, as observed in marine environment. Due to their scale, the funnel-shaped successions in the reservoir C may represent a prograding marine shelf or a prograding delta (Rider, 1999).

Reservoir D

In well A1(Fig.4.14), the upper part of reservoir D is characterized by cylindrical log shape patterns of about 45 ft (13.72 m) and 65 ft (19.81 m), which terminated at Gas-Oil-Contact (GOC) at 2608.78 m (8559 ft) (Table 4.5). The lowest part of the reservoir shows a prograding sand deposit of funnel shape log signature (Fig.4.14). Using (Shell, 1982) log motif classification scheme, the cylindrical GR log shape could be an inner fan channel and a slope channel environment. Reservoir D in well A1 is a channel deposit. Reservoir D in the well A2, shows characteristic bell shape log signatures and they are interpreted as a transgressive sand, deltaic or fluvial channel, deep tidal channel or tidal channel (Shell, 1982). In well A3, the reservoir D with bell-shaped successions is a transgressive sand and fluvial or deltaic channel (Fig.4.14).

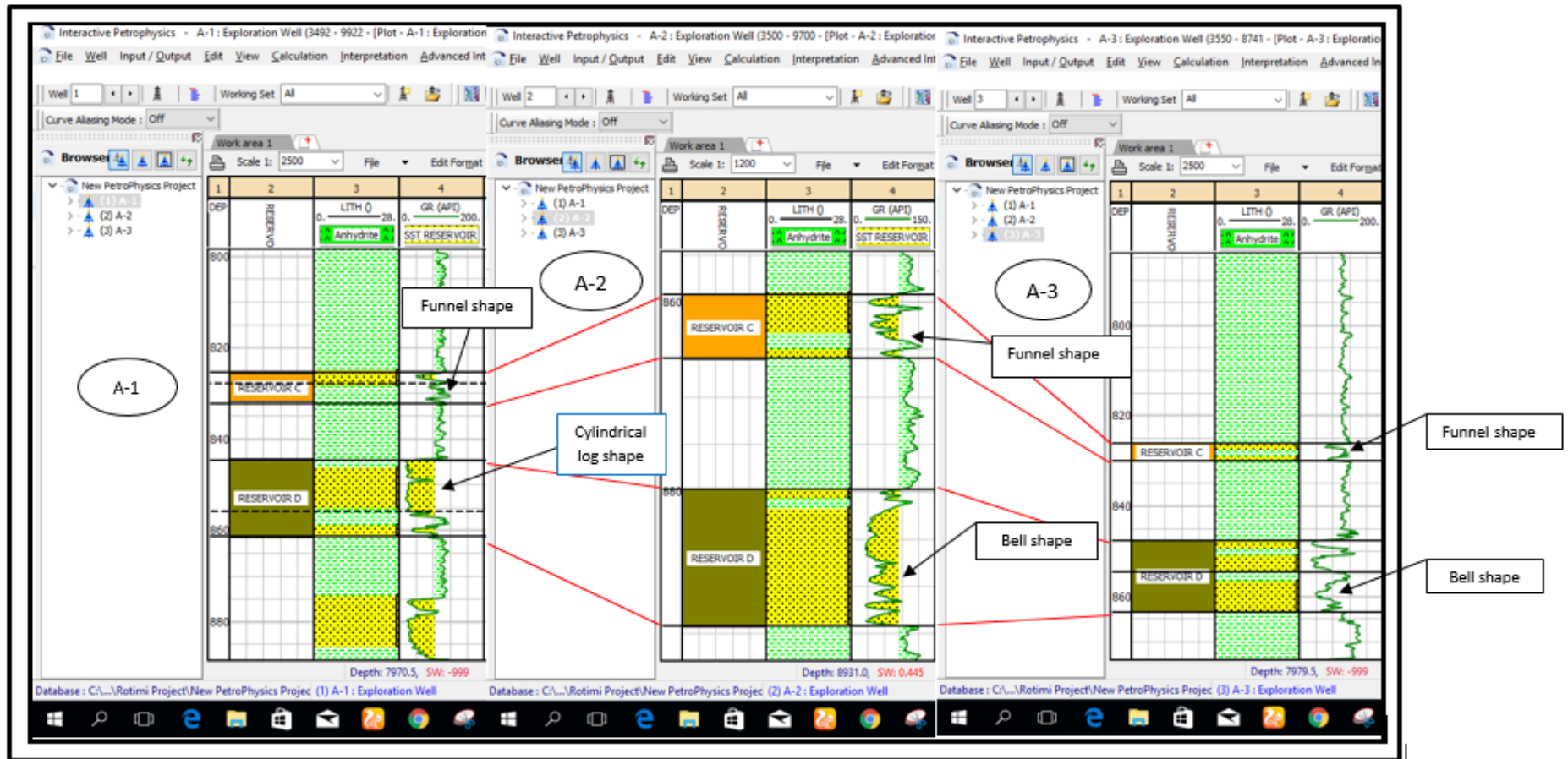


Figure 4.14: The Identification of Depositional Environments of Reservoirs C and D across The Three Wells Using GR Log Shapes

4.4 The Derivation of Reservoirs Shear Wave Information in The Study Area

The findings indicated that the synthetic P-wave log, obtained through Gassmann fluid replacement modeling, exhibits a strong correlation with the P-wave log observed in the field, as illustrated in Figure 4.15. This process was repeated for other reservoir at each well location and very good correlations were also achieved as depicted from Figures 4.16-4.17. The field P-wave crossplots from the given well logs and synthetic P-wave generated from reservoirs' initial parameters on Fluid Replacement Modeling (FRM) platform, resulted into very good correlations in all the reservoirs.

The good correlations obtained, means that the synthetic P-wave generated on FRM correlated with the field P-wave obtained from the field. Also, by plotting the computed shear wave log against the P-wave log for each reservoir, a localized empirical relation was generated which can be used to modify Castagna equation at each reservoir interval (Fig.4.18 - 4.20) Empirical trends were superimposed using the Least-square Linear Fit method and the equation of each line was derived. The V_p together with the constant in the formula formed the modified Castagna equation in the localized model (Figures 4.18, 4.19 and 4.20).

Castagna *et al.*, (1985) introduced an empirical formula to estimate shear wave velocity (V_s) from compressional wave velocity (V_p) in multimineral rocks saturated with brine. This formula is based on polynomial relationships between V_p and V_s in pure monomineralic lithologies, as further elaborated by Castagna *et al.*, (1993).

The equation was earlier expressed as:

$$V_p = 1.36 + 1.16 * V_s$$

Where; V_p is Velocity of compressional wave and V_s represents Velocity of shear wave.

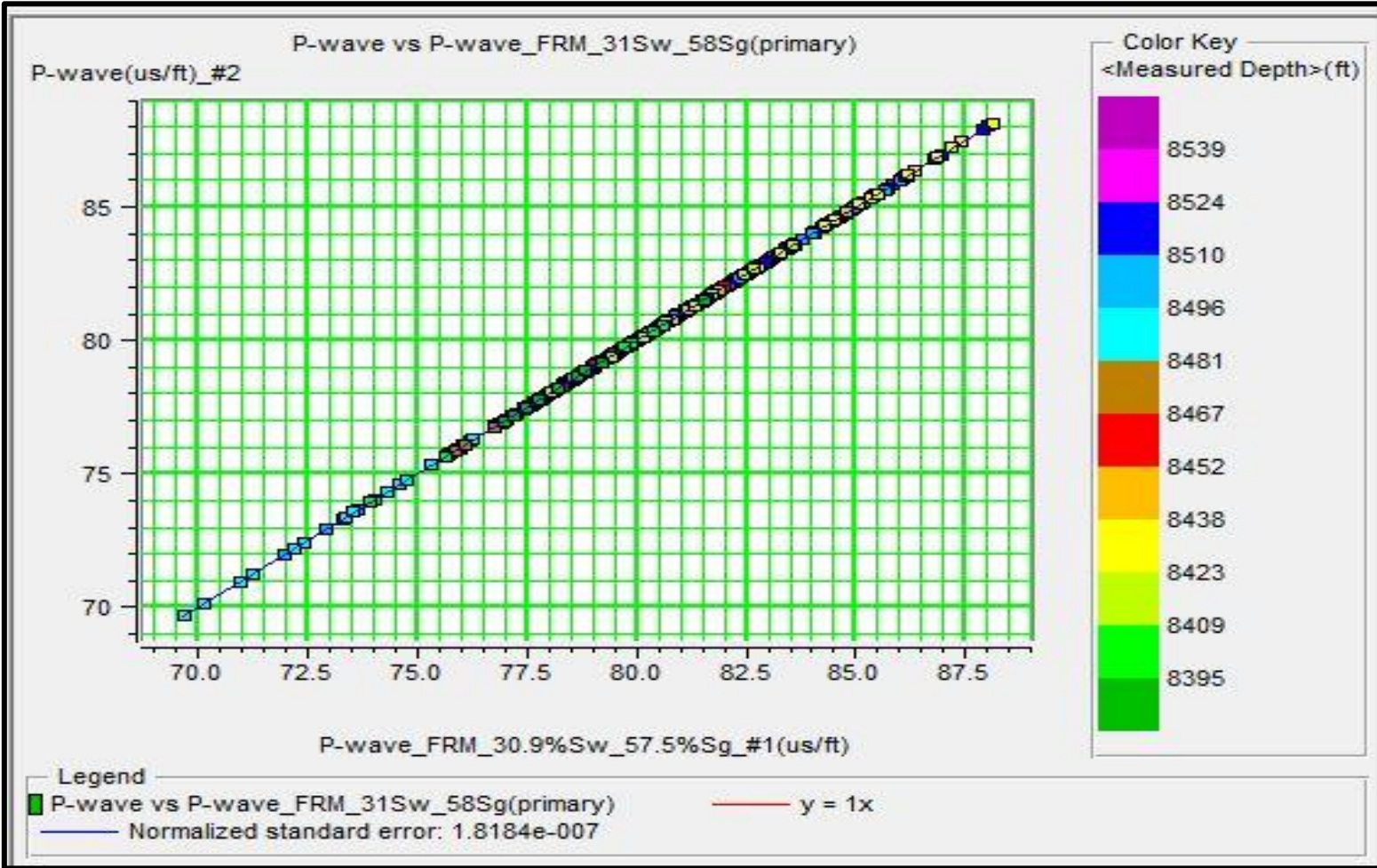


Figure 4.15: The Crossplot between Field P-Wave Log and Computed P-Wave Log for Reservoir D at Well A-1. There Is A Perfect Correlation between Both Logs With An Error of $1.8184e^{-007}$.

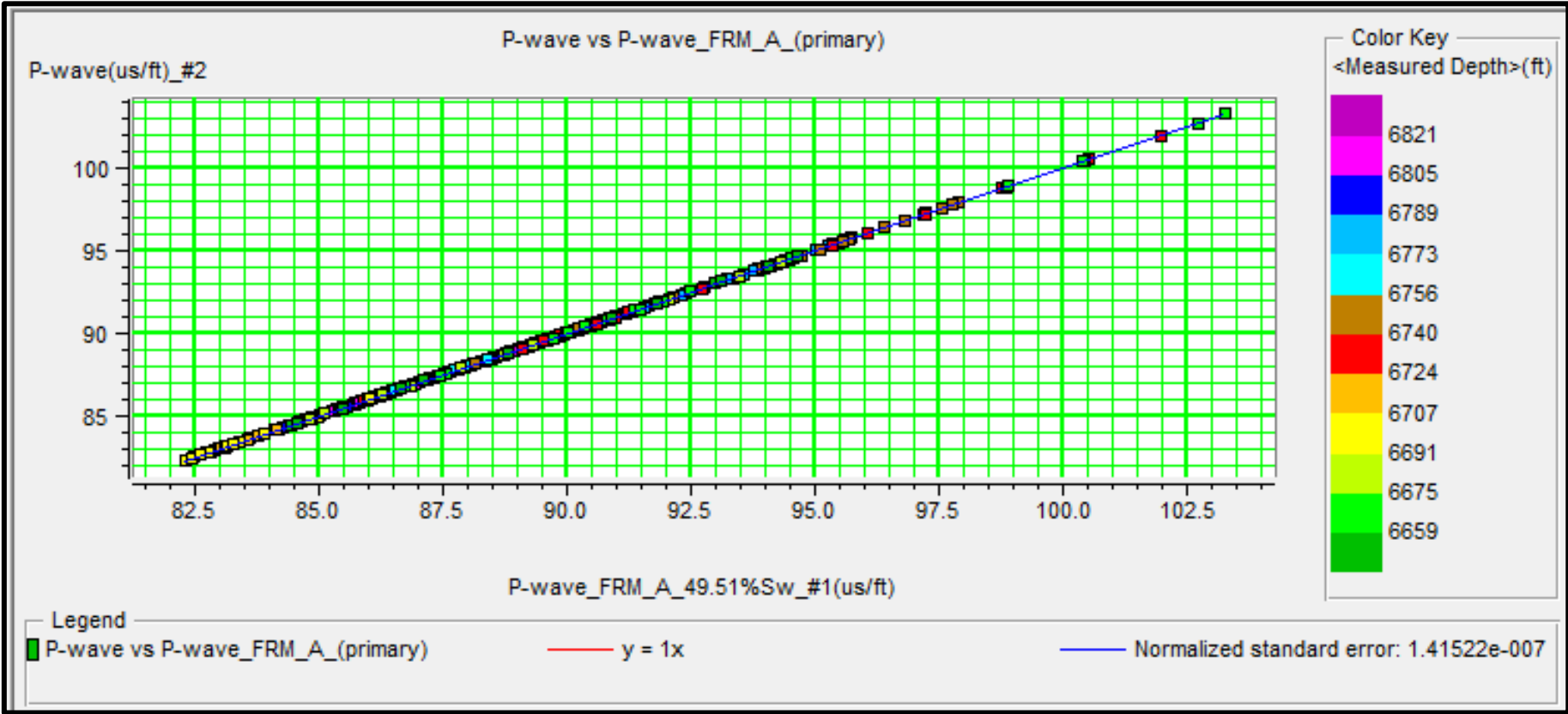


Figure 4.16: The Crossplot between Field P-Wave Log and Computed P-Wave Log for Reservoir A at Well A-2. There Is A Very Good Correlation between Both Logs With An Error of $1.41522e^{-007}$.

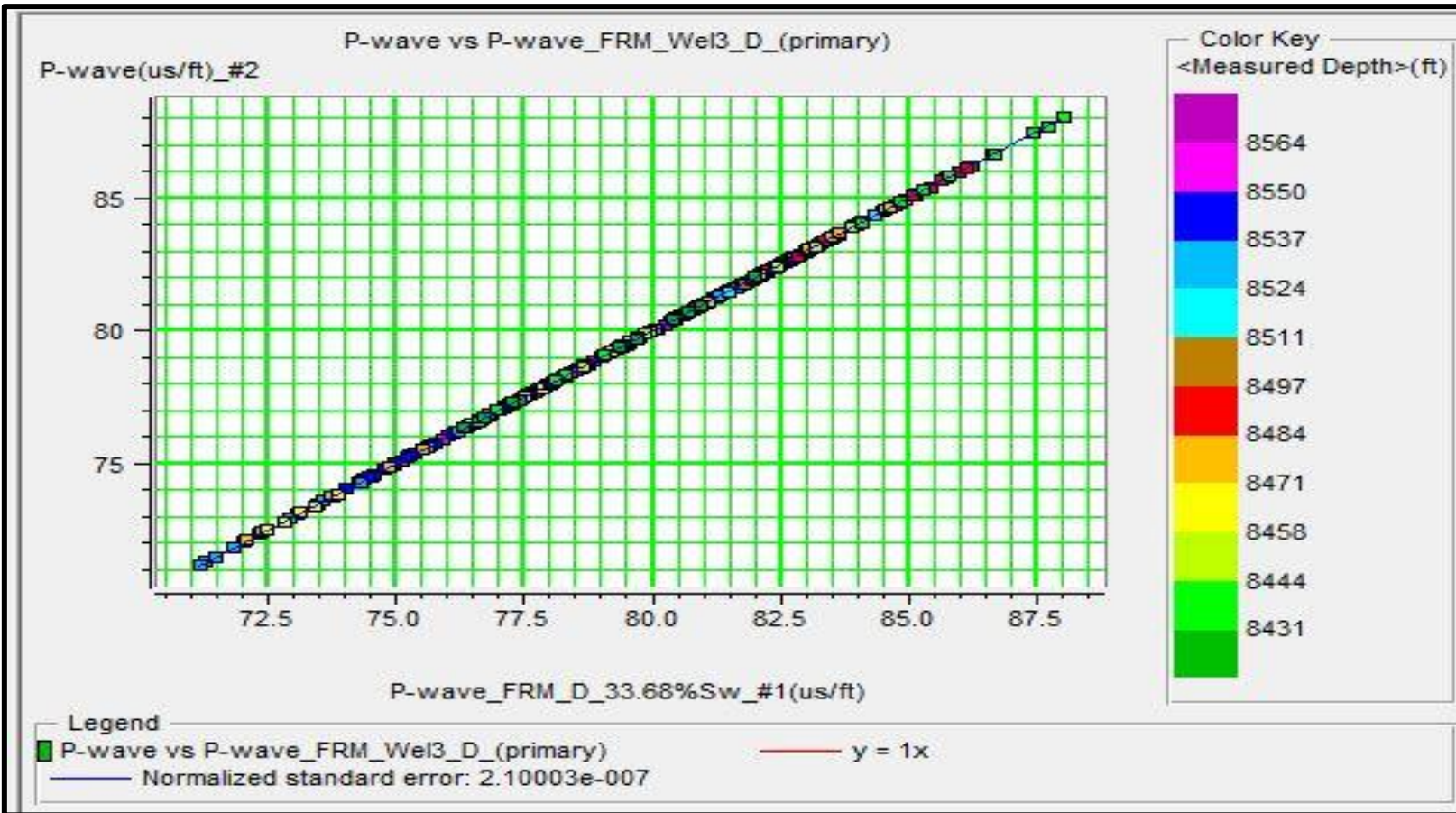


Figure 4.17: The Crossplot between Field P-Wave Log and Computed P-Wave Log for Reservoir D at Well A-3. There Is A Very Good Correlation between Both Logs With A Minimal Error of $2.10003e^{-007}$.

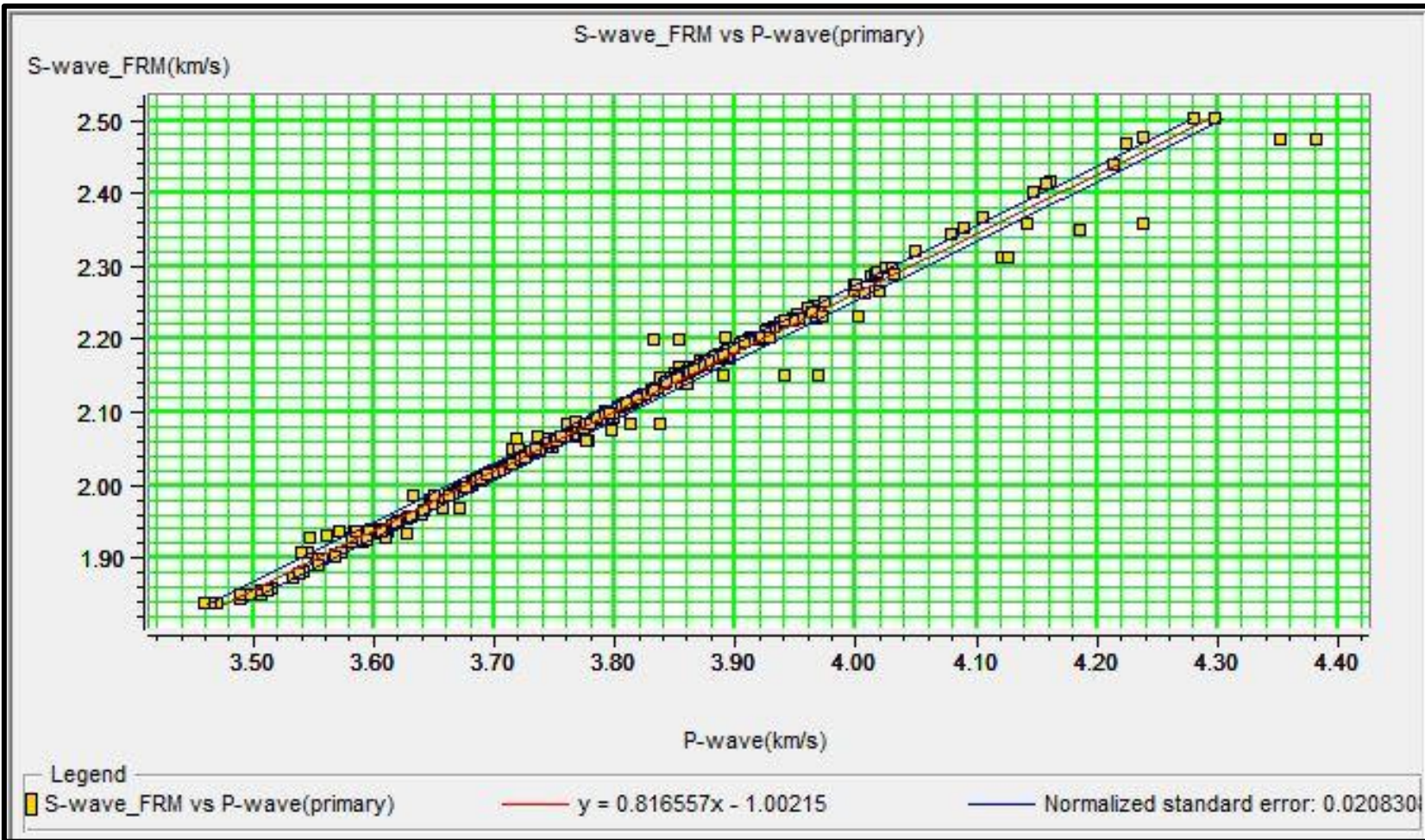


Figure 4.18: The Crossplot of P-Wave vs. Computed S-Wave Log for Reservoir D at Well A-1, With An Empirical Trend Superimposed. Note That X and Y in The Empirical Equation Are V_p and V_s Respectively.

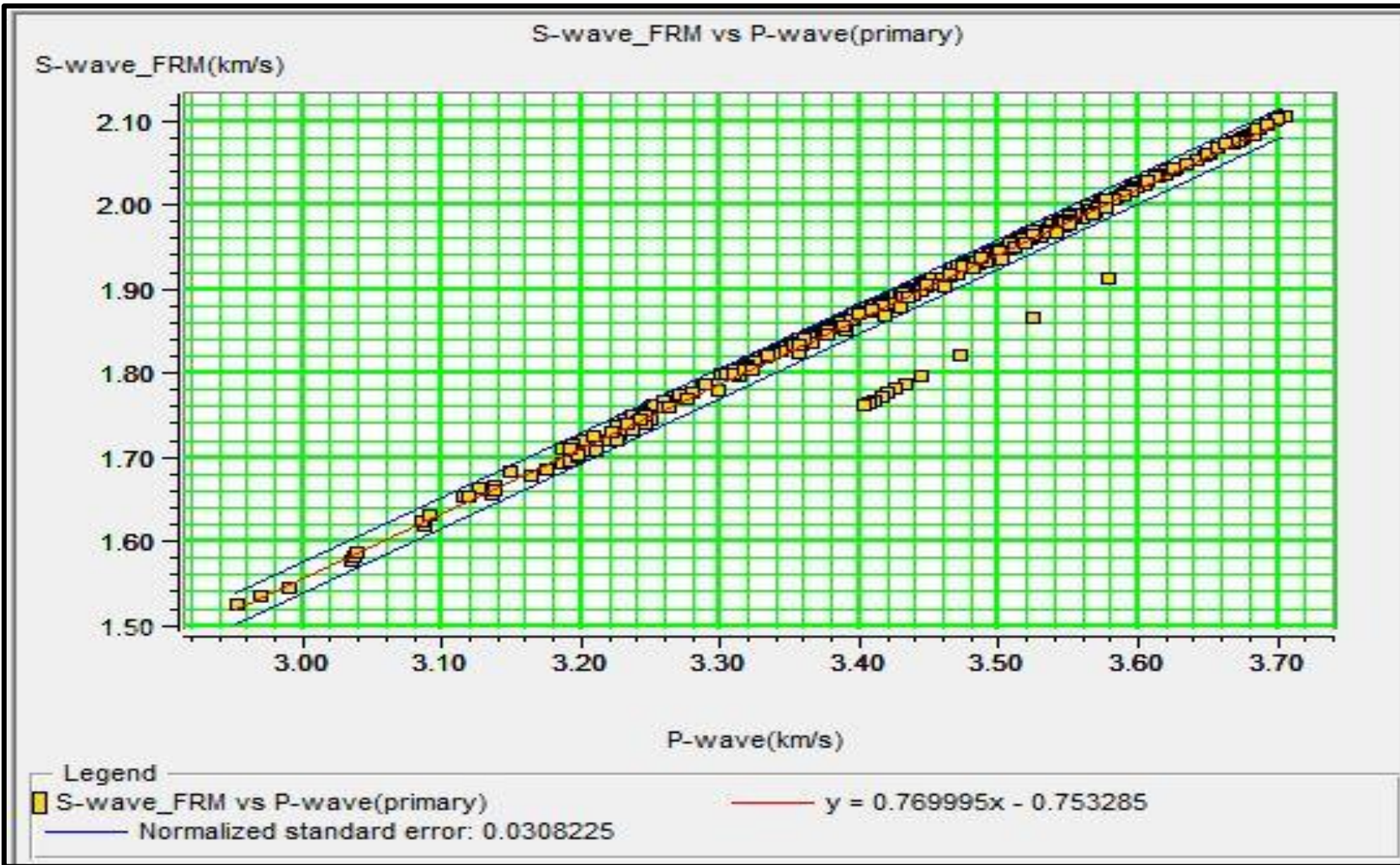


Figure 4.19: The Crossplot of P-Wave vs. Computed S-Wave Log for Reservoir A at Well A-2, With An Empirical Trend Superimposed. Note That X and Y in The Empirical Equation Are Vp and Vs Respectively

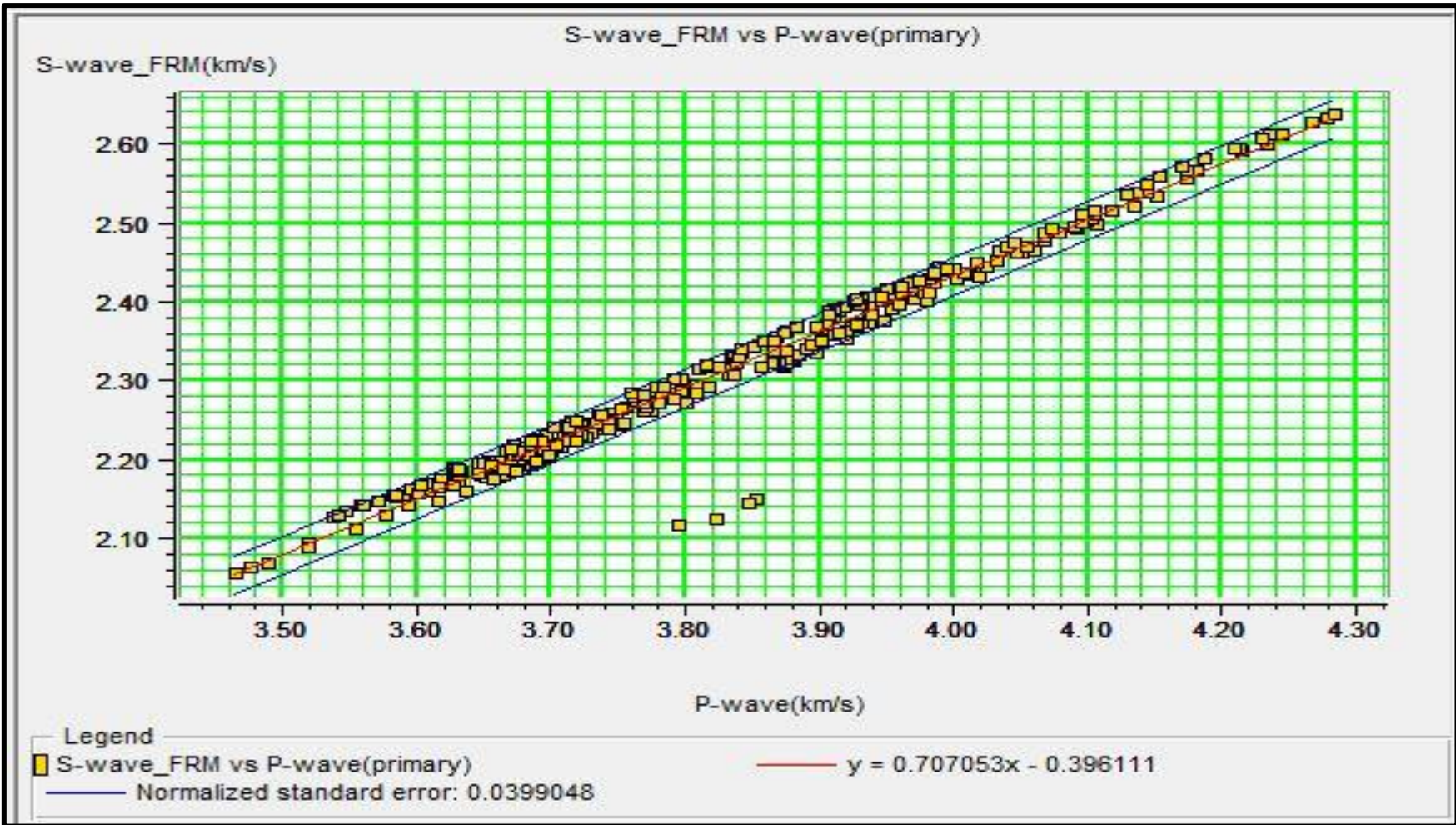


Figure 4.20: The Crossplot of P-Wave vs. Computed S-Wave Log for Reservoir D at Well A-3, With An Empirical Trend Superimposed. Note That X and Y in The Empirical Equation Are V_p and V_s Respectively.

4.5 Fluid Substitution Modeling

The results of the crossplot (Fig.4.21- 4.27) revealed the possible elastic, geomechanical, stress and pore pressure behaviour of each reservoir in a static state (at initial parameters) before production, and in a dynamic state, during production, in response to increasing water saturation. The elastic and mechanical responses of each reservoir to stress state during fluid substitution as water volume increases during production are shown in section 4.7.1 below. The selected reservoirs (A and D of well A1, A, B and D of well A2 and A and D of well A3) were picked for modeling on the account of their thicknesses (Tables 4.2- 4.4).

4.5.1 Static, Dynamic, Elastic and Mechanical Responses of The Reservoirs to Stress State

For reservoir A of well A1(Fig.4.21A-D), the plate A (Fig.4.21 A), is the reservoir A at initial (static) properties, such as 43% of water saturation and density of 2.3 g/cm^3 (Table 4.6) at initial condition before production. As the production of hydrocarbon commences, the water saturation increases from its original value of 43% towards 100% due to fluid substitution as water gradually replaces hydrocarbon (Fig.4.21 A-D and Table 4.6). It was observed that as water volume increases towards 100% due to hydrocarbon production, the data points move gradually along increasing acoustic impedance (Fig.4.21- plates B, C and D).

In addition, the major clusters in A, B and C (Fig.4.21) lie nearly perpendicular to the pressure plane. However, the cluster in D lies parallel to the pressure plane in the direction of decreasing pore-pressure. This implies that at the initial production stage, when the water saturation is only slightly increasing, the pressure regime of the reservoir will most likely be unaffected. However, as the water saturation tends towards 100% at later production stage, the pore pressure will fall, which might trigger corresponding increase of effective pressure and matrix stress.

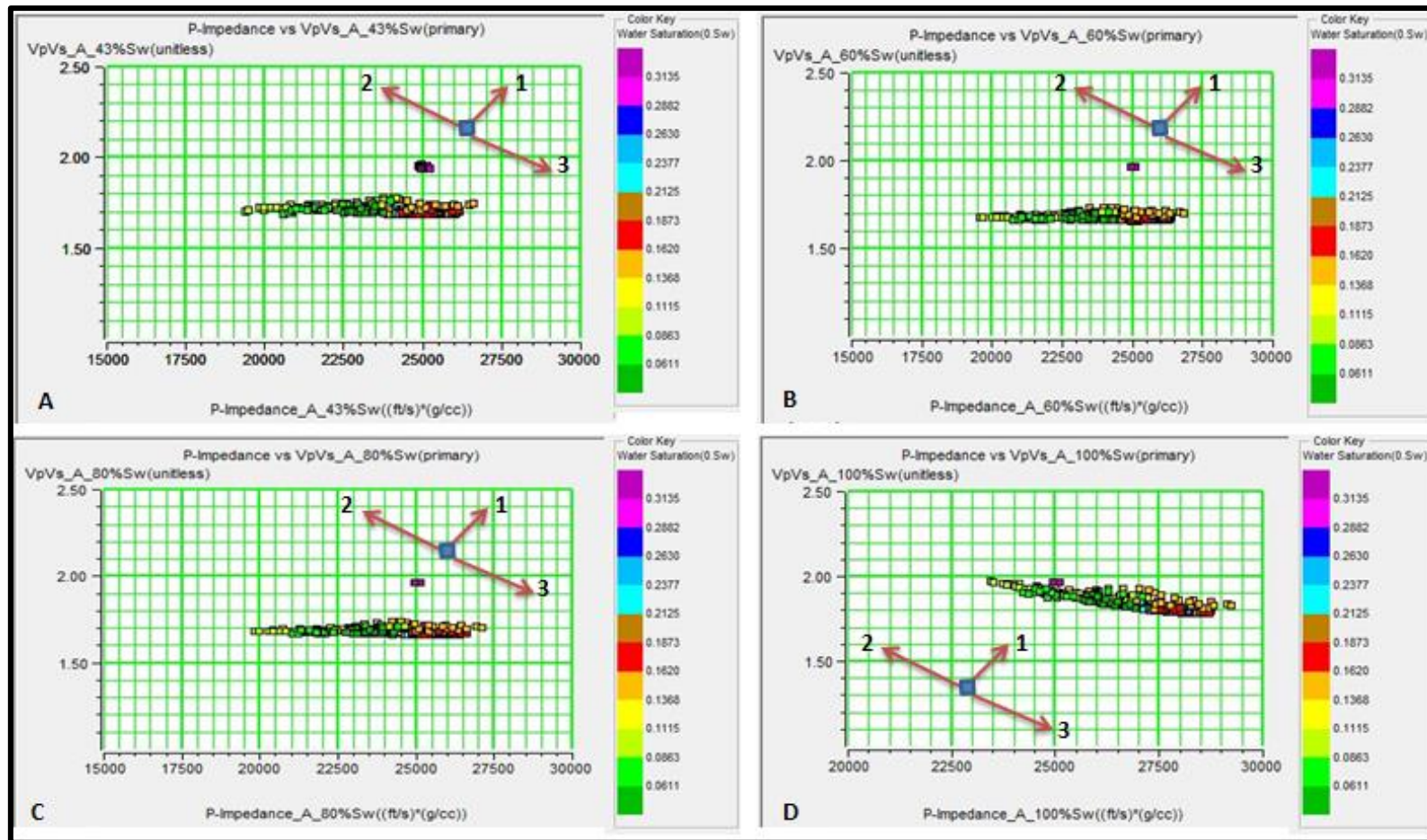


Figure 4.21: The Vp/Vs against P-Impedance Cross-Plots on Dynamic Rock-Physics Template (RPT) for Reservoir A in Well A-1 for Different Values of Water Saturation: A) Field Data at 43% Water Saturation; B, C, D Are Synthetic Data at 60%, 80% And 100% Water Saturation Respectively. The Arrows Indicate Different Geologic Trends (Conceptually): 1-Increasing Water Saturation; 2-Increasing Pore Pressure; 3-Decreasing Pore Pressure (Adapted from Avseth and Ødegaard, 2004).

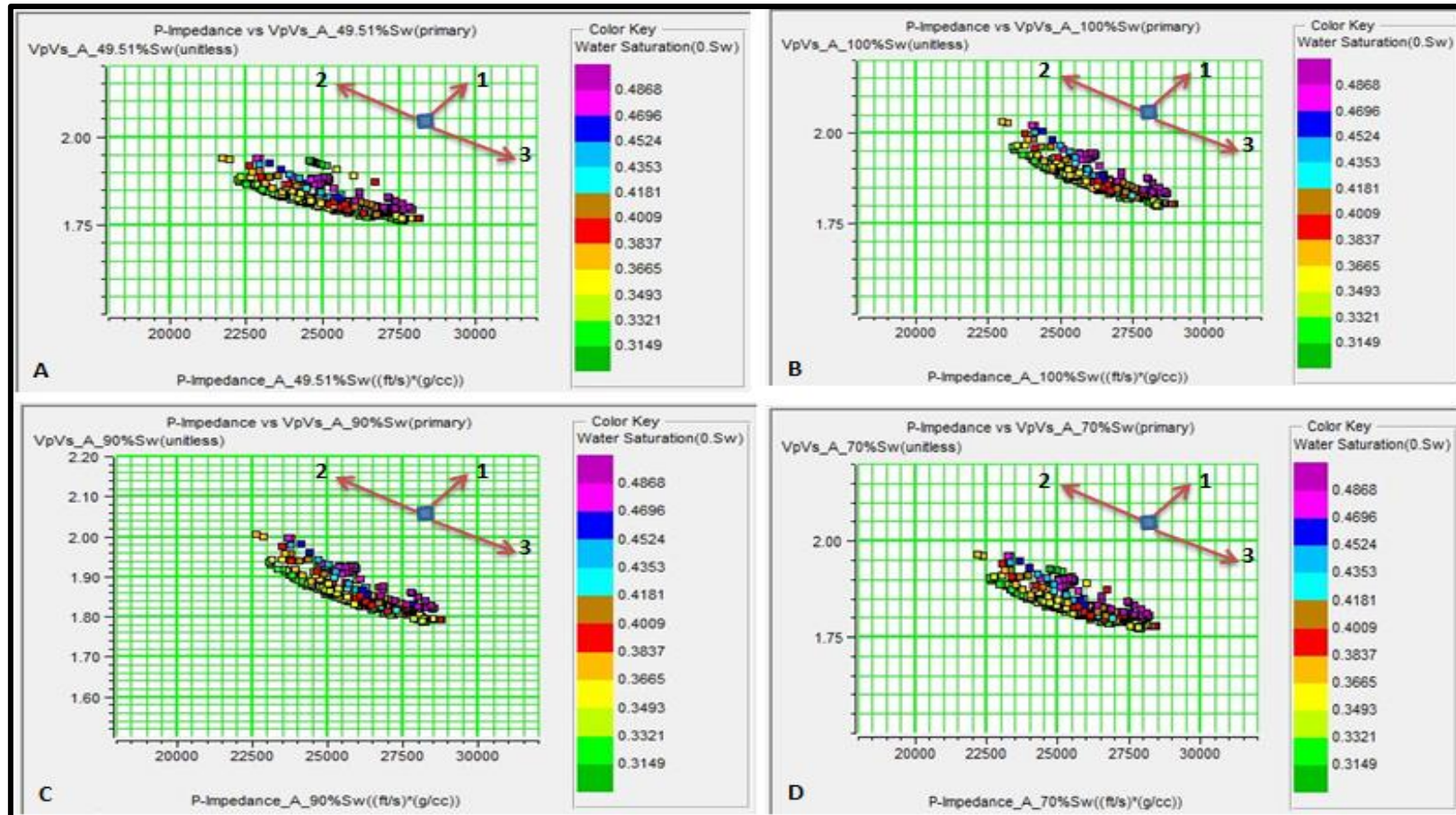


Figure 4.22: The Vp/Vs against P-Impedance Cross-Plots on Dynamic RPT for Reservoir D in Well A-1 for Different Values of Water Saturation: A) Field Data at 49.51% Water Saturation; B, C, D Are Synthetic Data at 70%, 90% and 100% Water Saturation Respectively. The Arrows Indicate Different Geologic Trends (Conceptually): 1-Increasing Water Saturation; 2-Increasing Pore Pressure; 3-Decreasing Pore Pressure (Adapted from Avseth and Ødegaard, 2004).

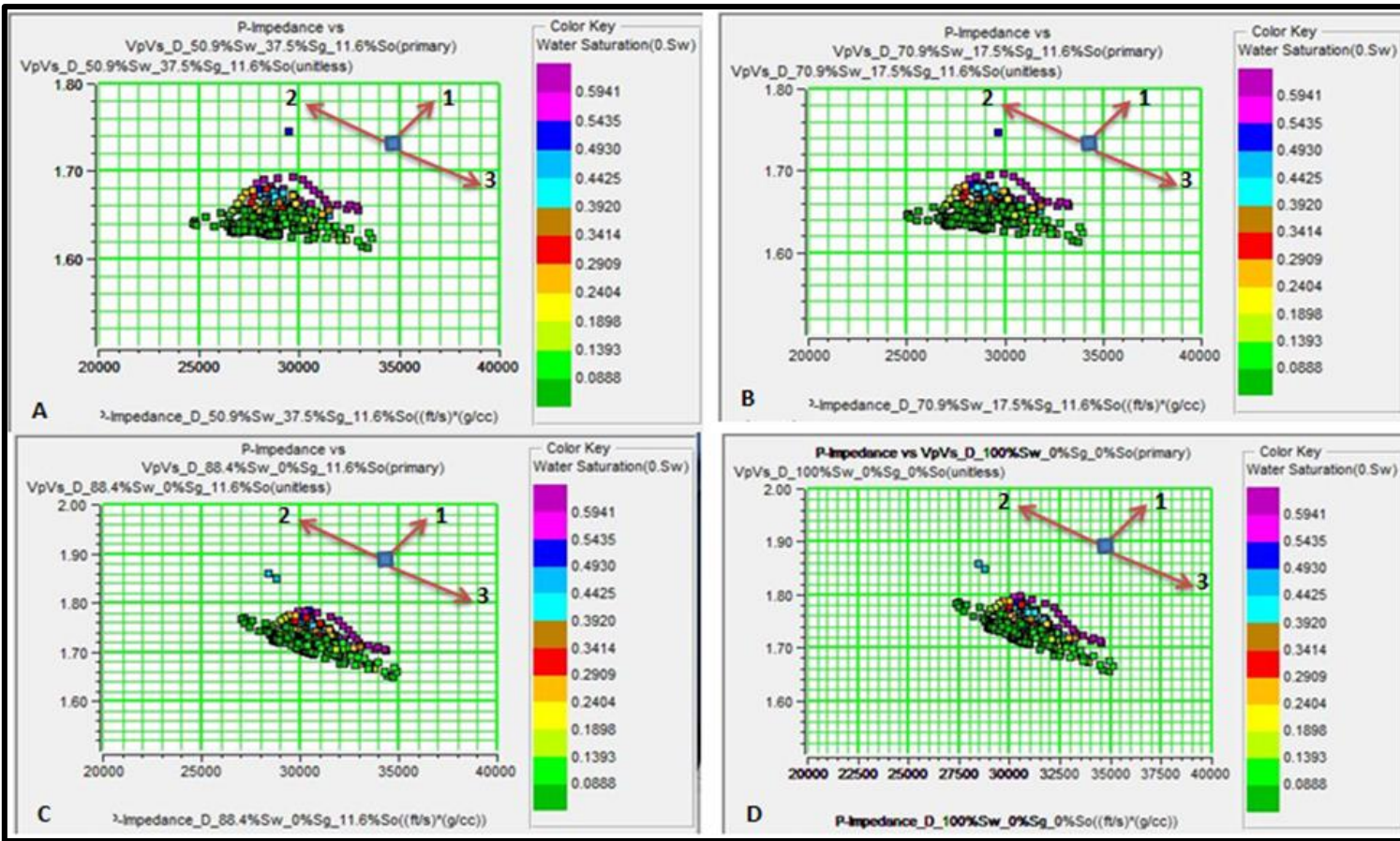


Figure 4.23: The Vp/Vs against P-Impedance Cross-Plots on Dynamic RPT for Reservoir A in Well A-2 for Different Values of Water Saturation: A) Field Data at 50.9% Water Saturation; B, C, D Are Synthetic Data at 70.9%, 88.4% And 100% Water Saturation Respectively. The Arrows Indicate Different Geologic Trends (Conceptually): 1-Increasing Water Saturation; 2-Increasing Pore Pressure; 3-Decreasing Pore Pressure (Adapted from Avseth and Ødegaard, 2004).

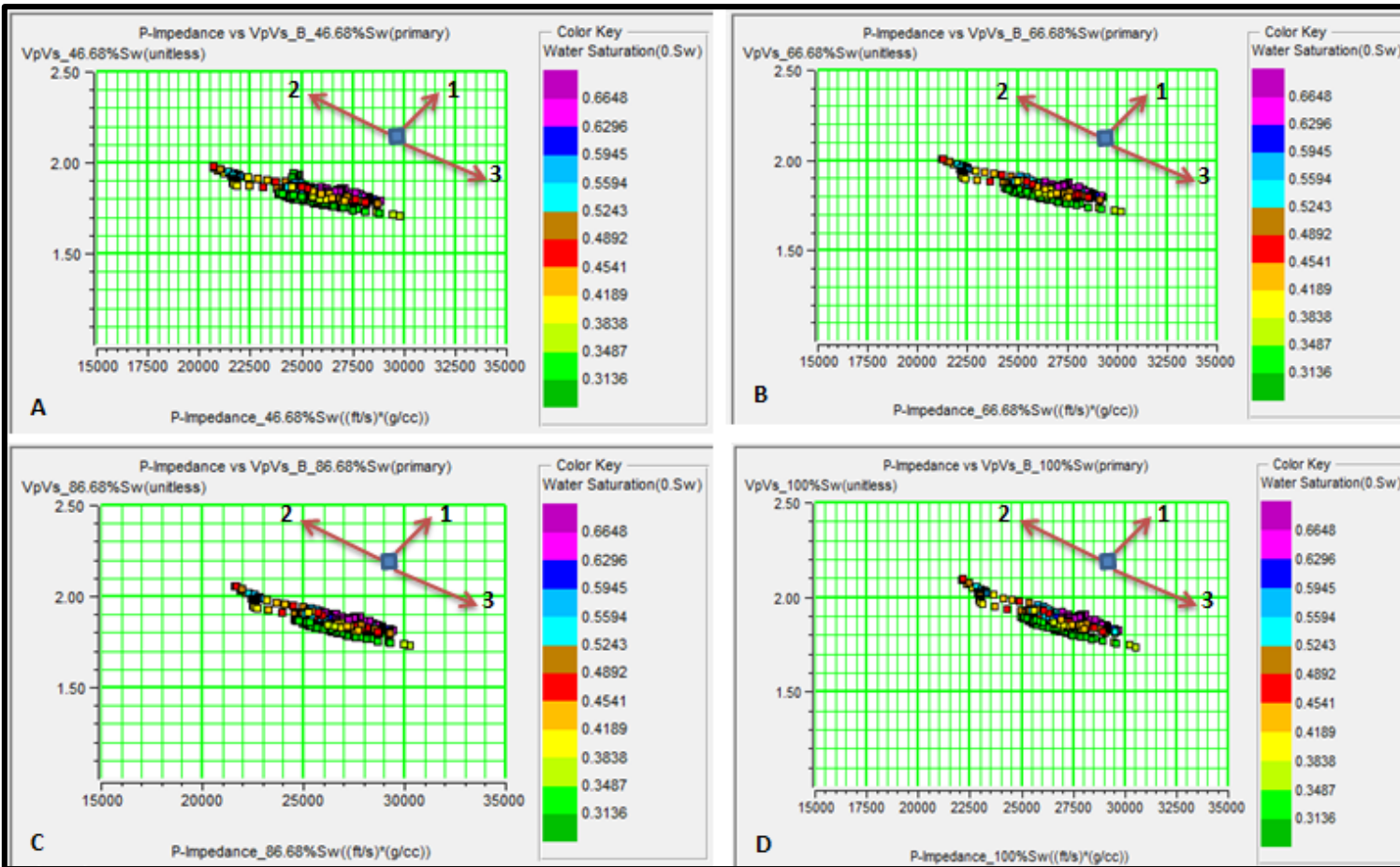


Figure 4.24: The Vp/Vs against P-Impedance Cross-Plots on Dynamic RPT for Reservoir B in Well A-2 for Different Values of Water Saturation: A) Field Data at 46.68% Water Saturation; B, C, D Are Synthetic Data at 66.68%, 86.68% And 100% Water Saturation Respectively. The Arrows Indicate Different Geologic Trends (Conceptually): 1-Increasing Water Saturation; 2-Increasing Pore Pressure; 3-Decreasing Pore Pressure (Adapted from Avseth and Ødegaard, 2004).

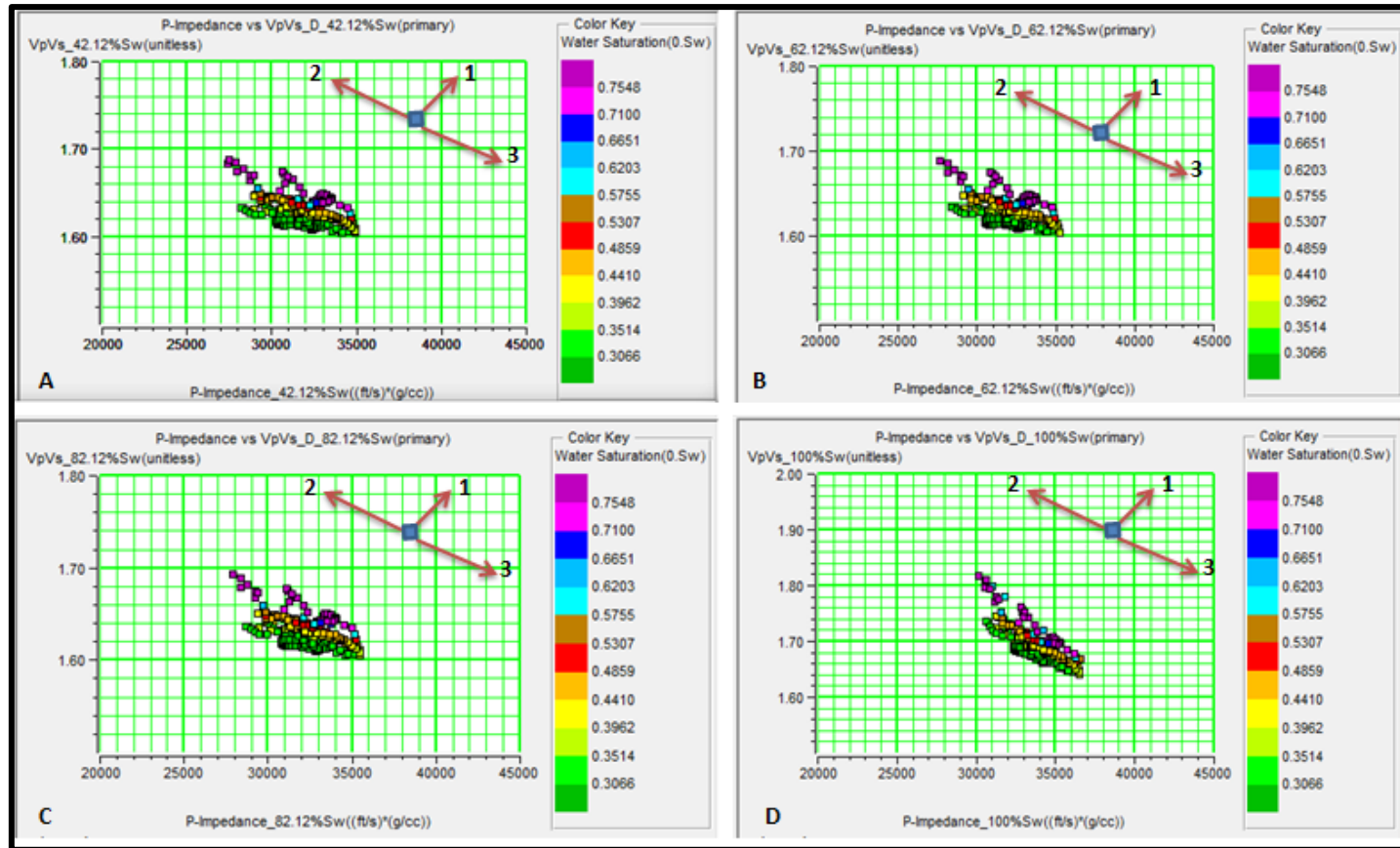


Figure 4.25: The Vp/Vs against P-Impedance Cross-Plots on Dynamic RPT for Reservoir D in Well A-2 for Different Values of Water Saturation: A) Field Data at 42.12% Water Saturation; B, C, D Are Synthetic Data at 62.12%, 82.12% And 100% Water Saturation Respectively. The Arrows Indicate Different Geologic Trends (Conceptually): 1-Increasing Water Saturation; 2-Increasing Pore Pressure; 3-Decreasing Pore Pressure (Adapted from Avseth and Ødegaard, 2004).

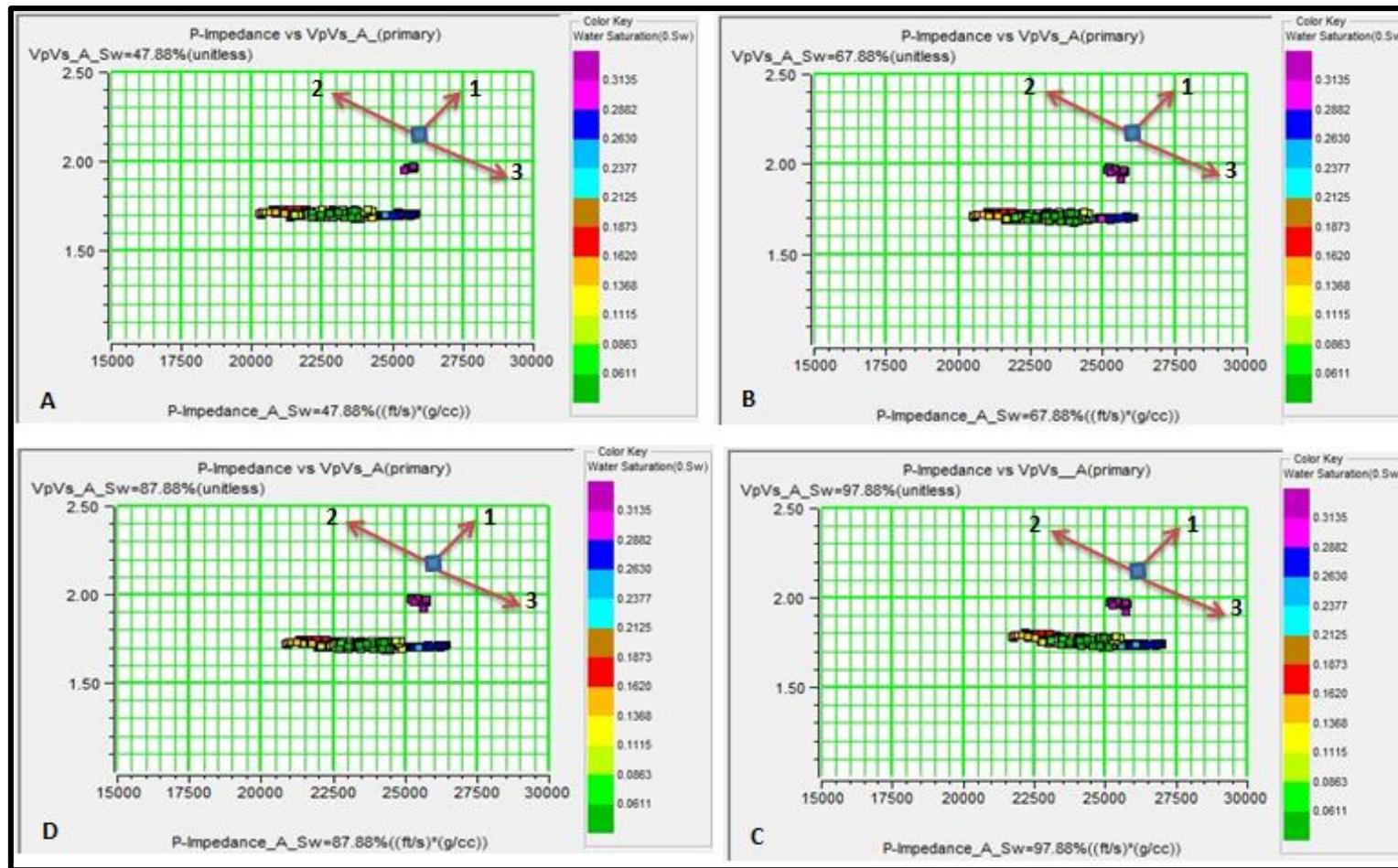


Figure 4.26: The Vp/Vs against P-Impedance Cross-Plots on Dynamic RPT for Reservoir A in Well A-3 for Different Values of Water Saturation: A) Field Data at 47.88% Water Saturation; B, C, D Are Synthetic Data at 67.88%, 87.88% and 97.88% Water Saturation Respectively. The Arrows Indicate Different Geologic Trends (Conceptually): 1-Increasing Water Saturation; 2-Increasing Pore Pressure; 3-Decreasing Pore Pressure (Adapted from Avseth and Ødegaard, 2004).

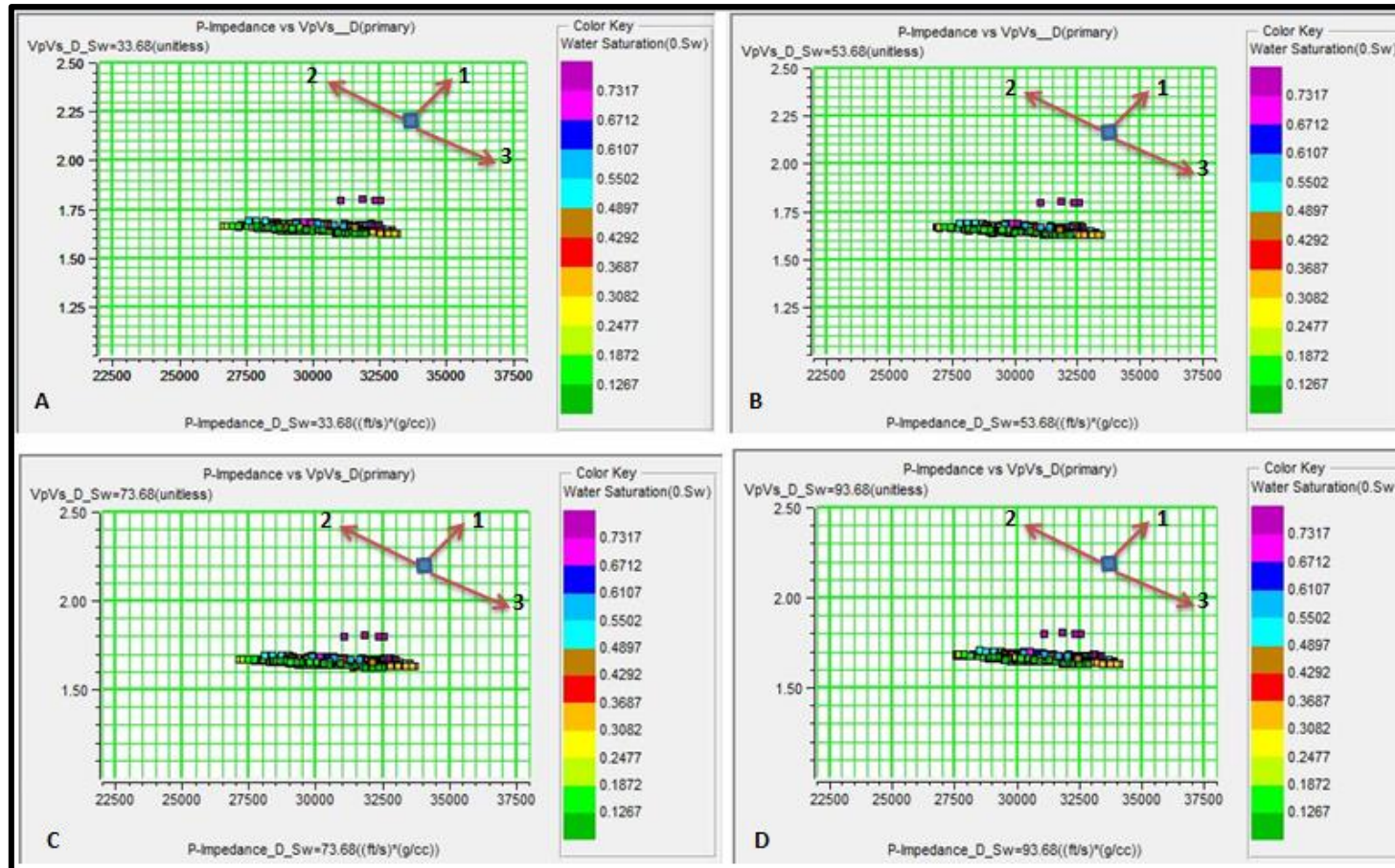


Figure 4.27: The Vp/Vs against P-Impedance Cross-Plots on Dynamic RPT for Reservoir D in Well A-3 for Different Values of Water Saturation: A) Field Data at 33.68% Water Saturation; B, C, D Are Synthetic Data at 53.68%, 73.68% and 93.68% Water Saturation Respectively. The Arrows Indicate Different Geologic Trends (Conceptually): 1-Increasing Water Saturation; 2-Increasing Pore Pressure; 3-Decreasing Pore Pressure (Adapted from Avseth and Ødegaard, 2004).

Table 4.6: Elastic Parameters of Reservoir A of Well A1 of Tetemu Field.

$Sw(\%)$	$Tc(\mu s/ft)$	$\rho(g/cm^3)$	$Ts(\mu s/ft)$	ν	ν (dry)	$Vp(km/s)$	$Vs(km/s)$	Vp/Vs	Acoustic impedance	Shear Impedance	$G(GPa)$	$K(Gpa)$	$Cb(1/K)$	E (Gpa)	UCS(Mpa)
43.00	98.64	2.328	170.71	0.2494	0.2481	3.0899	1.7855	1.7306	7.1925	4.1561	7.42066	12.3300	0.0811	18.5422	78.3030
50.00	98.96	2.344	171.30	0.2495	0.2481	3.0801	1.7794	1.7310	7.2188	4.1703	7.42051	12.3407	0.0810	18.5446	78.3127
60.00	99.39	2.366	172.12	0.2499	0.2481	3.0667	1.7708	1.7318	7.2572	4.1905	7.42061	12.3618	0.0809	18.5500	78.3352
70.00	99.79	2.389	172.95	0.2505	0.2481	3.0545	1.7624	1.7332	7.2978	4.2106	7.42059	12.3967	0.0807	18.5587	78.3708
80.00	100.11	2.412	173.77	0.2516	0.2481	3.0447	1.7540	1.7358	7.3436	4.2307	7.42066	12.4646	0.0802	18.5757	78.4404
90.00	100.15	2.435	174.59	0.2548	0.2481	3.0434	1.7458	1.7433	7.4099	4.2506	7.42067	12.6567	0.0790	18.6225	78.6324
100.00	92.66	2.458	175.41	0.3064	0.2481	3.2896	1.7377	1.8931	8.0842	4.2704	7.42065	16.6993	0.0599	19.3899	81.7784

Where,

$Sw(\%)$ = Water Saturation

$Tc(\mu s/ft)$ = Transit time of compressional wave

$Ts(\mu s/ft)$ = Transit time of shear wave

$\rho(g/cm^3)$ = Density of the rock

$Vp(km/s)$ = Velocity of Compressional wave

$Vs(km/s)$ = Velocity of shear wave

$G(GPa)$ = Shear modulus

K and E are Bulk and Young moduli respectively, measured in (GPa)

Cb = Bulk compressibility, which is $(1/K)$ in (GPa^{-1})

UCS = Unconfined Compressive Strength in (MPa)

ν = poisson ratio (for saturated and dry rock)

In reservoir D of well A1, reservoirs A, B and D of well A2 (Figure 4.22 – 4.25), the clusters lie perfectly along the pressure plane, in the direction of increasing acoustic impedance and decreasing pore pressure. Plates A in all the figures (Fig.4.22 - 4.25) were the crossplots of the acoustic impedance against the velocity ratios for reservoirs' field data at initial conditions, before fluid substitution in the reservoirs (D of well A1, A, B and D of well A2). Consequently, increase of water saturation (Fig.4.22 - 4.25 and Table 4.7 - 4.10) during production in these reservoirs, will most likely trigger gradual and steady drop in pore pressure, while the effective pressure may increase, inducing significant stress within the reservoir.

In reservoirs A and D of well A3 (Figures 4.26 and 4.27), plates A in the two figures represent the velocity ratios and acoustic impedance crossplots in reservoirs A and D at initial conditions, before the commencement of production while B, C and D represent the velocity ratios and acoustic impedance crossplots plates for forward modeling output at different values of water saturations (reservoirs at dynamic state) (Fig. 4.26, 4.27 and Table 4.11 and 4.12). However, the resulting clusters (Fig. 4.26 and 4.27) lie nearly perpendicularly to the pressure plane, but in the direction of increasing acoustic impedance. Consequently, reservoir A and D in well A-3 may not experience decrease of pore pressure due to increasing water saturation during production.

It should be noted from above, that good understanding of the impact of increasing water or brine on pore-pressure and stress state of the reservoirs during production is an important factor for designing new production wells, stabilizing existing wells, optimizing production and extending the life of a field (Avseth and Ødegaard, 2004). As corroborated by Avseth and Ødegaard, (2004), changes in horizontal stress within both the reservoir and cap rock formations will occur due to pore pressure depletion. The difference in pore pressure between the cap rock and reservoir drives fluid from cap rock into the reservoir. The regular seepage will impact the in-situ stress of the reservoir, which invariably will affect the stability of the well. The cap rock is also liable to deformation as the matrix stress increases due to decrease of pore pressure.

Table 4.7: Elastic Parameters of Reservoir D of Well A1 of Tetemu Field.

$S_w(\%)$	$T_c(\mu\text{s}/\text{ft})$	$V_p(\text{ft}/\text{s})$	$V_s(\text{m}/\text{s})$	$V_s(\text{ft}/\text{s})$	$T_s(\mu\text{s}/\text{ft})$	ν	$\nu_{\text{Dry rock}}$	$V_p(\text{km}/\text{s})$	$V_s(\text{km}/\text{s})$	ρ (g/cm^3)	$G(\text{GPa})$	$K(\text{Gpa})$	C_b (GPa^{-1})	E (Gpa)	UCS (Mpa)
30.9	77.752	12861.41	2385.26	7825.66	127.78	0.206	0.2054	3.92016	2.38526	2.4273	13.81004	18.88845	0.052942	33.312	138.8578
40.9	78.031	12815.37	2376.36	7796.46	128.26	0.206	0.2054	3.90612	2.37636	2.44551	13.81001	18.89979	0.052911	33.316	138.8736
50.9	78.303	12770.85	2367.56	7767.59	128.74	0.206	0.2054	3.89256	2.36756	2.46373	13.81005	18.91703	0.052862	33.322	138.8983
60.9	78.562	12728.86	2358.86	7739.04	129.21	0.207	0.2054	3.87976	2.35886	2.48194	13.81006	18.94604	0.052781	33.332	138.9394
70.9	78.786	12692.69	2350.25	7710.79	129.69	0.208	0.2054	3.86873	2.35025	2.50015	13.81002	19.00661	0.052613	33.352	139.0242
80.9	78.861	12680.54	2341.74	7682.87	130.16	0.21	0.2054	3.86503	2.34174	2.51836	13.81005	19.20698	0.052064	33.42	139.3032
90.9	76.595	13055.65	2335.42	7662.14	130.51	0.237	0.2054	3.97936	2.33542	2.53202	13.81011	21.68187	0.046121	34.175	142.3958
100	76.315	13103.52	2332.08	7651.18	130.7	0.241	0.2054	3.99395	2.33208	2.53928	13.81012	22.09221	0.045265	34.286	142.8531

Where,

$S_w(\%)$ = Water Saturation

$T_c(\mu\text{s}/\text{ft})$ = Transit time of compressional wave

$T_s(\mu\text{s}/\text{ft})$ = Transit time of shear wave

$\rho(\text{g}/\text{cm}^3)$ = Density of the rock

$V_p(\text{ft}/\text{s}$ and $\text{km}/\text{s})$ = Velocity of Compressional wave

$V_s(\text{ft}/\text{s}$ and $\text{km}/\text{s})$ = Velocity of shear wave

$G(\text{GPa})$ = Shear modulus

K and E represent Bulk and Young moduli respectively, measured in (GPa)

C_b = Bulk compressibility, which is $(1/K)$ in (GPa^{-1})

UCS = Unconfined Compressive Strength in (MPa)

ν = poisson ratio (for saturated and dry rock)

Table 4.8: Elastic Parameters of Reservoir A of Well A2 of Tetemu Field.

<i>Sw</i> (%)	<i>T_c</i> (μs/ft)	<i>V_p</i> (ft/s)	<i>ρ</i> (g/cm ³)	<i>V_s</i> (m/s)	<i>V_s</i> (ft/s)	<i>T_s</i> (μs/ft)	<i>ν</i> (sat.)	<i>ν</i> (dry rock)	<i>V_p</i> (km/s)	<i>V_s</i> (km/s)	<i>G</i> (GPa)	<i>K</i> (Gpa)	<i>C_b</i> (GPa ⁻¹)	<i>E</i> (Gpa)	<i>UCS</i> (Mpa)
49.51	89.356	11191.2	2.40801	1858.73	6098.2	163.983	0.2888	0.26296	3.41108	1.85873	8.3194	16.9259	0.059081	21.445	90.2031
60.00	89.225	11207.7	2.4164	1855.5	6087.6	164.268	0.2908	0.26296	3.4161	1.8555	8.3194	17.1063	0.058458	21.477	90.3338
70.00	89.043	11230.6	2.42479	1852.28	6077.03	164.554	0.293	0.26296	3.42307	1.85228	8.3193	17.3199	0.057737	21.513	90.485
80.00	88.797	11261.7	2.43319	1849.08	6066.54	164.839	0.2956	0.26296	3.43256	1.84908	8.3193	17.5766	0.056894	21.557	90.6631
90.00	88.466	11303.7	2.44158	1845.9	6056.1	165.123	0.2987	0.26296	3.44538	1.8459	8.3193	17.8906	0.055895	21.609	90.875
100.00	88.023	11360.7	2.44998	1842.74	6045.73	165.406	0.3025	0.26296	3.46274	1.84274	8.3194	18.2841	0.054692	21.671	91.1322

Where,

Sw (%) = Water Saturation

T_c (μs/ft) = Transit time of compressional wave

T_s (μs/ft) = Transit time of shear wave

ρ (g/cm³) = Density of the rock

V_p (ft/s and km/s) = Velocity of Compressional wave

V_s (ft/s and km/s) = Velocity of shear wave

G (GPa) = Shear modulus

K (GPa) = Bulk modulus

E (GPa) = Young modulus

C_b = Bulk compressibility, which is (1/*K*) in (GPa⁻¹)

UCS = Unconfined Compressive Strength in (MPa)

ν = poisson ratio (for saturated and dry rock)

Table 4.9: Elastic Parameters of Reservoir B of Well A2 of Tetemu Field.

<i>Sw</i> (%)	<i>Tc</i> (μ s/ft)	<i>Vp</i> (ft/s)	ρ (g/cm ³)	<i>Vs</i> (m/s)	<i>Vs</i> (ft/s)	<i>Ts</i> (μ s/ft)	ν (poison ratio)	ν (Dry rock)	<i>Vp</i> (km/s)	<i>Vs</i> (km/s)	<i>G</i> (GPa)	<i>K</i> (Gpa)	<i>Cb</i> (GPa ⁻¹)	<i>E</i> (Gpa)	<i>UCS</i> (Mpa)
46.68	94.157	10620.5	2.2979	1745.28	5725.98	174.642	0.2951	0.2578	3.23714	1.74528	6.9994	14.747	0.067809	18.13	76.61276527
56.68	93.91	10648.5	2.30597	1742.22	5715.94	174.949	0.2976	0.2578	3.24568	1.74222	6.9994	14.96	0.066847	18.165	76.75681556
66.68	93.575	10686.7	2.31404	1739.18	5705.97	175.255	0.305	0.2578	3.25729	1.73918	6.9994	15.22	0.065706	18.207	76.92878909
76.68	93.195	10730.2	2.3221	1736.16	5696.06	175.56	0.3038	0.2578	3.27056	1.73616	6.9994	15.51	0.064491	18.252	77.11269229
86.68	92.687	10789	2.33017	1733.15	5686.19	175.865	0.3077	0.2578	3.28848	1.73315	6.9994	15.87	0.063027	18.306	77.33553024
96.68	92.037	10865.2	2.33824	1730.16	5676.38	176.169	0.3123	0.2578	3.31173	1.73016	6.9994	16.31	0.061304	18.371	77.59975481
100.00	91.781	10895.5	2.34092	1729.17	5673.13	176.27	0.314	0.2578	3.32094	1.72917	6.9994	16.48	0.060663	18.395	77.69854453

Where,

Sw (%) = Water Saturation

Tc (μ s/ft) = Transit time of compressional wave

Ts (μ s/ft) = Transit time of shear wave

ρ (g/cm³) = Density of the rock

Vp (ft/s and km/s) = Velocity of Compressional wave

Vs (ft/s and km/s) = Velocity of shear wave

G (GPa) = Shear modulus

K and *E* represent Bulk and Young moduli respectively, measured in (GPa)

Cb = Bulk compressibility, which is (1/*K*) in (GPa⁻¹)

UCS = Unconfined Compressive Strength in (MPa)

ν = poisson ratio (for saturated and dry rock)

Table 4.10: Elastic Parameters of Reservoir D of Well A2 of Tetemu Field.

<i>Sw</i> (%)	<i>Tc</i> (μ s/ft)	<i>Vp</i> (ft/s)	ρ (g/cm ³)	<i>Vs</i> (m/s)	<i>Vs</i> (ft/s)	<i>Ts</i> (μ s/ft)	ν (poison ratio)	ν (Dry rock)	<i>Vp</i> (km/s)	<i>Vs</i> (km/s)	<i>G</i> (GPa)	<i>K</i> (Gpa)	<i>Cb</i> (GPa ⁻¹)	E	
														(Gpa)	<i>UCS</i> (Mpa)
42.12	86.2535	11593.73	2.491	2117.65	6947.67	143.933	0.219	0.219	3.534	2.118	11.17074	16.212	0.061682	27.253	114.02
52.12	86.5422	11555.06	2.509	2110.09	6922.87	144.449	0.220	0.219	3.522	2.110	11.17069	16.227	0.061627	27.257	114.03
62.12	86.8192	11518.19	2.527	2102.62	6898.36	144.962	0.220	0.219	3.511	2.103	11.17074	16.249	0.061544	27.264	114.06
72.12	87.0737	11484.52	2.545	2095.22	6874.08	145.474	0.221	0.219	3.500	2.095	11.17070	16.286	0.061403	27.276	114.11
82.12	87.2719	11458.44	2.562	2087.90	6850.07	145.984	0.222	0.219	3.493	2.088	11.17069	16.362	0.061116	27.300	114.21
92.12	87.2295	11464.01	2.580	2080.66	6826.31	146.492	0.225	0.219	3.494	2.081	11.17071	16.611	0.060201	27.376	114.52
100.00	82.7953	12077.98	2.594	2075.01	6807.78	146.891	0.267	0.219	3.681	2.075	11.17075	20.267	0.049342	28.311	118.35

Where,

Sw (%) = Water Saturation

Tc (μ s/ft) = Transit time of compressional wave

Ts (μ s/ft) = Transit time of shear wave

ρ (g/cm³) = Density of the rock

Vp (ft/s and km/s) = Velocity of Compressional wave

Vs (ft/s and km/s) = Velocity of shear wave

G (GPa) = Shear modulus

K and *E* represent Bulk and Young moduli respectively, measured in (GPa)

Cb = Bulk compressibility, which is (1/*K*) in (GPa⁻¹)

UCS = Unconfined Compressive Strength in (MPa)

ν = poisson ratio (for saturated and dry rock)

Table 4.11: Elastic Parameters of Reservoir A of Well A3 of Tetemu Field.

<i>Sw</i> (%)	<i>Tc</i> (μ s/ft)	<i>Vp</i> (ft/s)	ρ (g/cm ³)	<i>Vs</i> (m/s)	<i>Vs</i> (ft/s)	<i>Ts</i> (μ s/ft)	ν (sat.)	ν (dry)	<i>Vp</i> (km/s)	<i>Vs</i> (km/s)	<i>G</i> (GPa)	<i>K</i> (Gpa)	<i>Cb</i> (GPa ⁻¹)	<i>E</i> (Gpa)	<i>UCS</i> (Mpa)
47.88	97.3256	10274.79	2.242	1832.76	6012.99	166.307	0.2396	0.2380	3.1318	1.8328	7.53023	11.94703	0.083703	18.6684	78.82058788
57.88	97.7748	10227.58	2.265	1823.51	5982.64	167.150	0.2399	0.2380	3.1174	1.8235	7.53019	11.96699	0.083563	18.6738	78.84243948
67.88	98.1945	10183.87	2.287	1814.40	5952.76	167.989	0.2405	0.2380	3.1040	1.8144	7.53016	11.99889	0.083341	18.6823	78.87752406
77.88	98.5494	10147.20	2.310	1805.43	5923.33	168.824	0.2416	0.2380	3.0929	1.8054	7.53018	12.05842	0.082930	18.6983	78.94312976
87.88	98.6996	10131.75	2.333	1796.59	5894.32	169.655	0.2442	0.2380	3.0882	1.7966	7.53018	12.20855	0.081910	18.7380	79.10590650
97.88	96.7890	10331.75	2.356	1787.88	5865.75	170.481	0.2622	0.2380	3.1491	1.7879	7.53019	13.32159	0.075066	19.0089	80.21648939
100.00	91.0389	10984.32	2.361	1786.05	5859.74	170.656	0.3011	0.2380	3.3480	1.7861	7.53019	16.42004	0.060901	19.5951	82.62008395

Where,

Sw (%) = Water Saturation

Tc (μ s/ft) = Transit time of compressional wave

Ts (μ s/ft) = Transit time of shear wave

ρ (g/cm³) = Density of the rock

Vp (ft/s and km/s) = Velocity of Compressional wave

Vs (ft/s and km/s) = Velocity of shear wave

G (GPa) = Shear modulus

K and *E* represent Bulk and Young moduli respectively, measured in (GPa)

Cb = Bulk compressibility, which is (1/*K*) in (GPa⁻¹)

UCS = Unconfined Compressive Strength in (MPa)

ν = poisson ratio (for saturated and dry rock)

Table 4.12: Elastic Parameters of Reservoir D of Well A3 of Tetemu Field.

$Sw(\%)$	$Tc(\mu s/ft)$	$\rho(g/cm^3)$	$Ts(\mu s/ft)$	ν	ν (dry)	$Vp(km/s)$	$Vs(km/s)$	Vp/Vs	Acoustic impedance	Shear Impedance	$G(GPa)$	$K(Gpa)$	$Cb(1/K)$	E (Gpa)	UCS(Mpa)
33.68	78.74	2.350	130.03	0.2105	0.2099	3.8709	2.3440	1.6514	9.0974	5.5089	12.91279	17.9982	0.0556	31.2621	130.4544
43.68	79.06	2.370	130.58	0.2106	0.2099	3.8552	2.3342	1.6516	9.1367	5.5320	12.91281	18.0065	0.0555	31.2649	130.4660
53.68	79.38	2.390	131.12	0.2108	0.2099	3.8398	2.3245	1.6519	9.1764	5.5551	12.91281	18.0184	0.0555	31.2689	130.4823
63.68	79.69	2.410	131.67	0.2110	0.2099	3.8250	2.3149	1.6523	9.2167	5.5781	12.91281	18.0366	0.0554	31.2749	130.5073
73.68	79.98	2.429	132.21	0.2114	0.2099	3.8111	2.3055	1.6531	9.2586	5.6009	12.91284	18.0682	0.0553	31.2856	130.5508
83.68	80.23	2.449	132.74	0.2123	0.2099	3.7993	2.2961	1.6546	9.3052	5.6237	12.91282	18.1363	0.0551	31.3081	130.6433
93.68	80.26	2.467	133.28	0.2155	0.2099	3.7976	2.2869	1.6606	9.3688	5.6418	12.90242	18.3761	0.0544	31.3662	130.8814
100.00	77.44	2.482	133.62	0.2471	0.2099	3.9359	2.2811	1.7254	9.7669	5.6607	12.91278	21.2242	0.0471	32.2068	134.3280

Where,

$Sw (\%)$ = Water Saturation

$Tc (\mu s/ft)$ = Transit time of compressional wave

$Ts (\mu s/ft)$ = Transit time of shear wave

$\rho (g/cm^3)$ = Density of the rock

$Vp (km/s)$ = Velocity of Compressional wave

$Vs (km/s)$ = Velocity of shear wave

$G (GPa)$ = Shear modulus

K and E represent Bulk and Young moduli respectively, measured in (GPa)

Cb = Bulk compressibility, which is $(1/K)$ in (GPa^{-1})

UCS = Unconfined Compressive Strength in (MPa)

ν = poisson ratio (for saturated and dry rock)

4.6 Dynamic, Elastic and Geomechanical Responses During Fluid Replacement

Fluid replacement modeling built on the Gassmann theory was used to assess the impacts of fluid substitution on the reservoirs' properties (elastic and mechanical) during production. This was in order to make informed predictions of how the reservoirs would behave if such conditions exist during the production life history of the field. Two plausible production scenarios were modeled separately; increasing water saturation and increasing gas saturation by gas injection (enhanced recovery).

4.6.1 Increasing Water Saturation

The results of the forward modelling of both elastic and mechanical properties of the selected reservoirs (A and D of well A1, A, B and D of well A2 and A and D of well A3) of the field are shown in Tables 4.6 – 4.12 and presented as graphs as shown in Figures 4.28-38. The results revealed the reservoirs' initial parameters before production and the model output generated during production as water replaces hydrocarbon (fluid substitution) in the reservoirs. This process was achieved by gradually increasing the water saturation of each selected reservoir from its original value to 100%, while other factors were kept constant. The results are presented in Figures 4.28-4.38.

4.6.1.1 Fluid Saturation's Effects on Elastic Properties of The Field Reservoirs

The output seismic responses in terms of density (ρ), velocity of shear wave (V_s) and velocity of compressional wave (V_p) were recorded for each value of water saturation. According to Han and Batzle, (2004), the V_s , V_p and ρ play a direct role in controlling reservoirs' seismic behaviour. It was observed from this study that, as water saturation (S_w) increases, there was a corresponding increase in density (ρ) of the reservoirs (Tables 4.6 - 4.12 and Fig.4.28 and plot G of Fig. 4.29). This is because brine is the heaviest and least compressible fluid in the reservoirs (Han and Batzle, 2004, Xu *et al.*, 2016).

In addition to the above, the steady increase in density during hydrocarbon production as water volume increases was connected to the conventional increase in the bulk modulus and rigidity of the rock when a less dense hydrocarbon is replaced by denser brine (Dvorkin *et al.*, 2001, Xu *et al.*, 2016). Therefore, with increasing water saturation (S_w), the bulk density (ρ) value in reservoir A of well A1 (Fig.4.33 and Table 4.6) increases from the initial (in-situ) bulk density of 2.3 g/cm^3 to 2.5 g/cm^3 at 100% water saturation.

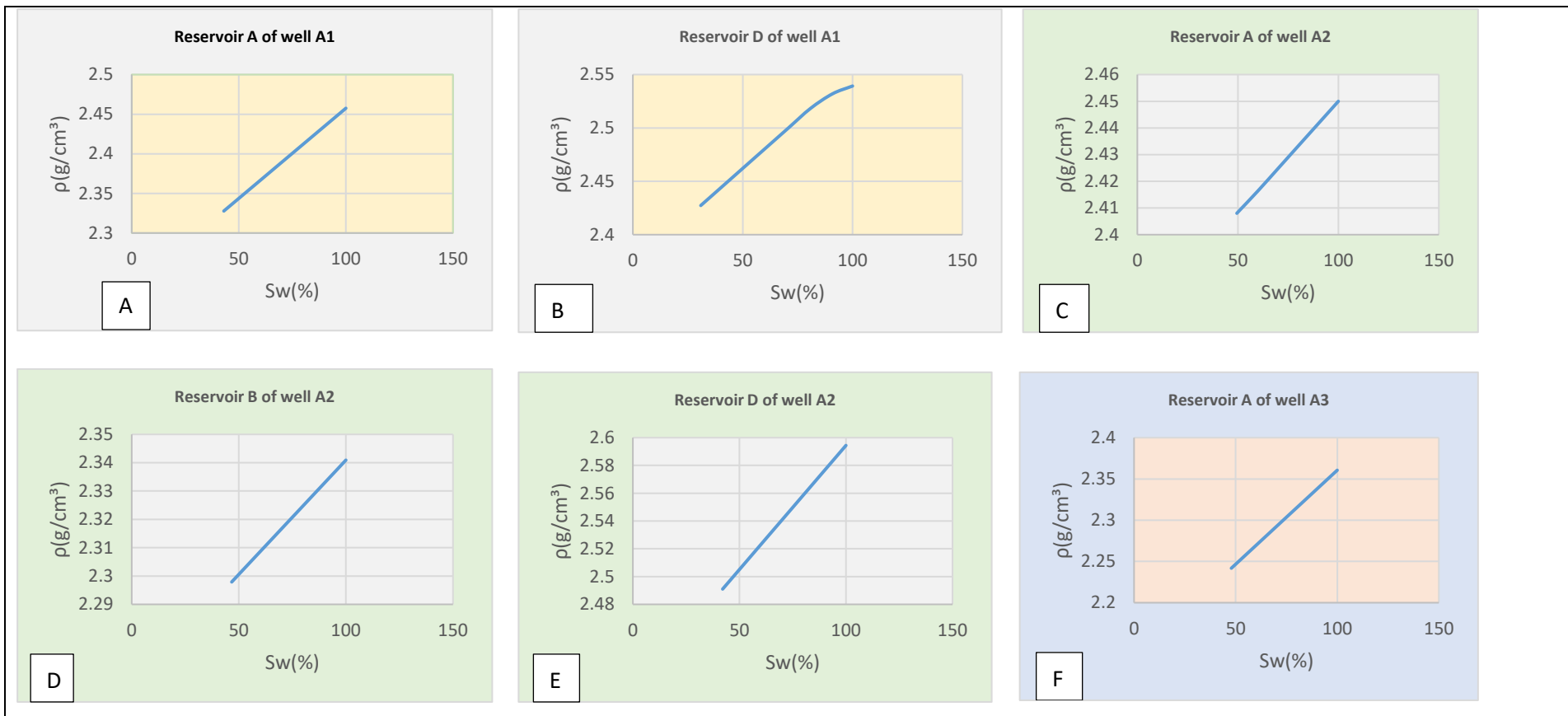


Figure 4.28: The Responses of Reservoir Elastic Parameter to Reservoir Fluid Replacement During Hydrocarbon Production As Water Saturation Increases Gradually from 0 to 100%: Plot A-F Revealed The Variation of Density, ρ (g/cm^3) With Increasing Water Saturation, S_w (%) in The Field Reservoirs.

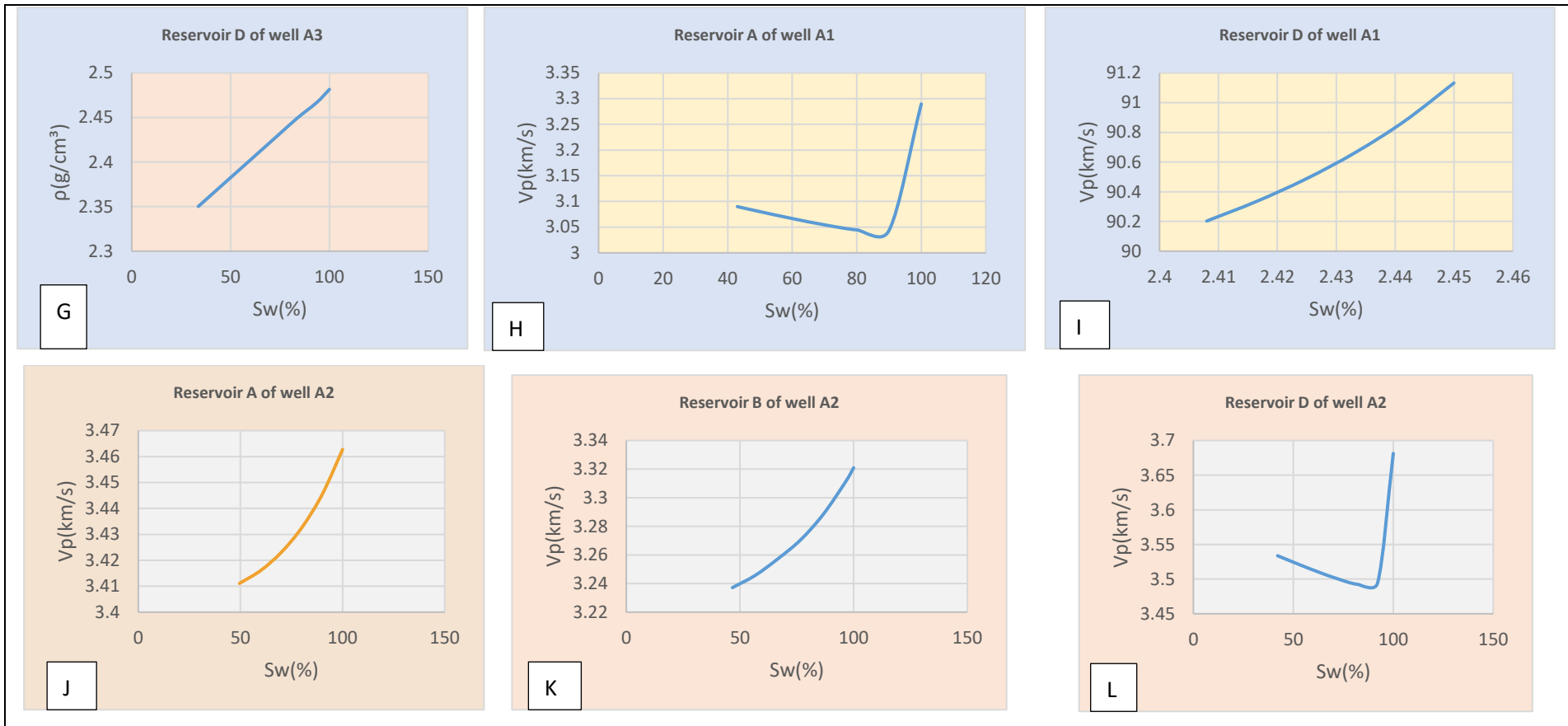


Figure 4.29: The Responses of Reservoir Elastic Parameters (Density, ρ and Compressional Wave Velocity, V_p) to Reservoir Fluid Replacement During Hydrocarbon Production as Water Saturation, S_w Increases Gradually from 0 to 100%: Plot H-L Showed The Behaviours of The Reservoir Compressional Wave Velocity, V_p and Density With Respect to Fluid Replacement by Adopting A Forward Modeling Approach.

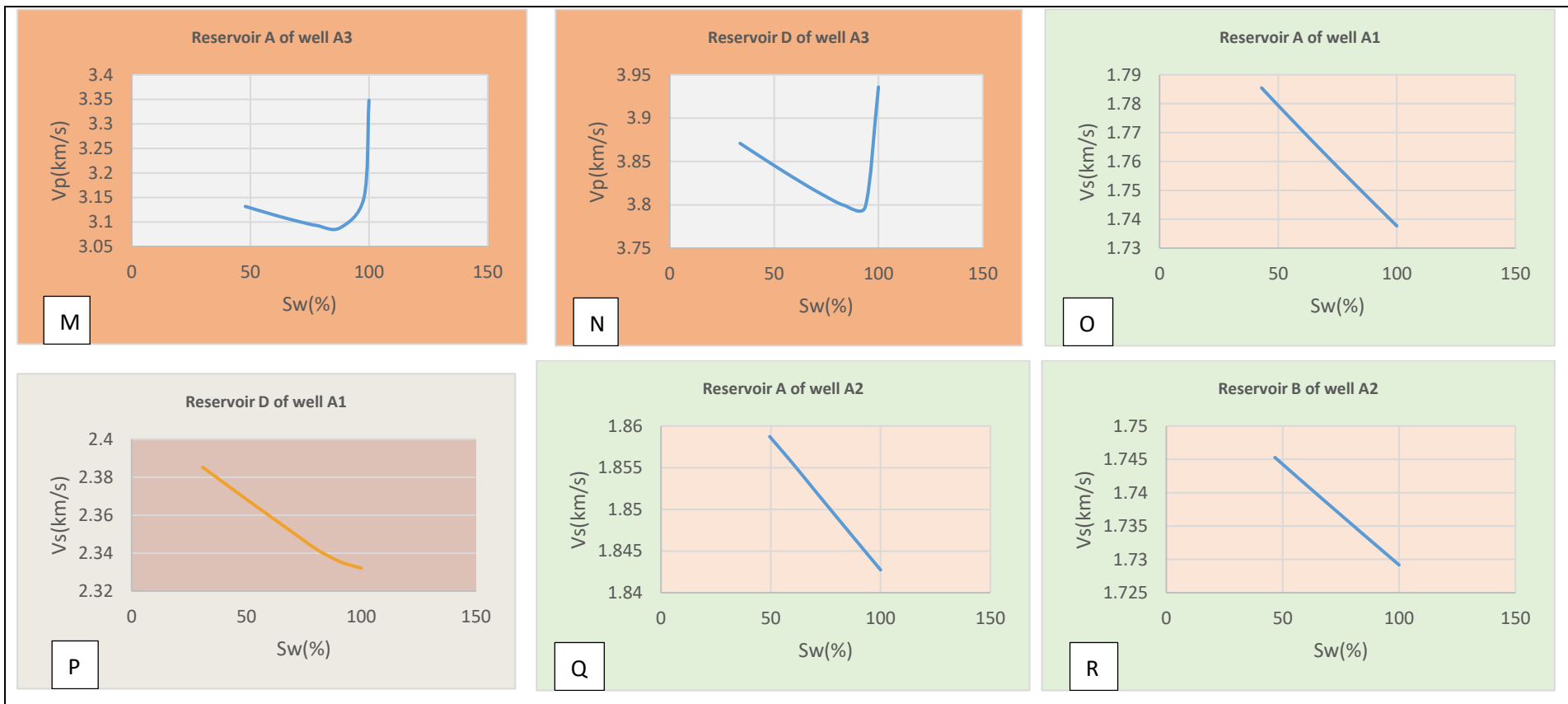


Figure 4.30: The Responses of Reservoir Elastic Parameters (Compressional Wave Velocity, V_p and Shear Wave Velocity, V_s) to Reservoir Fluid Replacement During Hydrocarbon Production as Water Saturation, S_w Increases Gradually from 0 to 100%: Plot M-R Showed The Behaviours of The Reservoir Compressional Wave Velocity, V_p And Shear Wave Velocity, V_s With Respect to Fluid Replacement by Adopting A Forward Modeling Approach.

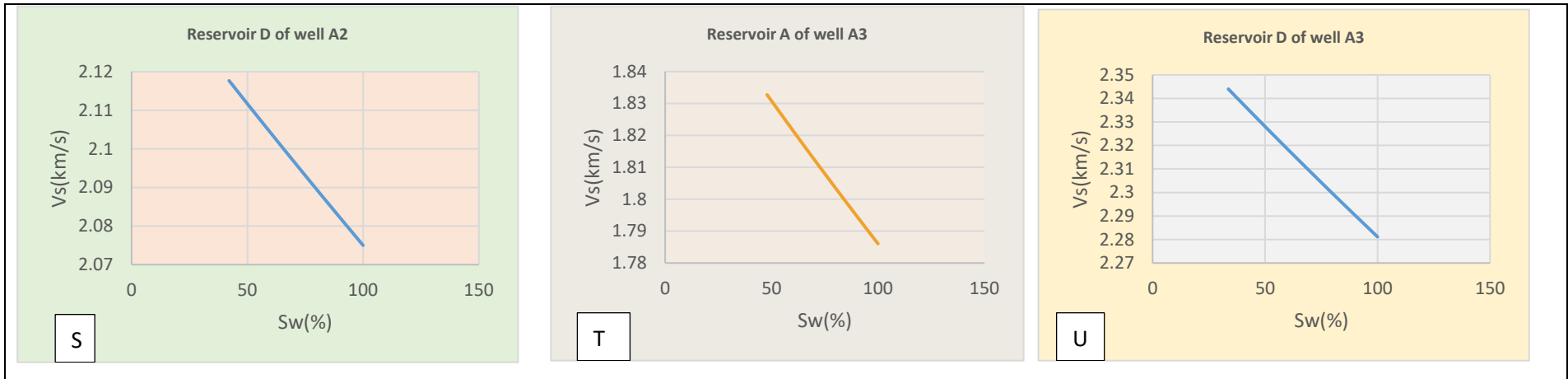


Figure 4.31: The Responses of Reservoir Shear Wave Velocity, V_s to Fluid Replacement During Hydrocarbon Production As Water Saturation Increases Gradually from 0 to 100%: Plot S-U Showed The Behaviours of The Reservoir Shear Wave Velocity With Respect to Fluid Replacement Using Forward Modeling Approach.

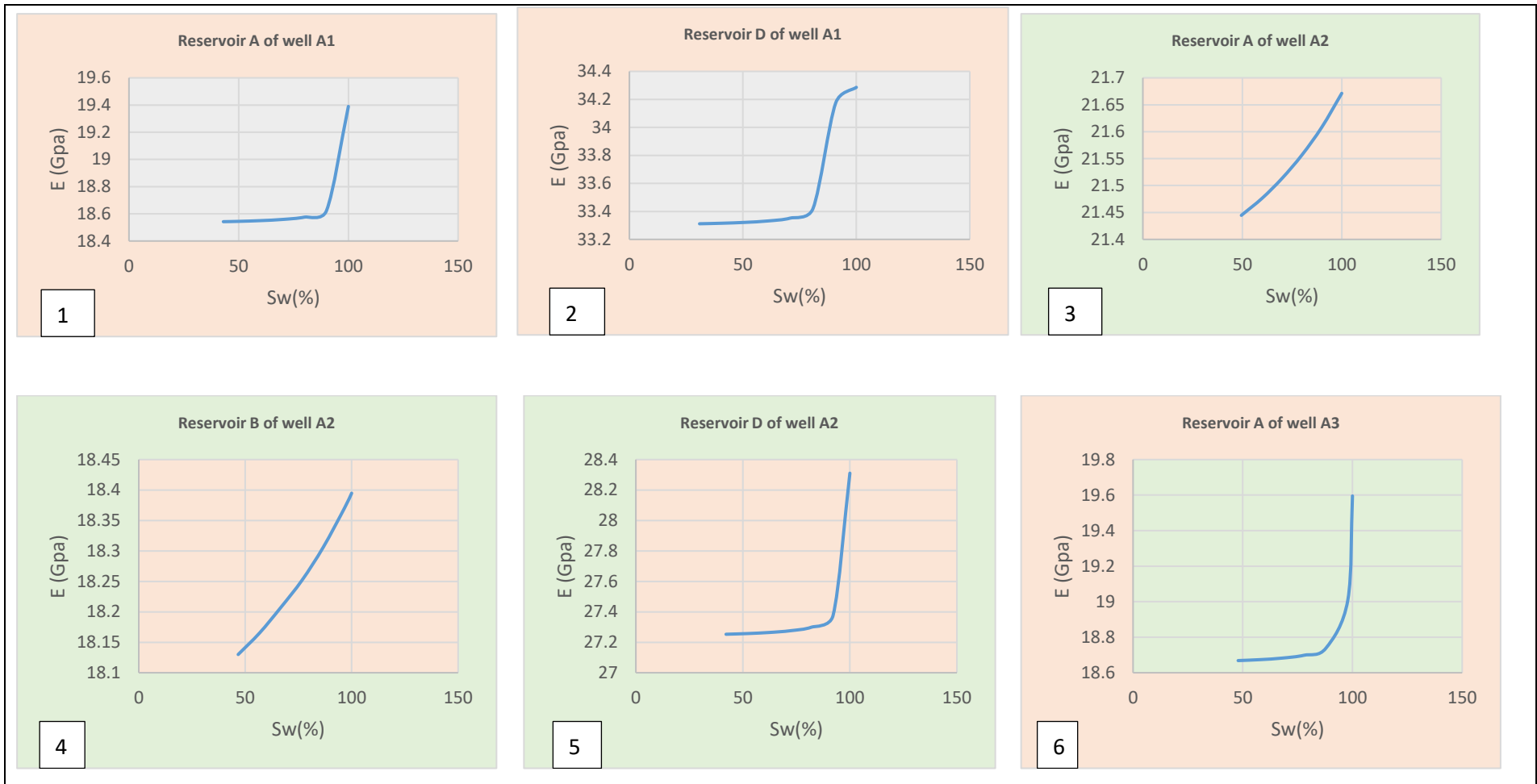


Figure 4.32: The Responses of Reservoir Mechanical Parameters (Young Modulus, E) to Reservoir Fluid Replacement During Hydrocarbon Production as Sw Increases from 0 to 100%: Plot 1-6 Showed The Reactions of The Reservoirs With Respect to Fluid Replacement Using A Forward Modeling Technique.

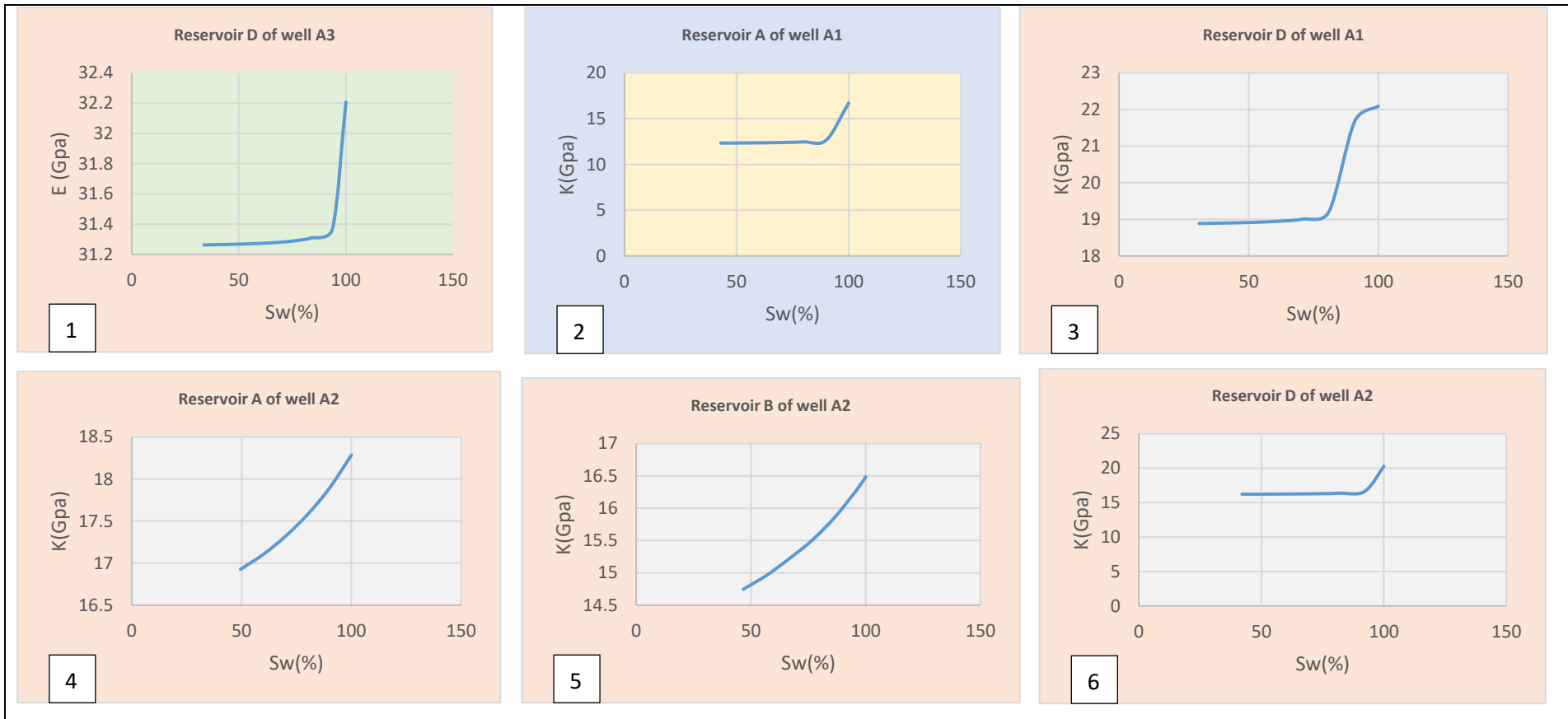


Figure 4.33: The Responses of Reservoir Mechanical Parameters (Young Modulus and Bulk Modulus) to Reservoir Fluid Substitution During Hydrocarbon Production As Water Saturation Increases from 0 to 100%: Plot 1-6 Showed The Behaviours of The Reservoir During Fluid Replacement by Adopting A Forward Modeling Method.

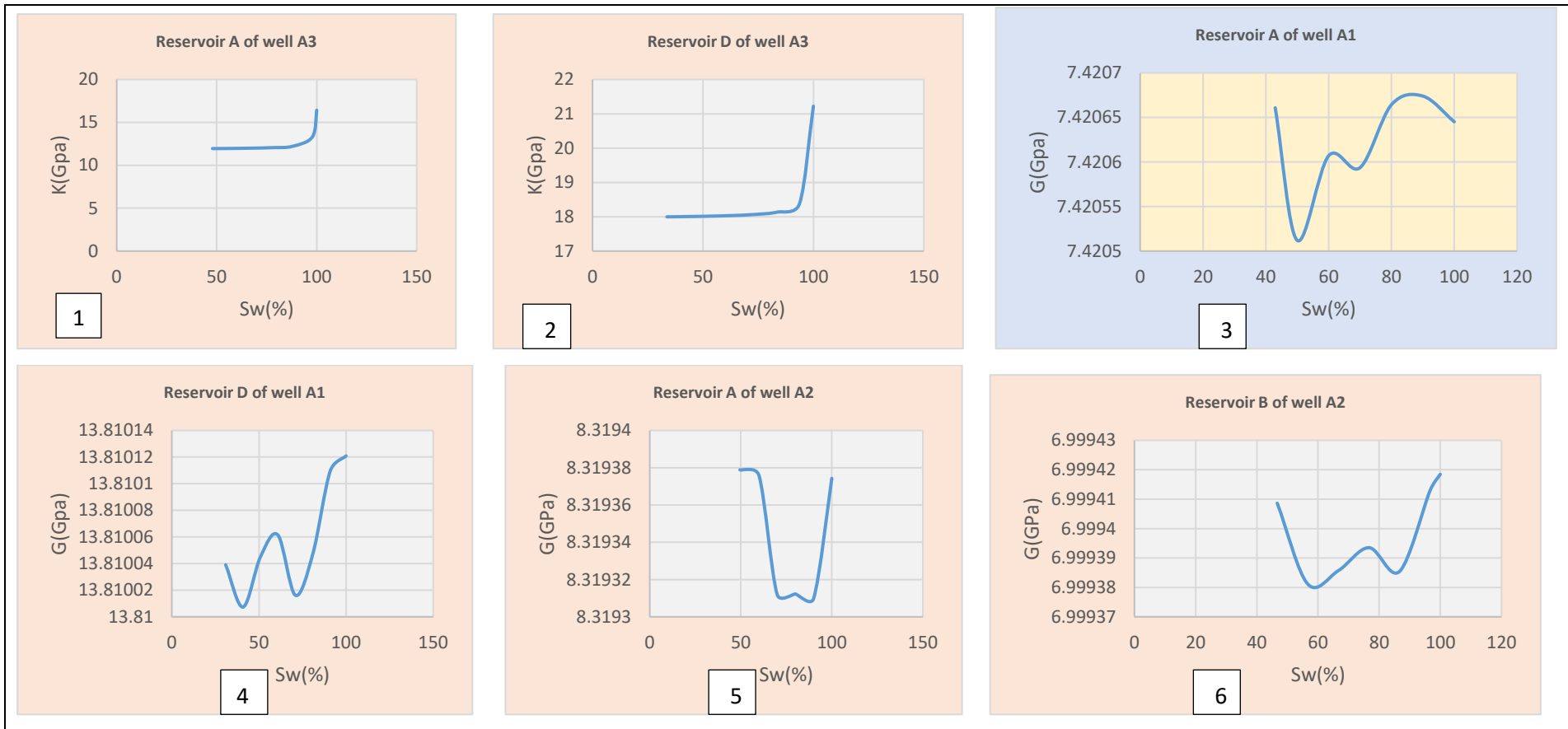


Figure 4.34: The Responses of Bulk Modulus And Shear Modulus to Fluid Substitution During Hydrocarbon Production As Sw Increases from 0 to 100%: Plot 1-6 Showed The Behaviours of The Reservoir During Fluid Replacement Using A Forward Modeling Method.

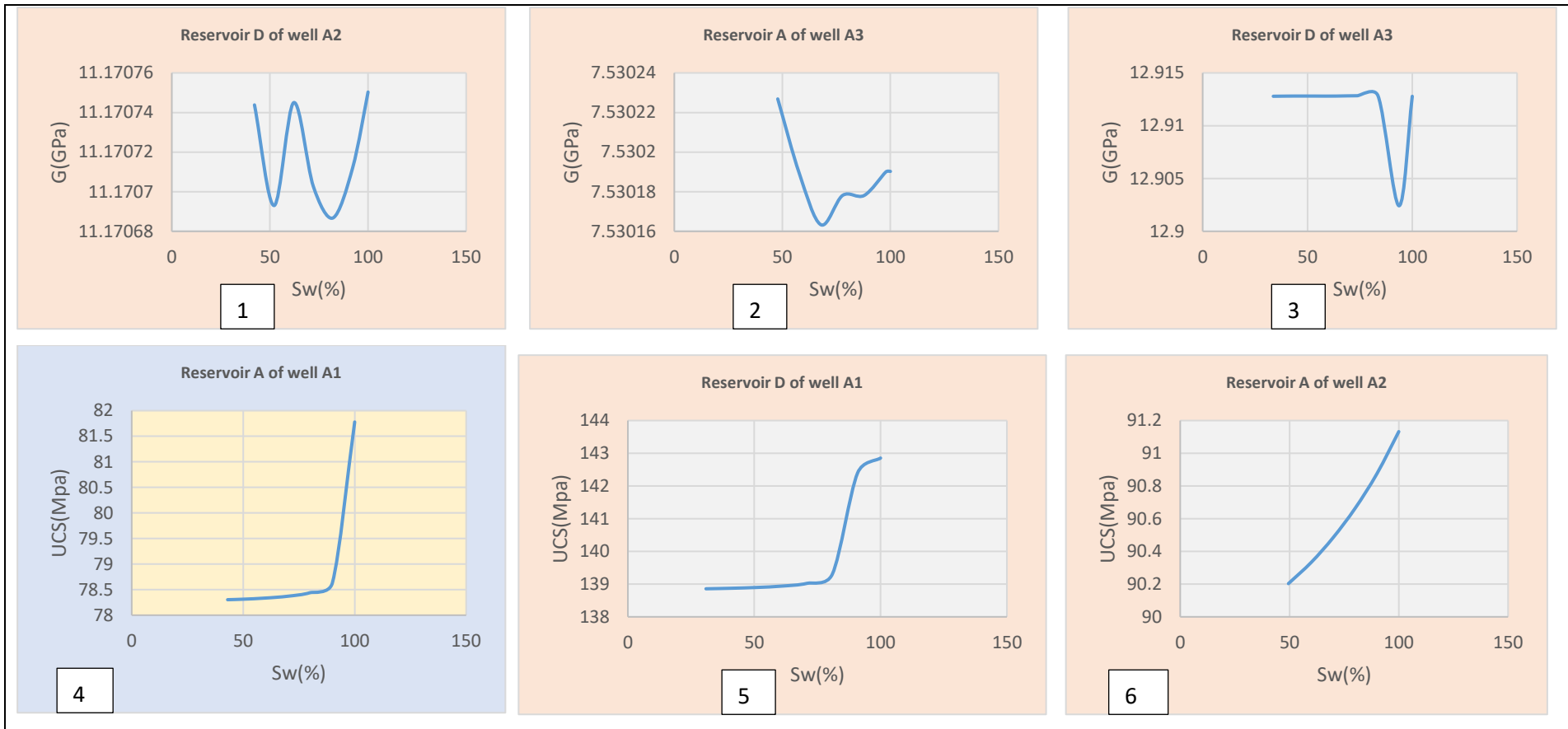


Figure 4.35: The Responses of Reservoir Mechanical Parameters (Shear Modulus and Unconfined Compressive Strength) to Fluid Replacement As Sw Increases from 0 to 100%: Plot 1-6 Revealed The Trend of Behaviours of The Reservoir During Fluid Replacement Using A Forward Modeling Method.

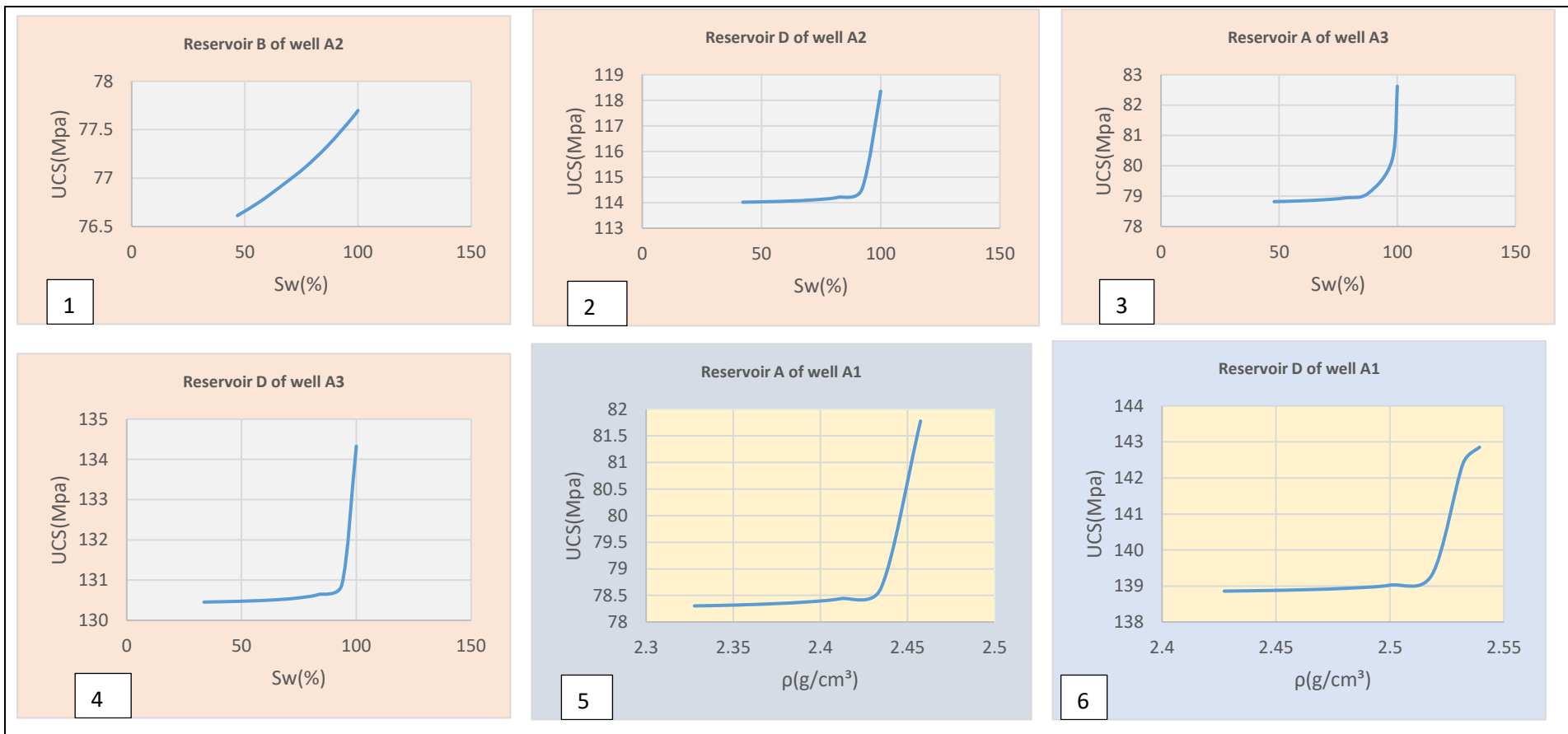


Figure 4.36: The Responses of UCS to Fluid Replacement (plot 1-4) As Sw Increases from 0 to 100%: Plot 5-6 Revealed The Variation of UCS With Density.

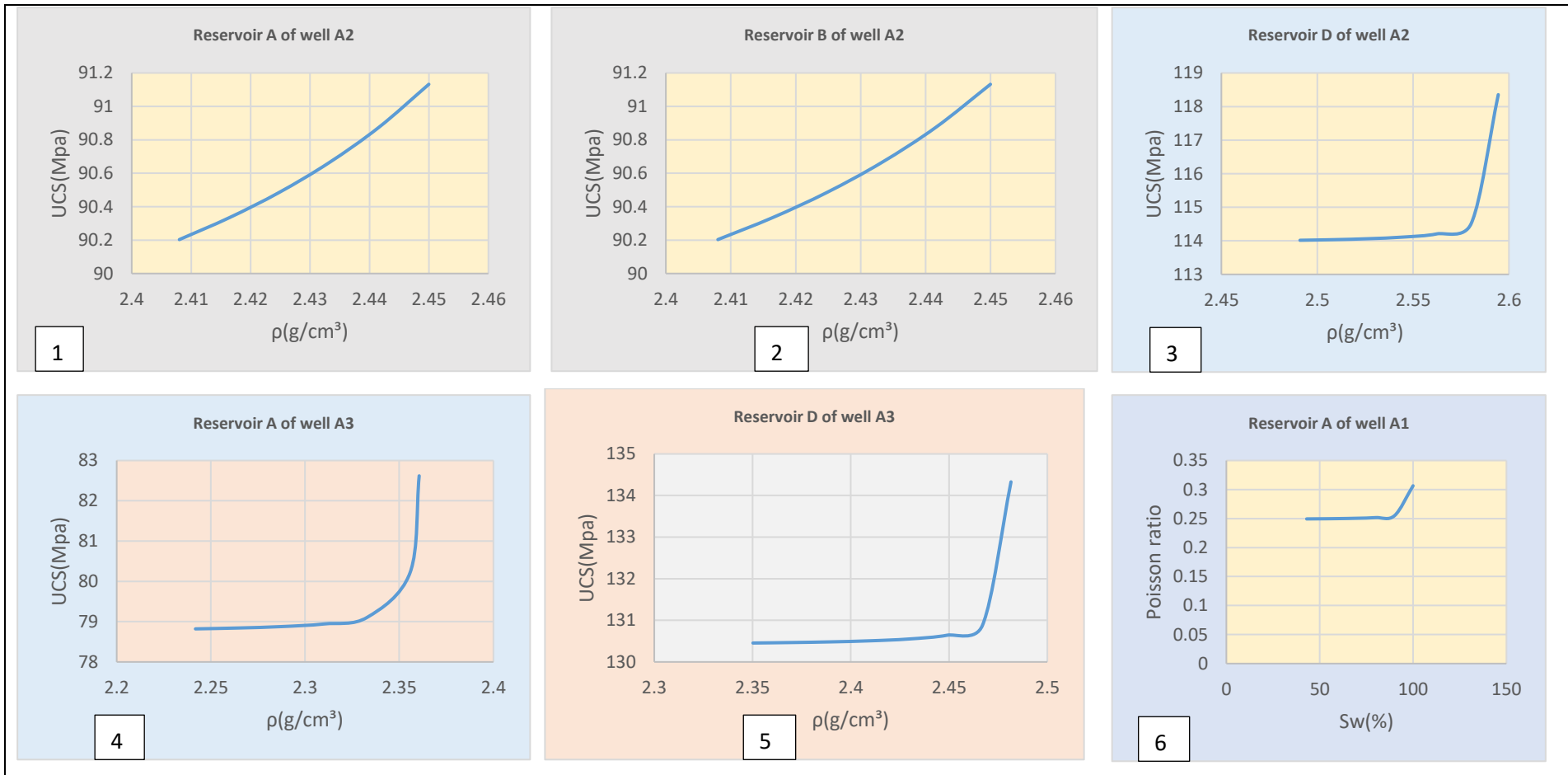


Figure 4.37: The Plot 1-5 Showed The Variation of The Reservoir Strength, UCS With Reservoir Rock Density While Plot 6 Revealed The Response of The Poisson Ratio to Fluid Replacement As S_w Increases from 0 to 100%.

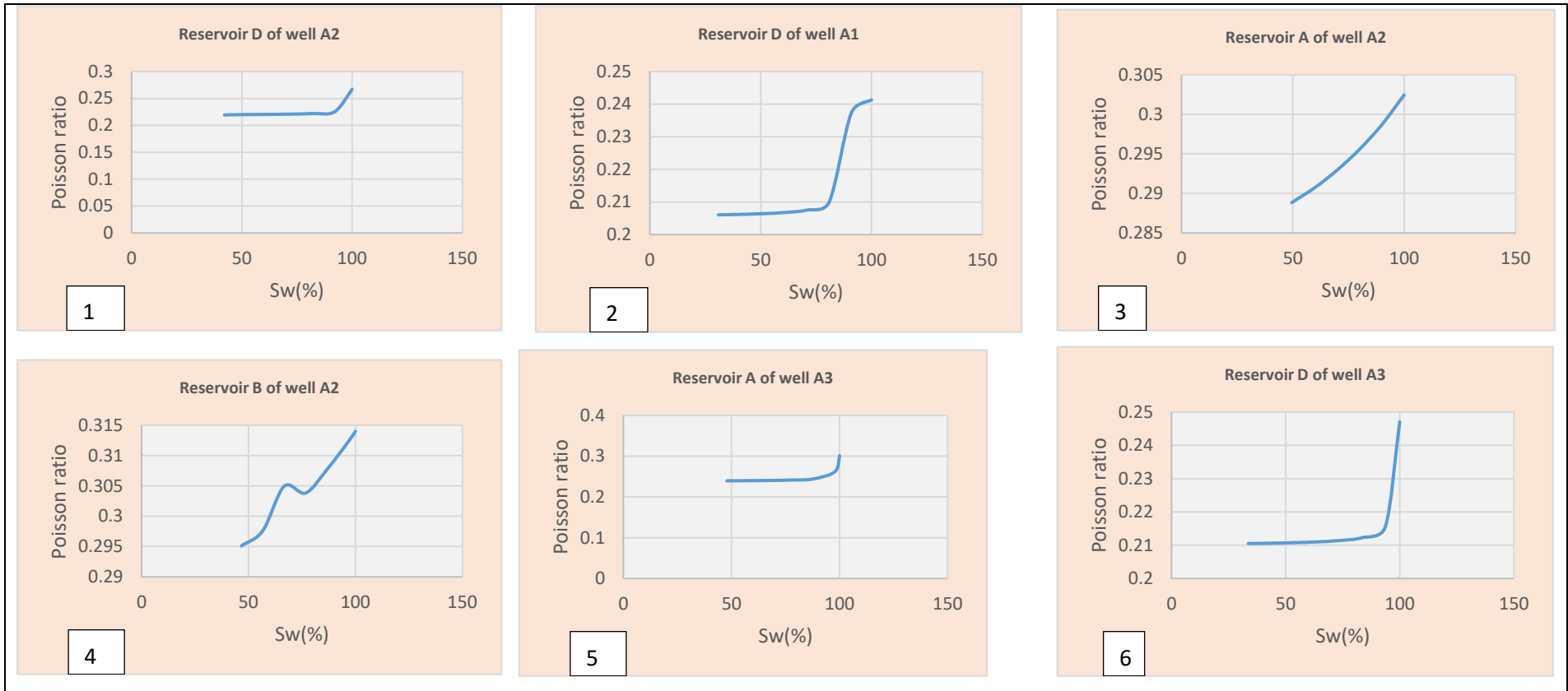


Figure 4.38: The Plot 1-6 Revealed The Response of The Poisson Ratio to Fluid Replacement As Sw Increases from 0 to 100% During Oil and Gas P roduction.

In reservoir D of well A1 (Table 4.7 and Fig.4.33), the increase in water saturation, generated a corresponding increase in bulk density from the initial value of 2.43 g/cm^3 at 30.9% water saturation to 2.54 g/cm^3 at 100% water saturation. It was observed from the reservoir A of well A2 (Table 4.8 and Fig.4.33), that as S_w increases from 49.51% to 100%, the bulk density also increases from 2.41 g/cm^3 to 2.45 g/cm^3 . In the reservoir B of well A2, the rise in S_w resulted to bulk density increase during production from 2.30 g/cm^3 at the initial water volume of 46.68% to 2.34 g/cm^3 at 100% water saturation (Table 4.9 and Fig.4.33). Also, in the reservoir D of well A2 (Table 4.10 and Fig.4.33), as the water saturation increases in the reservoir, the bulk density value also increases during production from 2.49 g/cm^3 at the initial water volume of 42.12% to 2.59 g/cm^3 at 100% saturation (water).

As shown in reservoir A of well A3 (Table 4.11 and Fig.4.34), the bulk density value increases from 2.24 g/cm^3 at the initial water volume of 47.88% to 2.36 g/cm^3 at 100% S_w during production. In the reservoir D of well A3 (Table 4.12 and Fig.4.34), the bulk density value increases from 2.35 g/cm^3 at the initial water volume of 33.68% to 2.48 g/cm^3 at 100% water saturation in the reservoir, during hydrocarbon production. The observed density – depth trends from the reservoirs across the three wells during hydrocarbon production show steady increase in density with depth (Tables 4.6 – 4.12).

The observed steady increase was due to the effect of cementation and compaction which increase the reservoir rock stiffness and density (Nton and Salami, 2016, Xu *et al.*, 2016). However, the response of compressional wave velocity (V_p) varies within the reservoirs (Fig.4.29 – 4.30) as the water saturation increases due to fluid replacement. It was observed that the compressional wave velocity, V_p increases steadily during production in the reservoirs A and B of well A2 (Fig.4.29 and Tables 4.8 and 4.9). But, in reservoirs A and D of well A1 (Fig.4.29 and Tables 4.6 and 4.7), compressional wave velocity, V_p decreases exponentially as the volume of water in the reservoir rises and suddenly increases again at about 85% to 100% water saturation. Similar trends were observed in the reservoir D of well A2 (Fig.4.29 and Table 4.10) and reservoirs A and D of well A3 (Fig.4.30 and Table 4.11 - 4.12) respectively.

According to Fertl, (1981), conventionally, velocity of compressional wave, V_p is expected to increase with increase in water saturation (S_w) due to density (ρ) increase as observed in reservoirs A and B of well A2 (Fig.4.29). Also, among the reservoir fluids, water or brine attenuates seismic P-wave the least (Han and Batzle, 2004). Hence in a conventional scenario, P-wave will increase as water gradually replaces brine in the reservoir as shown in reservoirs A and B of well A2 (Fig.4.29). Therefore, the responses of compressional wave velocity (V_p), observed in the reservoirs A and D of well A1 (Fig.4.29), reservoir D of well A2 (Fig.4.29) and reservoirs A and D of well A3 (Fig.4.30) were unconventional and anomalous (Fertl, 1981, Han and Batzle, 2004). The prominent factor that leads to unconventional decrease of P-wave velocity of a reservoir with increasing water saturation is the effects of dissolved gas in the fluid (Han and Batzle, 2004, Kumar, 2006).

According to Mavko *et al.*, (1998), a significant amount of gas mixed into the fluid increases the compressibility of the rock without affecting its bulk modulus. Also, presence of dissolved gas causes unusually high attenuation of P-wave in the brine-gas mixed medium (Batzle and Wang, 1992). Hence, the compressional wave attenuation in the affected reservoirs (A and D of well A1, D of well A2 and A and D of well A3) was attributed to gaseous hydrocarbon (Table 4.5). Therefore, significant amount of gas mixed with the reservoir fluid is the potential cause of anomalous decrease of V_p in the reservoirs as the water saturation increases. However, as the water saturation exceeds 80%, the gas effect becomes very insignificant as V_p increases rapidly towards 100% S_w .

The V_s value reduces as S_w increases from the initial values to 100% saturations in all the reservoirs during production (Fig.4.30- 4.31). According to Han and Batzle, (2004), shear waves do not propagate through liquids but they are only affected by the rock matrix. In the reservoir, the compressional velocity, V_p is attenuated by compressive fluids (gas) while the V_s is influenced by the reservoir rock matrix (Toksoz *et al.*, 1976). In this study, shear wave velocity decreases because among the various reservoir fluids, water supports shearing the least. Therefore, as water gradually replaces hydrocarbon in the reservoirs, the shearing ability of the rock decreases, this will result to reduction in shear wave velocity.

4.6.1.2 The Responses of The Reservoir's Mechanical Properties to Fluid Replacement

Han and Batzle, (2004) reported that V_p and V_s are not the best alone to indicate fluid saturation effect because they are both related to shear modulus and bulk density. Therefore, the effect of fluid saturation should be correlated with bulk modulus' change because bulk modulus is more sensitive to saturation. Therefore, the elastic parameters such as bulk modulus (K), young modulus (E), shear modulus (G), poisson ratio (ν) and unconfined compressive strength (UCS) (Tables 4.6 – 4.12) of the reservoirs were computed for each value of water saturation so that the variation effects of saturation on the reservoir properties can be determined.

4.6.1.2.1 The Young Modulus, E

Generally, the value of young modulus, E increases in all the reservoirs of the field as the volume of water increases during production (Fig.4.32 and plot 1 of Fig.4.33). But this value varies in different reservoirs according to their various fluid composition. In reservoirs A and D of well A1 (Fig.4.32), young modulus marginally rises as water volume increases in the reservoirs until 80% water saturations when there was a sudden jump to 100% water saturation. This was due to the dissolved gases in the brine and oil in reservoirs A and D respectively and immediately after the expulsion of hydrocarbon from both reservoirs, the value of E increases due to the increase in the volume of brine to 100%.

Similarly, in reservoir D of well A2 (Fig.4.32) and reservoirs A and D of well A3 (Fig.4.32 and plot 1 of Fig.4.33), the trend is the same. The gradual and marginal increase in the young modulus values till 80% water saturation could be attributed to dissolved gasses in hydrocarbon as the water saturation increases, then the sudden jump in value to 100% water saturation was due to complete hydrocarbon expulsion from the reservoirs. But in reservoirs A and B of well A2 (Fig.4.32), the trend is different. The value of young modulus, E increases exponentially with water saturation values. This is due to the presence of only oil in the reservoirs. The implication for this exponential increase in young modulus (E) against increasing water saturation is that, the resistance to deformation increases as the water volume rises in the reservoirs during production.

Lawson-Jack *et al.*, (2019), stated that E is defined as the reservoir's ability to resist deformation. Hence, water saturation increase in all the reservoirs of the field during production as fluid replacement takes place in the reservoirs may not have a significant adverse effects on the reservoirs stability, particularly, reservoirs A and B of well A2. Although, in other reservoirs where compressive fluid is found may alter the stiffness of the reservoirs which in turns may increase the chances of deformation.

4.6.1.2.2 The Bulk Modulus, K

According to Yu and Smith, (2011), if the bulk modulus, K is very big, that means the reservoir rock is also very stiff and it will not compress so much even under high pressure. They further stated that, the value of K in gases are very small, but it is higher in solids and liquids. In this study, as the volume of water increases in all the reservoirs across the three wells of the field, the value of bulk modulus, K varies in magnitude in all the reservoirs depending on the reservoir fluid (Fig.4.33 – 4.34 and Table 4.5). In reservoir A of well A1 (Fig.4.33), the value of bulk modulus marginally increases or almost steady as water volume increases during production until around 85% to 100% water saturation when a significant jump occurred.

The marginal increase was attributed to gas presence (gas-water interface) that reduces the stiffness of the reservoir and the sudden jump from 85% to 100% water saturation occurred due to complete expulsion of all hydrocarbon from the reservoir. Also, in reservoir D of well A1 (Fig.4.33), as water inflow increases into the reservoir, the bulk modulus value increases marginally (gas-oil interface) until a sudden rise in value occurred at 81% water saturation when all hydrocarbon have been expelled from the reservoir. The observed higher magnitude of increase in reservoir D compared to reservoir A in the same well was due to different reservoir fluid. According to Yu and Smith, (2011), the value of bulk modulus values in gases are very small, while values in solids and liquids are higher.

In reservoirs A and B of well A2, as water volume increases during production, there is a corresponding increase in value of bulk modulus of the reservoir rock (Fig.4.33). This trend occurred because the reservoirs are saturated with only oil such that as the denser brine gradually replaces less dense oil in the reservoir, the bulk modulus value increases. But in

reservoir D of well A2 (Fig.4.33), as water volume increases, the bulk modulus value has no significant rise until 81% when a little rise occurred till 100%. The lack of noticeable change in bulk modulus implied the presence of compressible fluid (gaseous hydrocarbon) in the reservoir which reduces the K and ρ of the reservoir rock. It should be noted that the compressibility is an inverse of bulk modulus (Smith *et al.*, 2003).

Also, in reservoir A of well A3 (Fig.4.34), the value of bulk modulus became steady during production without significant increase as the water volume rises in the reservoir, but there was a sudden rise in bulk modulus value at 84% to 100 % water saturation when all hydrocarbon (gas-water interface) has been expelled from the reservoir. Similar trend was observed in the reservoir D of well A3 (Fig.4.34). In this reservoir, the increase in water saturation during production has no significant effect on bulk modulus until 83% to 100 %, when an increase was observed as all gaseous hydrocarbon (gas-water interface) was expelled from the reservoir.

Therefore, the observed marginal increase or constant and relatively stable value of bulk modulus at the initial stage of the production in some reservoirs was attributed to dissolved gases that cause a drop in the density of the fluid and subsequently caused a reduction in bulk modulus. The sudden increase was caused by an increase in water volume due to fluid replacement (brine replaced hydrocarbon) within the reservoirs. The dissolution of gases in the oil reduces the density and subsequently reduces the bulk modulus while dissolution of gases in the brine or water has no significant effects on the value of K due to the uniqueness of water's molecular structure. Little amount of gas can be dissolved in water.

4.6.1.2.3 The Shear Modulus, G

Generally, as the volume of water increases in the reservoirs, the value of shear modulus, G does not have a definite trend (Fig.4.34 - 4.35 and Table 4.6 - 4.12). This behaviour of the shear modulus values could be attributed to the inhomogeneity and anisotropy condition of the reservoirs. This condition could be due to reservoir pressure, sorting and volume of clay within the reservoirs. Also, according to Li *et al.*, (2017) G is sensitive to clay content and differential pressure.

Although, Smith *et al.*, (2003) believed that G is not affected by reservoir fluid properties. The saturated bulk modulus, K of a rock is sensitive to the pore fluid composition while G is not ($G_{dry} = G_{wet}$) (Biot, 1956; Berryman and Milton, 1991). The Gassmann's theory suggested that G will not be affected under different saturations. However, G does not have a definite trend due to fluid saturations in this study. This view is also validated by other authors like Clark *et al.*, (1984) and others. The variation of G with fluids was studied and documented by Khazanehdari and Sothcott, (2003) for rock-fluid interactions study.

It was observed in all the reservoirs that G does not have a definite pattern but sensitive to brine. The sudden increase in the value of shear modulus, G was noticed in the pure brine after the expulsion of the hydrocarbon from the reservoir. Conversely, there was a decrease in the value of shear modulus, G as brine or water gradually replaces hydrocarbon during the early production stage in the reservoirs. In reservoir A of well A1 (Fig.4.34 and Table 4.6), the value of shear modulus, G decreases as S_w value increase to 50% from 43% until shear modulus, G reached the maximum value of 7.420674 GPa before a decrease at 100% water saturation. Also, in reservoir D of well A1, the value of shear modulus, G alternate within the reservoir from the initial value of 13.81004 GPa at water saturation of 30.9% to the highest point of 13.81012 GPa at 100% saturation (Fig 4.34 and Table 4.7).

The same alternation and lack of definite trend were observed in all other reservoirs of the field (Fig.4.34-4.35 and Table 4.8- 4.12). According to Adam *et al.*, (2006), weakening of G occurred when brine or water replaces a nonpolar fluid such as oil. The reduction of shear modulus, G immediately the water saturation increases in all the reservoirs was due to shear modulus weakning. The injection of brine of different temperature and salinity into a reservoir for enhance production will probably alter the framework, resulting into variation in the rock moduli.

4.6.1.2.4 The Unconfined Compressive Strength (UCS)

The UCS values in all the reservoirs of the study field (Fig 4.35 – 4.36). According to Chang *et al.*, (2006), the UCS of a rock depends on the elastic modulus, that is, the greater the rock strength, the bigger the elastic modulus of the material. In all the reservoirs with dissolved gasses such as reservoirs A and D of well A1(Fig.4.35), reservoir D of well A2 (Fig.4.36)

and reservoirs A and D in well A3 (Fig.4.36), the UCS value is not significant until after the expulsion of hydrocarbon where the brine has replaced hydrocarbon fluid with increased volume within the reservoirs.

In reservoir A of well A1, as the water saturation increases, the value of UCS increases from 78.30 MPa to 81.78 MPa, at 43% and 100% water saturation respectively. Also in reservoir B of well A1, the value of UCS increased from 138.86 MPa to 142.85 MPa, at 30.9% and 100% S_w respectively. In reservoirs A and B of well A2, the value of UCS increase exponentially with increasing water saturation, from the initial value of 90.20 GPa at 49.51% water saturation to 91.13 GPa at 100% water saturation in reservoir A (Table 4.8) and from the initial value of 76.61 MPa at 46.68% water saturation to 77.70 MPa at 100% water saturation in reservoir B (Table 4.9). In reservoir C of well A2, the value of UCS in the reservoir increases with increasing water saturation, S_w from the initial value of 114.02 MPa at 42.12% water saturation to 118.35 MPa at 100% water saturation (Fig.4.36 and Table 4.10). The UCS in the reservoir A of well A3 increases with increasing water saturation, S_w from the initial value of 78.82 MPa at 47.88% water saturation to 82.62 MPa at 100% water saturation (Fig.4.36 and Table 4.11).

In reservoir D of well A3, the value increases with increasing water volume, from the initial value of 130.45 MPa at 33.68% S_w to 134.33 MPa at 100% S_w (Fig.4.36 and Table 4.12). The exponential increase in UCS values in reservoirs A and B of well A2 was due to the fluid composition (oil). The increase in UCS in these two reservoirs imply an increase in mechanical and well-bored stability. This supported the view of Moos *et al.*, (2003), that increase in UCS means increase in reservoir mechanical and well-bore stability. Also, it was observed that the value of UCS increases with density in all the reservoirs of the three wells (Fig.4.36 – 4.37). The UCS reduces with the porosity (ϕ), increases with the density (ρ) of the reservoir and its magnitude increases as the depth increases.

This also supported the findings of Xu *et al.*, (2016). The increasing trend with depth was observed in all the lower reservoirs B, C and D (Table 4.6 – 4.12) of the three wells of the study field. The magnitude increases from reservoir A to D in each well. In reservoir A of well A1 (Table 4.6 and Fig.4.36), the UCS increases with density, from the initial value of 78.30 MPa at 2.33g/cm³ to the final value of 81.78 MPa at 2.46g/cm³ respectively. In

reservoir D of well A1 (Table 4.7 and Fig.4.36), the UCS increased from 138.86 MPa to 142.85 MPa when the rock density increased from 2.43 g/cm³ at 30.9% water saturation, to 2.54 g/cm³ at 100% water saturation. The value of UCS in reservoir A of well A2 (Table 4.8) increased from 90.20 MPa to 91.13 MPa when the reservoir rock density increased from 2.41 g/cm³ at 49.51 % water saturation to 2.45 g/cm³ at 100 % water saturation. In reservoir B of well A2 (Table 4.9), as water saturation increased from the initial value of 46.68 % to 100 %, the value of UCS increased from 76.61 MPa to 77.70 MPa as the reservoir rock density changed from 2.30 g/cm³ to 2.34 g/cm³.

Also, an increase in value of UCS from 114.02 MPa to 118.35 MPa was observed as the rock density increased from 2.50 g/cm³ to 2.60 g/cm³ when Sw increased to 100 % from 42.12 % in the reservoir D of well A2 (Table 4.10 and Fig.4.37). In reservoir A of well A3 (Table 4.11 and Fig.4.37), the UCS of the reservoir increased with density from 78.82 MPa at 2.24 g/cm³ to 82.62 MPa at 2.36 g/cm³ as the water volume increased from 47.88 % to 100%. Similarly, in reservoir D of well A3 (Table 4.12 and Fig.4.37), the UCS increased from 130.45 MPa to 134.33 MPa as the rock density increased to 2.48 g/cm³ from 2.35 g/cm³ when the water saturation rises from the initial value of 33.68 % to 100 %. The UCS is an important property that is useful to solve many geomechanical challenges such as instability in the wellbore during drilling, sand potential estimation and constraining stress magnitudes using wellbore failure observation (Santarelli *et al.*, 1989; Moos *et al.*, 2003; Zoback *et al.*, 2003).

4.6.1.2.5 Poisson Ratio, ν

It has a theoretical maximum value of 0.5 (Lawson – Jack *et al.*, 2019). In Tetemu field, the value of ν reduces or almost constant in gas sand and increases in oil sand and brine (Fig.4.37- 4.38 and Table 4.6 – 4.12). Generally, there was a vertical variation in the values of ν in all the wells before forward modeling (static condition). In well A1, the values were ≈ 0.25 in reservoir A and ≈ 0.21 in reservoir D. Also in well A2, ν is approximately 0.29, 0.30 and 0.22 in A, B and D reservoirs respectively. In well A3. The value of ν were approximately 0.24 and 0.21 in the reservoirs A and D respectively. But across the wells, the variation was not significant in values. From reservoir A, the calculated values across

the three wells were approximately 0.25, 0.29 and 0.24 in A1, A2 and A3 respectively. In reservoir D, 0.21, 0.22 and 0.21 were recorded in well A1, A2 and A3 respectively.

The vertical variation could be attributed to lithological changes, decreasing porosity with depth, clay content, fluid saturation, anisotropy and vertical heterogeneity. The above also supported the view of the following authors; (Pickering, 1970; Salem, 1993; Tiab and Donaldson, 1996; Salem, 2000; and Dvorkin *et. al.*, 2001). The modeling results showed that increasing water saturation lead to increase in poisson's ratio (ν) values during production in all the reservoirs (Table 4.6 - 4.12). Although, the magnitude of increase differs in all the reservoirs.

The value of ν , increases marginally in gas sand such that the magnitude is insignificant as observed in the reservoirs A of well A1 (Fig.4.37), reservoir D of well A2 (Fig.4.38) and reservoirs A and D of well A3 (Fig.4.38) until above 80% water saturation. The initial marginal increase was due to the attenuation of poisson's ratio by gaseous hydrocarbon, while the sudden increase after 80% was the effect of fluid replacement, as brine replaced hydrocarbon in the reservoir after the expulsion of gaseous hydrocarbon during the fluid substitution until 100% water saturation. Hence, gas saturation attenuates the poisson's ratio in the reservoir (Moos, 2006).

But in oil sand and brine, the magnitude of poisson's ratio is much larger and significant than in gas sand. According to Dvorkin *et. al.*, (2001), poisson's ratio is inverse of compressibility. In reservoir D of well A1 (Fig.4.38), there was a gradual increase in the value of ν , as water saturation increases until 70.90%, the magnitude suddenly jumped up because all the hydrocarbon in the reservoir has been produced and replaced with water in the reservoir. Also, in reservoir A of well A2 (Fig.4.38), the relationship between the two variables is linear because the value of ν , increases with the corresponding increase in S_w until all the hydrocarbon is expelled from the reservoir at 100% water saturation.

The same scenario was observed in the reservoir B of well A2 (Fig.4.38). Also, the value of ν , increases with the water saturation, S_w during production until there was complete fluid substitution. Generally, during oil and gas production in the field, fluid substitution occurs such that ν increases as brine replaces gas or oil in the reservoirs. Also, the reservoir gas

attenuates the poisson's ratio values until all the gaseous hydrocarbon are completely expelled from the reservoirs.

4.6.3 Increasing Gas Saturation (Enhanced Recovery)

An enhanced production scenario of increasing gas saturation was modeled for the selected reservoirs, those without gas saturation (reservoir C of well A1, A, B and C of well A2 and B and C of well A3) by increasing the value of gas saturation from 0% up to 80% while other factors were kept constant. The output seismic response of each reservoir was recorded in terms of ρ , V_p and V_s for each value of gas saturation, from which other elastic and geo-mechanical parameters were computed. The calculated results of the elastic and geo-mechanical parameters were summarized in Table 4.13 - 4.18 and presented graphically in Figures 4.39-4.46. The computed P and S- waves impedences, poisson ratio and velocity ratio of the field reservoirs are shown in Table 4.19- 4.24.

4.6.3.1 The Impact of Higher Gas Saturation on The Seismic Characteristics of Reservoirs.

The results revealed that increasing gas saturation affects each reservoir in a common way. In general, there is a steady decrease in density (Fig.4.39) in all the reservoirs due to gradual rise in the volume of gas. The steady drop in ρ was due to the conventional decrease in the rigidity and K of the rock when a denser reservoir fluid such as oil or brine is replaced by a less dense gas (Smith *et al.*, 2003). Increasing gas saturation reduces the stiffness of the rock, hence its density. Also, it was observed that, as gas saturation increases in the reservoirs, the value of shear wave velocity (V_s) increases (Fig.4.40). Shear wave velocity increases because among the various reservoir fluids, gas supports shearing the most (Berryman, 1999). According to Smith *et al.*, (2003), the shear velocity is greater in gas sand than in brine sand. Therefore, as gas gradually replaces hydrocarbon or water, the shearing ability of the rock is enhanced; this will result to increase in shear wave velocity.

Table 4.13: The Enhanced Operation Responses, Calculated Elastic and Geomechanical Parameters of Reservoir C of Well A1 of The Study Field.

Sg(%)	Tc(μs/ft)	Ts(μs/ft)	Vp(km/s)	Vs(km/s)	ρ(g/cc)	Z	Zs	G(GPa)	K(Gpa)	Cb(1/K)	E (Gpa)	UCS(Mpa)
0	85.561	150.877	3.562	2.020	2.451	8.730	4.951	10.002	17.765	0.056	25.264	105.862
10	87.909	150.479	3.467	2.026	2.438	8.452	4.938	10.002	15.971	0.063	24.823	104.056
20	87.908	150.081	3.467	2.031	2.425	8.408	4.925	10.002	15.817	0.063	24.782	103.884
30	87.761	149.682	3.473	2.036	2.412	8.377	4.912	10.002	15.759	0.063	24.766	103.820
40	87.571	149.281	3.481	2.042	2.399	8.350	4.899	10.002	15.729	0.064	24.758	103.787
50	87.363	148.880	3.489	2.047	2.386	8.325	4.885	10.002	15.711	0.064	24.752	103.765
60	87.146	148.477	3.498	2.053	2.373	8.301	4.872	10.002	15.698	0.064	24.749	103.751
70	86.922	148.073	3.507	2.058	2.360	8.277	4.859	10.002	15.689	0.064	24.747	103.741

Where:

Sg (%) = Gas saturation

Tc (μs/ft) = Compressional wave transit time

Ts (μs/ft) = Shear wave transit time

ρ (g/cm³) = Rock density

Vs and Vp represent the velocities of shear and compressional waves respectively in (km/s)

Z (Pa. s/ m³) = Acoustic impedance (P-wave impedance)

Zs (Pa. s/ m³) = S-wave impedance

G (GPa) = Shear modulus

K and E represent Bulk and Young moduli respectively, measured in (GPa)

Cb (GPa⁻¹) = Bulk compressibility, which is (1/K)

UCS (MPa) = Unconfined Compressive Strength

Table 4.14: The Modeling Responses (EOR), Calculated Elastic and Geomechanical Parameters of Reservoir A of Well A2 of The Study Wells.

Sg(%)	Tc(μs/ft)	Ts(μs/ft)	Vp(km/s)	Vs(km/s)	ρ(g/cc)	Z	Zs	G(GPa)	K(Gpa)	Cb(1/K)	E (Gpa)	UCS(Mpa)
0	89.356	163.983	3.411	1.859	2.408	8.214	4.476	8.319	16.926	0.059	21.445	90.203
10	91.972	162.740	3.314	1.873	2.400	7.955	4.496	8.420	15.136	0.066	21.309	89.647
20	91.903	162.195	3.317	1.879	2.384	7.908	4.481	8.420	14.999	0.067	21.278	89.522
30	91.681	161.648	3.325	1.886	2.368	7.873	4.466	8.420	14.949	0.067	21.267	89.476
40	91.416	161.099	3.334	1.892	2.352	7.843	4.450	8.420	14.923	0.067	21.261	89.452
50	91.131	160.549	3.345	1.898	2.336	7.814	4.435	8.420	14.907	0.067	21.258	89.437

Where:

Sg (%) = Gas saturation

Tc (μs/ft) = Compressional wave transit time

Ts (μs/ft) = Shear wave transit time

ρ (g/cm³) = Rock density

Vs and Vp represent the velocities of shear and compressional waves respectively in (km/s)

Z (Pa. s/ m³) = Acoustic impedance (P-wave impedance)

Zs (Pa. s/ m³) = S-wave impedance

G (GPa) = Shear modulus

K and E represent Bulk and Young moduli respectively, measured in (GPa)

Cb (GPa⁻¹) = Bulk compressibility, which is (1/K)

UCS (MPa) = Unconfined Compressive Strength

EOR = Enhanced oil recovery

Table 4.15: The Modeling Responses (EOR), Calculated Elastic and Geomechanical Parameters of Reservoir B of Well A2 of The Study Field.

Sg(%)	Tc(μs/ft)	Ts(μs/ft)	Vp(km/s)	Vs(km/s)	ρ(g/cc)	Z	Zs	G(GPa)	K(Gpa)	Cb(1/K)	E (Gpa)	UCS(Mpa)
0	94.157	174.642	3.237	1.745	2.298	7.439	4.010	6.999	14.747	0.068	18.130	76.613
10	98.573	174.055	3.092	1.751	2.282	7.058	3.997	6.999	12.491	0.080	17.693	74.823
20	98.634	173.467	3.090	1.757	2.267	7.006	3.983	6.999	12.317	0.081	17.654	74.661
30	98.443	172.875	3.096	1.763	2.252	6.972	3.970	6.999	12.253	0.082	17.639	74.602
40	98.181	172.282	3.104	1.769	2.236	6.942	3.956	6.999	12.220	0.082	17.632	74.570
50	97.888	171.686	3.114	1.775	2.221	6.915	3.943	6.999	12.199	0.082	17.627	74.551

Where:

Sg (%) = Gas saturation

Tc (μs/ft) = Compressional wave transit time

Ts (μs/ft) = Shear wave transit time

ρ (g/cm³) = Rock density

Vs and Vp represent the velocities of shear and compressional waves respectively in (km/s)

Z (Pa. s/ m³) = Acoustic impedance (P-wave impedance)

Zs (Pa. s/ m³) = S-wave impedance

G (GPa) = Shear modulus

K and E represent Bulk and Young moduli respectively, measured in (GPa)

Cb (GPa⁻¹) = Bulk compressibility, which is (1/K)

UCS (MPa) = Unconfined Compressive Strength

Table 4.16: The Enhanced Operation and Calculated Elastic / Geomechanical Parameters of Reservoir C of Well A2 of The Study Field.

Sg(%)	Tc(μs/ft)	Ts(μs/ft)	Vp(km/s)	Vs(km/s)	ρ(g/cc)	Z	Zs	G(GPa)	K(Gpa)	Cb(1/K)	E (Gpa)	UCS(Mpa)
0	94.714	175.572	3.218	1.736	2.473	7.959	4.294	7.454	15.676	0.064	19.303	81.421
10	99.550	175.108	3.062	1.741	2.460	7.533	4.282	7.454	13.125	0.076	18.803	79.371
20	99.712	174.643	3.057	1.745	2.447	7.481	4.271	7.454	12.928	0.077	18.757	79.184
30	99.603	174.176	3.060	1.750	2.434	7.449	4.260	7.454	12.855	0.078	18.740	79.115
40	99.418	173.709	3.066	1.755	2.421	7.423	4.248	7.454	12.818	0.078	18.731	79.078
50	99.200	173.240	3.073	1.759	2.408	7.399	4.237	7.454	12.795	0.078	18.726	79.055

Where:

Sg (%) = Gas saturation

Tc (μs/ft) = Compressional wave transit time

Ts (μs/ft) = Shear wave transit time

ρ (g/cm³) = Rock density

Vs and Vp represent the velocities of shear and compressional waves respectively in (km/s)

Z (Pa. s/ m³) = Acoustic impedance (P-wave impedance)

Zs (Pa. s/ m³) = S-wave impedance

G (GPa) = Shear modulus

K and E represent Bulk and Young moduli respectively, measured in (GPa)

Cb (GPa⁻¹) = Bulk compressibility, which is (1/K)

UCS (MPa) = Unconfined Compressive Strength

Table 4.17: The Enhanced Oil Recovery and Calculated Elastic / Geomechanical Parameters of Reservoir B of Well A3 of The Study Field.

Sg(%)	Tc(μs/ft)	Ts(μs/ft)	Vp(km/s)	Vs(km/s)	ρ(g/cc)	Z	Zs	G(GPa)	K(Gpa)	Cb(1/K)	E (Gpa)	UCS(Mpa)
0	90.195	163.678	3.379	1.862	2.292	7.745	4.268	7.948	15.577	0.064	20.377	85.828
10	92.514	161.342	3.295	1.889	2.275	7.495	4.298	8.119	13.867	0.072	20.379	85.835
20	92.417	162.455	3.298	1.876	2.258	7.446	4.236	7.948	13.962	0.072	20.041	84.447
30	92.161	161.841	3.307	1.883	2.241	7.411	4.220	7.948	13.912	0.072	20.029	84.399
40	91.858	161.224	3.318	1.891	2.224	7.379	4.204	7.948	13.886	0.072	20.023	84.375
50	91.535	160.604	3.330	1.898	2.207	7.348	4.188	7.948	13.870	0.072	20.020	84.360
60	91.201	159.982	3.342	1.905	2.190	7.318	4.172	7.948	13.859	0.072	20.017	84.349
70	90.860	159.358	3.355	1.913	2.173	7.288	4.155	7.948	13.851	0.072	20.015	84.342
80	90.513	158.731	3.367	1.920	2.155	7.258	4.139	7.948	13.845	0.072	20.014	84.336

Where:

Sg (%) = Gas saturation

Tc (μs/ft) = Compressional wave transit time

Ts (μs/ft) = Shear wave transit time

ρ (g/cm³) = Rock density

Vs and Vp represent the velocities of shear and compressional waves respectively in (km/s)

Z (Pa. s/ m³) = Acoustic impedance (P-wave impedance)

Zs (Pa. s/ m³) = S-wave impedance

G (GPa) = Shear modulus

K and E represent Bulk and Young moduli respectively, measured in (GPa)

Cb (GPa⁻¹) = Bulk compressibility, which is (1/K)

UCS (MPa) = Unconfined Compressive Strength

Table 4.18: The Enhanced Operation Responses, Calculated Elastic and Geomechanical Parameters of Reservoir C of Well A3 of The Study Field.

Sg(%)	Tc(μs/ft)	Ts(μs/ft)	Vp(km/s)	Vs(km/s)	ρ(g/cc)	Z	Zs	G(GPa)	K(Gpa)	Cb(1/K)	E (Gpa)	UCS(Mpa)
0	84.707	149.729	3.598	2.036	2.519	9.064	5.128	10.439	18.698	0.053	26.404	110.535
10	86.582	149.328	3.520	2.041	2.506	8.821	5.114	10.439	17.133	0.058	26.031	109.006
20	86.536	148.926	3.522	2.047	2.492	8.778	5.101	10.439	16.999	0.059	25.996	108.864
30	86.371	148.522	3.529	2.052	2.479	8.747	5.087	10.439	16.950	0.059	25.983	108.812
40	86.172	148.118	3.537	2.058	2.465	8.720	5.073	10.439	16.924	0.059	25.976	108.783
50	85.958	147.713	3.546	2.063	2.452	8.694	5.059	10.439	16.908	0.059	25.972	108.766
60	85.737	147.306	3.555	2.069	2.438	8.668	5.045	10.439	16.897	0.059	25.969	108.755
70	85.511	146.899	3.564	2.075	2.425	8.643	5.031	10.439	16.889	0.059	25.967	108.746

Where:

Sg (%) = Gas saturation

Tc (μs/ft) = Compressional wave transit time

Ts (μs/ft) = Shear wave transit time

ρ (g/cm³) = Rock density

Vs and Vp represent the velocities of shear and compressional waves respectively in (km/s)

Z (Pa. s/ m³) = Acoustic impedance (P-wave impedance)

Zs (Pa. s/ m³) = S-wave impedance

G (GPa) = Shear modulus

K and E represent Bulk and Young moduli respectively, measured in (GPa)

Cb (GPa⁻¹) = Bulk compressibility, which is (1/K)

UCS (MPa) = Unconfined Compressive Strength

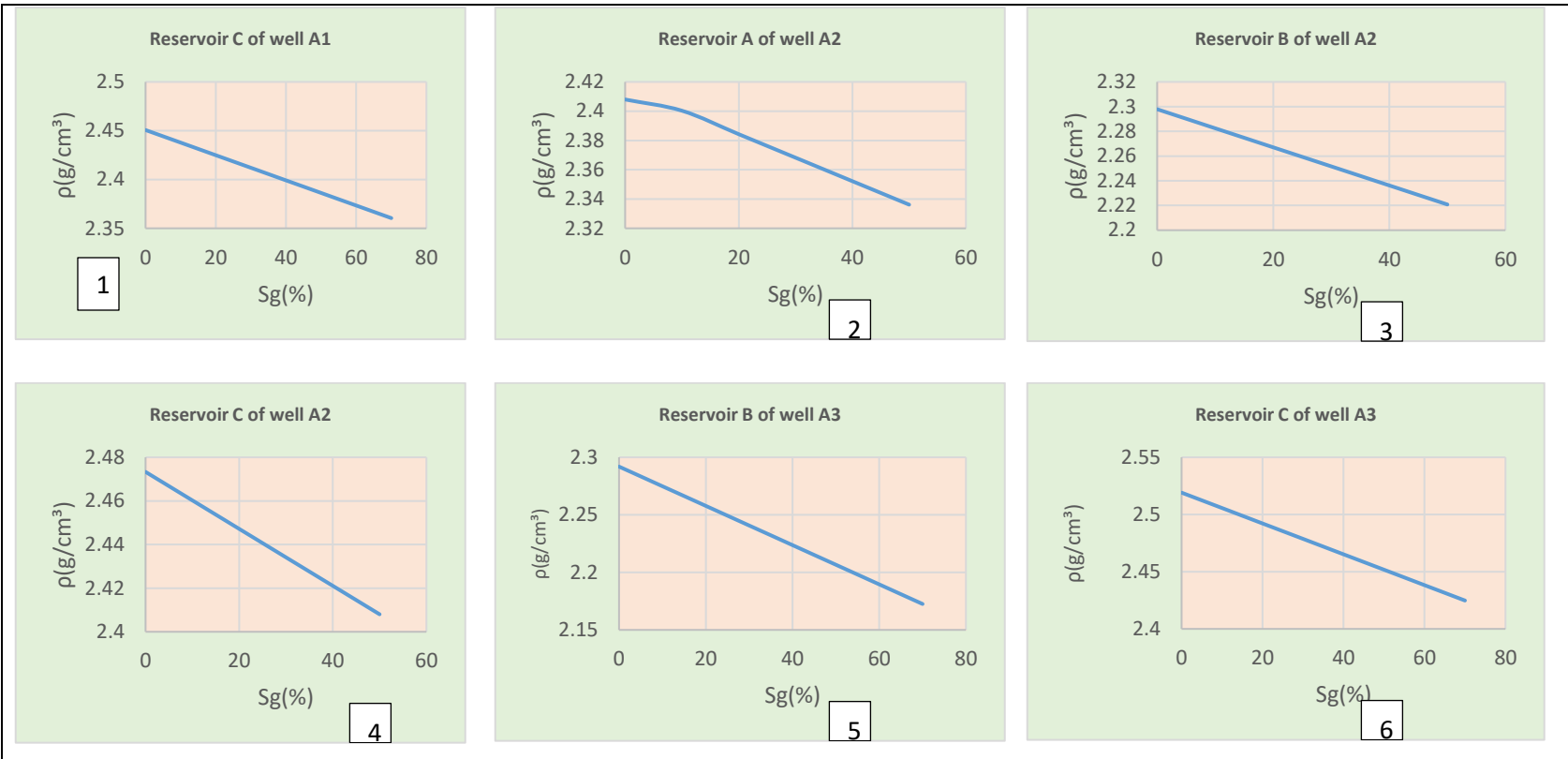


Figure 4.39: The Plots of Reservoirs' Elastic Parameters Behaviours During Enhanced Recovery Operations by Adopting A Forward Modeling Approach As Gas Saturation Increases from 0-80% in The Reservoirs: 1) Showed Gradual Reduction in Density, ρ As Gas Saturation, S_g Increases in Reservoir C of Well A1, Plot 2, 3, 4,5 and 6 Displayed Similar Trend During Hydrocarbon Production.

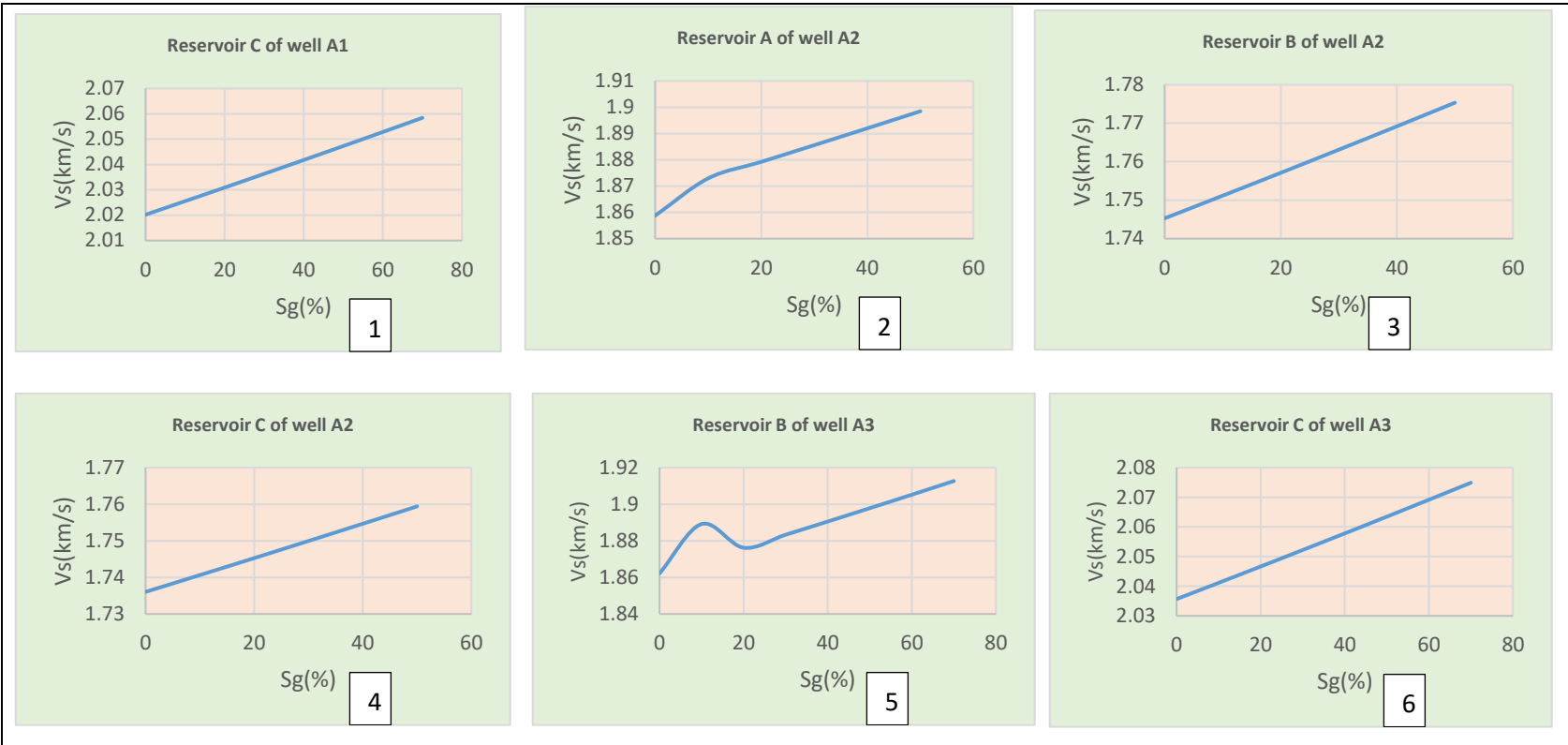


Figure 4.40: The Reservoirs Elastic Parameters, Shear Wave Response to Increasing Gas Saturation, from 0 to 80% During Enhanced Operations by Forward Modeling: Plot 1-6 Showed Gradual Increase in The Value of V_s During Fluid Replacement.

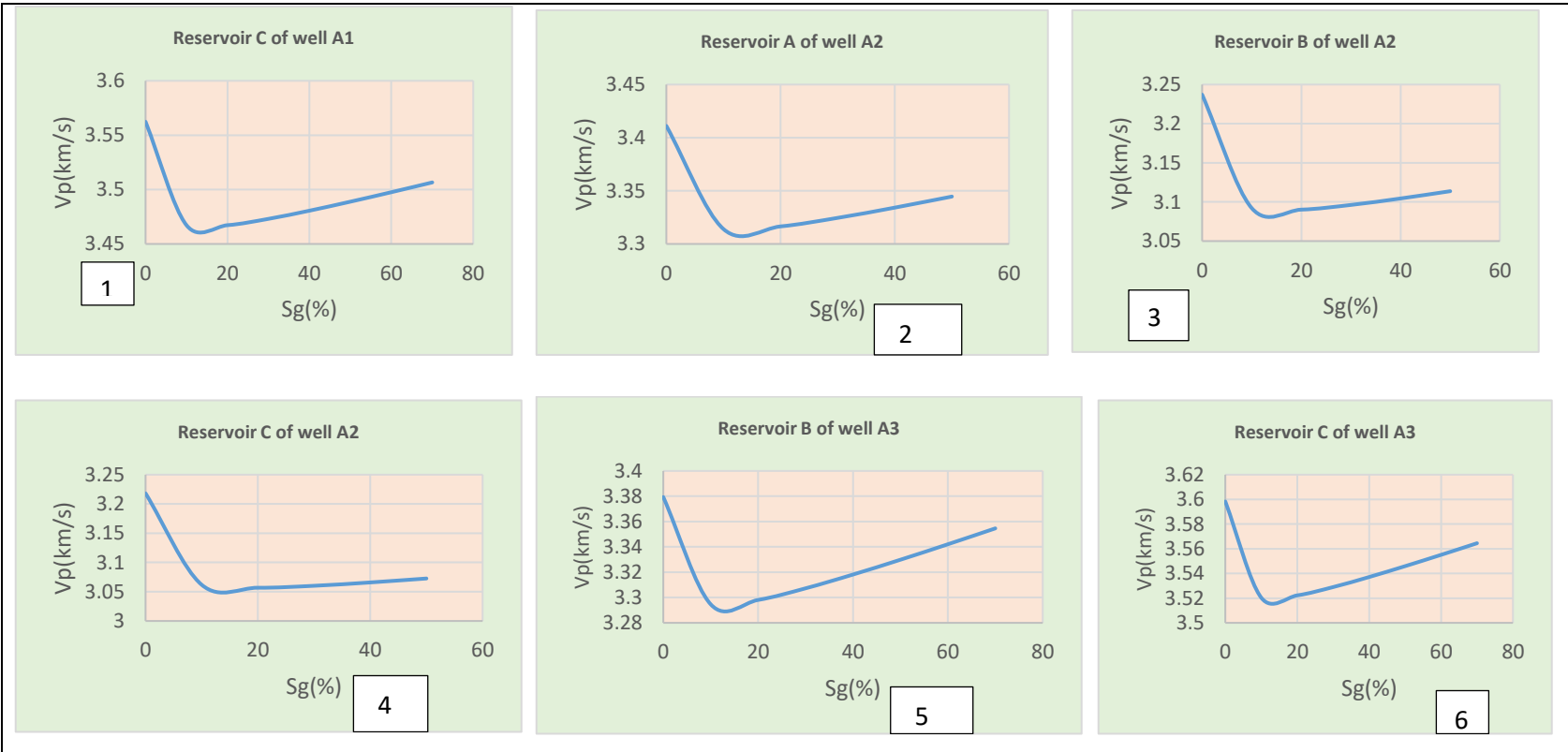


Figure 4.41: Plots 1- 6 Revealed The Reservoir’s Behaviours With Respect to Compressional Waves Velocity, V_p During Oil And Gas Production As S_g Increases from 0 to 80% Using A Forward Modeling Approach.

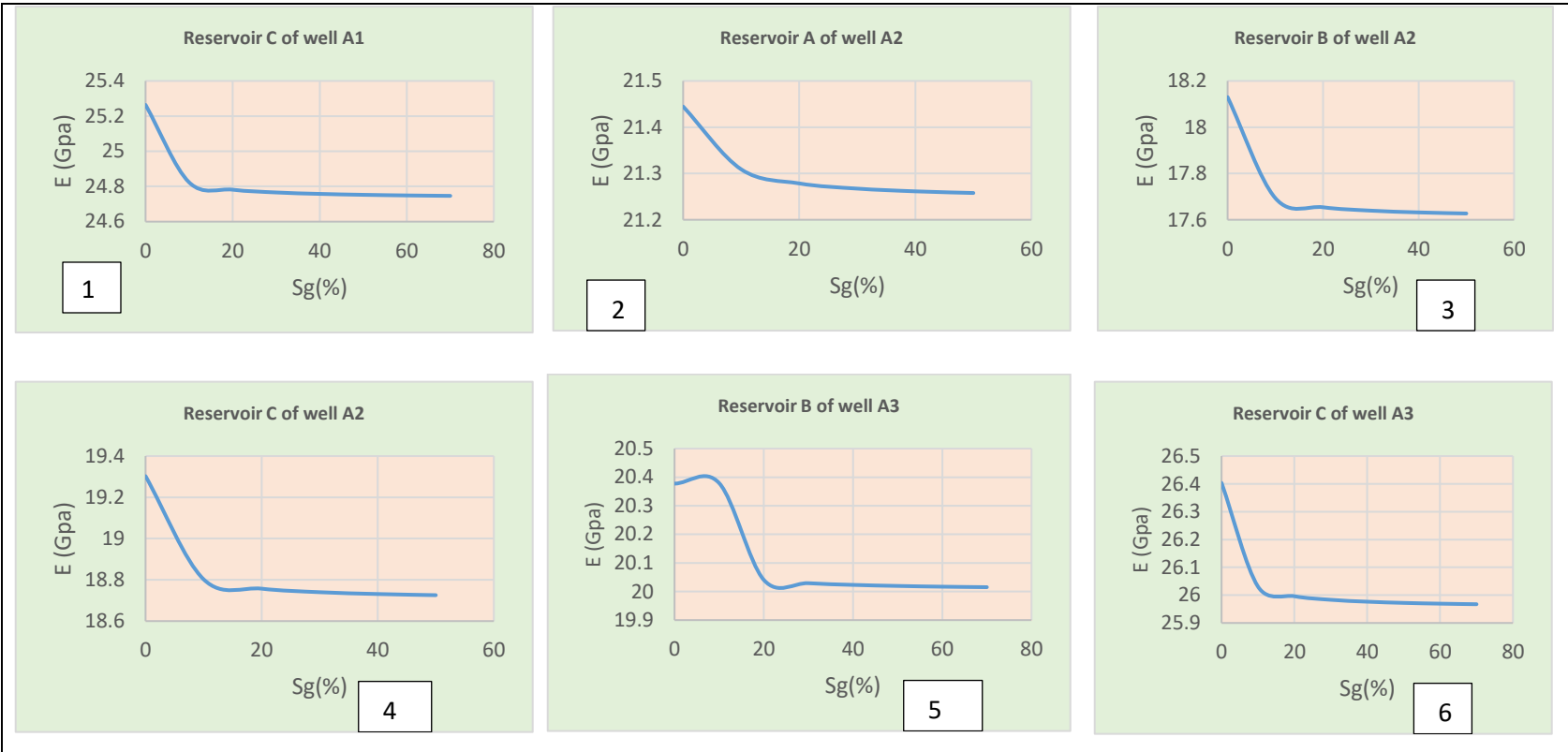


Figure 4.42: The Reservoirs Mechanical Parameters (E) Response to Increasing Sg, from 0 to 80%: Plot 1-6 Showed Responses of Specific Reservoirs During Hydrocarbon Production.

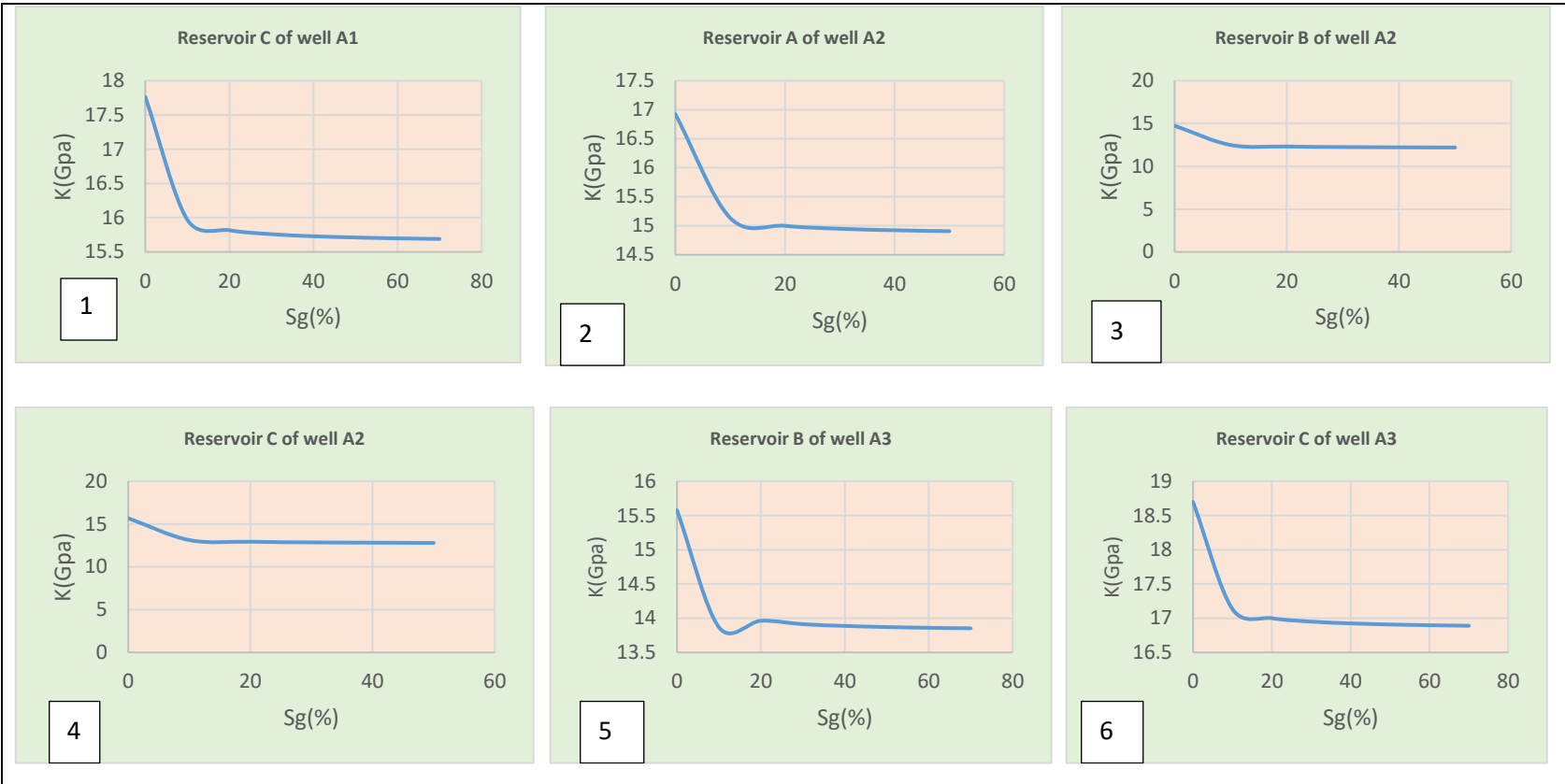


Figure 4.43: The Reservoirs' Bulk Modulus Responses to Increasing Gas Saturation, from 0 to 80% During Enhanced Recovery by Forward Modeling: Plot 1-6 Showed Responses of The Reservoirs During Production.

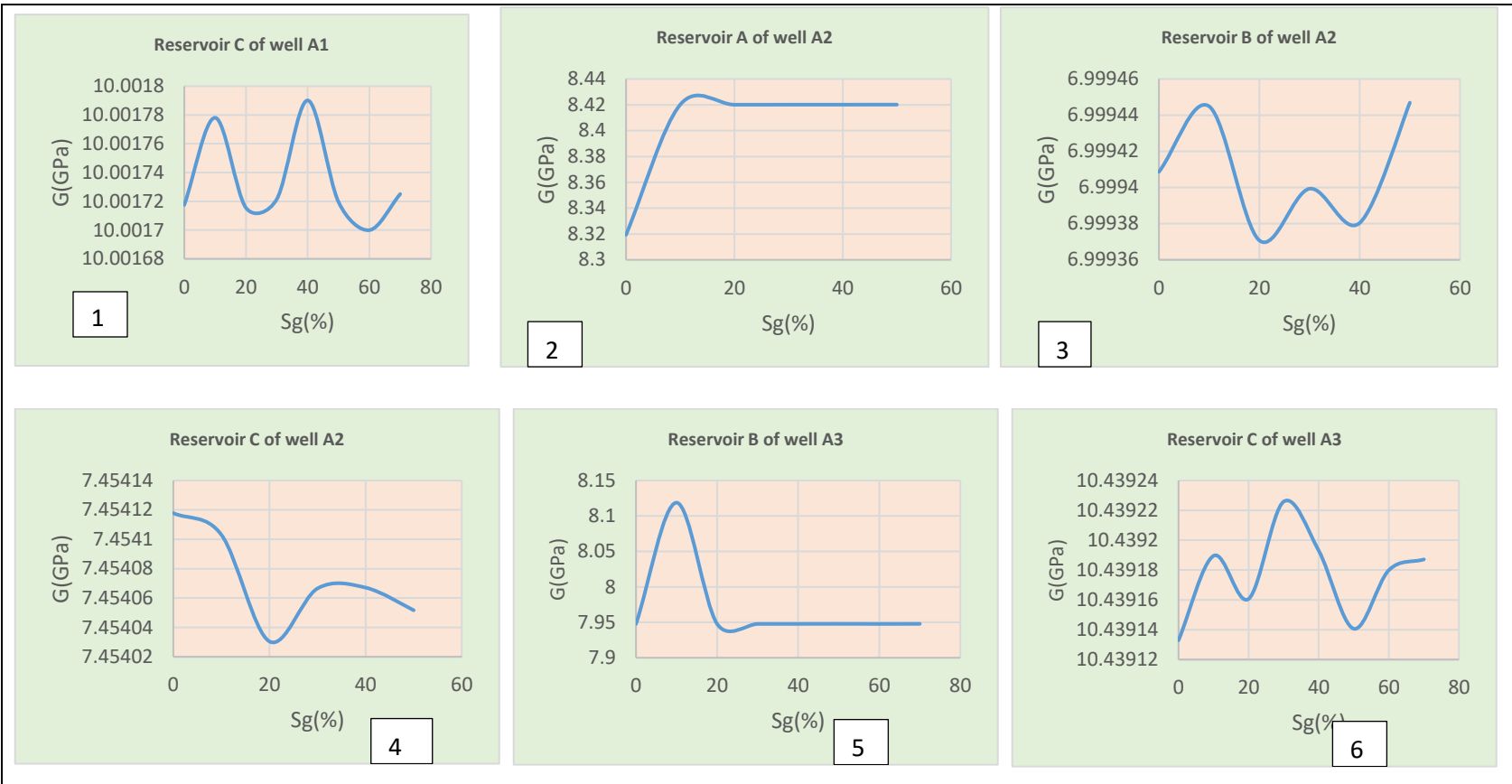


Figure 4.44: The Shear Modulus Behaviours to Increasing Sg from 0 to 80% During Production: Plot 1-6 Showed Responses of Specific Reservoirs.

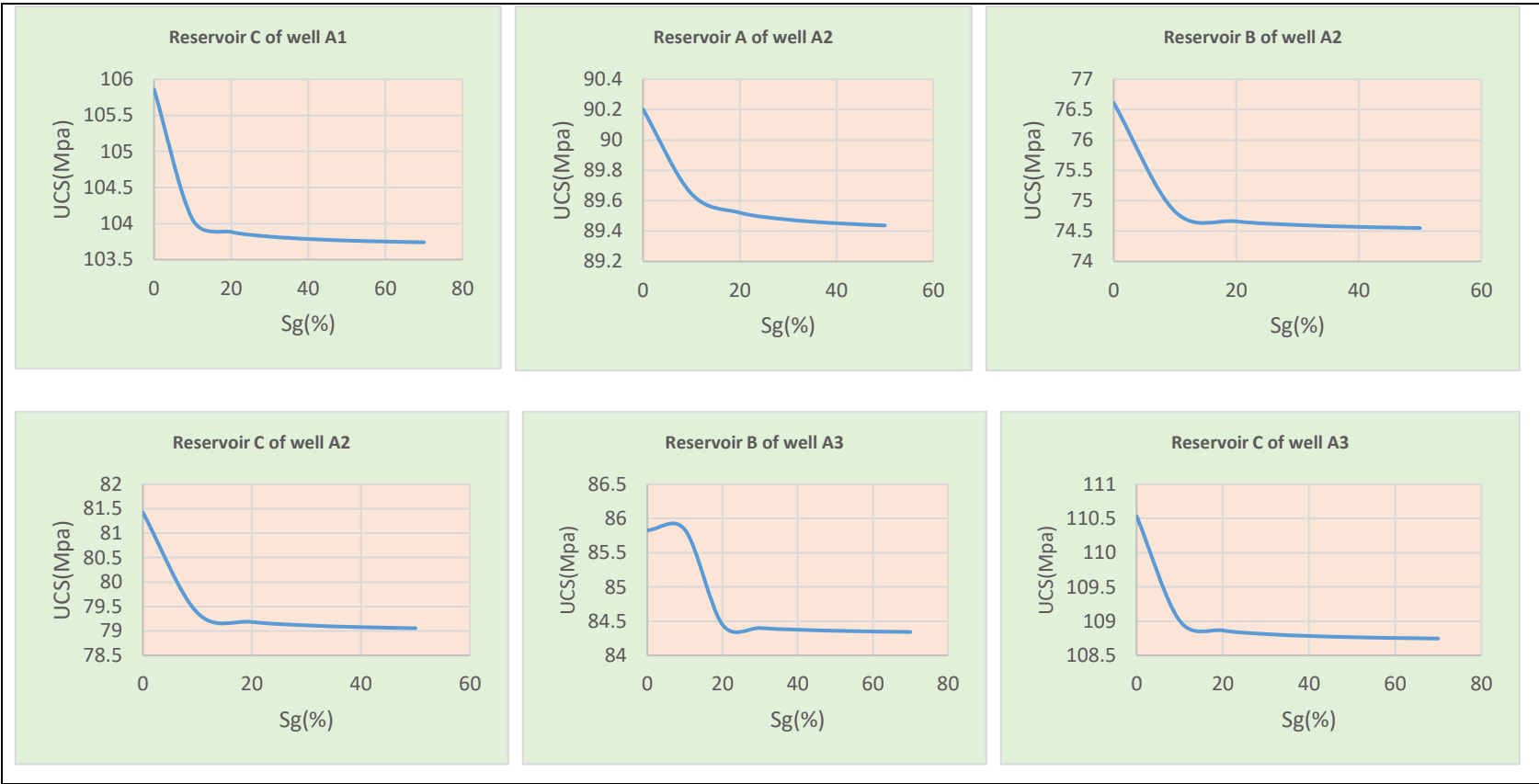


Figure 4.45: The Unconfined Compressive Strength, UCS Response to Increasing Gas Saturation, from 0 to 80% During Enhanced Recovery Operations by Forward Modeling: Plot 1-6 Showed Responses of Specific Reservoirs During Hydrocarbon Production.

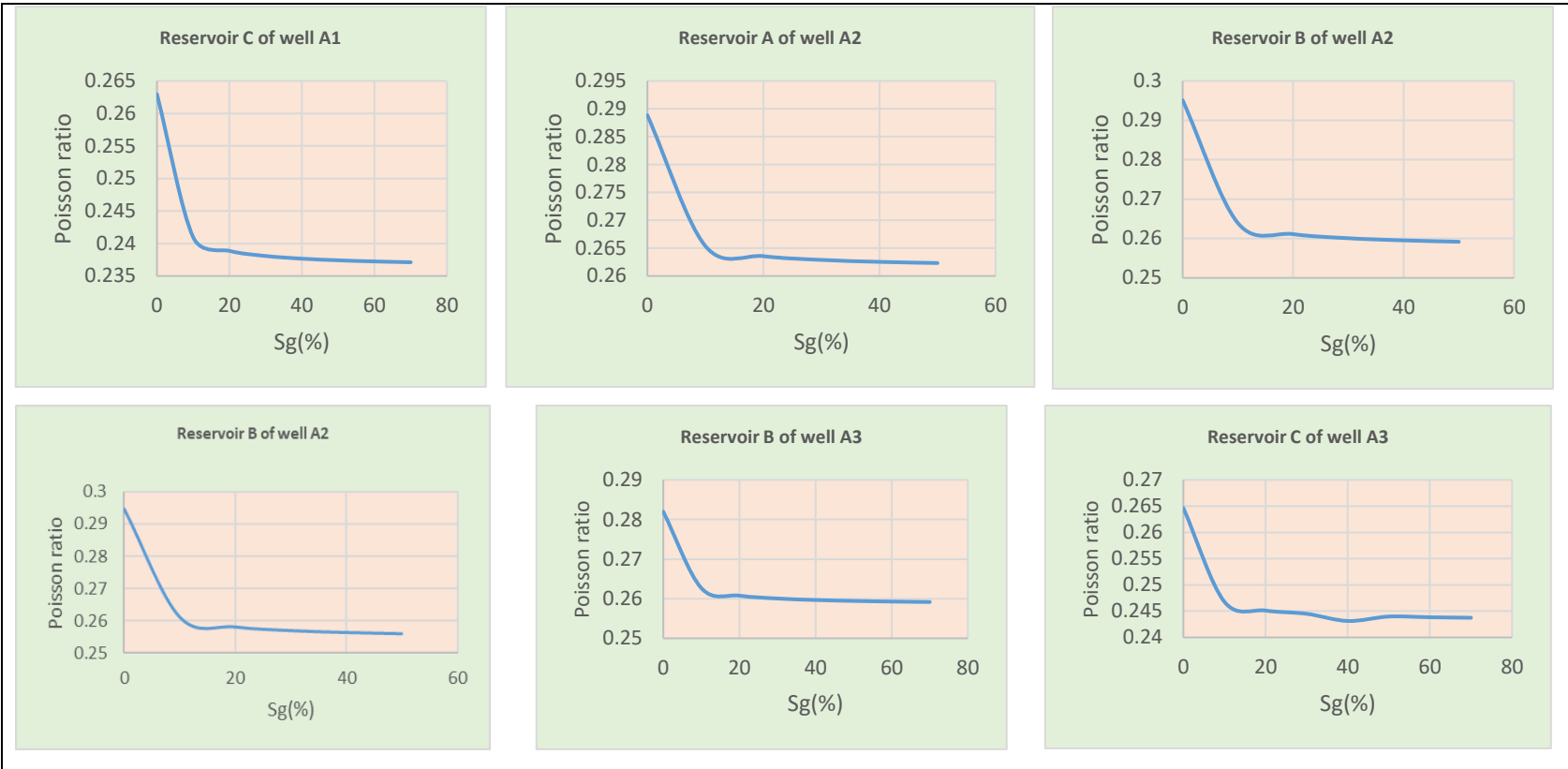


Figure 4.46: The Poisson Ratio Response to Increasing Sg, from 0 to 80% During Production: Plot 1-6 Showed Responses of Specific Reservoirs.

Table 4.19: The Computed P and S- Waves Impedenaces, Poisson Ratio and Velocity Ratio in Reservoir C of Well A1 of The Study Field.

$S_g(\%)$	$T_c(\mu s/ft)$	$T_s(\mu s/ft)$	$V_p(m/s)$	$V_s(m/s)$	$\rho(kg/m^3).10^3$	$\nu(Poisson's)$	$Z(\rho.V_p).10^3$	$Z(\rho.V_s).10^3$	V_p/V_s
0	85.56	150.88	3562.37	2020.19	2.45	0.2630	8730.30	4950.88	1.7634
10	87.91	150.48	3467.23	2025.53	2.44	0.2410	8452.46	4937.86	1.7118
20	87.91	150.08	3467.27	2030.90	2.42	0.2389	8407.85	4924.77	1.7073
30	87.76	149.68	3473.09	2036.32	2.41	0.2381	8377.19	4911.66	1.7056
40	87.57	149.28	3480.60	2041.79	2.40	0.2377	8350.46	4898.54	1.7047
50	87.36	148.88	3488.88	2047.29	2.39	0.2374	8325.35	4885.35	1.7041
60	87.15	148.48	3497.59	2052.84	2.37	0.2372	8301.04	4872.13	1.7038
70	86.92	148.07	3506.58	2058.44	2.36	0.2371	8277.19	4858.89	1.7035

Where:

$S_g(\%)$ = Gas saturation

$T_c(\mu s/ft)$ = Compressional wave transit time

$T_s(\mu s/ft)$ = Shear wave transit time

$\rho(kg/m^3)$ = Rock density

V_s and V_p represent the velocities of shear and compressional waves respectively in (m/s)

$Z(kg.m^{-2}.s^{-1})$ or $(Pa.s/ m^3)$ = Acoustic impedance (P-wave impedance)

$Z_s(kg.m^{-2}.s^{-1})$ or $(Pa.s/ m^3)$ = S-wave impedance

ν = Poisson's ratio (saturated)

Table 4.20: The Computed P and S- Waves Impedenaces, Poisson Ratio and Velocity Ratio in Reservoir A of Well A2 of The Field.

$S_g(\%)$	$T_c(\mu s/ft)$	$T_s(\mu s/ft)$	$V_p(m/s)$	$V_s(m/s)$	$\rho(kg/m^3).10^3$	$\nu(Poisson's)$	$Z(\rho.V_p).10^3$	$Z(\rho.V_s).10^3$	V_p/V_s
0	89.36	163.98	3411.08	1858.73	2.41	0.2888	8213.92	4475.84	1.8352
10	91.97	162.74	3314.04	1872.93	2.40	0.2654	7954.87	4495.69	1.7694
20	91.90	162.19	3316.53	1879.22	2.38	0.2636	7907.60	4480.62	1.7648
30	91.68	161.65	3324.56	1885.58	2.37	0.2629	7873.38	4465.52	1.7631
40	91.42	161.10	3334.21	1892.00	2.35	0.2625	7842.77	4450.38	1.7623
50	91.13	160.55	3344.62	1898.49	2.34	0.2623	7813.57	4435.18	1.7617

Where:

$S_g(\%)$ = Gas saturation

$T_c(\mu s/ft)$ = Compressional wave transit time

$T_s(\mu s/ft)$ = Shear wave transit time

$\rho(kg/m^3)$ = Rock density

V_s and V_p represent the velocities of shear and compressional waves respectively in (m/s)

$Z(kg.m^{-2}.s^{-1})$ or $(Pa.s/ m^3)$ = Acoustic impedance (P-wave impedance)

$Z_s(kg.m^{-2}.s^{-1})$ or $(Pa.s/ m^3)$ = S-wave impedance

ν = Poisson's ratio (saturated)

Table 4.21: Computed P and S- Waves Impedenaces, Poisson Ratio and Velocity Ratio in Reservoir B of Well A2 of The Study Field.

$S_g(\%)$	$T_c(\mu s/ft)$	$T_s(\mu s/ft)$	$V_p(m/s)$	$V_s(m/s)$	$\rho(kg/m^3).10^3$	$\nu(\text{Poisson's})$	$Z(\rho.V_p).10^3$	$Z(\rho.V_s).10^3$	V_p/V_s
0	94.16	174.64	3237.14	1745.28	2.30	0.2951	7438.63	4010.48	1.8548
10	98.57	174.06	3092.12	1751.17	2.28	0.2639	7057.69	3997.01	1.7657
20	98.63	173.47	3090.22	1757.11	2.27	0.2611	7005.69	3983.46	1.7587
30	98.44	172.88	3096.22	1763.12	2.25	0.2601	6971.54	3969.89	1.7561
40	98.18	172.28	3104.48	1769.19	2.24	0.2595	6942.24	3956.26	1.7547
50	97.89	171.69	3113.77	1775.33	2.22	0.2592	6915.00	3942.62	1.7539

Where:

$S_g(\%)$ = Gas saturation

$T_c(\mu s/ft)$ = Compressional wave transit time

$T_s(\mu s/ft)$ = Shear wave transit time

$\rho(kg/m^3)$ = Rock density

V_s and V_p represent the velocities of shear and compressional waves respectively in (m/s)

$Z(kg.m^{-2}.s^{-1})$ or $(Pa.s/ m^3)$ = Acoustic impedance (P-wave impedance)

$Z_s(kg.m^{-2}.s^{-1})$ or $(Pa.s/ m^3)$ = S-wave impedance

ν = Poisson's ratio (saturated)

Table 4.22: Computed P and S- Waves Impedenaces, Poisson Ratio and Velocity Ratio in Reservoir C of Well A2 of The Field.

$S_g(\%)$	$T_c(\mu s/ft)$	$T_s(\mu s/ft)$	$V_p(m/s)$	$V_s(m/s)$	$\rho(kg/m^3).10^3$	$\nu(\text{Poisson's})$	$Z(\rho.V_p).10^3$	$Z(\rho.V_s).10^3$	V_p/V_s
0	94.71	175.57	3218.13	1736.04	2.47	0.2948	7959.39	4293.75	1.8537
10	99.55	175.11	3061.77	1740.64	2.46	0.2612	7532.69	4282.39	1.7590
20	99.71	174.64	3056.81	1745.27	2.45	0.2582	7480.57	4270.99	1.7515
30	99.60	174.18	3060.14	1749.95	2.43	0.2570	7448.75	4259.59	1.7487
40	99.42	173.71	3065.84	1754.66	2.42	0.2564	7422.62	4248.15	1.7473
50	99.20	173.24	3072.58	1759.41	2.41	0.2561	7398.81	4236.68	1.7464

Where:

$S_g(\%)$ = Gas saturation

$T_c(\mu s/ft)$ = Compressional wave transit time

$T_s(\mu s/ft)$ = Shear wave transit time

$\rho(kg/m^3)$ = Rock density

V_s and V_p represent the velocities of shear and compressional waves respectively in (m/s)

$Z(kg.m^{-2}.s^{-1})$ or $(Pa.s/ m^3)$ = Acoustic impedance (P-wave impedance)

$Z_s(kg.m^{-2}.s^{-1})$ or $(Pa.s/ m^3)$ = S-wave impedance

ν = Poisson's ratio (saturated)

Table 4.23: Computed P and S- waves Impedenaces, Poisson Ratio and Velocity Ratio in Reservoir B of Well A3 of The Study Field.

$S_g(\%)$	$T_c(\mu s/ft)$	$T_s(\mu s/ft)$	$V_p(m/s)$	$V_s(m/s)$	$\rho(kg/m^3).10^3$	$\nu(\text{Poisson's})$	$Z(\rho.V_p).10^3$	$Z(\rho.V_s).10^3$	V_p/V_s
0	90.19	163.68	3379.36	1862.19	2.29	0.2820	7745.15	4267.95	1.8147
10	92.51	161.34	3294.62	1889.16	2.27	0.2627	7494.74	4297.54	1.7440
20	92.42	162.46	3298.11	1876.21	2.26	0.2608	7446.44	4236.09	1.7579
30	92.16	161.84	3307.27	1883.33	2.24	0.2601	7410.71	4220.03	1.7561
40	91.86	161.22	3318.16	1890.54	2.22	0.2597	7378.54	4203.96	1.7551
50	91.54	160.60	3329.87	1897.84	2.21	0.2594	7347.76	4187.81	1.7546
60	91.20	159.98	3342.07	1905.21	2.19	0.2593	7317.66	4171.57	1.7542
70	90.86	159.36	3354.62	1912.68	2.17	0.2592	7287.95	4155.32	1.7539
80	90.51	158.73	3367.46	1920.23	2.16	0.2591	7258.39	4138.96	1.7537

Where:

$S_g(\%)$ = Gas saturation

$T_c(\mu s/ft)$ = Compressional wave transit time

$T_s(\mu s/ft)$ = Shear wave transit time

$\rho(kg/m^3)$ = Rock density

V_s and V_p represent the velocities of shear and compressional waves respectively in (m/s)

$Z(kg.m^{-2}.s^{-1})$ or $(Pa.s/ m^3)$ = Acoustic impedance (P-wave impedance)

$Z_s(kg.m^{-2}.s^{-1})$ or $(Pa.s/ m^3)$ = S-wave impedance

ν = Poisson's ratio (saturated)

Table 4.24: Computed P and S- Waves Impedenaces, Poisson Ratio and Velocity Ratio in Reservoir C of Well A3 of The Field.

Sg(%)	Tc(μs/ft)	Ts(μs/ft)	Vp(m/s)	Vs(m/s)	ρ(kg/m ³).10 ³	υ(Poisson's)	Z(ρ.Vp).10 ³	Z(ρ.Vs).10 ³	Vp/Vs
0	84.71	149.73	3598.29	2035.68	2.52	0.2646	9064.45	5128.08	1.7676
10	86.58	149.33	3520.35	2041.15	2.51	0.2468	8820.70	5114.37	1.7247
20	86.54	148.93	3522.25	2046.66	2.49	0.2451	8777.98	5100.58	1.7210
30	86.37	148.52	3528.97	2052.22	2.48	0.2445	8747.19	5086.80	1.7196
40	86.17	148.12	3537.11	2057.82	2.47	0.2431	8719.69	5072.94	1.7189
50	85.96	147.71	3545.90	2063.46	2.45	0.2440	8693.59	5059.05	1.7184
60	85.74	147.31	3555.06	2069.16	2.44	0.2438	8668.13	5045.13	1.7181
70	85.51	146.90	3564.47	2074.90	2.42	0.2437	8643.07	5031.18	1.7179

Where:

Sg (%) = Gas saturation

Tc (μs/ft) = Compressional wave transit time

Ts (μs/ft) = Shear wave transit time

ρ (kg/m³) = Rock density

Vs and Vp represent the velocities of shear and compressional waves respectively in (m/s)

Z (kg.m⁻².s⁻¹) or (Pa.s/ m³) = Acoustic impedance (P-wave impedance)

Zs (kg.m⁻².s⁻¹) or (Pa.s/ m³) = S-wave impedance

υ = Poisson's ratio (saturated)

However, the V_p response showed anomalous change across all selected reservoirs as the gas saturation increases (Fig.4.41). For example, a drop in V_p occur from 0 to 20% S_g , followed by a continuous increase as the gas saturation exceeds 20%. Conventionally, P-wave is expected to decrease with increase in gas saturation due to reduction in density and bulk modulus (Smith *et al.*, 2003). The conventional phenomenon was satisfied as the S_g increases to 20% from 0. However, the phenomenon failed beyond 20% gas saturation due to increase in V_p . This unusual rise in V_p with increasing S_g are related to two conditions; the relationship between shrinking rock density and elastic modulus, and pressure regime.

The gradual increase of V_p as S_g exceeds 20% happened because the shrinking rock density influence exceeds the descending elastic modulus. At the initial stage, when the gas saturation was less than 20%, a little amount of gas generates a big effect on the value of K , resulting into drop in P-wave velocity. As the gas saturation increases, the obvious change occurs in the value of ρ rather than K so that V_p increases as S_g rises in the reservoirs. Also, pressure is another factor that could trigger anomalous increase in V_p as S_g increases. According to Ogagarue and Anine (2016), pore pressure increase may result to increase in V_p . Generally, V_p is sensitive to both saturation and pore pressure, and presence of gas can induce abnormally high pressure at very shallow depths. The increase in compressional wave velocity after the gas saturation exceeds 20%, could also be attributed to induced pore pressure increase.

4.8.3.2 Geomechanical Responses of The Reservoirs to Increasing Gas Saturation

The enhanced production scenario and the resulting responses on the reservoirs' properties were evaluated and the reservoirs behaviours were studied based on the responses of its elastic parameters (young modulus, bulk modulus, unconfined compressive strength and poisson ratio).

4.6.3.2.1 Young Modulus, E

The modeling result revealed that young modulus, E in all the reservoirs decreases with increasing gas saturation, S_g in all the wells (Fig.4.42). The magnitude of E , increased significantly from initial stage (0-20% gas saturation) and decreases slightly from 20% gas saturation to 80% gas saturation. The reduction in the young modulus, E was due to decrease

in the brittleness of the reservoir rock particularly at initial stage of the enhanced operation where the saturation was low. Reduction in the value of E after 20% gas saturation in all the reservoirs may adversely affect the possibility of this enhanced production due to continuous decrease in the reservoir strength.

4.6.3.2.2 Bulk Modulus, K

In all the reservoirs across the three wells of the field, the bulk modulus, K reduces with increasing gas saturation (Fig.4.43). According to Han and Batzle, (2004), as the value of K gets bigger, the pore fluid becomes stiffer. As the gas saturation increases during the fluid substitution in the reservoir, the rigidity and the rock stiffness reduce, hence the value of K and density, ρ dropped. Therefore, increase in gas saturation in the reservoirs, resulted to a corresponding decrease in bulk modulus and reservoirs' bulk density as denser reservoir fluid such as oil or brine is replaced by a less dense gas due to fluid replacement. Hence, it renders this operation unsuitable due to the reduction of the reservoir rigidity and stiffness.

4.6.3.2.3 Shear Modulus, G

The value of G in all the reservoirs across the three wells varied widely (Fig.4.44). This variation could be due to a number of factors such as; inhomogeneous nature of the rock, clay content, properties of the fluid, effective pressure, pore structures and insensitivity to gas saturation (Biot, (1956) and Berryman and Milton, (1991)). Although, in all the reservoirs, except reservoir C of well A2 (Fig.4.130), the value of G increased as S_g increased to 10% from 0 at the initial stage of the enhanced operations and thereafter showed no definite trend. This behaviour is largely due to insensitivity of shear modulus to gas saturation (Smith *et al.*,2003). Hence, this parameter may not be very important in the understanding of the responses of these reservoirs to enhanced operation due to the insensitivity to gas saturation.

4.6.3.2.4 Unconfined Compressive Strength (UCS)

The value of UCS in all reservoirs across the three wells of the field decreases with increasing gas saturation, S_g (Fig.4.45). A significant reduction in UCS was observed at low gas saturation and as the saturation increases, the effect becomes negligible. The decreasing value of UCS implies reduction in the reservoir mechanical stability and well-

bore instability. Therefore, enhanced production may not be a good option for hydrocarbon production in some of these reservoirs due to significant reduction in reservoir strength as a result of gas injection into the reservoirs.

4.6.3.2.5 Poisson Ratio

According to Jianmeng *et al.*, (2016), poisson effect occurs when a rock is compressed in a certain direction and the resulting expansion is felt in other two directions perpendicular to the direction of compression. Hence, poisson ratio is a property that characterised materials in a lateral deformation. The forward modeling of these reservoirs during enhanced operation revealed that poisson ratio, ν decreases with increasing gas saturation, S_g , in all the reservoirs across the three wells of the field (Table 4.19- 4.24 and Fig.4.46).

This results, when compare with the earlier results of the increasing S_w in the reservoirs of the field, poisson ratio declined significantly in gas. Hence, ν value is essential in quantitative reservoir fluid identification, more importantly gaseous hydrocarbon identification. In the earlier results, the modeling results showed that increasing water saturation lead to increase in poisson's ratio (ν) values as compared to decrease in value in increasing gas saturation in all the reservoirs (Table 4.6 - 4.12). Although, the magnitude of increase differs in all the reservoirs.

4.6.2 Sand Production Potential

Over 70% of hydrocarbon deposits are found in sand units (sandstone reservoirs) where production of sand may be a challenge during oil and gas production (Ahad *et al.*, 2020; Khamehchi and Reisi, 2015). It was reported by Khamehchi and Reisi, (2015) that sanding occurs due to sand influx during oil/gas production and some of the effects include casing or tubing buckling, abrasion of downhole casing or tubing, sand bridging in flow lines and/or tubing, compaction and erosion and casing or liners failure. The reservoirs's sand production possibility was estimated using an empirical relationship involving the ratio of shear modulus, G to bulk compressibility, C_b . Results were highlighted as shown in Table 4.25 – 4.31.

Tiab and Donaldson, (2004), established that the empirical formular suggested a threshold for sand to occur at $G/C_b = 0.8 \times 10^{12} \text{ psi}^2$ where the ratio is $< 0.8 \times 10^{12} \text{ psi}^2$ suggest a high potential for sanding. Although, Ghalambor *et al.*, (2015) suggested that this empirical

relationship only valid if sand will be a challenge at the present conditions but the ratios can not determine a sand-free state. In the reservoir A of well A1 (Table 4.25), the possibility of the reservoir to produce sand as water volume increases during production was estimated using the G/Cb ratio. The calculated values of the ratio at each level of water saturation (S_w) during production is greater than the threshold value of $G/Cb = 0.8 \times 10^{12} \text{ psi}^2$ that is used as sanding limit. The calculated ratios for all reservoirs (Table 4.25 – 4.31) were greater than the threshold value of $G/Cb = 0.8 \times 10^{12} \text{ psi}^2$, which eliminates the potential for sand production in all the reservoirs.

Sand production prediction is an essential stage during the reservoir evaluation and analysis Ben Mahmud *et al.*, (2019). It involves sand production prediction during oil and gas production particularly during the two scenarios (increasing S_w and S_g) in the production forecast of Tetemu field. The results showed that none of the reservoirs of the three wells has potential for sand production even with increasing water saturation. In addition to the above technique, formation porosity can be used as a guide to show if sand control is needed. According to Penberthy Jr. and Shaughnessy, (1992), if the value of porosity, $\phi > 30\%$, then the necessary requirement for sand control will be required due to poor formation consolidation and if $\phi < 20\%$, It is not likely to have a need for sand control due to formation consolidation.

They suggested that ϕ values between 20–30% range is where ambiguity is observed. Hence, sand control is required hydrocarbon reservoirs with high values of $\phi > 30\%$ while it is not needed for reservoirs with $\phi < 20\%$ (Alford *et al.*, 2012). All the reservoirs across the three wells of the field have porosity values that are less than 30% (Table 4.32, 4.33 and 4.34) and so, the combinations of the sand control techniques employed established a no case for sand control since there is no sanding potential in all the reservoirs.

Table 4.25: Elastic Constants Calculation for The Prediction of Sand Production in Reservoir A of Well A1 of The Study Field.

Sw(%)	G (GPa)	K (Gpa)	Cb (1/K)	G (psi)	K (psi)	G/Cb (10 ¹² Psi ²)
43	7.421	12.330	0.081	1076277.81	1788318.87	1.9247*10 ¹²
50	7.421	12.341	0.081	1076256.22	1789870.47	1.9264*10 ¹²
60	7.421	12.362	0.081	1076269.99	1792925.49	1.9297*10 ¹²
70	7.421	12.397	0.081	1076268.06	1797990.58	1.9351*10 ¹²
80	7.421	12.465	0.080	1076278.31	1807839.49	1.9457*10 ¹²
90	7.421	12.657	0.079	1076279.72	1835706.61	1.9757*10 ¹²
100	7.421	16.699	0.060	1076275.53	2422039.71	2.6068*10 ¹²

Where;

Sw = water saturation (%)

G = Shear modulus (psi)

K = Bulk modulus (psi)

Table 4.26: The Calculated Elastic Constants for Sand Production Prediction in Reservoir D of Well A1 of The Study Field.

<i>Sw</i> (%)	<i>G</i> (GPa)	<i>K</i> (Gpa)	<i>C_b</i>		<i>K</i> (psi)	<i>G/C_b</i> (10 ¹² Psi ²)
			(GPa ⁻¹)	<i>G</i> (psi)		
30.9	13.81004	18.88845	0.052942	2002980.44	2739543.53	5.4873 * 10 ¹²
40.9	13.81001	18.89979	0.052911	2002975.85	2741187.32	5.4905 * 10 ¹²
50.9	13.81005	18.91703	0.052862	2002981.33	2743688.06	5.4956 * 10 ¹²
60.9	13.81006	18.94604	0.052781	2002983.69	2747896.11	5.5040 * 10 ¹²
70.9	13.81002	19.00661	0.052613	2002977.13	2756680.99	5.5216 * 10 ¹²
80.9	13.81005	19.20698	0.052064	2002981.62	2785742.52	5.5798 * 10 ¹²
90.9	13.81011	21.68187	0.046121	2002990.66	3144694.35	6.2988 * 10 ¹²
100	13.81012	22.09221	0.045265	2002992.32	3204209.37	6.4180 * 10 ¹²

Where;

Sw = water saturation (%)

G = Shear modulus (psi)

K = Bulk modulus (psi)

Table 4.27: The Calculated Elastic Constants for Sand Production Prediction in Reservoir A of Well A2 of The Study Field.

<i>Sw</i> (%)	<i>G</i> (GPa)	<i>K</i> (Gpa)	<i>Cb</i> (GPa ⁻¹)	<i>G</i> (psi)	<i>K</i> (psi)	<i>G/Cb</i> (10 ¹² Psi ²)
49.51	8.3194	16.9259	0.0590812	1206626.07	2454892.18	2.9621 *10 ¹²
60.00	8.3194	17.1063	0.058458	1206625.63	2481062.24	2.9937 *10 ¹²
70.00	8.3193	17.3199	0.0577371	1206616.36	2512041.82	3.0311 *10 ¹²
80.00	8.3193	17.5766	0.0568939	1206616.41	2549270.16	3.0760 *10 ¹²
90.00	8.3193	17.8906	0.0558951	1206616.06	2594823.05	3.1310 *10 ¹²
100.00	8.3194	18.2841	0.0546922	1206625.41	2651895.08	3.1998 * 10 ¹²

Where;

Sw = water saturation (%)

G = Shear modulus (psi)

K = Bulk modulus (psi)

Table 4.28: Summary of The Data and Calculated Elastic Constants for Sand Production Prediction in Reservoir B of Well A2 of The Study Field.

<i>Sw (%)</i>	<i>K</i>			<i>G/Cb</i>		
	<i>G (GPa)</i>	<i>(Gpa)</i>	<i>Cb (GPa⁻¹)</i>	<i>G (psi)</i>	<i>K (psi)</i>	<i>(10¹²Psi²)</i>
46.68	6.999409	14.75	0.0678087	1015180.23	2138928.69	2.1714 * 10 ¹²
56.68	6.999381	14.96	0.0668469	1015176.24	2169704.91	2.2026 * 10 ¹²
66.68	6.999386	15.22	0.0657057	1015176.91	2207386.99	2.2409 * 10 ¹²
76.68	6.999394	15.51	0.0644914	1015178.04	2248950.02	2.2831 * 10 ¹²
86.68	6.999385	15.87	0.0630269	1015176.87	2301206.69	2.3361 * 10 ¹²
96.68	6.999413	16.31	0.0613039	1015180.86	2365883.70	2.4018 * 10 ¹²
100.00	6.999418	16.48	0.0606625	1015181.65	2390898.62	2.4272 * 10 ¹²

Where;

Sw = water saturation (%)

G = Shear modulus (psi)

K = Bulk modulus (psi)

Table 4.29: The Calculated Elastic Constants for Sand Production Prediction in Reservoir D of Well A2 of The Study Field.

<i>Sw</i> (%)	<i>G</i> (GPa)	<i>K</i> (Gpa)	<i>C_b</i>			
			(GPa ⁻¹)	<i>G</i> (psi)	<i>K</i> (psi)	<i>G/C_b</i> (10 ¹² Psi ²)
42.12	11.17074	16.2121	0.0617	1620182.34	2351371.56	3.8097 * 10 ¹²
52.12	11.17069	16.2266	0.0616	1620174.97	2353480.56	3.8131 * 10 ¹²
62.12	11.17074	16.2486	0.0615	1620182.51	2356659.23	3.8182 * 10 ¹²
72.12	11.17070	16.2858	0.0614	1620176.37	2362060.57	3.8270 * 10 ¹²
82.12	11.17069	16.3623	0.0611	1620174.06	2373160.71	3.8449 * 10 ¹²
92.12	11.17071	16.6109	0.0602	1620177.72	2409209.35	3.9033 * 10 ¹²
100.00	11.17075	20.2666	0.0493	1620183.29	2939428.47	4.7624 * 10 ¹²

Where;

Sw = water saturation (%)

G = Shear modulus (psi)

K = Bulk modulus (psi)

Table 4.30: Summary of The Data and Calculated Elastic Constants for Sand Production Prediction in Reservoir A of Well A3 of The Study Field.

<i>Sw</i> (%)	<i>G</i> (GPa)	<i>K</i> (Gpa)	<i>Cb</i> (GPa ⁻¹)	<i>G</i> (psi)	<i>K</i> (psi)	<i>G/Cb</i> (10 ¹² Psi ²)
47.88	7.53023	11.9470	0.08370279	1092169.04	1732773.83	1.8925 * 10 ¹²
57.88	7.53019	11.9670	0.08356320	1092163.57	1735668.41	1.8956 * 10 ¹²
67.88	7.53016	11.9989	0.08334107	1092159.82	1740294.35	1.9007 * 10 ¹²
77.88	7.53018	12.0584	0.08292960	1092161.97	1748929.16	1.9101 * 10 ¹²
87.88	7.53018	12.2086	0.08190978	1092161.97	1770704.31	1.9339 * 10 ¹²
97.88	7.53019	13.3216	0.07506611	1092163.69	1932136.87	2.1102 * 10 ¹²
100.00	7.53019	16.4200	0.06090119	1092163.73	2381529.63	2.6010 * 10 ¹²

Where;

Sw = water saturation (%)

G = Shear modulus (psi)

K = Bulk modulus (psi)

Table 4.31: The Calculated Elastic Constants for Sand Production Prediction in Reservoir D of Well A3 of The Study Field.

<i>Sw</i> (%)	<i>G</i> (GPa)	<i>K</i> (Gpa)	<i>Cb</i> (GPa ⁻¹)	<i>G</i> (psi)	<i>K</i> (psi)	<i>G/Cb</i> (10 ¹² Psi ²)
33.68	12.91279	17.998	0.055561	1872845.01	2610421.72	4.8889 * 10 ¹²
43.68	12.91281	18.007	0.055535	1872848.11	2611631.44	4.8912 * 10 ¹²
53.68	12.91281	18.018	0.055499	1872847.69	2613353.80	4.8944 * 10 ¹²
63.68	12.91281	18.037	0.055443	1872847.79	2615990.82	4.8994 * 10 ¹²
73.68	12.91284	18.068	0.055346	1872852.38	2620579.61	4.9080 * 10 ¹²
83.68	12.91282	18.136	0.055138	1872849.08	2630457.74	4.9265 * 10 ¹²
93.68	12.90242	18.376	0.054419	1871340.85	2665230.79	4.9876 * 10 ¹²
100.00	12.91278	21.224	0.047116	1872844.47	3078313.74	5.7652 * 10 ¹²

Where;

Sw = water saturation (%)

G = Shear modulus (psi)

K = Bulk modulus (psi)

Table 4.32: Summary of The Petrophysical /Mechanical Parameters of Well A1 of The Study Field.

PETROPHYSICAL PARAMETERS FOR A-1 WELL RESERVOIRS										MECHANICAL PARAMETERS FOR A-1 WELL RESERVOIRS			
A-1 RESERVOIRS	Sand Top	Sand Bottom	Gross Sand/Thickness	Net Thickness	N/G	Hydrocarbon Type	V _{shale}	Effective Porosity	S _w	K	E	UCS	G
	(ft)	(ft)	(ft)	(ft)			(dec)	(dec)	(dec)	(GPa)	(GPa)	(MPa)	(GPa)
RESERVOIR A	6606.67	6856.87	250.2	205.58	0.822	GAS /WATER	0.1445	0.2044	0.425	12.33	18.5421866	78.30297	7.42066085
RESERVOIR B	7385.74	7544.5	158.76	55.75	0.351	OIL	0.1778	0.1775	0.6411	-	-	-	-
RESERVOIR C	8256.48	8319.94	63.46	22.5	0.355	OIL / WATER	0.1114	0.1816	0.3112	-	-	-	-
RESERVOIR D	8443.83	8617.13	173.3	142.5	0.822	GAS / OIL	0.0698	0.1983	0.3091	18.88845	33.3116597	138.8578	13.810039

Where,

N/G = Net-Gross ratio

V_{shale} = Shale volume

S_w (%) = water saturation

G (GPa) = Shear modulus

K and E represent Bulk and Young moduli respectively, measured in (GPa)

UCS (MPa) = Unconfined Compressive Strength

Table 4.33: Summary of The Petrophysical /Mechanical Parameters of Well A2 of The Study Field.

PETROPHYSICAL PARAMETERS FOR A-2 WELL RESERVOIRS										MECHANICAL PARAMETERS FOR A-1 WELL RESERVOIRS			
A-2 RESERVOIRS	Sand Top	Sand Bottom	Gross Sand/Thickness	Net Thickness	N/G	Hydrocarbon Type	V _{shale}	Effective Porosity	S _w	K	E	UCS	G
	(ft)	(ft)	(ft)	(ft)			(dec)	(dec)	(dec)	(GPa)	(GPa)	(MPa)	(GPa)
RESERVOIR A	6707.81	6903.73	195.92	180.48	0.921	OIL	0.0939	0.2283	0.4951	16.92586	21.4446522	90.20307	8.31937888
RESERVOIR B	7521	7770	249	157.25	0.632	OIL	0.136	0.2105	0.4668	14.74737	18.1299427	76.61277	6.99940864
RESERVOIR C	8592.5	8660.97	68.47	42.5	0.621	OIL	0.0945	0.1823	0.4847	-	-	-	-
RESERVOIR D	8796.34	8943.89	147.55	82	0.556	GAS	0.0452	0.1716	0.4212	16.21211	27.2528279	114.0166	11.1707438

Where,

N/G = Net-Gross ratio

V_{shale} = Shale volume

S_w (%) = water saturation

G (GPa) = Shear modulus

K and E represent Bulk and Young moduli respectively, measured in (GPa)

UCS (MPa) = Unconfined Compressive Strength

Table 4.34: Summary of The Petrophysical /Mechanical Parameters of Well A3 of The Study Field.

PETROPHYSICAL PARAMETERS FOR A-3 WELL RESERVOIRS										MECHANICAL PARAMETERS FOR A-1 WELL RESERVOIRS			
A-3 RESERVOIRS	Sand Top	Sand Bottom	Gross Sand/Thickness	Net Thickness	N/G	Hydrocarbon Type	V _{shale}	Effective Porosity	S _w	K	E	UCS	G
	(ft)	(ft)	(ft)	(ft)			(dec)	(dec)	(dec)	(GPa)	(GPa)	(MPa)	(GPa)
RESERVOIR A	6596.5	6798	201.5	138.5	0.687	GAS / WATER	0.1678	0.2158	0.4788	11.94703	18.6684361	78.82059	7.53022686
RESERVOIR B	7409	7434.5	25.5	15	0.588	OIL	0.0975	0.254	0.2153	-	-	-	-
RESERVOIR C	8262.5	8300.5	38	18	0.474	OIL	0.1358	0.1956	0.2922	-	-	-	-
RESERVOIR D	8477	8636	159	98.75	0.621	GAS / WATER	0.1087	0.1912	0.3368	17.99819	31.2620535	130.4544	12.9127885

Where,

N/G = Net-Gross ratio

V_{shale} = Shale volume

S_w (%) = water saturation

G (GPa) = Shear modulus

K and E represent Bulk and Young moduli respectively, measured in (GPa)

UCS (MPa) = Unconfined Compressive Strength

CHAPTER FIVE

SUMMARY AND CONCLUSIONS

5.1 Summary

This research employed well logs and seismic data for attribute-driven Fluid Replacement Modeling (FRM) and reservoir characterization of Tetemu Field, onshore, Niger Delta. A suite of well logs such as density, gamma ray, neutron, sonic and resistivity were employed for well - based rock-physics and petrophysical analyses of wells A1, A2 and A3 of the study field. Petrophysical analysis was done using Integrated petrophysical (IP) software while fluid substitution and rock physics interpretation were executed using dynamic Rock Physics Templates (RPT) and forward modeling by Hampson-Russell software.

Petrophysical interpretation revealed five oil-bearing reservoirs, notably A to D across the three wells of the field. The environments of deposition were interpreted as marginal marine and the reservoirs were deposited in fluvial channel sands, progradational and deltaic sands based on GR log signatures. Reservoirs A and D were the best sand units with average values of 82% and 67%. The NGR reduces as the hydrodynamics flow dropped due to reduction in depositional energy from proximal to distal. The calculated average of shale volume (Vsh) across the wells were 14%, 15%, 11% and 7% for reservoirs A, B, C and D respectively. All the values were lower than 15% which implied that the reservoirs were relatively clean. The Vsh increases basinward, from the proximal to the distal part of Tetemu field towards the south in the direction of lower hydrodynamic flow.

The porosity (ϕ) values were relatively constant, without significant variation across each reservoir. This means, compaction and diagenetic changes have very little effect on ϕ of the reservoirs. Reservoir fluids comprised gas, oil and water based on the resistivity, and neutron- density combination logs interpretation for fluid differentiation,

particularly gaseous hydrocarbon. Furthermore, this study revealed that V_p reflected pore fluids and matrix of the rock while V_s was insensitive to fluid in the pores. Hence, both V_p and V_s with elastic modulus were good indicators of reservoir fluids. The combination of Castagna and Gassmann relations were integrated into FRM to create localized models for each reservoir at each well location.

The RPT generated from the crossplot of velocity ratios against acoustic impedance along each pay interval revealed gradual and steady drop in pore pressure in reservoirs D of well A1, and A, B and D of well A2, during production and consequently inducing significant stress within the reservoirs. The depletion pore pressure could lead horizontal stress changes which drives fluid from cap rock into the reservoirs. The continuous seepage could affect the in-situ stress of the reservoir, which invariably will affect the well stability and caused cap rock deformation. FRM based on Gassmann theory showed steady increase in density (ρ) and decrease in V_s . The increase in ρ was because brine is the most dense and least compressible fluid in the reservoirs.

However, the increase in density – depth trends was due to cementation and compaction which increased the reservoir rock stiffness and ρ . In addition to that, increase in ρ during production could be attributed to the conventional increase in the rigidity and K when a less dense hydrocarbon is replaced by denser brine. V_p increased in reservoirs A and B of well A2 but in A and D of wells A1 and A3, and D of well A2, it decreased exponentially with S_w . This unconventional trend was attributed to dissolved gases. However, V_s reduced as S_w increased from the initial values to 100%. The effect of saturating fluid was more in V_p than V_s . V_p was attenuated by the gaseous hydrocarbon while the reservoir rock matrix affected the V_s . The combination of the two provided a quick-look as a gas indicator.

The Poisson ratio, ν reduced in gas sand and increased in oil sand and brine. The vertical variation in ν across the wells prior to FRM could be attributed to lithological changes, decreasing ϕ with depth, clay content, fluid saturation, anisotropy and vertical heterogeneity. FRM showed that ν increased as S_w increased during production. The value increased marginally in gas sand as observed in reservoirs A of well A1, D of well A2 and A and D of well A3. It was much higher in oil sand and brine. The value of E increased with S_w and varied in reservoirs. In reservoirs A and D of wells A1 and A3, and D of well A2, E marginally increased. This was attributed to dissolved gases in brine

and oil. But in reservoirs A and B of well A2, E increased exponentially with S_w . This was connected to oil only in the reservoirs.

Also, K varied in magnitude in the reservoirs. In reservoir A of well A1, K marginally increased or steady due to gas-water interface. In reservoir D of well A1 which was gas-oil interface, the magnitude was higher. In reservoirs A and B of well A2, there was a corresponding increase in K with S_w . This was due to only oil in the reservoirs such that as the denser brine gradually replaces less dense oil, the value of K increased. The marginal change in K in reservoir D was due to dissolved gases that reduces the ρ of the fluid and subsequently caused a reduction in K. because compressibility is an inverse of K. The dissolution of gases in the oil reduces the ρ and subsequently reduces the K while dissolution of gases in water has little effects on K due to the uniqueness of water's molecular structure because little gas can be dissolved in water.

In all reservoirs with dissolved gasses such as A and D of wells A1 and A3, and D of well A2, the UCS value is not significant until after the expulsion of hydrocarbon. The reservoirs strength increased exponentially with S_w in reservoirs A and B of well A2 due to the presence of oil (only). This implied mechanical and well-bored stability. The sand production prediction was derived from the empirical relationship of the ratio of G to C_b . This relationship means that $G/C_b = 0.8 \times 10^{12} \text{ psi}^2$ is a threshold value for sanding to occur but value less than $0.8 \times 10^{12} \text{ psi}^2$ implies a high probability for sand potential. None of the reservoirs has ratio less than the threshold value at various levels of S_w . In addition to the above technique, formation ϕ indicated that the sand control was not needed because, none of the reservoir has ϕ value that was greater than 30%. Hence, the combinations of both techniques established a no case for sand control since there was no sanding potential in all the reservoirs.

Enhanced production scenario for the selected reservoirs revealed steady decrease in ρ and increase in V_s . The steady decrease in ρ was attributed to the conventional decrease in the rigidity and K of the rock when a denser reservoir fluid such as oil or brine is replaced by a less dense gas. Increasing S_g reduces the stiffness of the rock, hence its ρ . V_s increased because among reservoir fluids, gas supports shearing the most. Therefore, as gas gradually replaces oil or water, the shearing ability of the rock was enhanced. However, the unconventional increase in V_p as S_g exceeds 20% was due to the influence of induced pore pressure. As the S_g increases, the rigidity and the stiffness of the rock

reduces, hence its K and ρ dropped as oil or brine was replaced by a less dense gas. FRM revealed decrease in E with S_g due to decrease in the brittleness of the reservoir rock particularly at the initial stage where S_g was low. The reservoirs' strength decreased with increasing S_g so the value of ν .

5.2 Conclusion

Five oil-bearing reservoirs, notably A to D were delineated across the three wells of the field. The reservoirs were deposited in fluvial channel sands, progradational and deltaic sands based on log signatures. The NGR showed good reservoir quality with reservoirs A and D being the best sand units with average values of 82% and 67%. The NGR reduced from proximal to distal part of Tetemu field as the hydrodynamic flow dropped due to reduction in depositional energy. The V_{sh} in the reservoirs were lower than 15% which implied relatively clean. The V_{sh} increased from the proximal to the distal, in the direction of lower hydrodynamic flow. The ϕ_e were relatively constant, without significant variation across reservoirs. The average values in reservoirs A, B, C and D were 21%, 21%, 18% and 19% respectively which implied that compaction and diagenetic changes have very little effect on ϕ . Reservoirs fluids comprised oil, water and gas.

Rock physics analysis revealed that V_p reflects pore fluids and the matrix of the rock, while V_s does not show sensitivity to the fluids (pore fluids). Both V_p and V_s with elastic modulus was a good indicator of reservoir fluids. The combination of Castagna model and Gassmann's relations were integrated into FRM to create localized models for each reservoir at each well location. Dynamic RPT revealed that increasing S_w triggered gradual and steady drop in pore pressure thereby inducing significant stress in reservoirs D of well A1 and A, B and D of well A2. The increase in UCS of some reservoirs implied mechanical and well-bored stability and reservoir's strength were attenuated by dissolved gasses. The combinations of sand control techniques employed established a no case for sand control since there was no sanding potential in the reservoirs. The ν were attenuated by S_g while higher values were recorded in oil sand and brine because ν is an inverse of compressibility.

An enhanced production scenario revealed that the shearing ability of the reservoir rocks were enhanced and hence became more unstable as gas gradually replaced oil or water. Reduction in E was due to decreased in the brittleness of the reservoir rocks due to S_g .

Also, K reduced with increasing S_g during FRM and hence caused a significant reduction in the rigidity and the stiffness of the reservoirs. The decrease in UCS resulted in the reservoir rocks' weakness and well instability. In this study, FRM revealed that the unconventional behaviours in the reservoirs' seismic, elastic and mechanical properties were attributed to the presence of compressional fluid (gas). FRM involving well-based rock physics and petrophysical analyses served as a modeling tool for reservoir evaluation, monitoring and performance and essentially useful to establish production forecast as shown in this study.

5.3 Recommendations

It is suggested that this technique should be included as a component of the 3-D reservoir modeling process in the oil and gas industries. This integration will enhance the dependability of 3-D reservoir models, enabling them to serve as more accurate prediction tools for reliable production forecasts and field development strategies.

5.4 Contributions to Knowledge

The significance of this research lies in its ability to successfully address fluid-related challenges and offer a methodology for monitoring reservoir performance during production through the application of rock-physics modeling.

REFERENCES

- Adam, L., Batzle, M. and Brevik, I.,** (2006). Gassmann fluid substitution and shear modulus variability in carbonates at laboratory seismic and ultrasonic frequencies. *GEOPHYSICS*, vol. 71 (6), 2006; pp1–13.
- Lukumon Adeoti, Njoku Onyekachi, Olawale Babatunde Olatinsu, Julius Fatoba and Millicent Bello,** 2014: Static Reservoir Modeling Using Well Log and 3-D Seismic Data in a KN Field, Offshore Niger Delta, Nigeria. *International Journal of Geosciences*, 2014, 5, 93-106.
- Adeoye, T.O., and Enikanselu, P.,** 2009. Reservoir Mapping and Volumetric Analysis using Seismic and Well Data; *Ocean Journal of Applied Sciences*. 2(4):66-67.
- Adepelumi, A. A., Alao, O. A and Kutemi, T. F.,** 2011: Reservoir characterization and evaluation of depositional trend of the Gombe sandstone, southern Chad basin Nigeria. *Journal of Petroleum and Gas Engineering* Vol. 2(6), pp. 118-131.
- Adiela, U.P.,** 2016, Reservoir Characterisation of X- Field, Onshore, Niger Delta, Nigeria. *International Research Journal of Interdisciplinary & Multidisciplinary*. Volume-II, Issue-II, March 2016, Page No. 83-89.
- Ahad, N.A., Jami, M. & Tyson, S.,** 2020. A review of experimental studies on sand screen selection for unconsolidated sandstone reservoirs. *J Petrol Explor Prod Technol* (2020). <https://doi.org/10.1007/s13202-019-00826-y>
- Alford, J., Blyth, M., Tollefsen, E., Crowe, J., Loreto, J., Mohammed, S., Pistre, V. and Herrera, A.R.,** 2012. Sonic logging while drilling – shear answers, *Oilfield Rev.* spring 24
- Archie, G.E.,** (1942): The electrical resistivity log as an aid in determining some reservoir characteristics. *Journal of Petroleum Technol.*, 5: 54-62.
- Archie, G.E.,** 1950: An Introduction to Petrophysics of reservoir rock. *American Association Petroleum Geologists, Bulletin*, Vol. 34, 943p
- Asquith, G. and Gibson, C.R.,** 1982: *Basic Well Log Analysis for Geologists*. ISSN 0891816526, 2: 216

- Asquith, G.** 2004: Basic Well Log Analysis. AAPG Methods in Exploration Series, American Association of Petroleum Geologists: Tulsa, OK. 16:112-135.
- Asquith, G. and Krygowski, D.,** 2004: Basic Well Log Analysis. American Association of Petroleum Geologists, Series, 16p.
- Attewell, P.B. and Farmer, I.W.,** (1976). Principles of engineering geology. Chapman and Hall, London.
- Avbovbo, A.A.,** 1978: Tertiary lithostratigraphy of Niger Delta. American Association of Petroleum Geologists Bulletin 62, 295–300.
- Avseth, P. and Odegaard, E.,** 2004. Well log and seismic data analysis using rock physics templates, first break 22 (10)
- Avseth, P. Gary Mavko, Jack Dvorkin, and Tapan Mukerji,** (2001): Rock physics and seismic properties of sands and shales as a function of burial depth. SEG Technical Program Expanded Abstracts 2001, 1780-1783.
- Batzle, M. and Wang, Z.,** 1992 "Seismic Properties of Pore Fluids." Geophysics, doi:10.1190/1.1443207.
- Beka, F. T., and Oti, M. N.,** 1995, The distal offshore Niger Delta: frontier prospects of a mature petroleum province, *in*, Oti, M.N., and Postma, G., eds., Geology of Deltas: Rotterdam, A.A. Balkema, p. 237-241.
- Ben Mahmud, H., Van Hong, L. and Lestariono, Y.,** 2019. Sand production: A smart control framework for risk mitigation, Petroleum, <https://doi.org/10.1016/j.ptlm.2019.04.002>
- Berryman, J. G.,** 1999, Origin of Gassmann's equations: Geophysics, 64, 1627–1629.
- Berryman, J. G., and Milton, G. W.,** 1991, Exact results for generalized Gassmann's equation in composite porous media with two constituents: Geophysics, 56, 1950–1960.
- Biot, M. A.,** 1956, Theory of propagation of elastic waves in a fluid saturated porous solid. I. Low frequency range and II. Higher-frequency range: Acoust. Soc. Am., 28, 168–191

- Bourgoyne, A.T., Millheim, K. K., Chenevert, M.E. and Young, F.S.,** 1986. Applied Drilling Engineering, SPE Book Series.
- Bradley, W. B.,** 1979. Mathematical concept-stress cloud can predict borehole failure. Oil and Gas Journal, 1979, 77(8): 92–101.
- Burke, K.,** (1972). Longshore drift, Submarine Canyons and Submarine Fans in Development of Niger Delta. AAPG Bulletin, Vol.56, pp. 1975-1983.
- Carmichael, R.S.,**1982. Handbook of Physical Properties of Rocks, Vol. 2, 1-228. Boca Raton, Florida: CRC Press Inc.
- Castagna, J. P., Batzle, M. L. and Eastwood, R. L.** (1985)."Relationships between compressional-wave and shear-wave velocities in clastic silicate rocks". Geophysics. 50 (4): 571–581.
- Castagna, J.P., Batzle, M.L., Kan, T.K., Backus, M.M.** (1993). The link between rock properties and AVO response, Offset-dependent reflectivity-Theory and practice of AVO analysis: SEG, Vol. 8, pp. 135-171.
- Chang, C., Zoback, M.D. and Khaksar, A.,** (2006). Empirical relations between rock strength and physical properties in sedimentary rocks, Journal of Petroleum Science and Engineering 51 (2006) 223–237
- Clark, V. A., Tittmann, B. R. and T.W. Spencer,** 1984. Rock lithology and porosity determination from shear and compressional wave velocity: Geophysics, 49, 1188– 1195
- Cohen, H.A. and McClay, K.,** (1996) Sedimentation and shale tectonics of the northwestern Niger Delta. Front Marine and Petroleum Geology 13: 313-328.
- Coleman, J.M., and Prior, D.B.,** (1980): Deltaic sand bodies: A 1980 short course, education course, Note series #5, AAPG P.195.
- Corredor, F., Shaw, J.H., and Bilotti, F.,** (2005): Structural styles in the deep-water fold and thrust belts of the Niger Delta. American Association of Petroleum Geologists Bulletin 89, 753–780.
- Damuth, J.E.,** (1994) Neogene gravity tectonics and depositional processes on the deep Niger Delta. continental margins Marine and Petroleum Geology 11: 320-346.

- Daniel, J.T. and Richard E.B.**, (2003): Applied subsurface geological mapping. 2nd ed.pp.60-105.
- Darvishpour, A., Cheraghi, S. M., Wood, D. A., * and Ghorbani, H.** 2019. Wellbore stability analysis to determine the safe mud weight window for sandstone layers, *Petroleum Exploration and Development*, 46(5): 1031–1038.
- Doust, H.**, 1989. The Niger Delta: Hydrocarbon Potential of a Major Tertiary Delta Province Coastal Lowlands, *Geology and Geotechnology*. Proceedings of the KNGMG Symposium “Coastal Lowland Geology and Geotechnology”. Dordrecht, Kluwe, pp.203-212.
- Doust, H.**, 1990. Geological Society, London, Special Publications 1990, v. 50, p. 365
- Doust, H., and Omatsola, E.M.**, 1990. Niger Delta, In: *Divergent/Passive Margins Basins*. Edwards, and P.A. Santagrossi (eds), AAPG memoir v. 48, pp. 239-248.
- Dubois, M.K., A.P. Byrnes, T.R. Carr, G.C. Bohling, and J.H. Doveton**, 2003: Multiscale geologic and petrophysical modeling of the giant Hugoton gas field (Permian), Kansas and Oklahoma, in P. M. Harris and L. J. Weber, eds., *Giant reservoirs of the world: From rocks to reservoir characterization and modeling*: American Association of Petroleum Geologists, Memoir 88.
- Dubrule, O.**,2003, *Geostatistics for seismic data integration in earth models*. EAGE distinguished instructor series No. 6, 282 p.
- Dvorkin, J. and Nur, A.** (1998). Time-Average Equation Revisited, Department of Geophysics, Stanford University, Stanford, Ca 94305-2215, *Geophysics*, 63 (2): 460–464.
- Dvorkin, J., Moos, D., Packwood, J., and Nur, A.** (2001). Identifying Patchy Saturation from Well Logs, Department of Geophysics: Stanford University, Short Note.
- Dvorkin, J., Prasad, M., Sakai, A., and Lavoie, D.**, (1999): Elasticity of marine sediments: Rock physics modeling. *Geophysical research letters* 26 (12), 1781-1784

- Edwards, J.D., and Santogrossi, P.A.,** 1990, Summary and conclusions, *in*, Edwards, J.D., and Santogrossi, P.A., eds., Divergent/passive Margin Basins, AAPG Memoir 48: Tulsa, American Association of Petroleum Geologists, P. 239-248.
- Ejedawe, J.E.,** (1981) Patterns of incidence of oil reserves in Niger Delta Basin: American Association of Petroleum Geologists Bulletin, 65, 1574-1585.
- Ejedawe, J.E.,** (2007) An unpublished report on the Niger Delta submitted to SPDC Warri.
- Ejedawe, J.E., Coker, S.J.L., Lambert-Aikhionbare, D.O., Alofe, K.B., and Adoh, F.O.,** 1984, Evolution of oil-generative window and oil and gas occurrence in Tertiary Niger Delta Basin: American Association of Petroleum Geologists, v. 68, p. 1744-1751.
- Ekweozor, C.M.,** 2004. Source rocks of giant hydrocarbon deposits in deep offshore, Niger delta. In: Proceeding of Nigerian Association of Petroleum Explorationists, Regional West Africa Deepwater Conference, Abuja, Nigeria (Abstracts).
- Ekweozor, C.M., Daukoru, E.M.,** 1984: Petroleum source bed evaluation of the Tertiary Niger Delta-reply. American Association of Petroleum Geologists Bulletin 68, 390–394.
- Ekweozor, C. M., Okogun, J.I., Ekong, D.E.U., and Maxwell J.R.,** 1979, Preliminary organic geochemical studies of samples from the Niger Delta, Nigeria: Part 1, analysis of crude oils for triterpanes: Chemical Geology, v 27, p. 11-28.
- Ekweozor, C.M. and Okoye, N.V.,** 1980: Petroleum source-bed evaluation of the Tertiary Niger Delta. American Association of Petroleum Geologists Bulletin 64, 1251–1259.
- Ellis D.V. and Singer J.M.,** (2007) Introduction to Well Log Interpretation: Finding the Hydrocarbon. In: Ellis D.V., Singer J.M. (eds) Well Logging for Earth Scientists. Springer, Dordrecht.
- Ellis D.V. and Singer J.M.,** 2008. Well logging for Earth Scientists. 2nd ed. 17-675.

- Emeka, N. E., Beka, F. T. and Nwachukwu, J.,** 2015: Integrated Static Reservoir Modeling: A Case Study of the “Alpha” Field. *International Journal of Science Inventions Today*, 4(2), 151-163.
- Emery, D. and Myers, K.J.,** (1996). *Sequence Stratigraphy*. Blackwell Science, Oxford, 297. <http://dx.doi.org/10.1002/9781444313710>
- Evamy, B.D., Harembourne, J., Kamerling, P., Knaap, W.A., Molley, F.A., and Rowlands, P. H.,** (1978): Hydrocarbon habitat of Tertiary Niger Delta. *AAPG Bulletin*, Vol. 62, pp. 1-39.
- Fertl, W.H.** 1981. Openhole Crossplot Concepts. A Powerful Technique in Well Log Analysis. *J Pet Technol* 33 (3): 535-549. SPE-8115-PA.
- Fertl, W.H. and DeVries, M.R.,** 1997. Coal Evaluation Using Geophysical Well Logs, paper F. *Trans., 1997 Formation Evaluation Symposium*, Canadian Well Logging Society, 1–17.
- Fjær, E., Horsrud, P., Raaen, A.M., Risnes, R., and Holt, R.M.,** 1992. Petroleum Related Rock Mechanics, 1-338. Amsterdam: *Developments in Petroleum Science* No. 33, Elsevier, Amsterdam.
- Fidelis, A. A. and Akaha, C.,** 2016. Geomechanical Evaluation of an onshore oil field in the Niger Delta, Nigeria. *Journal of Applied Geology and Geophysics (IOSR-JAGG)*, Vol. 4, Iss.1 pp. 99-111.
- Frankl, E.J., Cordry, E.A.,** 1967. The Niger Delta oil province: Recent developments onshore and offshore. In: *Proceeding of the 7th World Petroleum Congress*, Mexico City, vol. 1b, pp. 195–209.
- Frost, B.R.,** (1997) A Cretaceous Niger Delta Petroleum System, *in*, *Extended Abstracts*, AAPG/ABGP Hedberg Research Symposium, Petroleum Systems of the South Atlantic Margin, November 16-19, 1997, Rio de Janeiro, Brazil.
- Gassmann, F.** (1951). Elastic waves through a packing of spheres. *Geophysics*, 16, 673-685.
- Ghalambor, A., Hayatdavoudi, A. and Aicocer, C. F.,** 2015 Predicting Sand Production in U. S Gulf Coast Gas Wells Producing Free Water, SPE.

- Gluyas, J. and Swarbrick, R.,** 2004, Petroleum Geoscience. Blackwell, Oxford, 239 p.
- Greenberg, M.L, and Castagna, J.P.,** (1992). Shear –wave velocity estimation in porous rocks: theoretical formulation, preliminary verification applications 1, Geophysical prospecting 40 (2), 195-209.
- Guo, B.,** 2019, Petroleum reservoir properties. In Well Productivity Handbook (Second Edition), pp.17-51. Gulf Professional Publishing.
- Haack, R.C., Sundararaman, P., and Dahl, J.,** (1997). Niger Delta petroleum System, *in*, Extended Abstracts, AAPG/ABGP Hedberg Research Symposium, Petroleum Systems of the South Atlantic Margin, November 16-19, 1997, Rio de Janeiro, Brazil.
- Haldersen, H. H. and Dasleth, E.,** 1993 “Challenges in Reservoir Characterization,” AAPG Bulletin, Vol. 77, No. 1, 1993, pp. 541-551
- Han, De-hua and Batzle, Michael L.,** 2004, Gassmann’s equation and fluid-saturation effects on seismic velocities. Geophysics, Vol. 69, No.2, P. 398-405
- Holt, R.M., Ingsoy, P., and Mikkelsen, M.,** 1989. Rock Mechanical Analysis of North Sea Reservoir Formations. SPE Form Eval 4 (1): 33-37. SPE-16796 PA.
- Hooper, R. J., Fitzsimmons, R. J., Grant, N., Vendeville, B. C.,** (2002) The role deformation in controlling depositional patterns in the south-central Niger Delta. West Africa Journal of Structural Geology 24: 847-859.
- Hospers, J.,** (1965): Gravity Field and Structure of the Niger Delta, Nigeria, West Africa; Geological Society of America Bulletin, Vol.76, pp407-422.
- Jianmeng Sun, Xiaohan Wei and Xuelian Chen,** (2016). Fluid identification in tight sandstone reservoirs based on a new rock physics model. Journal of Geophysics and Engineering, volume 13, Issue 4, August, 2016, Pp. 526-535
- Kaplan, A., Lusser, C.U., and Norton, I.O.,** (1994): Tectonic Map of the world, Panel10: Tulsa, American Association of Petroleum Geologists, Scale 1: 10,000,000.

- Khamehchi, E. and Reisi, E.,** (2015): Sand production prediction using ratio of shear modulus to bulk compressibility (case study), *Egyptian Journal of Petroleum*, 24: 113-118.
- Khazanehdari, J., and J. Sothcott,** 2003. Variation in dynamic elastic shear modulus of sandstone upon fluid saturation and substitution: *Geophysics*, 68, 472–481
- Klett, T.R., Ahlbrandt, T.S., Schmoker, J.W. and Dolton, J.L.** (1997). Ranking of the world's oil and gas provinces by known petroleum volumes. U.S. Geological Survey Open-file Report-97-463, CD-ROM. pp. 56 – 58.
- Kramers, J.W.** (1994). Integrated Reservoir Characterization: from the well to the numerical model, Proceedings, 14th World Petroleum Congress, John Wiley & Sons, 1994
- Krief, M.J.; Garat, J.; Stellingwerff, J.; Ventre, J.** (1990): A petrophysical interpretation using the velocities of P and S waves (full wave form sonic). *Log Anal.* **58**, 355–369
- Krusi, H.R.,** (1994) Overpressure prediction; A contribution towards safer drilling, *Nigeria Association of Petroleum Explorationists Bull.* **9**, 86-91.
- Kulke, H.,** (1995). Regional Petroleum Geology of the World. Part II: Africa, America, Australia and Antarctica: Berlin, Gebrüder Borntraeger., pp143-172.
- Kumar, D.,** 2006, A tutorial on Gassmann Fluid Substitution: Formulation, Algorithm and Matlab code: *Geohorizons*, 11, 4-12
- Lake, I. W., Carrol, H. B. and Wesson, T. C.,** 1991 “Reservoir Characterization,” Academic Press, San Diego, 1991.
- Lambert-Aikhionbare, D. O., and Ibe, A.C.,** (1984) Petroleum source-bed evaluation of the Tertiary Niger Delta: discussion: *American Association of Petroleum Geologists Bulletin*, 68, 387-394.
- Larionov, V. V.** (1969), Radiometry of boreholes (in Russian), NEDRA, Moscow.

- Lawson-Jack, O., Etim D. Uko, Iyeneomie Tamunobereton-Ari and Matthew A. Alabraba**, (2019): Geomechanical Characterization of a Reservoir in Part of Niger Delta, Nigeria. *Asian Journal of Applied Science and Technology (AJAST)*. Vol. 3, Issue 1, Pp 10-30.
- Lehner, P., and De Ruiter, P.A.C.**, (1977): Structural history of Atlantic Margin of Africa. *AAPG Bulletin*, Vol. 61, pp961-981.
- Li, D., Wei, J., Di, B., Ding, P. and Shuai, D.**, 2017. The effect of fluid saturation on the dynamic shear modulus of tight sandstones. *Journal of Geophysics and Engineering*, Vol. 14 (5), pp 1072–1086,
- Lucia, F. J. and Fogg, G. E.**, 1990 “Geologic/Stochastic Mapping of Heterogeneity in a Carbonate Reservoir,” *Journal of Petroleum Technology*, Vol. 42, No. 1, 1990, pp. 1298- 1303
- Magbagbeola, O., and Brian, W.J.**, (2007): Sequence Stratigraphy and Syndepositional deformation of the Agbada Formation, Robertkiri Field, Niger Delta, Nigeria. *AAPG Bulletin* 91, 945-958.
- Mavko, G., Mukerji, T., and Dvorkin, J.**, 1998. *The Rock Physics Handbook, Tools for Analysing Seismic Properties*, Cambridge University Press. pp. 300-437
- Merki, P.**, 1972. *Structural Geology of the Cenozoic Niger Delta: In Africa Geology* (T. F. J. Dessauvague and A. J. Whiteman eds). 1972. Ibadan University press, pp.635-646.
- Mode, A.W. and Anyiam, A.O.**, (2007): Reservoir Characterization: Implications from Petrophysical Data of the “Paradise-Field”, Niger Delta, Nigeria. *Pacific Journal of Science and Technology*, Volume 8. Number 2. November 2007 (Fall)
- Moldowan, J.M., Seifert, W.K., Gallegos, E.J.**, 1985: Relationship between Petroleum Composition and Depositional Environment of Petroleum Source Rocks. *American Association of Petroleum Geologists Bulletin* 69, 1255–1268.
- Montmayeur, H. and Graves, R.M.**, 1985. Prediction of Static Elastic/Mechanical Properties of Consolidated and Unconsolidated Sands from Acoustic Measurements: Basic Measurements. Presented at the SPE Annual Technical

Conference and Exhibition, Las Vegas, Nevada, 22-26 September 1985. SPE-14159-MS. <http://dx.doi.org/10.2118/14159-MS>

Montmayeur, H. and Graves, R.M. 1986. Prediction of Static Elastic/Mechanical Properties of Consolidated and Unconsolidated Sands From Acoustic Measurements: Correlations. Presented at the SPE Annual Technical Conference and Exhibition, New Orleans, Louisiana, 5-8 October 1986. SPE-15644-MS. <http://dx.doi.org/10.2118/15644-MS>

Moos, D., Peska, P., Finkbeiner, T., Zoback, M.D., 2003. Comprehensive wellbore stability analysis utilizing quantitative risk assessment. J. Pet. Sci. Eng. 38, 97–110.

Moos, D. (2006). Geomechanics. Applied to Drilling Engineering Vol.II, 1-173.

Nelson, C. S and James, N. P., 2000. Marine Cements in Mid-Tertiary cool-water shelf limestones of New Zealand and Southern Australia. Sediment 47, 609-629.

Nton, M., and Olumiyiwa, O., 2012: Facies Interpretation from Well Logs: Applied to SMEKS Field, Offshore Western Niger Delta. AAPG International Conference & Exhibition, Singapore, pp. 1-24, article #90155.

Nton, M. and Salami, R., 2016: Reservoir Characteristics and Palaeo-Depositional Environment of Duski Field, Onshore, Niger Delta, Nigeria. Global Journal of Geological Sciences, Vol.,14, 2016, pp. 49-63.

Nwachukwu, J.I. and Chukwurah, P.I., (1986). Organic matter of Agbada Formation, Niger Delta, Nigeria: American Association of Petroleum Geologists Bulletin, Volume 70, pp. 48-55.

Nwachukwu, J.I., Oluwole, A.F., Asubiojo, O.I., Filby, R.H., Grimm, C.A., and Fitzgerald, S., 1995, A geochemical evaluation of Niger Delta crude oils, *in*, Oti, M.N., and Postma, G., eds., Geology of Deltas: Rotterdam, A.A. Balkema, p. 287-300.

Obiadi, I.I. and Obiadi C.M., (2016) Structural Deformation and Depositional Processes: Insights from the Greater Ughelli Depobelt, Niger Delta, Nigeria. Oil Gas Res 2:118. doi: 10.4172/2472-0518.1000118

- Obi-Chidi Adaeze and Adiola U.P**, 2016: Facies Modelling and Petrophysical Properties of X-Field, Onshore, Niger Delta, Nigeria. International Journal of Science Inventions Today, 5(2), 136-151.
- Ogagarue, D.O. and Anine, L. A.**, (2016). An Integration of Rock Physics, AVO Modeling and Analysis for Reservoir Fluid and Lithology Discrimination in A Niger Delta, Deep Water Block, Journal of Applied Geology and Geophysics (IOSR-JAGG) Volume 4, Issue 2, pp 36-46
- Ojo, A.O.**, (1996). Pre-drill prospect evaluation in deep water Nigeria. Nig. Assoc. Petrol. Explo. Bull., 11: 11-22.
- Olabode S. Matthew, Jason Won, George Udoekong, Olaoluwa O. Ibilola, and Dolapo Dixon**, 2010: Resolving the Structural Complexities in the Deepwater Niger-Delta Fold and Thrust Belt: A Case Study from the Western Lobe, Nigerian Offshore Depobelt. AAPG International Conference and Exhibition, Calgary, Alberta, Canada, September 12-15, 2010
- Oladipo, M. K**, 2011. Integrated Reservoir Characterization: A Case Study of an Onshore Reservoir in Niger Delta Basin, Nigeria. Unpublished Master Thesis, African University of Science and Technology, 2015.
- Oyedele, K.F., Oladele, S., Ogagarue, D.O. and Bakare, K.** (2012): Sequence Stratigraphic Approach to Hydrocarbon Exploration in Bobsaa field, onshore Niger Delta. Journal of Petroleum and Gas Exploration Research, Vol. 2(6) pp.106-114.
- Patrick, D. D., Gerilyn, S.S. and John, P.C.**, 2002: "OutcropBase Reservoir Characterization: A Composite Phylloid-Algal Mound, Western Orogrande Basin (New Mexico)," AAPG Bulletin, Vol. 86, No. 1, 2002, pp. 780.
- Penberthy Jr., W.L. and Shaughnessy, C.M.**, 1992. Sand Control, SPE Book Series, vol.1, Society of Petroleum Engineers, Richardson, TX, 1992.
- Petroconsultants**, (1996): Petroleum exploration and production database, Houston Texas, Petroconsultants, Inc.

- Pickering, D. J.** (1970). Anisotropic elastic parameters for soil. *Geotechnique* 20, 271-276.
- Pickett, G.R.** (1963): Acoustic character logs and their applications in formation evaluation. *J. Pet. Technol.* **15**, 659–667 (1963)
- Purnamasari, I.A., Khairy, H, Abdeldayem, A.L. and Ismail, W.,** 2014. Rock Physics Modeling and Fluid Substitution Studies in Sandstone Reservoir. *Journal of Applied Sciences*, 14: 1180-1185.
- Raymer, L.L., Hunt, E.R., Gardner, J.S.,** (1980). An Improved Sonic Transit Time-to-Porosity Transform: Society of Professional Well Log Analysis, 21st Annual Logging Symposium, Transactions.
- Reijers, J.A.,** 1996. Selected Chapters on Geology; Sedimentary Geology and sequence Stratigraphy in Nigeria and a Field Guide, 1996
- Reijers, T.J.A.,** (2011): Stratigraphy and Sedimentology of the Niger Delta. *Geologos*, Vol. 17(3), pp. 133-162.
- Reijers, T.J.A., Petters, S.W., and Nwajide, C.S.,** (1997): The Niger Delta Basin, in Selley, R.C, (ed.), *African Basin-Sedimentary Basin of the World 3*: Amsterdam, Elsevier science, pp. 151-172.
- Reyment, R. A.,** (1965): Aspect of geology of Nigeria, Ibadan, University of Ibadan Press.
- Reyment, R. A.,** (1969): Ammonite biostratigraphy, continental drift, and oscillatory transgressions: *Nature*, V. 224, p. 137-140.
- Rider, M.H.,** (1999): *Geologic Interpretation of Well Logs*. 2nd ed. Whittles Publishing: Caithness.
- Salem, H. S.** (1993). A preliminary study of the physical properties of the Terra Nova and Hibernia oil fields in the Jeanne d'Arc Basin, offshore Newfoundland, Canada. Geological Survey of Canada, Halifax, NS, OFR 2686, Dossier Public.

- Salem, H.S.**, (2000). Poisson's ratio and the porosity of surface soils and shallow sediments, determined from seismic compressional and shear wave velocities. *Geotechnique* 50, No. 4, 461- 463.
- Santarelli, F.J., Detienne, J.L., Zundel, J.P.**, 1989. Determination of the mechanical properties of deep reservoir sandstones to assess the likelihood of sand production. In: Maury, V., Fourmaintraux, D. (Eds.), *Rock at Great Depth*. A.A.Balkema, Brookfield, VT, pp. 779–787
- Sayers, C. M. and Chopra** (2009): Introduction to this special section - Rock Physics. *The Leading Edge* 28 (1), 15-16.
- Schlumberger**. (1974). *Log Interpretation Charts*, Schlumberger Educational Services, New York, 83p.
- Schlumberger**. (1985): Well Evaluation Conference, Nigeria. International Human Resources Development Corporation (IHRDC) Publication, Boston. Pp. 16-60.
- Schlumberger**. 1989. *Log Interpretation, Principles and Application*. Schlumberger Wireline and Testing: Houston, Texas. pp. 21-89.
- Schlumberger Petrel*** Software: Seismic-to-Simulation, Version 2009.
- Selley, R.C** (1978): Porosity gradient in the North Sea oil-bearing sandstones, *Journal of the Geological Society of London*, Vol. 135, No. 1, pp. 119-132.
- Selley, R.C.** (1997). *Elements of Petroleum Geology*: Publish by Freeman and Company, 3rd edition, pp. 37-299.
- Selley, R.C.** (1998). *Elements of Petroleum Geology*: Publish by Freeman and Company, pp. 37-299.
- Serra, O. and Sulpice, L.**, (1975): Transactions of the SPWLA 16th Annual Logging Symposium Paper W, Sedimentological analysis of shale-sand series from well logs
- Shannon, P.M. and N. Naylor**. 1989. *Petroleum Basin Studies*. Graham and Trotman Limited: London, UK. 153-169.
- Shell** (1982). *Well Log Interpretation*. Chapter 11-13.

- Short, K.C., and Stauble, A.J.,** (1967). Outline of Geology of Niger Delta: AAPG Bulletin, V.51, pp. 761-779
- Singh, V., Yemez, I., & Sotomayor, J.** (2013). Key Factors Affecting 3D Reservoir Interpretation and Modelling Outcomes: Industry Perspectives. Current Journal of Applied Science and Technology, 3(3),376-405.
- Smith, T.M., Sondergeld, C.H., and Rai, C.S.,** 2003. Gassmann fluid substitutions: A tutorial, Geophysics Vol 68, No.2, P. 430-440
- Stacher, P.,** (1995). Present understanding of the Niger Delta hydrocarbon habitat, In: Oti, M.N., and Postma, G. (eds.), Geology of Deltas: Rotterdam, A.A. Balkema, pp.257-267.
- Stephen T.,** 2007. An Introduction to Reservoir Modeling, ISBN 978-1-906928-07-0
- Stoneley, R.,** 1966. The Niger Delta in the light of the theory of Continental Drift. Geological Magazine v. 105, pp. 385-397.
- Tearpock, D. J. and Bischke, R. E.,** 2003. Applied subsurface geological mapping with structural methods. 2nd edition. Prentice Hall, PTR, Upper saddle, River, New Jersey.
- Tiab, D. and Donaldson, E. C.** (1996) Petrophysics. Theory and practice of measuring reservoir rock and fluid transport properties. Houston, TX: Gulf Publishing.
- Tiab, D. and Donaldson, E.C.** (2004). Petrophysics: The Theory and practice of measuring reservoir rock and fluid transport properties. Gulf Professional Publishing, USA.
- Tixier, M.P., Alger, R.P., and Doh, C.A.** (1959). Sonic Logging. J Pet Technol Trans., AIME, 216: 106.
- Tixier, M.P., Loveless, G.W., and Anderson, R.A.,** 1975. Estimation of Formation Strength From the Mechanical-Properties Log (incudes associated paper 6400). J Pet Technol 27 (3): 283-293. SPE-4532-PA.
- Toksoz M.N, Cheng C.H, Timur A.,** (1976) Velocities of seismic waves in porous rocks. Geophysics 41:621–645

- Toluwalpe A.O., Beka, F. T. and Akagbosu P.,** (2015): Field Development Plans Using Seismic Reservoir Characterization and Modeling; A Niger Delta 3D Case Study. *International Journal of Science Inventions Today*, 4(2), 164-173.
- Tomasso, M.P.G,** (2010), Reservoir Characterisation for Geological Static Modeling. Enhance Oil Recovery Institute, University of Wyoming. 1-57 p.
- Tuttle, L.W., Charpentier, R.R. and Brownfield, M.E.** (1999): The Niger Delta Petroleum System, Niger Delta province, Nigeria, Cameroon and Equatorial Guinea, Africa. Denver: USGS Open-File Report 99-50, pp.65.
- Vahidoddin, Fattahpour, V., Mahdi Moosavi, M., and Mahdi Mehranpour, M.,** 2012. An experimental investigation on the effect of grain size on oil-well sand production. *Petrol. Sci.* 9 (3) (2012) 343–353
- Van Rensbergen, Pieter, Morley, C.K., Ang, D.W., Hoan, T.Q. and Lam, N.T.,** 1999. “Structural Evolution of Shale Diapirs from Reactive Rise to Mud Volcanism: 3D Seismic Data from the Baram Delta, Offshore Brunei Darussalam.” *Journal of the Geological Society* 156: 633–650.
- Veeken, C.A.M., Davies, D.R., Kanter, C.J. and Kooijman, A.P.,** 1991. Sand production prediction review: developing an integrated approach, SPE 22792, in: Annual Technical Conference and Exhibition of the Society of Petroleum Engineers, Dallas, TX, 1991.
- Veeken, P.C.H.,** (1983): seismic Stratigraphy, basin analysis and reservoir characterization: Klaus Helbig and Sven Treitel, (Eds), vol. 37, pp. 111-234. Elsevier Science Ltd., Amsterdam
- Veeken P.C.H.,** (2007): Seismic stratigraphy, basin analysis and reservoir characterization, *Handbook of Geophysics Exploration*, Elsevier, Vol. 37, pp. 421-424.
- Veeken, P.C.H. and Da Silva, M,** 2004, Seismic inversion and some of their constraints. *First Break* 22 (6), 47-70.
- Veeken, P.C.H. and Rauch-Davies, M,** 2006, AVO attribute analysis and seismic reservoir characterisation. *First Break* 24 (2), 41-52.

- Weber, K.** (1971): Sedimentological aspects of oil fields in the Niger Delta. *Geologie en Mijnbouw*, volume 50, pp.559-576.
- Weber, K.J.**, 1986. Hydrocarbon Distribution Patterns in Nigerian Growth Fault Structures Controlled by Structural Style and Stratigraphy: *AAPG Bulletin*, V. 70, pp. 661-662.
- Weber, K. J., and Daukoru, E.M.** 1975. Petroleum geology of the Niger Delta Proceedings of the Ninth World Petroleum Congress, *Geology: London*, Applied Science Publishers, Ltd., 2, 210-221.
- Weber, K.J. and Van Geuns, L.C**, 1990, Framework for constructing clastic reservoir simulation models. *Journal of Petroleum Technology* 42 (10), 1248-1297.
- Whiteman, A.**, 1982. Nigeria: its Petroleum Geology Resources and Potential. Graham and Trotman, London. Vol.1; pp. 394.
- Worthington, P. F.**, 1991 “Reservoir Characterization at the Mesoscopic Scale,” In: I. W. Lake, H. B. Carrol and T. C. Wesson, Eds., *Reservoir characterization*, Academic Press, Waltham, 1991, pp. 123-165.
- Wu, B., Bahri, C., Carigali Sdn Bhd, Tan, C.P., Li, Q., Rahim, H., Kartoatmodjo, G., Wong, T.f., & David, C.** (1997). The transition from brittle faulting to cataclastic flow in porous sandstones: Mechanical deformation.” *Journal of Geophysical Research*, 102 (B2), 3009–3025.
- Wyllie, M.R.J., Gregory, A.R., and Gardner, L.W.**, (1956). Elastic Wave Velocities in Heterogeneous and Porous Media. *Geophysics*, 21 (1): 41-70.
- Wyllie, M.R.J., and Rose W.D.** 1950. Some Theoretical Considerations Related to the Qualitative Evaluations of the Physical Characteristics of Rock from Electric Log Data. *Journal of Petroleum Technology* v. 189, pp. 105-110.
- Xiao, H. and Suppe, J.** 1992. Origin of rollover. *American Association of Petroleum Geologists Bulletin*. 76, 509 – 529
- Xu, H., Zhou, W., Xie, R., Da, L., Xiao, C., Shan, Y., and Zhang, H.**, 2016. Characterization of Rock Mechanical Properties Using Lab Tests and Numerical

- Yale, D.P.**, 1994. Static and Dynamic Rock Mechanical Properties in the Hugoton and Panoma Fields, Kansas. Presented at the SPE Mid-Continent Gas Symposium, Amarillo, Texas, 22-24
- Yu, J.H.Y. and Smith, M.** (2011). Carbonate Reservoir Characterization with Rock Property Invasion for Edwards Reef Complex, *the 73rd EAGE Conference and Exhibition incorporating SPE Europe*, 23 -26 May, Vienna, Austria, 346-350
- Zoback D.** (2007). Reservoir Geomechanics. Cambridge University Press, New York.
- Zoback, M.D., Barton, C.A., Brudy, M., Castillo, D.A., Finkbeiner, T., Grollmund, B.R., Moos, D.B., Peska, P., Ward, C.D., Wiprut, D.J.**, 2003. Determination of stress orientation and magnitude in deep wells. *Int. J. Rock Mech. Min. Sci.* 40, 1049–1076.